

# **Nanostructured Composite Materials for Energy Storage and Conversion**

**Collection of articles**

**Project manager Jānis Kleperis**

**Nanostrukturēti kompozītmateriāli  
enerģijas uzkrāšanai  
un pārveidošanai**

**Rakstu krājums**

**Projekta vadītājs Jānis Kleperis**

**Rīga 2019**

Nanostructured Composite Materials for Energy Storage and Conversion: collection of articles = Nanostrukturēti kompozītmateriāli enerģijas uzkrāšanai un pārveidošanai: rakstu krājums. Kleperis, J. (sast., proj. vad.). Rīga: LU Akadēmiskais apgāds, 2019, 157. lpp.

Latvijas Universitātes Cietvielu fizikas institūta, Latvijas Valsts koksnes ķīmijas institūta, Rīgas Tehniskās universitātes Materiālzinātnes un lietišķās ķīmijas fakultātes Neorganiskās ķīmijas institūta, Latvijas Universitātes Ķīmijas fakultātes, Latvijas Universitātes Bioloģijas fakultātes zinātnieku pētnieciskie rezultāti LZP sadarbības projektā Nr. 666 2014.–2017. gadā.

Reviewers / recenzenti:

- 1) Dr. habil. **Yuriy A. Maletin**, Head of the Department of Nanostructured Carbon Materials for Energy Storage, Institute for Sorption and Problems of Endoecology, National Academy of Sciences of Ukraine, Kiev / Ukrainas Zinātņu akadēmijas Sorbcijas un endoekoloģijas problēmu institūta Enerģētikas uzglabāšanai paredzēto nanostrukturēto oglekļa materiālu nodaļas vadītājs. E-pasts: *ymaletin@yunasko.com*
- 2) Prof. Dr. habil. **Artūrs Medvids**, Head of the Laboratory of Semiconductor Physics, Institute of Technical Physics, Riga Technical University / Rīgas Tehniskās universitātes Materiālzinātnes un lietišķās ķīmijas fakultātes Tehniskās fizikas institūta Pusvadītāju fizikas katedras vadītājs. E-pasts: *Arturs.Medvids@rtu.lv*
- 3) Dr. **Anatolijs Šarakovskis**, Deputy Director for Study Process, Head of Spectroscopy Laboratory, Institute of Solid State Physics, University of Latvia / Latvijas Universitātes Cietvielu fizikas institūta direktora vietnieks mācību darbā, Spektroskopijas laboratorijas vadītājs. E-pasts: *anatolijs.sarakovskis@cfi.lu.lv*



**FLPP**  
FUNDAMENTĀLIE UN  
LIETIŠĶĪE PĒTĪJUMU  
PROJEKTI



LATVIJAS UNIVERSITĀTES  
CIETVIELU FIZIKAS INSTITŪTS  
INSTITUTE OF SOLID STATE PHYSICS  
UNIVERSITY OF LATVIA

Angļu valodas redaktore: Andra Damberga

Latviešu valodas redaktore: Ruta Puriņa

Maketētāja: Rudīte Kravale

ISBN 978-9934-18-411-6

<http://doi.org/10.22364/ncmesc>

© Latvijas Universitāte, 2019

© Autori, 2019

## Contents

Foreword / Priekšvārds . . . . .	5
Introduction / Ievads ( <i>J. Kleperis</i> ) . . . . .	7
1. Synthesis and research of carbon materials with controlled porosity / Oglekļa materiālu ar kontrolētu porainību sintēze un izpēte ( <i>G. Dobele, A. Volperts, L. Jašina, A. Žūriņš</i> ) . . . . .	9
2. Synthesis and research of electrode and solid electrolyte materials for lithium ion batteries / Litija jonu bateriju elektrodu materiālu un cieto elektrolītu sintēze un izpēte ( <i>A. Dindune, J. Ronis, D. Valdniece, A. Orliukas, T. Salkus, V. Venckute</i> ) . . . . .	25
3. Ionic liquids and their modification with lithium salts – synthesis and studies / Jonu šķidrums un to modificēšana ar litija sāļiem – sintēze un pētījumi ( <i>A. Zicmanis, S. Briča, G. Vaivars, E. Sprūģis, J. Singatulovs</i> ) . . . . .	54
4. Selection and modification of microorganisms and substrates for acquiring and separation of energy carriers / Mikroorganismu un substrātu atlase un modifikācija enerģijas nesēju ieguvei un atdalīšanai ( <i>I. Dimanta, M. Paiders, A. Gruduls, V. Nikolajeva</i> ) . . . . .	69
5. Nanostructured materials and their thin films for Li-ion battery electrodes: synthesis, research and performance / Nanostrukturēti materiāli un to plānās kārtiņas Li-jonu bateriju elektrodēm: sintēze, pētījumi un darbība ( <i>G. Kučinskis, K. Kaprāns, G. Bajārs</i> ) . . . . .	101
6. Nanostructured TiO <sub>2</sub> -based materials with photocatalytic properties / Nanostrukturēti TiO <sub>2</sub> materiāli un kompozīti ar fotokatalītiskām īpašībām ( <i>A. Knoks, L. Grīnberga, J. Kleperis, I. Liepiņa, G. Bajārs</i> ) . . . . .	124
7. Synthesis and research of nanosized materials for hydrogen storage applications / Nanomateriālu sintēze un pētījumi ūdeņraža uzglabāšanas pielietojumiem. ( <i>P. Lesničenko, I. Lukoševičs, L. Grīnberga, J. Kleperis</i> ) . . . . .	139
About authors / Ziņas par autoriem . . . . .	152



## Foreword

This teaching aid is intended to support studies of interdisciplinary science branch – Material Science to be used by students of material physics, material science, general chemistry, chemical engineering and applied chemistry, biotechnology, material technologies, engineering and related courses.

The main objective is to demonstrate the relationship between material sciences, physics, chemistry and biology to the daily life, connection with new technology solutions in the energy sector and the economy as a whole, and particularly the importance of nanomaterials as chemical energy harvesters and savers to contribute to the growing use of renewable energy resources.

The achievements of researchers from five different Latvian research institutions working together for four years in the Latvian Scientific Council's Research Collaboration project "Synthesis and studies on controlled porosity composite thin layers and systems for energy storage and conversion applications" in comparison with EU and global research are emphasized in the current collection of articles.

## Priekšvārds

Mācību metodiskais līdzeklis paredzēts izmantošanai materiālfizikas, materiālzinātnes, vispārīgās ķīmijas, biotehnoloģijas, inženierķīmijas un lietišķās ķīmijas kursu studentu mācību procesā.

Galvenais mērķis – parādīt materiālzinātnes, fizikas un ķīmijas zināšanu saistību ar ikdienas dzīves norisēm, jauno tehnoloģiju risinājumiem enerģētikā un tautsaimniecībā kopumā un it sevišķi – nanomateriālu kompozītu kā ķīmiskās enerģijas uzkrājēju nozīmi atjaunojamo enerģijas resursu arvien plašākā izmantošanā.

Akcentēti piecu dažādu Latvijas pētniecības iestāžu pētnieku sasniegumi (salīdzinot tos ar sasniegumiem Eiropas Savienībā un pasaulē) nanostrukturētu materiālu sintēzē un pētniecībā, kā arī enerģijas uzkrāšanā un pārveidošanā. Šādi panākumi gūti, četrus gadus strādājot kopā Latvijas Zinātnes padomes pētnieciskās sadarbības projektā "Kontrolējamas porainības kompozītmateriālu sintēze un pētījumi plāno slāņu un to sistēmu iegūšanai enerģijas uzkrāšanas un pārveidošanas pielietojumiem".



## levads

Projekta mērķis ir, izmantojot specifiskas struktūras oglekļa un litija/ūdeņraža interkalātu kompozītmateriālus, iegūt un pētīt elektrodu slāņus litija baterijām, superkondensatoriem un mikroorganismu degšūnām enerģijas uzkrāšanas un pārveidošanas pielietojumiem. Mērķis tiek īstenots kā vairāku zinātniski pētniecisko institūciju sinerģija 4 zinātnes nozarēs un 8 apakšnozarēs. Elektrodu plāno slāņu ieguve un pētniecība, arī baterijas un degšūnas prototipa izstrāde, attiecināma uz fiziku (13) un tās apakšnozarēm: materiālu fiziku (13.5), cietvielu fiziku (13.1); oglekļa materiālu sintēze – uz ķīmijas (20) apakšnozari “koksnes ķīmija” (20.11), kā arī uz materiālzinātnes (26) apakšnozari “koksnes materiāli un tehnoloģija” (26.4); litija un ūdeņraža interkalātu sintēze un īpašību, struktūru pētījumi attiecas uz ķīmijas (20) apakšnozarēm – neorganisko ķīmiju (20.1) un fizikālo ķīmiju (20.5); ūdeņradi ražojošo mikroorganismu atlase un modificēšana, pārbaude mikroorganismu degšūnās attiecas uz bioloģijas (3) apakšnozarēm “biofizika” (3.2), “mikrobioloģija” (3.11). Projekta konsorciju veido zinātniskas organizācijas (3 zinātniskie institūti un 2 Latvijas Universitātes fakultātes), jo Latvijā nav nevienas atsevišķas zinātniskās institūcijas, kurā tiktu veikti pētījumi visās iepriekš minētās zinātnes apakšnozarēs. Plānotā 3 nozaru un 8 apakšnozaru sinerģija un iepriekšējā pieredze piešķir projektam īpašas priekšrocības un rada pamatu izvirzītā ambiciozā mērķa realizācijas iespējai.

Projekta pētnieciskais darbs ietver jaunu materiālu radīšanu un mikroorganismu atlasi un modificēšanu, izmantojot Latvijā pieejamos resursus – koksni, dūņas vietējās ūdenskrātuvēs un notekūdeņu baseinos, kā arī organiskos ražošanas atkritumus, mikroorganismus no LU Latvijas Mikroorganismu kultūru kolekcijas. LU Ķīmijas fakultātes, Latvijas Valsts koksnes ķīmijas institūta un RTU Neorganiskās ķīmijas institūta pieredze izmantota izejvielu sintēzē kompozītmateriālu plāno slāņu un litija elektrolīta iegūšanai, LU Cietvielu fizikas institūta (CFI) tehnoloģiskās iespējas izmantotas plāno slāņu iegūšanai gan ar magnetrona izputināšanas, gan ar impulsu lāzera metodi. Savukārt LU Bioloģijas fakultātes pieredze un laboratorijas izmantotas mikroorganismu noteikšanā, atlasē, modificēšanā ūdeņraža iegūšanai. Projekta realizācijas rezultātā ir iegūtas jaunas zināšanas par oglekļa materiāliem ar nepieciešamām īpašībām enerģijas uzkrāšanai un par kompozītiem plānslāņu elektrodu iegūšanai litija baterijām, hibrīdbaterijām, mikroorganismu degšūnas elektrodiem, kā arī litija elektrolītu, ūdeņradi ražojošo mikroorganismu kultūrām.

Rezultāti apkopoti 32 publikācijās, 37 ziņojumos 24 vietējās un starptautiskās konferencēs, demonstrēti izstādēs un zinātnes popularizācijas pasākumos. Aizstāvētas 4 zinātņu doktora disertācijas, un tiek gatavotas aizstāvēšanai vēl 5; aizstāvēti 17 zinātņu maģistra darbi. Liels darbs tika ieguldīts sabiedrības izglītošanā, sevišķi jaunākās paaudzes informēšanā, izglītošanā un iesaistīšanā praktiskās aktivitātēs (izstādes (*Minox*, “Vide un enerģija” u. c.), notika sacensības-konkursi (“Saules kauss”), individuāls darbs ar skolēniem laboratorijās (skolēnu zinātniski pētnieciskie darbi), lekcijas skolās (Ilze Dimanta,

Ainārs Knoks, Pēteris Lesničenoks, Līga Grīnberga)), informējot skolēnus gan par sievietēm zinātnē saistībā ar *L'Oreal* stipendijām, gan par nanomateriāliem un ūdeņradi. Jauniegūtās zināšanas projekta realizācijā apspriestas plašākai sabiedrībai pieejamos informācijas resursos, piemēram, 2017. gada 27. aprīlī LTV raidījumā "Izgudrotāji", izstādē "Zināt! Tas ir Latvijas dabā!", kur varēja iepazīties ar zinātnes kalendāru un videomateriāliem; 2016. gadā – Ilzes Dimantas publicitātes pasākumos pēc *L'Oreal* balvas "Sievietēm zinātnē" iegūšanas; 2014.–2017. gadā – LU CFI stendā izstādē "Vide un enerģija".

# 1. Synthesis and research of carbon materials with controlled porosity

## Oglekļa materiālu ar kontrolētu porainību sintēze un izpēte

**Galina Dobele, Aleksandrs Volperts, Lilija Jašina, Aivars Žūriņš**

Latvian State Institute of Wood Chemistry  
Dzērbenes iela 27, Rīga, LV-1006, Latvia  
E-mail: [gdobele@edi.lv](mailto:gdobele@edi.lv)

### Contents

1. <i>Synthesis and research of carbon materials with controlled porosity</i> . . . . .	9
1.1. <i>Introduction</i> . . . . .	10
1.2. <i>Literature review</i> . . . . .	10
1.2.1. <i>Thermochemical activation</i> . . . . .	10
1.2.2. <i>Hydroxides and salts of alkali metals</i> . . . . .	10
1.2.3. <i>Description of pores</i> . . . . .	11
1.2.4. <i>Development of surface structure of biomass-derived carbon materials</i> . . . . .	11
1.2.5. <i>Carbon materials for electrochemical capacitor electrodes</i> . . . . .	12
1.3. <i>Materials and methods</i> . . . . .	14
1.3.1. <i>Precursor carbonization, activation and demineralization</i> . . . . .	14
1.3.2. <i>Supercapacitor electrodes and testing</i> . . . . .	15
1.3.3. <i>AC testing methods</i> . . . . .	15
1.4. <i>Results</i> . . . . .	16
1.4.1. <i>AC structural properties</i> . . . . .	16
1.4.2. <i>Relationship between AC properties and electrochemical characteristics of SC with inorganic electrolyte</i> . . . . .	17
1.5. <i>Conclusions</i> . . . . .	22
1.6. <i>References</i> . . . . .	22
1.7. <i>Kopsavilkums</i> . . . . .	24

### 1.1. Introduction

The application of activated carbon (AC) and its various modifications is of a significant scientific and practical importance, since the use of these materials in various technological areas is on a constant increase – they can be applied for sorption, in rare earth metal membrane separation, metallurgy, electronics, aero- and space technologies, as well as nuclear energy development.

New studies are devoted to the possibilities of AC application, which are being used and developed in the framework of nanotechnologies [1–3]. Specifics of carbon atom electron shell properties place nanoporous carbon materials (NCM) among the most promising nanomaterials, which can be used in various areas of electronics and energetics [4], [5]. Currently, the investments in nanotechnology account for approximately 9 billion dollars

annually, one third of studies being carried out in the USA. Other important investors are the EU and Japan. There are forecasts predicting that in 2017 the number of employees in nanotechnology-based industries could reach 2 million, and the total value of goods produced by nanotechnologies could rise to 1 trillion dollars.

Development of various types of electrochemical devices using NCM is a prerequisite for long-term ecologically friendly technologies, which, in their turn, can provide the development of many technical areas with minimal energy and reagent consumption.

## 1.2. Literature review

### 1.2.1. Thermochemical activation

Treatment of renewable biomass for the production of highly porous carbonaceous materials using chemical activation is of interest worldwide, since these materials can be impregnated easily [6]. By altering conditions of chemical activation, it is possible to control total porosity, pore size distribution and properties of surface functional groups.

For the production of AC, the most crucial technical and economic conditions are precursor properties, uniformity, availability and low costs of both raw materials and activator.

Contrary to steam activation chemical process is faster and proceeds at lower temperatures [1, 7–9]. The main advantage of thermochemical activation is ability to synthesize AC with higher specific surface, which reaches theoretical limits (more than 3000 m<sup>2</sup>/g according to BET theory) [10, 11]. Usually, alkali metals hydroxides and carbonates are used as activation agents (most often those containing Na and K cations), as well as ZnCl<sub>2</sub>, H<sub>3</sub>PO<sub>4</sub>. In some cases, K<sub>2</sub>S, AlCl<sub>3</sub>, FeCl<sub>3</sub>, SnCl<sub>2</sub>, etc. are used.

Activators can be separated into two groups according to the mechanism of their action: acidic-alkali (ZnCl<sub>2</sub>, H<sub>3</sub>PO<sub>4</sub>) and redox (KOH, NaOH, K<sub>2</sub>CO<sub>3</sub>) mechanism. The details of chemical activation agent interaction mechanisms are not completely explored; however, it is known that agents that belong to both groups activate aliphatic compounds transformations, especially scission of aryl-alkyl C-C bonds. Also, they selectively remove oxygen, hydrogen and other heteroatoms with simultaneous carbonization.

### 1.2.2. Hydroxides and salts of alkali metals

Efficiency of metal hydroxides as activators in redox processes for AC synthesis has been proven repeatedly. Alkali activation process comprises four main stages: 1) impregnation or mixing of precursor with alkali (ratio 1–7 g/g), 2) heating up to activation temperature (700–900 °C); 3) isothermal treatment (1–5 hours) at activation temperature; 4) mixture cooling and AC demineralization [12]–[14]. AC forms in the end of stage three.

Hydroxides of alkali metals interact with coals, wood and its components already at room temperature [15]. In the temperature range 600–800 °C, organic material reactions with alkali are much more vigorous.

Thermally initiated reactions with MeOH (where Me = K<sup>+</sup> or Na<sup>+</sup>) lead to three main processes:

1. formation of metal containing surface complexes;
2. their transformation into carbonates and oxides (mostly Me<sub>2</sub>CO<sub>3</sub> and Me<sub>2</sub>O) as a result of the reaction with C atoms at the edges of graphene layers;
3. reduction of Me<sub>2</sub>CO<sub>3</sub> and Me<sub>2</sub>O to metals and their intercalation into interlayer space of crystallites.

Reduction and intercalation of metals are two main factors defining formation of adsorbent nanoporous structure [16]. If the process takes place in the ideal conditions, the type of precursor (biomass, coal, etc.) is of no real importance. The efficiency of porous structure development is directly dependent on the presence of oxygen in the functional groups of carbon material surface [17]. AC characteristics are also significantly influenced by the ratio MeOH/precursor and type of hydroxide. Without alkali agents, it is virtually impossible to obtain highly porous material with developed nanoporous structure [18].

### **1.2.3. Description of the pore structure**

When the wood is activated, it forms AC with wide spectrum of specific surface and pore size distribution, which are governed by the conditions of activation. AC have a multitude of pores and thus large specific surface, volume and, as a result, high sorption ability (1 g of AC can have the specific surface from 500 to 2500 m<sup>2</sup>/g, depending on the method of synthesis).

AC have macro-, meso- and micropores. Depending on sizes of the molecules to be adsorbed on the carbon surface, it is necessary to synthesize AC with various pore size distributions. Classification of pores is based on their linear sizes, namely, width for slit-like pores, or diameter or radius for cylindrical or spherical ones. According to IUPAC, pores are classified, as follows [8], [19], [20]:

- micropores < 2 nm
- mesopores 2–50 nm
- macropores 50–200 nm

The role of macropores in the sorption process is to provide transport pathways for the molecules of the adsorbed substance and to enable them to reach deeper into the sorbent particles. Their surface is not extensive, around 0.5–2 m<sup>2</sup>/g, and the sorption in these pores is the same as in the case of non-porous carbon with the same chemical composition.

Mesopores are being formed at the stage of carbonization, and at the next step – activation. The most important factor in the synthesis of mesoporous materials is precursor structure. Their specific surface is from 10 up to 400 m<sup>2</sup>/g. Mesopores significantly influence sorption of larger molecules [20].

Micropores form, when precursor is activated with oxidation agent or in thermal treatment process in the presence of chemical activator. The main property of micropores is that their size is comparable to the size of adsorbed molecules and adsorption energy in these pores is higher than in macro- and mesopores. Micropores have considerable sorption volumes and play the main role in sorption processes [1]. Term “nanopores” is often used as a synonym for micropores.

Ability of AC to adsorb various molecules is governed by its surface structure, as well as composition of surface functional groups and their composition. The most reaction able are oxygen containing functional groups, such as phenol-, carbonyl-, carboxyl-, ether-, enol- and lacto [1], [8]. For the industrial applications, the brands of AC are described by using specific porosity parameters, adsorption ability and particle sizes. Nowadays, 40% of AC is being produced from wood, 40% – from brown coal or lignite, 10% from peat and around 10% from coconut shells [1].

### **1.2.4. Development of surface structure of biomass-derived carbon materials**

Development of surface structure of the biomass-derived carbon materials takes place at the all stages of their thermal treatment. In the temperature range of 600–1000 °C,

heteroatoms are being removed from precursor, carbon partially transforms into  $sp^2$ -hybridization state and is partially removed in a form of volatile or liquid products. In the bulk form of carbon material solid network, graphene structures consist of flat polynuclear aromatic molecules with two-dimensional distribution of carbon atoms. With the increase of temperature, the parallel graphene layers form clusters, which size and structural distribution degree increase with the increase of treatment temperature [21].

Charcoals have a low porosity and consist of elementary crystallites, which are separated with slit-like pores, however, these pores are filled and blocked with chaotic carbon residue (coke). In the process of activation, the filled pores open up and porosity develops. By varying precursor and activation conditions, it is possible to control total porosity and pore size distribution.

The increase of the temperature intensifies condensation reactions, thereby starting the localization of graphite units and formation graphite-like microcrystalline structure, or, in other words, the coalescence of aromatic layer or “graphene planes”. [21].

Carbon material properties and activation conditions define the size and number of graphene layers, and sizes and orientation of crystallites define material's texture and electric conductivity.

Activated carbon structure consists of flat layered packages formed by condensed hexagonal rings of aromatic carbon. The orientation of separate moieties in microcrystallites is random, and the layers are independently tilted towards one another [22] – this kind of structure is called turbostratic. The average thickness of microcrystallites is 1–1.3 nm, which means that they contain 13–20 condensed hexagonal aromatic ring layers [23]. At the next stage of activation, a part of microcrystalline aromatic rings burns out and slit-like pores form – not only between the borders of crystallites, but also inside their bulk.

Carbon has four allotropic forms – diamond ( $sp^3$  – hybridization), graphite ( $sp^2$  – hybridization), nanotubes ( $sp^2$  – hybridization), carbene ( $sp$  – hybridization) and fullerenes (twisted  $sp^2$  – hybridization). Only two of these forms, namely, diamond and graphite, can be found in nature, others are obtained via synthesis. The multiple properties of carbon are not limited by the variety of its allotropic forms and are governed by a number of its physical properties [24].

Carbonization of carbon materials takes place in the solid state, and crystallite mobility is limited, leading to the formation of rigid amorphous structure containing disordered graphene layers. Further thermal treatment does not lead to graphitization, and these materials are being called non-graphitizable carbon forms.

### 1.2.5. Carbon materials for electrochemical capacitor electrodes

From the 1980s, highly porous carbon materials are being used not only for sorption technologies, but also for electric energy accumulation and transfer without using electrical power sources, as well as for energy consumption peaks. Electrochemical capacitors with double electric layer or supercapacitors (SC) are among the most important developments in this area, and in these devices AC are used as electrodes [25]–[28]. The concept of double electric layer was developed by Helmholtz [29]. The first double layer capacitors were patented by General Electric in 1957 [30]. Charge accumulation and preservation in electrochemical capacitors take place in double electric layer, which forms on the electrode/electrolyte interface, consequently, the electrode material has to meet a number of requirements, such as low density, electric conductivity, and developed porous structure, which should fit ions and molecules of electrolyte (Fig. 1.1).

During charging, the positive charges gradually accumulate on one plate (positive electrode), while the negative charges accumulate on the other plate (negative electrode). When the external voltage difference is removed, both the positive and negative charges remain at their corresponding electrodes. This way, the capacitor plays a role in separating electrical charges. The voltage difference between the two electrodes is called the cell voltage of the capacitor. If these electrodes are connected by using a conductive wire with or without a load, a discharging process occurs—the positive and negative charges will gradually combine through the wire. Thus, the capacitor plays a role in charge storage and delivery [4], [31].

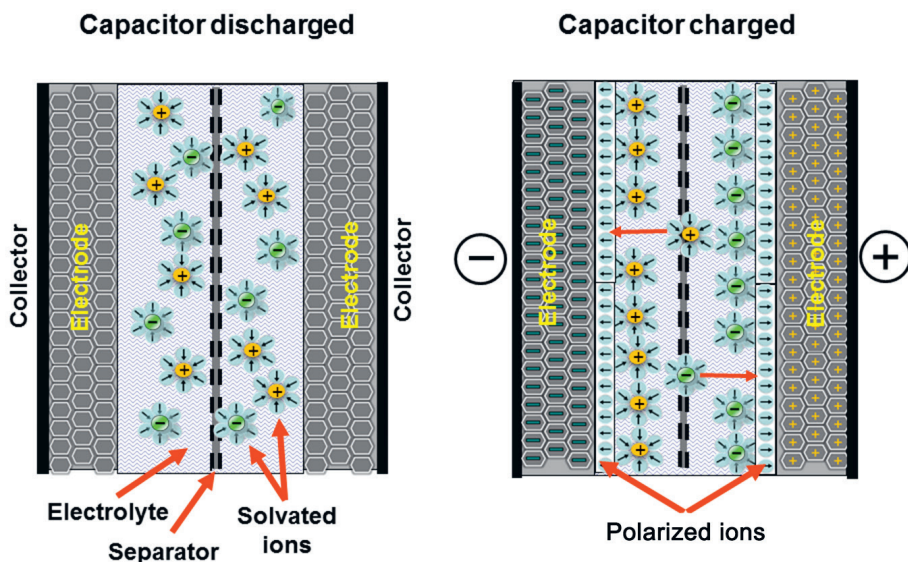


Figure 1.1. Operation principles of supercapacitor

When charged, a capacitor connected in a circuit will act as a voltage source for a short time. Its capacitance ( $C$ ), which is measured in farads ( $F$ ), is the ratio of electric charge on each electrode ( $Q$ ) to the potential difference between them ( $V$ ), so that [4]:

$$C = Q/V$$

For a typical parallel plate capacitor, capacitance is proportional to the area of each electrode and the permittivity of the dielectric, and inversely proportional to the distance between the electrodes.

Two primary attributes of a capacitor are its energy and power density, both of which can be expressed as a quantity per unit weight (specific energy or power) or per unit volume ( $F/g$  or  $F/mm^3$ ). The energy stored in a capacitor is related to the charge at each interface and the potential difference, and therefore is directly proportional to its capacitance.

Electrochemical double layer capacitors hold the position between batteries, which can accumulate large amounts of energy and conventional capacitors, which can release energy in milliseconds (Fig. 1.2). SC are widely used in automotive production (braking energy recuperation, improvement of engine start up, electrical stabilization), industry (forklifts,

elevators), as well as in customer electronics. SC can provide a higher energy density in comparison with dielectric capacitors, and higher power density than batteries [31], [32]. SC attract interest in various areas, since they are able to release high power in a short period of time – seconds or less. They can be used in cars, trams, buses, construction cranes, lifts and many other appliances. Meeting the demands for worldwide consumption of SC requires both new approaches and electrode material development. The carbon material best suited for this aim has to have low cost, wide nanotexture spectrum and structural variance, as well as high electric conductivity.

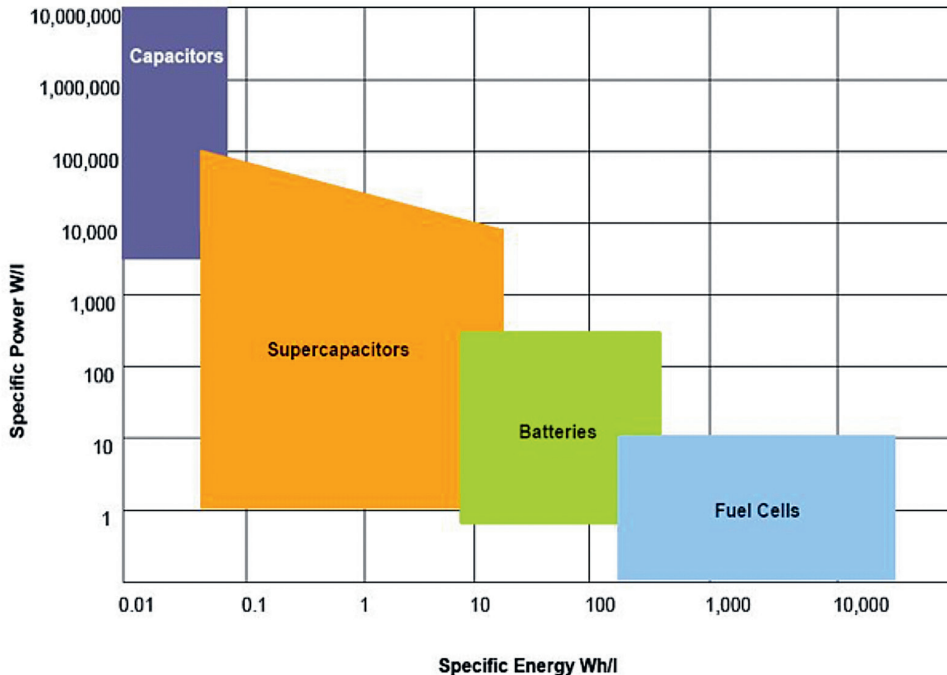


Figure 1.2. Comparison of specific energy and power in dielectric capacitors, SC, accumulators and fuel cells

### 1.3. Materials and methods

#### 1.3.1. Precursor carbonization, activation and demineralization

White alder and birch wood mechanical processing wastes and charcoal (SIA File 2000, Koceni, Latvia) were used as raw materials.

The main stage of AC synthesis from wood and lignocellulosic materials is activation with sodium hydroxide, and the whole process consists of the following steps: 1) Carbonization; 2) Impregnation with alkali; 3) Activation; 4) Demineralization. Two thermal treatment stages are used for the AC synthesis. Carbonization includes heating of precursor up to 300–500 °C and treatment at this temperature for 90–300 min. Activation was performed at 600–800 °C for 60–120 minutes in stream of argon. The schematic representation of AC synthesis is shown in Fig. 1.3.

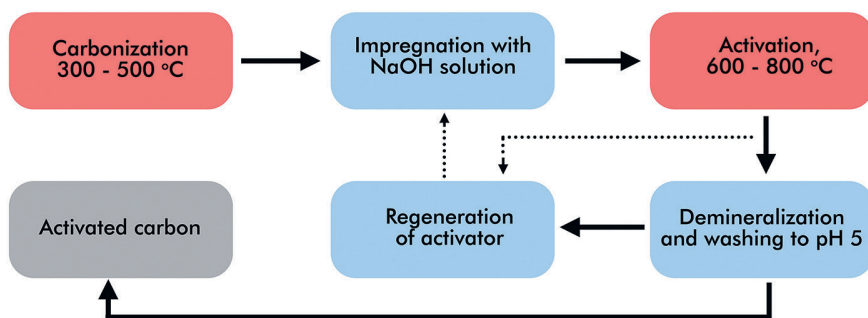


Figure 1.3. AC synthesis on the base of plant biomass

### 1.3.2. Supercapacitor electrodes and testing

AC was mixed with ethanol and then with PTFE water suspension as a binder, which was brought to a pasty condition and then calendared in rollers. Then the electrodes were dried and impregnated with 4.9 M sulfuric acid under vacuum. Porous polypropylene membrane was used as a separator, and 200  $\mu\text{m}$  thermos-expanded graphite foil served as a substrate-current collector. Thus, the mass of the cell includes all of the components mentioned above. Thickness of assembled electrode was 400  $\mu\text{m}$  ( $\pm 10\%$ ), active area of electrodes was 4.15  $\text{cm}^2$ , and areal density was 19–24  $\text{mg}/\text{cm}^2$ . The electrode thickness was chosen as the most important parameter.

SC cell was pressed at 1 MPa between gold plates connected to potentiostat Elins 30-S. Contact resistance between gold plates and SC cell, as well as resistance of wiring was less than 2% of SC intrinsic resistance, and their input was not taken into account for further calculations.

Carbons were tested by cyclic voltammetry. Each SC cell was first cycled in the 0–1000 mV range at 20 mV/s rate until stable voltammograms were observed. Then cells were charged and discharged in the galvanostatic mode with the aim to reach discharge times of 10 and 200 s. The former is related to breaking energy recuperation and the latter to situations, where capacity is not governed by this relatively small current and can be used to assess SC maximum capacitance. Intrinsic resistance was determined from the potential drop on current peak at the initiation of the discharge. To determine power density, SC cells were charged in a potentiostatic mode at 1 V from 5 min. Then cells were charged and discharged aiming at discharge times of 10 and 200 s.

### 1.3.3. AC testing methods

Laser diffraction was used to control changes of AC particles' sizes during refining process. Specific surface, pore size and volume were calculated by using  $\text{N}_2$  adsorption isotherms applying BET, DR and DFT theories. Raman spectroscopy was used to study structural changes of AC. Elemental composition was determined by using CHNS elemental analysis. Study of volatiles formation in carbonization and activation processes was performed by using TG/MS technique. Thermodynamical interaction (heat evolution) determination of activated carbons surface functional groups with liquids depending on activation condition was performed by using immersion calorimetry. Ash content was determined according STM D2866 standard. Microstructure of obtained AC was studied with electron scanning microscopy.

## 1.4. Structural and electrochemical properties of activated carbons

The aim of this study was the elucidation of the dependence of porous structure of alkali activated carbons as a function of synthesis' parameters and measurement of the electrochemical characteristics of supercapacitors made applying AC electrodes.

### 1.4.1. AC structural properties

**AC dispersity.** It is known that when AC are used in electrochemical devices, the electric resistance decreases with the decrease of AC particles' size, since it leads to the enhancement of effective surface contact between power source and electrode, as well as the number of contacts among the particles of active material, which results in a better electron percolation in electrode [33], [34].

Besides, it was found that AC particles decrease down to  $\sim 0.6 \mu\text{m}$  positively influences SC capacity, since it provides for a better pore availability and their decreased depth, which significantly improves migration and adsorption of electrolyte ions [34].

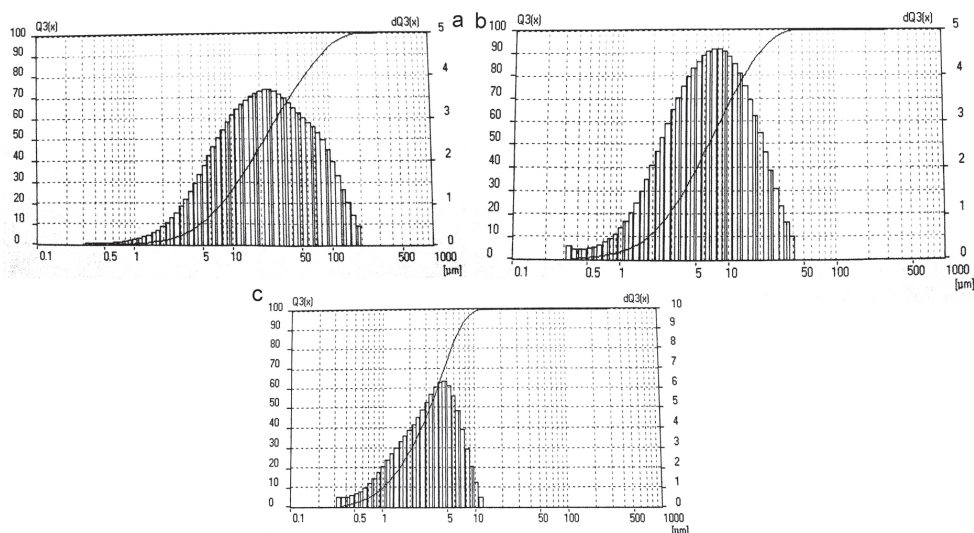
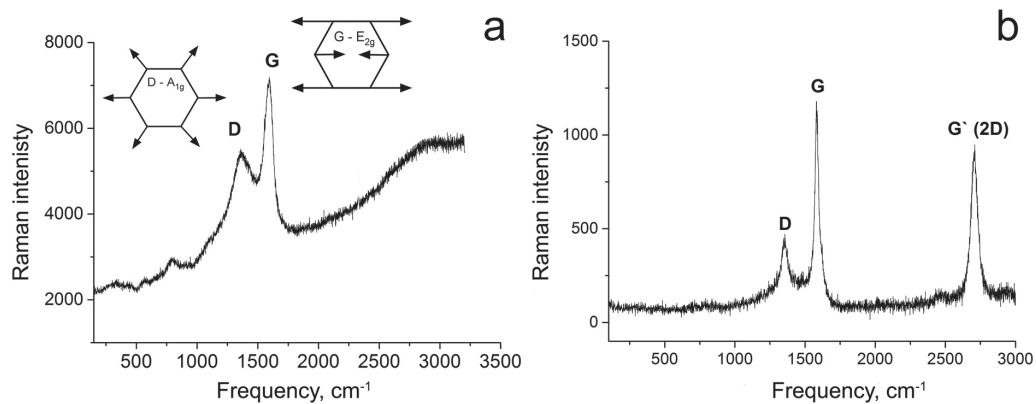


Figure 1.4. AC particle size changes in the process of refining: (a) Retch SM100 knife-type mill; (b) CBM-3H ball mill, 1-hour processing; (c) CBM-3H ball mill, 1-hour processing

To achieve uniform carbonizate particle size, the material first underwent rough treatment in knife-type mill, and then was refined in the ball-type vibrating mill (1 and 2 hours) to achieve particle size in the range of 1–5  $\mu\text{m}$  with a relatively narrow distribution. The changes in material particle size were detected by using laser diffraction (illustration in Fig. 1.4).

It should be noted that SC life cycle is negatively influenced by the particles with sub-micron size [35], thus, the chosen particle size can be asserted as the most beneficial for the study.

**Raman spectroscopy.** The tests of AC structure were performed by using Raman spectroscopy. According to a widespread opinion, solid phase of carbons predominantly consists of polyaromatic graphene clusters (crystallites) [36], [37]. Raman spectra of carbonized wood and AC obtained from carbonized wood at 700  $^{\circ}\text{C}$  in the presence of NaOH are shown in the Fig. 1.5.



**Figure 1.5. Raman spectra of wood carbonizate (a) and AC (Carbonizate-P + NaOH, K = 2, activation temperature 700 °C) (b) (D – amorphous carbon structure; G – graphite structure; G' (or 2D) – two-dimensional carbon structures (graphenes))**

The Raman-active vibration numbering for natural single-crystal graphite exhibits a single Raman peak at around 1580 cm<sup>-1</sup>, called the **G** peak. This peak is associated with the in-plane C–C stretching mode of the *sp*<sub>2</sub> hybridized carbon atoms. For polycrystalline graphite, depending on the size of the crystallites, a second peak at 1350 cm<sup>-1</sup> appears, namely, the disorder or **D** peak. When the degree of material crystallinity decreases carbon phase becomes glassy, both the G and the D peaks broaden (Fig. 1.5 (a)) [38]. Three Raman scattering peaks at around 1364, 1596 and 2325 cm<sup>-1</sup> are observed in the case of AC (Fig. 1.5 (b)). The peak at 1580 cm<sup>-1</sup> (G band) is attributed to an E<sub>2g</sub> mode of graphite and is related to the vibration of *sp*<sub>2</sub> – bonded carbon atoms. For polycrystalline graphite, depending on the size of the crystallites, a second peak at 1350 cm<sup>-1</sup> appears, namely, the disorder or D peak. Decreasing particle size or bending of the lattice fringes may activate this band, and this phenomenon can be observed after activation [38]. Additionally, peak G' (or 2D) ~2500 cm<sup>-1</sup> can be seen for the activated sample (1.5. (b)) – it is characteristic to graphenes and point at the presence of two-dimensional structures.

Raman spectroscopy data allow calculating of crystallites sizes of obtained AC, which is important for stabile operation of electrochemical high capacity devices. As a result of Raman spectra deconvolution and numerical integration, the calculation of average sizes of crystallites for the samples under study ~9.8 nm was implemented, which was beneficial for the electrochemical devices [39].

#### **1.4.2. Relationship between AC properties and electrochemical characteristics of SC with inorganic electrolyte**

In order to evaluate the influence of AC properties on SC characteristics, a number of experiments was performed to assess the most promising conditions of synthesis, which would enable achieving the highest specific capacitance and power of SC. As mentioned before, the most viable raw material for this task is wood carbonizate. It already has been shown [40] that AC obtained from birch or white alder wood have practically identical porous structure properties, and it can be assumed that both wood types are interchangeable within the scope of this work.

Wood-based AC with different NaOH mass ratios to carbonizate (further denoted as K) equal to 3.7 and 1.25 were obtained by using two stage thermochemical synthesis (1 – carbonization at 400 °C, 2 – activation) (Table 1.1, samples T-1 and T-2). Sample T-2 was synthesized from commercial charcoal on the base of white alder (SIA “Fille 2000”) and activated in the same conditions as T-1 without additional carbonization. Comparatively cheap commercial charcoal is considered as a precursor due to three reasons: firstly, it will allow to synthesize AC in one stage, secondly – a local readily available feedstock can be used to synthesize material with a high added value, thirdly – this material has stable properties, and is produced in Latvia in large quantities.

All three samples have high specific surfaces ( $S_{\text{BET}}$  T-1 – 3297 m<sup>2</sup>/g, T-2 – 3304 m<sup>2</sup>/g and T-3 – 1659 m<sup>2</sup>/g), and similar micropore volumes ( $V_{\text{mikro}}$  T-1 – 823 m<sup>3</sup>/g, T-2 – 828 m<sup>3</sup>/g and T-3 – 791 m<sup>3</sup>/g) despite the differences in surface areas. This is an indication of prominent presence of mesoporosity in the structure samples activated at 700 °C and K = 3.7.

All the samples are good candidates for SC or as highly effective sorbents regardless of their differences in porosity. It was found that structural parameters for samples T-1 and T-2 are similar. This is an indication of possibility to use commercial charcoals as a precursor in further experiments.

Samples T-1 and T-2, and commercial AC from various countries were tested as electrodes in SC with H<sub>2</sub>SO<sub>4</sub> electrolyte. For T-1 and T-2, specific capacitances were, respectively, 310 and 318 F/g (Table 1.1).

However, probably due to the high pore volume of synthesized AC, electrodes had low density and, respectively, electrolyte volume was high and inefficient. The high capacity of SC was prominent only based on dry mass calculation, and it was less meaningful, if calculated on the basis of whole cell weight (Table 1.1).

*Table 1.1. Comparison of characteristics of SC with electrodes made from synthesized and commercial AC and carbon fiber cloth (2M H<sub>2</sub>SO<sub>4</sub> electrolyte)*

Sample	Specific capacitance F/g (at 0.3 A/g)	Specific resistance, Ohm/cm	Pore volume (width < 10 nm), mm <sup>3</sup> /g	Electrolyte volume, mm <sup>3</sup> /g	Cell specific power, Wh/kg
<b>T-1 (700 °C, K = 3.7)</b>	<b>310</b>	<b>4.5</b>	1550	2311	<b>2.16</b>
<b>T-2 (700 °C, K = 3.7)</b>	318	<b>4.3</b>	1290	2202	<b>2.23</b>
<b>T-3 (600 °C, K = 1.25)</b>	<b>390</b>	<b>4.6</b>	799	1401	<b>3.06</b>
YP-50F Kuraray (Japan)	182	4	800	1350	1.81
V2 EnerG2 (USA)	182	4	800	1290	1.85
XH-001W Shanxi Xinhui (China)	254	4.4	1000	1670	2.4
Carbon fabric UVIS- AK – T 0.41 (Russia)	211	7.5	370	1170	2.35
Maxsorb-3 (Japan)	320	–	–	2800	–

To elucidate the dependence of SC properties from AC porosity, the unorthodox approach was taken – AC pore volume reduction at varying temperatures and K-ratio. The results of wood-based AC porous structure tests are presented in Fig. 1.6.

Based on the isotherms of AC synthesized in the temperature range 600–800 °C ( $K = 2$ ) (Fig. 1.6 (a)), it can be concluded that adsorbed gas volume increases in activation temperature range from 600 to 700 °C at  $K = 2$  and isotherms belong to Type I, which indicates that AC are microporous. Isotherm of AC activated at 800 °C is different from those of ACs synthesized at lower temperatures and illustrates the presence of both micro- and mesopores. The same effect is observed in Fig. 1.6 (b), showing isotherms of AC activated at 700 °C with  $K$  values between 1 and 3.7. At  $K = 1$  and 2, isotherms correspond to microporous sorbent (Type I) and with the increase of activator/ carbonizate ratio, both the isotherms and adsorption mechanisms are changed.

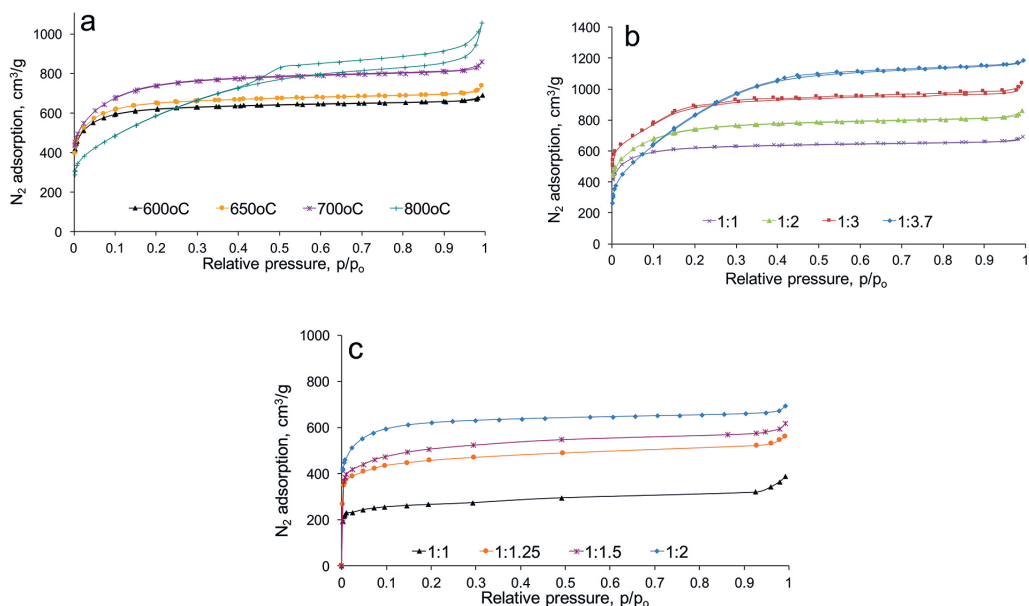


**Figure 1.6.**  $N_2$  adsorption isotherms for AC synthesized in various conditions: (a)  $K = 2$ , activation temperature variation 600–700 °C; (b) activation temperature 700 °C,  $K$  variation 1–3.7; (c) activation temperature 600 °C,  $K$  variation 1–2

At  $K = 3.7$ , the shape of isotherm changes starting at the relative pressure 0.1 and upward, illustrates that pore filling is governed by both volume filling and capillary condensation and that mesopores are present, as well as wider pore size distribution. Isotherms of AC activated at 600 °C and lower  $K$  (Fig. 1.6 (c)) also illustrate that with increasing  $K$  in the range from 1 to 2, the volume of adsorbed nitrogen increases and samples are microporous.

The synthesized AC were used as electrodes in SC cells with sulfuric acid electrolyte. Porous structure and SC characteristics relationships are shown in Fig. 1.7.

The calculations based on data of isotherms show that activator ratio increase ( $K$  varies from 1.5 to 3.7) at 700 °C leads to the development of specific surface ( $S_{\text{BET}}$ ) and total volume ( $V_{\text{total}}$ ), however, micropore volume ( $V_{\text{micro}}$ ) increases until  $K = 2$ , and after that remains practically the same (Fig. 1.7 a). With the increase of pore volume, the amount of adsorbed electrolyte ( $V_{\text{H}_2\text{SO}_4}$ ) increases until  $K = 2.25$ , remains the same until  $K = 3$ , and after that rapidly increases again. With the alteration of activator ration, the specific capacitance of SC changes negligibly. It is the same for all samples in the range of  $K$  from 1.7 to 3.7 – 310 F/g.

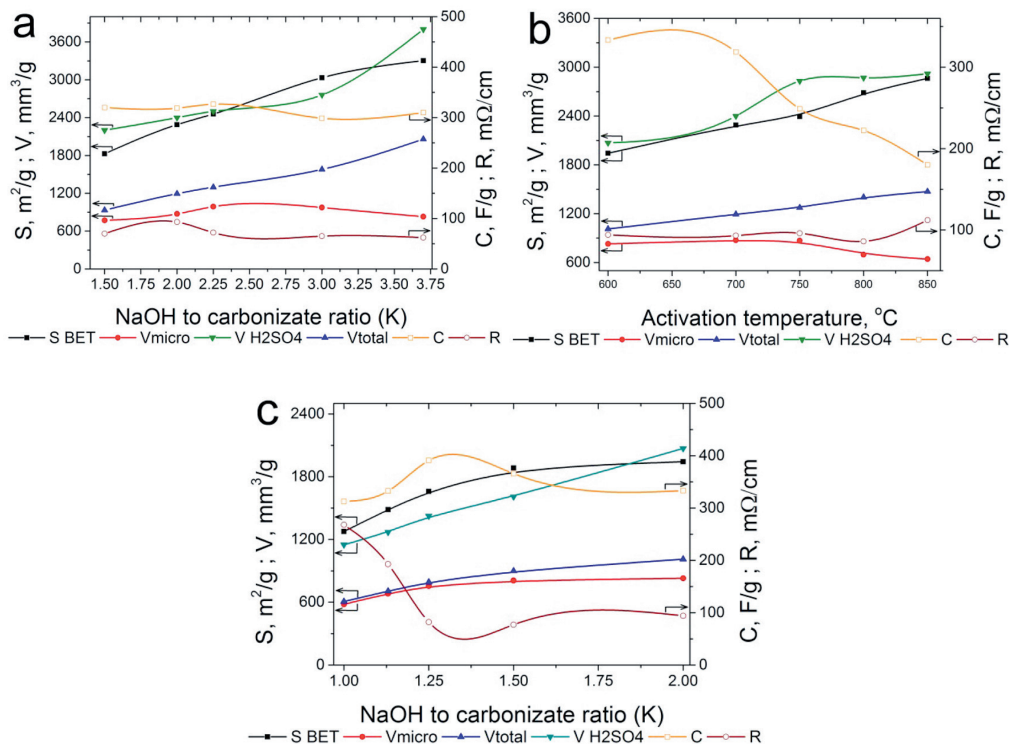


Figure 1.7. Dependence of AC porous structure and SC characteristics from: (a)  $K$  at 700 °C; (b) activation temperature at  $K = 2$ ; (c)  $K$  at 600 °C  
 $S_{\text{BET}}$ ,  $V_{\text{micro}}$ ,  $V_{\text{total}}$ ,  $V_{\text{H}_2\text{SO}_4}$  – volume of adsorbed electrolyte,  $R$  – resistance and  $C$  – specific capacitance

The insignificant influence of  $K$  at 700 °C on the capacity (Fig. 1.7 (a)) can be explained by the fact that a minimal pore volume is required for the electrical double layer formation. Probably, there is a factor, which counteracts the positive effect of mesoporosity increment – this observation can be interpreted by the change of oxygen-containing functional groups on the surface. These groups can contribute to SC capacitance due to redox reactions (also called the pseudocapacitance effect) and can also elevate the hydrophilicity of surface pores, where EDL is formed. This parameter will be evaluated and discussed further below.

Another important parameter influencing carbon material properties in the process of synthesis is activation temperature. The characteristics of AC activated at 600–850 °C and  $K = 2$  are presented in Fig. 1.7 (b). With the increasing activation temperature keeping the constant activator ratio, the total pore volume does not change significantly, but the micropore volume reaches its maximum at 700 °C, and after that a negative trend can be observed. The same is true for SC capacity, which practically does not change in 600–700 °C range – it is 330 F/g in case of 600 °C, but it is lowered to 180 F/g in case of 850 °C. This means that, in this case, activation temperature and activator ratio decrease positively influences SC electrochemical characteristics, as well as AC production expenses.

At higher activation temperatures, the total volume of electrolyte in the electrodes increases significantly. At the same time, the intrinsic resistance practically does not change with activation temperature increment in the range from 600 °C to 800 °C (Fig. 1.7 (b)). At the higher activation temperatures, the resistance increases, probably due to the presence of larger pore volumes. Most likely, the capacitance decrement with activation temperature increase can be explained by the decrease of C-O groups content on the carbon surface, a parameter, which influences pseudocapacitance.

Thus, the activation temperature decrement positively influenced specific properties of SC taking into account cell mass. The experimental data for AC synthesized at lower activator to precursor ratios and 600°C are presented in Fig. 1.7 (c). The increase of NaOH ratio from 1 to 2 leads to higher values of total and micropore volumes, and in the  $K$  range 1.5–2 the latter does not change. An increase of porosity entails an increase of adsorbed electrolyte volume. With the elevation of  $K$  from 1 to 1.25, the capacitance of SC increases and its resistance rapidly decreases, reaching maximum and minimum, respectively (Table 1.1, sample T-3). With a further increase of  $K$  from 1.25 to 2, the capacity decreases with practically constant values of electrode resistance.

The alterations in wood activation conditions, specifically, decrease of activation temperature and  $K$ , lead to an increase of specific power capacity up to 30% calculating on elementary cell mass.

The activation temperature or/and activator ratio increment lead to formation of additional pores, which adsorb electrolyte. Probably, pore walls become thinner with the increase of activation temperature, which can negatively influence EDL formation. This assumption was proven by authors of [41], who found that potential distribution in CM has the main influence on the system capacity compared to potential distribution in the aqueous electrolyte. Solid phase contribution into the SC intrinsic resistance for the electrolytes with high and low ionic conductivity is different. For the water-based electrolyte with higher ionic conductivity, its effect is more pronounced than that of the organic electrolyte. The lower cell wall thicknesses can have a negative influence on the solid phase coherency, which, in its turn, leads to increase of ohmic losses due to a diminished contact between carbon particles in the electrodes.

Judging from the dependency of SC characteristics on activation temperature, the increase of adsorbed electrolyte volume is not accompanied with intrinsic resistance decrement and specific capacitance increment. This can be explained by two factors. Firstly, deepening of pores can cause difficulties for ion penetration because of gating and uneven charge distribution inside micropores. Secondly, narrower micropores can have a positive influence on specific capacitance due to distortion of ions' solvation shells inside carbon nanostructure, which leads to a closer approach of the ion center to the electrode surface and results in an improved capacitance.

## 1.5. Conclusions

The principal possibility for obtaining of nanoporous activated carbons from hardwood and charcoal by using thermochemical activation, are studied. This research has resulted in award of one international patent and one patent issued in the Republic of Latvia.

The optimal properties of wood thermochemical activation for activated carbons' porous structure formation and adsorption properties, providing necessary electric double layer formation in supercapacitor electrodes were determined.

The correlation was determined between parameters of activated carbon synthesis, porous structure and properties of supercapacitors with aqueous electrolyte. It was found that in the case of sulfuric acid electrolyte application of activated carbon with pore volume  $790 \text{ m}^3/\text{g}$  and specific surface  $1660 \text{ m}^2/\text{g}$  led to development of supercapacitor with specific capacitance of  $390 \text{ F/g}$  and power  $3.06 \text{ Wh/kg}$ .

## 1.6. References

1. Marsh, H. and Rodriguez-Reinoso, F. (eds.). (2006) *Activated Carbon*. Amsterdam: Elsevier Science.
2. Díaz-Terán, J., Nevskaiia, D. M., Fierro, J. L. G., et al. (2003) Study of chemical activation process of a lignocellulosic material with KOH by XPS and XRD. *Microporous Mesoporous Mater.*, 60(1–3), 173–181.
3. Lillo-Ródenas, M. A., Juan-Juan, J., Cazorla-Amorós, D. and Linares-Solano, A. (2004) About reactions occurring during chemical activation with hydroxides. *Carbon N. Y.*, 42(7), 1371–1375.
4. Béguin, F. and Frackowiak, E. (eds.). (2013) *Supercapacitors: materials, systems, and applications*. Zurich: Wiley-VCH.
5. Harper, T. (ed.). (2011) Global Funding of Nanotechnologies & Its Impact. *Cientifica*, London, 8.
6. Schüth, F., Sing, K. S. W. and Weitkamp, J. (eds.). (2002) *Handbook of porous solids*. Zurich: Wiley-VCH.
7. Ioannidou, O. and Zabaniotou, A. (2007) Agricultural residues as precursors for activated carbon production. *A review. Renew. Sustain. Energy Rev.*, 11(9), 1966–2005.
8. Bansal, R. C. and Goyal, M. (eds.). (2005) *Activated carbon adsorption*. Taylor & Francis.
9. Микова, Н. М., Иванов, И. П., Парфёнов, В. А et al. (2011) Влияние условий термической и химической модификации на свойства углеродных материалов, получаемых из древесины берёзы. *Журнал Сибирского федерального университета. Серия: Химия*, 4, 356–368.
10. Lillo-Ródenas, M. A., Marco-Lozar, J. P., Cazorla-Amorós, D. and Linares-Solano, A. (2007) Activated carbons prepared by pyrolysis of mixtures of carbon precursor/alkaline hydroxide. *J. Anal. Appl. Pyrolysis*, 80(1), 166–174.
11. Tamarkina, Y. V., Shendrik, T. G., Kucherenko, V. A. and Khabarova, T. V. (2015) Conversion of Alexandriya brown coal into microporous carbons under alkali activation. *Chemistry (Easton)*, 5(1), 24–36.
12. Béguin, F. and Elzbieta, F. (eds.). (2010) *Carbons for electrochemical energy storage and conversion systems*. Boca Raton: CRC Press.
13. Torné-Fernández, V., Mateo-Sanz, J. M., Montané, D. and Fierro, V. (2009) Statistical Optimization of the Synthesis of Highly Microporous Carbons by Chemical Activation of Kraft Lignin with NaOH. *J. Chem. Eng. Data*, 54(8), 2216–2221.
14. Babel, K. and Jurewicz, K. (2004) KOH activated carbon fabrics as supercapacitor material. *J. Phys. Chem. Solids*, 65(2–3), 275–280.

15. Camier, R. and Siemon, S. (1978) Colloidal structure of Victorian brown coals. 1. Alkaline digestion of brown coal. *Fuel*, 57(2), 85–88.
16. McKee, D. W. (1983) Mechanisms of the alkali metal catalysed gasification of carbon. *Fuel*, 62(2), 170–175.
17. Eletsksii, P. M., Yakovlev, V. A., Fenelonov, V. B. and Parmon, V. N. (2008) Texture and adsorptive properties of microporous amorphous carbon materials prepared by the chemical activation of carbonized high-ash biomass. *Kinet. Catal.*, 49(5), 708–719.
18. Тамаркина, Ю. В., Цыба, Н. Н., Кучеренко, В. А and Шендрик, Т. Г. (2013) Получение пористых материалов щелочной активацией ископаемых углей разной степени метаморфизма. *Вопросы химии и химической технологии*, 3, 132–137.
19. Rouquerol, F., Rouquerol, J., Sing, K. S. W., et al. (eds.). (2014) *Adsorption by powders and porous solids*. Academic Press.
20. Gregg, S. J. and Sing, K. S. W. (eds.). (1982) *Adsorption, surface area, and porosity*. London: Academic Press.
21. Кузнецов, Б. Н. (1999) Синтез и применение углеродных сорбентов. *Соросовский образовательный журнал*, No.12, 29–34.
22. Когановский, А. М. (ed.). (1983) *Адсорбционная технология очистки сточных вод*. Киев: Наукова думка.
23. Delhaes, P. (ed.). (2011) *Carbon-based solids and materials*. ISTE.
24. Fitzer, E., Kochling, K.-H., Boehm, H. P. and Marsh, H. (1995) Recommended terminology for the description of carbon as a solid (IUPAC Recommendations 1995). *Pure Appl. Chem.*, 67(3), 473–506.
25. Candelaria, S. L., et al. (2012) Nanostructured carbon for energy storage and conversion. *Nano Energy*, 1(2), 195–220.
26. Inagaki, M., Konno, H. and Tanaike, O. (2010) Carbon materials for electrochemical capacitors. *J. Power Sources*, 195(24), 7880–7903.
27. Qiao, W., Yoon, S. and Isao, M. (2006) KOH Activation of Needle Coke to Develop Activated Carbons for High-Performance EDLC. *Energy Fuels*, 20(4), 1680–1684.
28. Zeng, K., Wu, D., Fu, R., et al. (2008) Preparation and electrochemical properties of pitch-based activated carbon aerogels. *Electrochim. Acta*, 53(18), 5711–5715.
29. Helmholtz, H. (1853) Ueber einige Gesetze der Vertheilung elektrischer Ströme in körperlichen Leitern mit Anwendung auf die thierisch-elektrischen Versuche. *Ann. der Phys. und Chemie*, 165(6), 211–233.
30. Becke, H. I. (1954) *Low voltage electrolytic capacitor*, US2800616 A.
31. Yu, A., Chabot, V. and Zhang, J. (eds.). (2013) *Electrochemical supercapacitors for energy storage and delivery: fundamentals and applications*. CRC Press.
32. Conway, B. E. (ed.). (1999) *Electrochemical Supercapacitors Scientific Fundamentals and Technological Applications*. Kluwer Acad., Plenum., NY, p. 736.
33. Pandolfo, A. G., Wilson, G. J., Huynh, T. D and Hollenkamp, A. F. (2010) The influence of conductive additives and inter-particle voids in carbon EDLC electrodes. *Fuel Cells*, 10(5), 856–864.
34. Portet, C., Yushin, G. and Gogotsi, Y. (2008) Effect of Carbon Particle Size on Electrochemical Performance of EDLC. *J. Electrochem. Soc.*, 155(7), A531.
35. Rennie, A. J. R., Martins, V. L., Smith, R. M. and Hall, P. J. (2016) Influence of Particle Size Distribution on the Performance of Ionic Liquid-based Electrochemical Double Layer Capacitors. *Sci. Rep.*, 6(1), 22062.
36. Shabalina, I. L. (2014) *Ultra-High Temperature Materials I Carbon (Graphene/Graphite) and Refractory Metals*. A Comprehensive Guide and Reference Book.
37. Aliofkhaeizadeh, M., Ali, N., Williams, W. I., et al. (2016) *Graphene science handbook. Fabrication methods*. CRC Press.
38. Lazzarini, A., et al. (2016) A comprehensive approach to investigate the structural and surface properties of activated carbons and related Pd-based catalysts. *Catal. Sci. Technol.*, 6(13), 4910–4922.

39. Cançado, L. G., et al. (2006) General equation for the determination of the crystallite size  $L_a$  of nanographite by Raman spectroscopy. *Appl. Phys. Lett.*, 88(16), 163106.
40. Dobele, G., Vervikishko, D., Volperts, A. and Bogdanovich, N. (2013) Characterization of the pore structure of nanoporous activated carbons produced from wood waste. *Holzforschung*, 67(5), 587–594.
41. Shkolnikov, E. I., Sidorova, E. V., Malakhov, A. O., Volkov, V. V., Julbe, A., and Ayrál, A. (2011) Estimation of pore size distribution in MCM-41-type silica using a simple desorption technique. *Adsorption*, 17(6), 911–918.

## 1.7. Kopsavilkums

Aktīvētā oglekļa (AO) un dažādu tā modifikāciju pielietošanas iespējas mūsdienās izraisa ķīmiķu, fiziķu un citu materiālzinātņu nozaru zinātnieku padziļinātu interesi. Mūsdienās oglekļa materiālu (OM) struktūras izpētei ir būtiska zinātniska un praktiska nozīme, jo nemitīgi paplašinās OM izmantošanas iespējas dažādās tehnikas nozarēs, nodrošinot gan retzemju metālu izdalīšanas membrānu tehnoloģiju, gan radioelektronikas, aviokosmiskās tehnikas un atomenerģētikas attīstības progresu. Jauni pētījumu virzieni ir saistīti ar AO izmantošanu nozarēs, kurās tiek lietotas un attīstītas nanotehnoloģijas. Nanoizmēru struktūras piedod materiāliem noderīgas, bet dažreiz arī unikālas īpašības. Oglekļa atomu elektronu apvalku aizpildīšanas īpatnību dēļ nanoporainie oglekļa materiāli (NOM) ieņem vienu no vadošajām vietām perspektīvo nanomateriālu vidū, piemēram, dažādās stratēģiskās elektronikas un enerģētikas nozarēs. Nanotehnoloģijas izpētes projektu izmaksas mūsdienās visā pasaulē ir vairāk nekā 9 miljardi dolāru gadā. Trešdaļu no visām investīcijām nanotehnoloģijas izpētē veic ASV. Citi galvenie investori nanotehnoloģijas tirgū ir Eiropas Savienība un Japāna. 2017. gadā ar nanotehnoloģijām saistītajās rūpniecības nozarēs strādājošā personāla skaits sasniedza divus miljonus cilvēku, bet ar nanomateriālu tehnoloģijām iegūto preču summārā vērtība rēķināma triljonus dolāru. Dažādas funkcionālas nozīmes elektroķīmisku iekārtu ražošanas attīstība, izmantojot OM, ir priekšnoteikums ilgtspējīgu ekoloģiski tīru tehnoloģiju izstrādei, kas savukārt nodrošina dažādu tehnisku rūpniecības nozaru attīstību ar minimālu enerģijas un reaģentu patēriņu.

Mūsu darbā izpētīta principiāla iespēja un izstrādāti oriģinālas tehnoloģijas pamati nanoporaino aktivēto ogļu iegūšanai termokīmiskās aktivācijas ceļā no lapu koksnes, tās atlikumiem un kokogles.

Noteikti optimālie koksnes termokīmiskās aktivācijas apstākļi aktīvo ogļu porainās struktūras veidošanai un adsorbcijas īpašībām, kas nepieciešami elektriskā dubultslāņa veidošanai superkondensatoru elektrodos. Noteiktas likumsakarības starp aktivēto ogļu iegūšanas apstākļiem, porainas struktūras parametriem un superkondensatora ar ūdens elektrolītu raksturlielumiem. Atrasts, ka sērskābes elektrolīta gadījumā, lietojot ogles ar īpatnējo poru tilpumu  $790 \text{ mm}^3/\text{g}$  un īpatnējo virsmu  $1660 \text{ m}^2/\text{g}$ , superkondensatora kapacitāte bija  $390 \text{ F/g}$  un jauda –  $3,06 \text{ Wh/kg}$ .

## 2. Synthesis and research of electrode and solid electrolyte materials for lithium ion batteries

### Litija jonu bateriju elektrodu materiālu un cieta elektrolītu sintēze un izpēte

Antonija Dindune<sup>1</sup>, Jānis Ronis<sup>1</sup>, Dagnija Valdniece<sup>1</sup>, Antanas Orliukas<sup>2</sup>,  
Tomas Salkus<sup>2</sup>, Vilma Venckute<sup>2</sup>

1 – Faculty of Materials Science and Applied Chemistry, Riga Technical University  
Paula Valdena iela 3/7, Riga, LV-1048, Latvia

2 – Department of Radiophysics, Faculty of Physics, Vilnius University  
Saulėtekio ave. 3, Vilnius, LT-10222, Lithuania  
E-mail: [antonija.dindune@rtu.lv](mailto:antonija.dindune@rtu.lv)

#### Contents

2. Synthesis and research of electrode and solid electrolyte materials for lithium ion batteries . . . . .	25
2.1. Introduction . . . . .	26
2.2. Experiments: Technologies and research methods of synthesis . . . . .	26
2.3. Structure and lithium ion transport in NASICON-type solid electrolytes . . . . .	30
2.4. Electrical properties of NASICON-type compounds . . . . .	38
2.5. Anomalies of electrical properties of $\text{LiFeP}_2\text{O}_7$ and $\text{Li}_{0.9}\text{Fe}_{0.9}\text{Ti}_{0.1}\text{P}_2\text{O}_7$ pyrophosphate ceramics . . . .	41
2.6. Influence of stoichiometry on the electrical properties of $\text{Li}_{4x}\text{Ti}_{1-x}\text{P}_2\text{O}_7$ pyrophosphate ceramics . . .	42
2.7. Electrical properties of $\text{LiFePO}_4$ and $\text{LiFePO}_4/\text{C}$ ceramics in the broad frequency range . . . . .	43
2.8. Study of the $\text{Li}_3\text{Fe}_{1.2}\text{Sc}_{0.75}\text{Y}_{0.05}(\text{PO}_4)_3$ ceramics by impedance and Mössbauer spectroscopy . . . . .	44
2.9. NASICON-type $\text{Na}_3\text{M}_2(\text{PO}_4)_3$ ( $\text{M} = \text{divalent metal}$ ) pyrophosphates . . . . .	46
2.10. Preparation, structure, surface and impedance spectroscopy of $\text{Na}_2\text{Zn}_{0.5}\text{Mn}_{0.5}\text{P}_2\text{O}_7$ ceramics . . . .	47
2.11. Synthesis, structure and impedance spectroscopy of $\text{NaCsZn}_{0.5}\text{Mn}_{0.5}\text{P}_2\text{O}_7$ pyro-phosphate ceramics . . . . .	48
2.12. Conclusions . . . . .	49
2.13. References . . . . .	51
2.14. Kopsavilkums . . . . .	53

## 2.1. Introduction

Investigated NASICON-type materials can be used as charge separators for solid electrolyte batteries. Also, pyrophosphate and olivine materials can serve as cathode materials for lithium, sodium solid electrolyte batteries. The NASICON crystallographic structure  $\text{NaA}_2^{\text{IV}}(\text{PO}_4)_3$  ( $\text{A}^{\text{IV}} = \text{Ge}, \text{Ti}$  and  $\text{Zr}$ ) was identified in 1968 [1, 2]. The structure can be described as a covalent skeleton  $[\text{A}_2\text{P}_3\text{O}_{12}]^-$  constituted of  $\text{AO}_6$  octahedra and  $\text{PO}_4$  tetrahedra, which form 3D interconnected channels and two types of interstitial positions ( $\text{M}'$  and  $\text{M}''$ ) where conductor cations are distributed. The conductor cations move from one site to another through bottlenecks, the size of which depends on the nature of the skeleton ions and on the carrier concentration in both type of sites ( $\text{M}'$  and  $\text{M}''$ ) Consequently, the structural and electrical properties of NASICON-type compounds vary with the composition of the framework. For example, the compound family with general formula  $\text{Li}_{1-4x}\text{Ti}_{2-x}\text{M}_x(\text{PO}_4)_3$  ( $\text{M} = \text{Al}, \text{Ga}, \text{In}, \text{Sc}$ ) was investigated [3]. The substitution of  $\text{Ti}^{4+}$  by smaller  $\text{Me}^{3+}$  cations changed unit cell dimensions of the NASICON framework and leads the increase of ionic conductivity by about 3 orders of magnitude. The aim of this work was the preparation  $\text{Li}^+$  ( $\text{Na}^+$ ) solid electrolytes and investigation the relationship between the crystal structure, elemental composition and peculiarities of ionic transport in these materials.

Several groups of inorganic solid NASICON-type lithium ion and the sodium-ion conductors were synthesized for the investigation.

A. Lithium ion conducting NASICON-type materials is interesting in terms of solid electrolytes for Li ion batteries. The total and bulk conductivity values of  $\text{LiTi}_2(\text{PO}_4)_3$  ceramic are about  $2.5 \cdot 10^{-6}$  and  $6.3 \cdot 10^{-5} \text{ Scm}^{-1}$ , respectively [4]. In order to increase its electrical conductivity, modified NASICON-type compounds  $\text{Li}_{1+4x}\text{Ti}_{2-x}(\text{PO}_4)_3$  ( $x = 0.2, 0.5$ ),  $\text{Li}_{1.3}\text{Al}_y\text{Y}_{x-y}\text{Ti}_{1.7}(\text{PO}_4)_3$  ( $x = 0.3; y = 0.1, 0.2$ ),  $\text{Li}_{1+4x}\text{Ti}_{2-x}\text{Nb}_y\text{P}_{3-y}\text{O}_{12}$  ( $x = 0.1, 0.2, 0.3$  and  $y = 0, 0.1, 0.2, 0.3$ ),  $\text{Li}_3\text{Fe}_{1.2}\text{Sc}_{0.75}\text{Y}_{0.05}(\text{PO}_4)_3$  were synthesized.

B. Also several cathode materials for Li ion batteries were prepared. Lately pyrophosphates gain more and more attention as possible cathode materials [5]. In this work  $\text{Li}_{1-x}\text{Fe}_{1-x}\text{Ti}_x\text{P}_2\text{O}_7$  ( $x = 0, 0.1$ ) and new  $\text{Li}_{4x}\text{Ti}_{1-x}\text{P}_2\text{O}_7$  ( $x = 0, 0.06, 0.1, 0.2$ ) pyrophosphates were synthesized.  $\text{LiFePO}_4$  and  $\text{LiFePO}_4/\text{C}$  cathode materials with olivine crystal structure were also obtained.

C. A further progress in development of secondary batteries for electrochemical energy storage requires the development of new ion-conducting materials. Among various alternatives to the Li-ion batteries, the sodium-ion batteries are promising as attractive cathode materials due to the abundant resources and the low cost of sodium [6]. We continue to search for new Na-based pyrophosphate materials for application in the secondary sodium ion batteries. Powders were synthesized by solid state reaction  $\text{Na}_2\text{Zn}_{0.5}\text{Mn}_{0.5}\text{P}_2\text{O}_7$ ,  $\text{NaCsZn}_{0.5}\text{Mn}_{0.5}\text{P}_2\text{O}_7$ ,  $\text{Na}_2\text{MnP}_2\text{O}_7$  [7, 8].

## 2.2. Experiments: Technologies and research methods of synthesis

Lithium and sodium solid electrolytes were synthesized and their ceramics were sintered. The powders of investigated compounds were synthesized by solid state reaction. Solid phase starting materials are used for this method of synthesis. The starting materials are mixed together and milled. Milling was performed in ethanol. Several milling and heating steps ensure that all the starting materials will come into contact with each other for reaction. The sequences of synthesis of some investigated compounds are shown below (see Fig. 2.1–2.6).

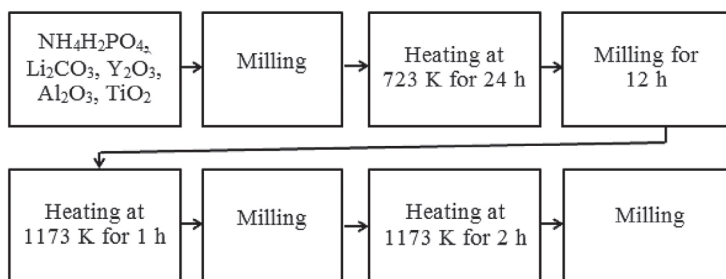


Figure 2.1. Synthesis of  $\text{Li}_{1.3}\text{Al}_y\text{Y}_{x-y}\text{Ti}_{1.7}(\text{PO}_4)_3$  by solid state reaction

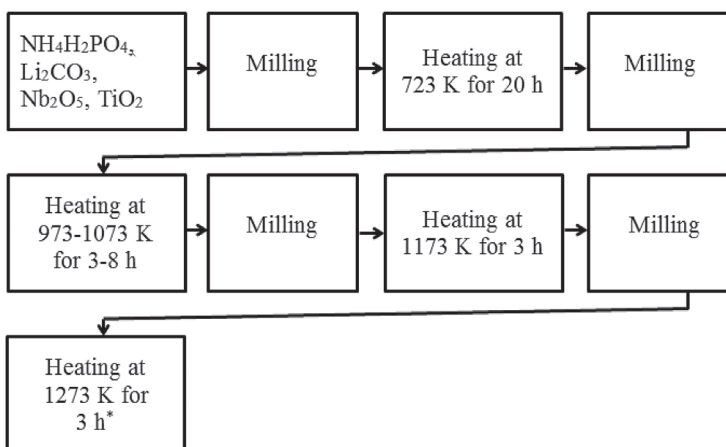


Figure 2.2. Synthesis of  $\text{Li}_{1+4x}\text{Ti}_{2-x}\text{Nb}_y\text{P}_{3-y}\text{O}_{12}$  by solid state reaction

\* The heating step for the compound with  $y = 0.1$  was 1473 K for 2 h

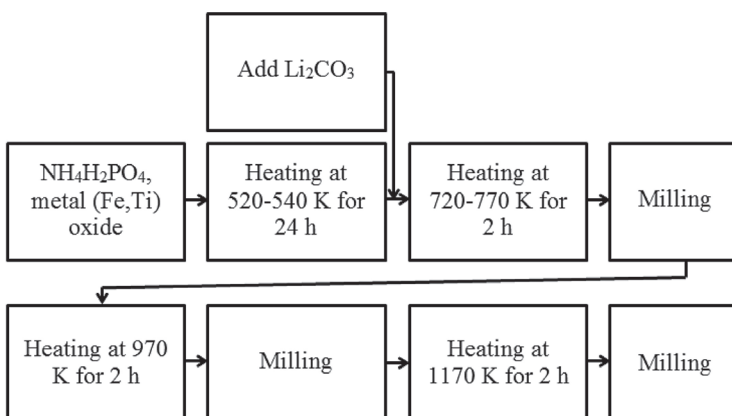


Figure 2.3. Synthesis of  $\text{LiFeP}_2\text{O}_7$  and  $\text{Li}_{0.9}\text{Fe}_{0.9}\text{Ti}_{0.1}\text{P}_2\text{O}_7$  by solid state reaction

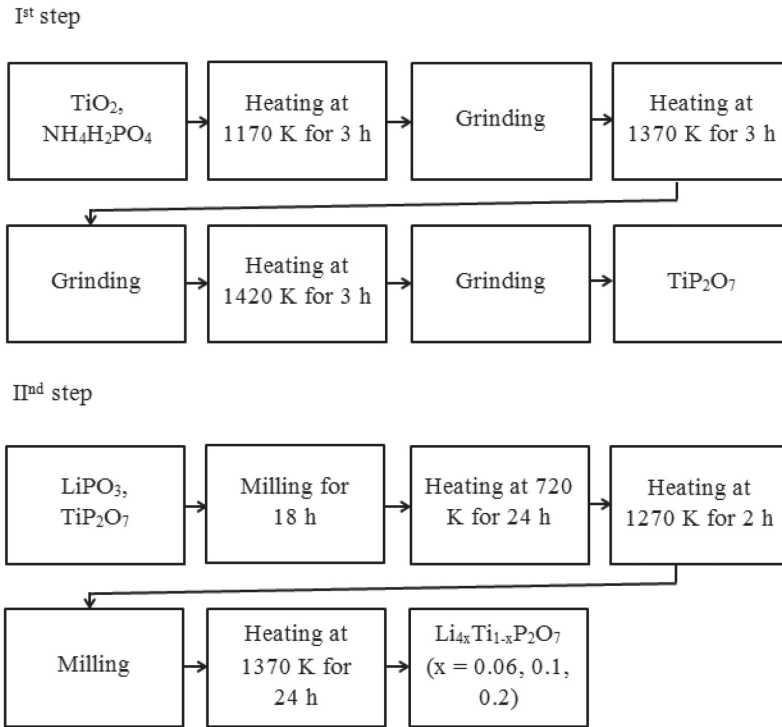


Figure 2.4. Synthesis of  $\text{Li}_{4x}\text{Ti}_{1-x}\text{P}_2\text{O}_7$  ( $x = 0, 0.06, 0.1, 0.2$ ) by solid state reaction

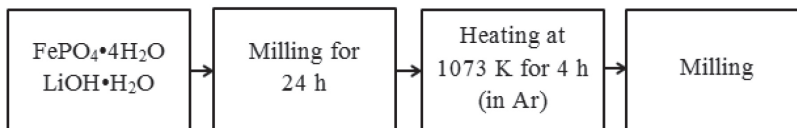


Figure 2.5. Synthesis of  $\text{LiFePO}_4$  by solid state reaction

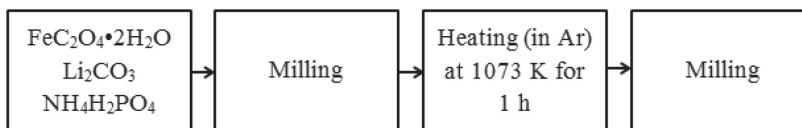


Figure 2.6. Synthesis of  $\text{LiFePO}_4/\text{C}$  by solid state reaction

**Solid electrolyte ceramics fabrication technology:** In order to prepare ceramics, powders of solid electrolytes were uniaxially cold-pressed into pellets at pressures between 150–300 MPa. Most pellets were sintered in air. Sintering temperatures ( $T_s$ ) and sintering times ( $t_s$ ) are presented in Table 2.1. The heating and cooling rate in the furnace was 5 K/min.

Before sintering pellets are heated at 673 K for 1 h. Densities of the pellets ( $d$ ) were evaluated by measuring geometry and mass of the pellets. Relative densities of the ceramics were calculated according to formula  $d_r = (d/d_{\text{XRD}}) \cdot 100\%$ , where  $d_{\text{XRD}}$  is the theoretical density calculated from XRD patterns of the compounds. Relative densities of the investigated ceramics are also presented in Table 2.1.

Table 2.1. Preparation conditions and relative densities of ceramics

Compounds	Pressure $P$ , Pa	Sintering temperature $T_s$ , K	Sintering time $t_s$ , h	Relative density $d_r$ , %
$\text{Li}_{1.8}\text{Ti}_{1.8}(\text{PO}_4)_3$	300	1363	1	95
$\text{Li}_3\text{Ti}_{1.5}(\text{PO}_4)_3$	300	923	1	81
$\text{Li}_{1.4}\text{Ti}_{1.9}\text{P}_3\text{O}_{12}$	300	1343	1	
$\text{Li}_{1.4}\text{Ti}_{1.9}\text{Nb}_{0.1}\text{P}_{2.9}\text{O}_{12}$	300	1223	1	
$\text{Li}_{1.8}\text{Ti}_{1.8}\text{Nb}_{0.2}\text{P}_{2.8}\text{O}_{12}$	300	1223	1	
$\text{Li}_{2.2}\text{Ti}_{1.7}\text{Nb}_{0.3}\text{P}_{2.7}\text{O}_{12}$	300	1223	1	
$\text{Li}_{1.3}\text{Al}_{0.2}\text{Y}_{0.1}\text{Ti}_{1.7}(\text{PO}_4)$	300	1373	1	
$\text{Li}_{1.3}\text{Al}_{0.1}\text{Y}_{0.2}\text{Ti}_{1.7}(\text{PO}_4)$	300	1373	1	
$\text{LiFePO}_4$	300	1073	10	85.8
$\text{LiFePO}_4/\text{C}$	300	1073 (in Ar)	1	73.7
$\text{Li}_4\text{Ti}_5\text{O}_{12}$	150	1173	10	79
$\text{Li}_4\text{Ti}_{4.95}\text{Ta}_{0.05}\text{O}_{12}$	150	1173	10	86
$\text{Li}_4\text{Ti}_{4.95}\text{Nb}_{0.05}\text{O}_{12}$	150	1173	10	83
$\text{LiFeP}_2\text{O}_7$	300	1173	2	73
$\text{Li}_{0.9}\text{Fe}_{0.9}\text{Ti}_{0.1}\text{P}_2\text{O}_7$	300	1173	2	71
$\text{TiP}_2\text{O}_7$	150	1460	3	92
$\text{Li}_{0.24}\text{Ti}_{0.94}\text{P}_2\text{O}_7$	150	1370	1	
$\text{Li}_{0.4}\text{Ti}_{0.9}\text{P}_2\text{O}_7$	150	1270	1	
$\text{Li}_{0.8}\text{Ti}_{0.8}\text{P}_2\text{O}_7$	150	1170	1	

Structural peculiarities of the compounds were investigated, using X-ray diffraction technique (XRD). For the investigations of electrical properties, the ceramic samples were sintered. The ceramic samples were investigated by using Impedance Spectroscopy (IS) in broad frequency range and temperature interval. Surfaces of the ceramics were investigated with X-ray Photoelectron Spectroscopy (XPS), Scanning Electron Microscopy

(SEM) and Energy dispersive X-ray Spectroscopy (EDX). The investigation of iron valents' state in some materials with Fe was performed, using Mössbauer spectroscopy method.

**X-ray diffraction (XRD).** Structural investigation of the materials was carried out with X-ray diffraction (XRD) technique. The structure parameters at room temperature were obtained from the X-ray powder diffraction, using Bruker D8 Advance equipment in the region  $2\theta = 10\text{--}70$  degrees, step  $0.01\text{--}0.02$  degrees, time per step  $1\text{--}8$  sec.,  $\text{CuK}\alpha_1$  radiation. The lattice parameters were deduced by fitting the XRD patterns with software TOPAS v. 4.1 and SCANIX v. 2.16 (Matpol).

**Impedance Spectroscopy (IS).** The electrical properties of the ceramics were investigated by broadband impedance spectroscopy. Measurements of complex electrical conductivity ( $\tilde{\sigma} = \sigma' + i\sigma''$ ), complex impedance ( $\tilde{\rho} = \rho' - i\rho''$ ) and complex dielectric permittivity ( $\tilde{\epsilon} = \epsilon' - i\epsilon''$ ) of the ceramics were carried out in air in the temperature interval from room temperature (RT) to 780 K and in the frequency range from 10 Hz to 3 GHz. The impedance spectrometer was used for the electrical measurements in the low frequency range up to 2 MHz by the 2- and 4-probe method [9], while in the microwave region a setup with a coaxial line connected to the Agilent E5062A network analyser was used [10]. Platinum paste (Gwent Electronics Materials Ltd.) was used to prepare electrodes on investigated samples.

**X-ray Photoelectron Spectroscopy (XPS)** or Electron Spectroscopy for Chemical Analysis (ESCA) is a powerful method of surface analysis. It collects information about surface layer of approximately 10 nm. In this work, XPS were recorded by LAS-3000 (ISA-Riber) surface analysis equipment. The instrument was equipped with double-pass cylindrical mirror analyser MAC2.

**Scanning electron microscopy (SEM) and energy-dispersive X-ray spectroscopy (EDX)** techniques were used for the analysis of chemical composition of the investigated compounds. Both techniques are integrated in TM3000 – Hitachi equipment, which was used for the investigation. Ceramics were prepared for SEM/EDX investigation. Pellets were broken and measurements were performed on the broken edge.

**Mössbauer spectra** were recorded with a conventional constant acceleration spectrometer in the transmission geometry. The density of the absorber was about  $10\text{ mg/cm}^2$  of natural Fe. The Co(Rh) source with the activity of 5 mCi was held at room temperature. The closed cycle helium Mössbauer cryostat (ARS Inc.) was used for the measurements at 10 K – 350 K. The Mössbauer furnace (WissEl GmbH) was used for the measurements at 300 K – 600 K. The temperature values during the measurements were kept at around the set point with the 1 % precision. The velocity scale was calibrated using the magnetic sextet of a high-purity iron foil absorber as the standard. The line width obtained for the  $25\ \mu\text{m}$  iron foil was  $0.26\pm 0.02\text{ mm/s}$  at ambient temperature. All the experimental spectra were fitted using Lorentzian lines by the least-squares method using a commercially available WinNormos package in IgorPro 5.05A environment. All isomer shifts reported in this work refer to the  $^{57}\text{Co(Rh)}$  source at a room temperature [11].

### 2.3. Structure and lithium ion transport in NASICON-type solid electrolytes

Structure of the investigated lithium solid electrolytes was investigated by X-Ray diffraction analysis. Refined lattice parameters and theoretical densities at room temperature are presented in Table 2.2.

Table 2.2. Lattice parameters and theoretical densities of the powders

Compound	Space group	a, Å	b, Å	c, Å	V, Å <sup>3</sup>	d <sub>XRD</sub> g/cm <sup>3</sup>	Z
Li <sub>1,8</sub> Ti <sub>1,8</sub> (PO) <sub>4,3</sub>	R $\bar{3}$ c	8.5162(4)		20.8482(30)	1309.5	2.9	6
Li <sub>3</sub> Ti <sub>1,5</sub> (PO) <sub>4,3</sub>	R $\bar{3}$ c	8.5144(5)		20.8762(60)	1310.8	2.85	6
Li <sub>1,4</sub> Ti <sub>1,9</sub> P <sub>3</sub> O <sub>12</sub>	R $\bar{3}$ c	8.5137(2)		20.8587(5)	1309.36	2.93	6
Li <sub>1,4</sub> Ti <sub>1,9</sub> Nb <sub>0,1</sub> P <sub>2,9</sub> O <sub>12</sub>	R $\bar{3}$ c	8.5267(23)		20.8608(53)	1313.49	2.97	6
Li <sub>1,8</sub> Ti <sub>1,8</sub> Nb <sub>0,2</sub> P <sub>2,8</sub> O <sub>12</sub>	R $\bar{3}$ c	8.5257(6)		20.8975(35)	1315.49	3	6
Li <sub>2,2</sub> Ti <sub>1,7</sub> Nb <sub>0,3</sub> P <sub>2,7</sub> O <sub>12</sub>	R $\bar{3}$ c	8.5242(7)		20.8976(27)	1315.04	3.03	6
Li <sub>1,3</sub> Al <sub>0,2</sub> Y <sub>0,1</sub> Ti <sub>1,7</sub> (PO) <sub>4,3</sub>	R $\bar{3}$ c	8.5054(4)		20.8247(12)	1304.68	2.974	6
Li <sub>1,3</sub> Al <sub>0,1</sub> Y <sub>0,2</sub> Ti <sub>1,7</sub> (PO) <sub>4,3</sub>	R $\bar{3}$ c	8.5109(4)		20.8372(16)	1307.1	3.016	6
LiFePO <sub>4</sub>	Pnma					3.6	
LiFePO <sub>4</sub> /C	Pnma					3.42	
Li <sub>4</sub> Ti <sub>5</sub> O <sub>12</sub>	Fd $\bar{3}$ m	8.3586			584.004	3.48	
Li <sub>4</sub> Ti <sub>4,95</sub> Ta <sub>0,05</sub> O <sub>12</sub>	Fd $\bar{3}$ m	8.3627			584.85	3.48	
Li <sub>4</sub> Ti <sub>4,95</sub> Nb <sub>0,05</sub> O <sub>12</sub>	Fd $\bar{3}$ m	8.3633			584.98	3.48	
LiFeP <sub>2</sub> O <sub>7</sub>	P2 <sub>1</sub>	4.8240(2)	8.0828(3)	6.9390(2)	255.19	3.081	
Li <sub>0,9</sub> Fe <sub>0,9</sub> Ti <sub>0,1</sub> P <sub>2</sub> O <sub>7</sub>	P2 <sub>1</sub>	4.8239(4)	8.0786(6)	6.9365(5)	255.09	3.063	
TiP <sub>2</sub> O <sub>7</sub>	Pa $\bar{3}$	23.6249(2)				3.015	108
Li <sub>0,24</sub> Ti <sub>0,94</sub> P <sub>2</sub> O <sub>7</sub>	Pa $\bar{3}$	23.6229(2)				3	108
Li <sub>0,4</sub> Ti <sub>0,9</sub> P <sub>2</sub> O <sub>7</sub>	Pa $\bar{3}$	23.6235(2)				2.99	108
Li <sub>0,8</sub> Ti <sub>0,8</sub> P <sub>2</sub> O <sub>7</sub>	Pa $\bar{3}$	23.6262(2)				2.96	108

**NASICON-type structure compounds.** Fig. 2.7 shows powder X-ray diffraction patterns of  $\text{Li}_{1.3}\text{Al}_y\text{Y}_{x-y}\text{Ti}_{1.7}(\text{PO}_4)_3$  ( $x = 0.3$ ;  $y = 0.1, 0.2$ ) prepared by solid state reaction. Small amounts (up to 1.5 %) of  $\text{LiTiPO}_5$  and  $\text{YPO}_5$  were detected as impurities and marked with asterisks in Fig. 2.7. At the room temperature, the  $\text{Li}_{1.3}\text{Al}_y\text{Y}_{x-y}\text{Ti}_{1.7}(\text{PO}_4)_3$  ( $x = 0.3$ ;  $y = 0.1, 0.2$ ) compounds belong to the rhombohedral symmetry (space group  $R\bar{3}c$ ) with six formula units in the unit cell [13]. The lattice parameters, unit cell volume ( $V$ ) and theoretical density ( $d_t$ ) of the investigated compounds are presented in Table 2.2.

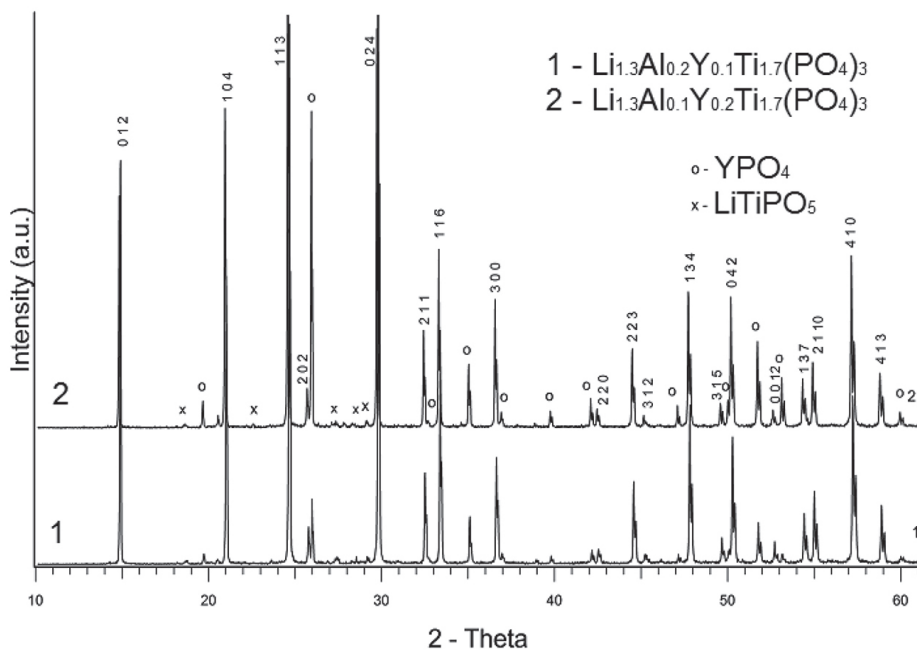


Figure 2.7. Powder X-ray diffraction patterns of  $\text{Li}_{1.3}\text{Al}_y\text{Y}_{x-y}\text{Ti}_{1.7}(\text{PO}_4)_3$  ( $x = 0.3$ ;  $y = 0.1, 0.2$ ) recorded at room temperature

A partial substitution of  $\text{Al}^{3+}$  by  $\text{Y}^{3+}$  in  $\text{Li}_{1.3}\text{Al}_y\text{Y}_{x-y}\text{Ti}_{1.7}(\text{PO}_4)_3$  ( $x = 0.3$ ;  $y = 0.1, 0.2$ ) causes the increase in the lattice parameters and theoretical density of the compound. This variation can be caused by different ionic radii of  $\text{Y}^{3+}$  and  $\text{Al}^{3+}$  ions. The ionic radii of  $\text{Y}^{3+}$  and  $\text{Al}^{3+}$  are 1.04 Å and 0.675 Å, respectively. On the other hand, the analysis of XRD patterns shows impurities of  $\text{YPO}_4$  and  $\text{LiTiPO}_5$ , which can influence the above-mentioned parameters.

Fig. 2.8 shows powder X-ray diffraction patterns of  $\text{Li}_{1+4x}\text{Ti}_{2-x}\text{Nb}_y\text{P}_{3-y}\text{O}_{12}$  ( $x = 0.1, 0.2, 0.3$ ;  $y = 0, 0.1, 0.2, 0.3$ ) compounds. The results of XRD data analysis have shown that  $\text{LiTiPO}_5$  impurities are present in compounds with  $y = 0, 0.1, 0.2$ , and they are marked with asterisks. In compounds with  $y = 0, 0.1, 0.2$  the amounts of impurities were found to be 2%, 3%, 8%, respectively. The investigated compounds belong to hexagonal symmetry (space group  $R\bar{3}c$ ). The lattice parameters, unit cell volume ( $V$ ), theoretical density ( $d_{x\text{-ray}}$ ) and formula units in the lattice ( $Z$ ) of the investigated compounds are presented in Table 2.2. The relative density of the ceramics was found to be 94 % of the theoretical density [12].

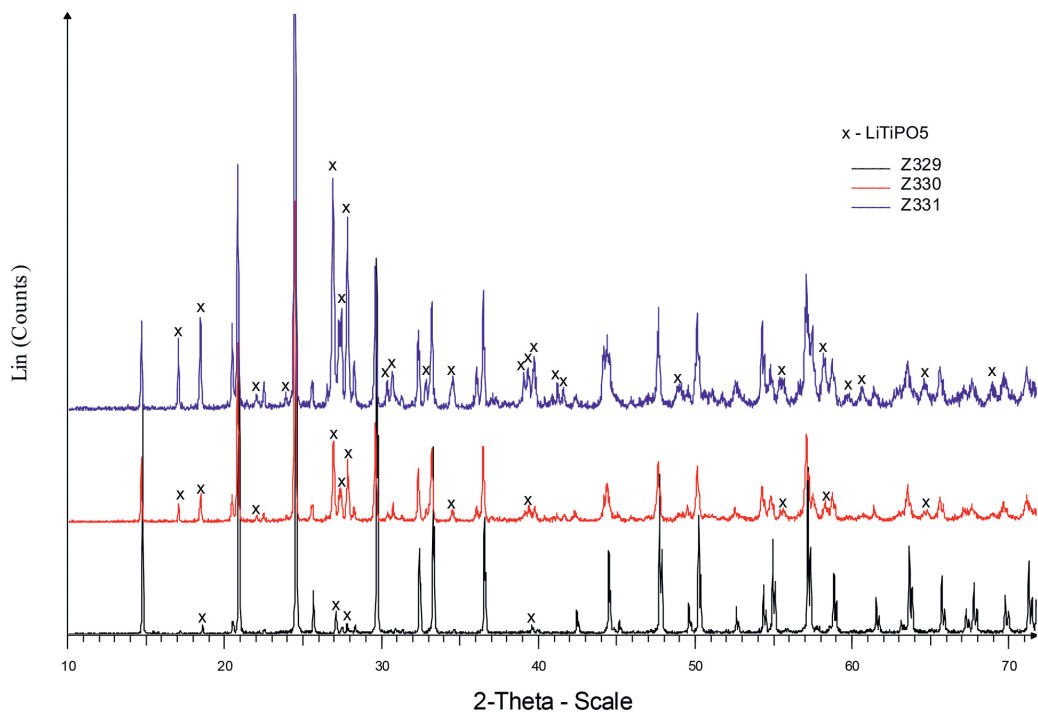


Figure 2.8. The powder X-ray diffraction patterns of  $\text{Li}_{1+4x}\text{Ti}_{2-x}\text{Nb}_y\text{P}_{3-y}\text{O}_{12}$  compounds:

$\text{Li}_{1.4}\text{Ti}_{1.9}\text{P}_3\text{O}_{12}$  ( $x = 0.1$ ,  $y = 0$ ) – (black),

$\text{Li}_{1.4}\text{Ti}_{1.9}\text{Nb}_{0.1}\text{P}_{2.9}\text{O}_{12}$  ( $x = 0.1$ ,  $y = 0.1$ ) – (red),

$\text{Li}_{1.8}\text{Ti}_{1.8}\text{Nb}_{0.2}\text{P}_{2.8}\text{O}_{12}$  ( $x = 0.2$ ,  $y = 0.2$ ) – (blue)

The amounts of up to 0.8 wt. % and 5 wt. % of  $\text{LiTiPO}_5$  and  $\text{Li}_4(\text{P}_2\text{O}_7)$  in compounds  $\text{Li}_{1+4x}\text{Ti}_{2-x}(\text{PO}_4)_3$  with  $x = 0.2$  and  $0.5$ , respectively, were found. The amounts of impurities were estimated from the intensities and their square analysis of XRD patterns.  $\text{LiTiPO}_5$  and  $\text{Li}_4(\text{P}_2\text{O}_7)$  belong to orthorhombic and triclinic symmetry group and are marked with asterisks on the XRD patterns in Fig. 2.9. At room temperature the  $\text{Li}_{1+4x}\text{Ti}_{2-x}(\text{PO}_4)_3$  (where  $x = 0.2, 0.5$ ) compounds belong to the rhombohedral symmetry (space group  $R\bar{3}c$ ) with six formula units in the unit cell. The lattice  $a$ ,  $c$  parameters, volume ( $V$ ), theoretical density ( $d_t$ ) of the ceramics are presented in Table 2.2.

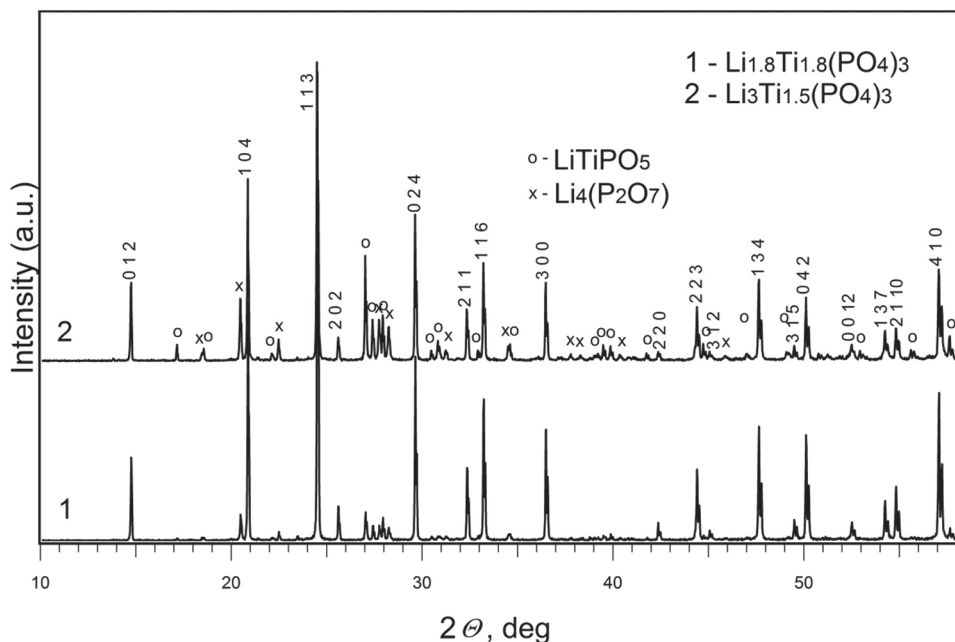


Figure 2.9. XRD patterns of  $\text{Li}_{1+4x}\text{Ti}_{2-x}(\text{PO}_4)_3$  (where  $x = 0.2, 0.5$ ) at room temperature

The increase of Li content (Fig. 2.9) leads to the increase of volume of the lattice and decrease of the theoretical density of the compounds. This variation can be caused by the different values of the ionic radii of  $\text{Li}^+$  and  $\text{Ti}^{4+}$  ions. The ionic radii of  $\text{Li}^+$  and  $\text{Ti}^{4+}$  are 0.92 Å and 0.74 Å, respectively. On the other hand, the analysis of XRD patterns shows the impurities of  $\text{LiTiPO}_5$  and  $\text{Li}_4(\text{P}_2\text{O}_7)$ , which can also influence the above-mentioned parameters [14].

### XRD spectra of $\text{LiFeP}_2\text{O}_7$ and $\text{Li}_{0.9}\text{Fe}_{0.9}\text{Ti}_{0.1}\text{P}_2\text{O}_7$ pyrophosphates at various temperatures

X-ray powder diffraction analysis was performed at temperatures  $T = 300, 440, 540$  and  $680$  K. The X-ray diffraction patterns of [15]  $\text{LiFeP}_2\text{O}_7$  and  $\text{Li}_{0.9}\text{Fe}_{0.9}\text{Ti}_{0.1}\text{P}_2\text{O}_7$  powders at 300 K and 680 K are presented in Fig. 2.10. Crystal structure of  $\text{LiFeP}_2\text{O}_7$  powders has been indexed as monoclinic system (s.g.  $\text{P}2_1$ ) in all the investigated temperatures. The structure of  $\text{Li}_{0.9}\text{Fe}_{0.9}\text{Ti}_{0.1}\text{P}_2\text{O}_7$  powders was also indexed as monoclinic system with  $\text{P}2_1$  space group. Based on the observation of the same space group and other examples of partial Fe substitution in  $\text{LiFeP}_2\text{O}_7$ , it is expected that Ti partially replaces Fe atoms at their original sites, but calculated and difference curves (Fig. 2.10) indicates several additional peaks and intensity discrepancies.

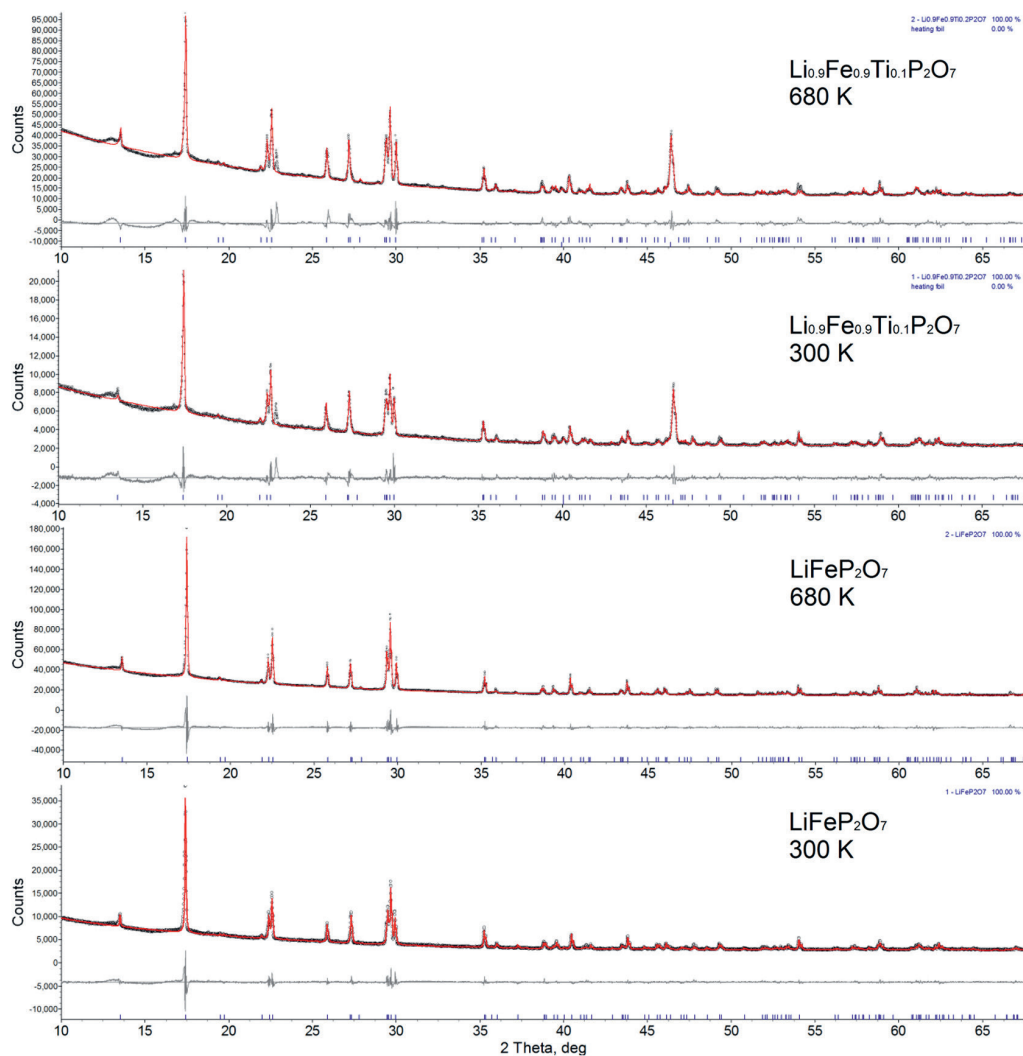


Figure 2.10. X-ray diffraction patterns for  $\text{Li}_{0.9}\text{Fe}_{0.9}\text{Ti}_{0.1}\text{P}_2\text{O}_7$  and  $\text{LiFeP}_2\text{O}_7$  compounds at 300 K and 680 K temperature

The peaks at roughly 40.0 and 46.6 degrees are known to be caused by heating element (Pt-Rh foil) and were included in the structure refinement as a Pawley phase (cubic, s. g. Fm-3 m,  $a \approx 4.8242$ ). The exact cause of the strong peak at roughly 23.00 degrees and some minor peaks (for example at 16.89, 24.49 and 26.09) is not clear, therefore, it is not presented in the refinement (Fig. 2.10.). However, it is probable that later peaks belong to the monoclinic  $\text{Fe}(\text{PO}_3)_3$  phase (it could consist up to 6 wt. %), which was reported in [16]. The attempts to refine  $\text{Li}_{0.9}\text{Fe}_{0.9}\text{Ti}_{0.1}\text{P}_2\text{O}_7$  XRD data using another Ti sites or other space group were not successful, therefore, despite the observed inadequacies, we assume that the structure is generally correct.

The additional modest improvement of XRD data refinement was observed after occupation coefficients (occ) were varied freely: for all atomic positions of  $\text{LiFeP}_2\text{O}_7$ , refined occ was close to 0.9, meanwhile, for  $\text{Li}_{0.9}\text{Fe}_{0.9}\text{Ti}_{0.1}\text{P}_2\text{O}_7$  refined occ values had a tendency to be smaller by a value of 0.2–0.3 and for some sites even lower than 0.5. Variation of occ are accompanied by inadequate changes of isotropic temperature factors (beq), therefore, in the presented XRD data refinement variation of beq was limited (the chosen variation range limits were from 0 to 1). Under such restrictions, beq relaxed to values close to 0 and 1: for  $\text{LiFeP}_2\text{O}_7$  at 300 K beq relaxed to value of 0 only for Lithium and two oxygen atomic sites (four oxygen sites at 680 K); for  $\text{Li}_{0.9}\text{Fe}_{0.9}\text{Ti}_{0.1}\text{P}_2\text{O}_7$  at 300 K beq relaxed to value of 0 for iron, lithium and two oxygen sites; for  $\text{Li}_{0.9}\text{Fe}_{0.9}\text{Ti}_{0.1}\text{P}_2\text{O}_7$  680 K beq relaxed to value of 0 for lithium and six oxygen sites. Both of these effects (occ and beq variations) could be caused by the insufficient data quality, which is reduced due to possible changes of heating foil curvature, X-ray beam cropping and scattering by heating chamber windows, relatively small acquisition times. On the other hand, the anomalies of lattice parameters and tendency of occ changes of the atoms in the both compounds can be related to disordering in the unit cells of the compounds. This assumption is also supported by the observed differences in P/Fe atomic concentration ratios and variations of  $\text{Fe}^{2+}$  and  $\text{Fe}^{3+}$  states.

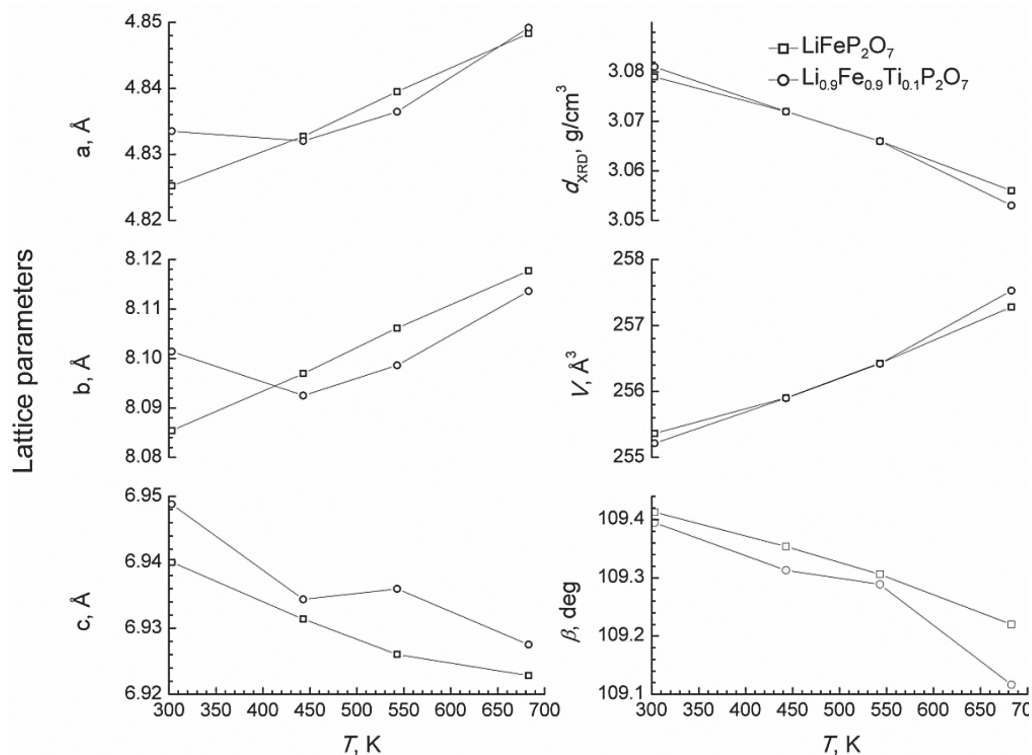


Figure 2.11. Lattice parameters (a, b, c), angle ( $\beta$ ), volume (V), theoretical density ( $d_{\text{XRD}}$ ) of  $\text{Li}_{0.9}\text{Fe}_{0.9}\text{Ti}_{0.1}\text{P}_2\text{O}_7$  and  $\text{LiFeP}_2\text{O}_7$  compounds determined from XRD analysis at different temperatures

The refined lattice (a, b, c) parameters, volume of the unit cell (V), theoretical ( $d_{\text{XRD}}$ ) density of the ceramics at room temperature are summarized in Table 2.2. The temperature dependences of the lattice parameters, V,  $\beta$  of the investigated compounds are shown in Fig. 2.11. The volumes of the cells increase,  $\beta$  and densities decrease with increase of the temperature. The anomalies of lattice parameters of  $\text{LiFeP}_2\text{O}_7$  and  $\text{Li}_{0.9}\text{Fe}_{0.9}\text{Ti}_{0.1}\text{P}_2\text{O}_7$  in the temperature range 543 to 680 K were found. The anomalies of lattice parameters in the both compounds can be related to disordering in the unit cells of the compounds. It is worth to note, that the space group of both compounds at 300 K and 683 K temperature remains the same.

**Crystal structure of  $\text{Li}_{4x}\text{Ti}_{1-x}\text{P}_2\text{O}_7$  ( $x = 0, 0.06, 0.1, 0.2$ ) pyrophosphates.** XRD analysis at room temperature confirmed that obtained  $\text{Ti}_2\text{P}_2\text{O}_7$  powder belongs to cubic symmetry with space group  $\text{Pa}\bar{3}$  as Results of X-ray diffraction analysis also show that  $\text{Li}_{4x}\text{Ti}_{1-x}\text{P}_2\text{O}_7$  ( $x = 0.06, 0.1, 0.2$ ) compounds have cubic superstructure and the same space group as  $\text{Ti}_2\text{P}_2\text{O}_7$ . The obtained XRD patterns are shown in Fig. 2.12. The increase of lithium amount in the system  $\text{Li}_{4x}\text{Ti}_{1-x}\text{P}_2\text{O}_7$  slightly decreased the theoretical density of the compounds (see Table 2.2).

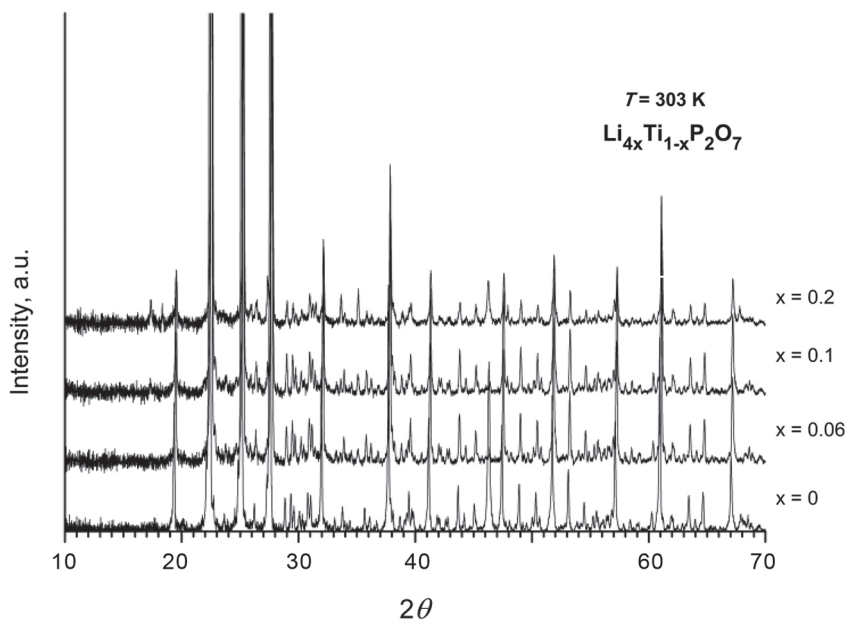


Figure 2.12. X-ray diffraction patterns of  $\text{Li}_{4x}\text{Ti}_{1-x}\text{P}_2\text{O}_7$  (where  $x = 0, 0.06, 0.1, 0.2$ ) powders

#### 2.4. Electrical properties of NASICON-type compounds

The impedance spectroscopy investigation of the ionic conductivity in the wide frequency and in the broad temperature ranges allows to separate charge carrier transport processes in bulk and in grain boundaries of the ceramics. The results of the investigation of electrical conductivities have shown [13] that the increase of stoichiometric parameter  $y$  in  $\text{Li}_{1.3}\text{Al}_y\text{Y}_{x-y}\text{Ti}_{1.7}(\text{PO}_4)_3$  ( $x = 0.3$ ;  $y = 0, 0.1, 0.15, 0.2, 0.3$ ) system leads to the increase of  $\sigma_b$  values (see Fig. 2.13 and Table 2.3).

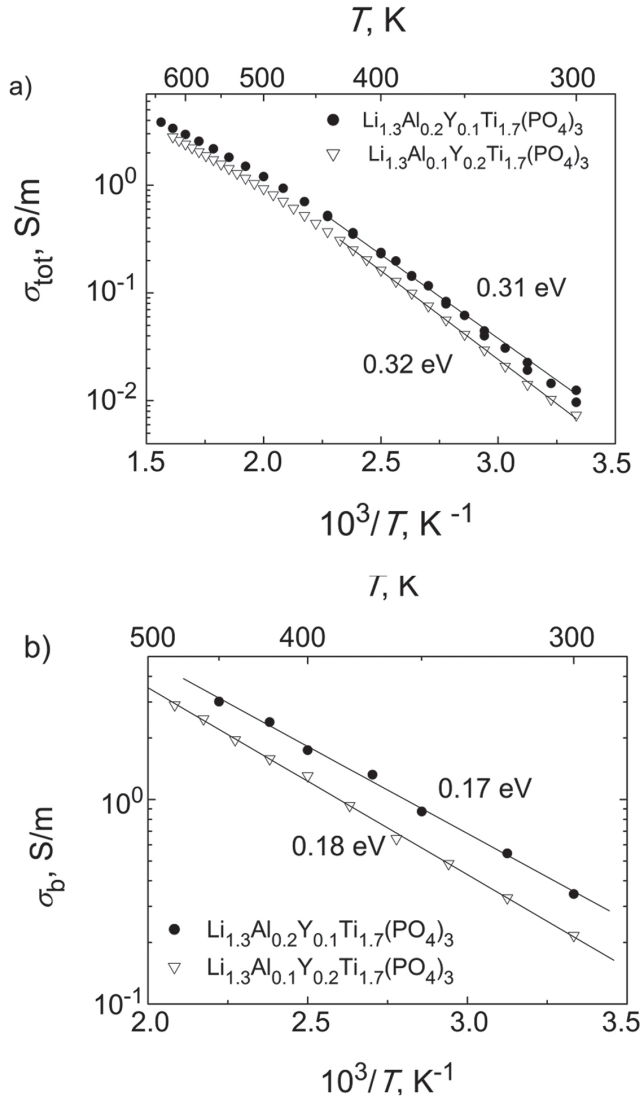


Figure 2.13. Temperature dependences of total (a) and bulk (b) conductivities of  $\text{Li}_{1.3}\text{Al}_y\text{Y}_{x-y}\text{Ti}_{1.7}(\text{PO}_4)_3$  ( $x = 0.3$ ;  $y = 0.1, 0.2$ ) ceramics

Table 2.3.  $\sigma_b$ ,  $\sigma_{tot}$ , their activation energies and activation energy of the relaxation frequency in bulk of  $\text{Li}_{1.3}\text{Al}_y\text{Y}_{x-y}\text{Ti}_{1.7}(\text{PO}_4)_3$  ( $x = 0.3$ ;  $y = 0, 0.1, 0.15, 0.2, 0.3$ ) ceramic samples at 300 K

Compounds'	$\sigma_b$ S/m	$\Delta E_{\sigma_b}$ , eV	$\Delta E_f$ , eV	$\sigma_{tot}$ , S/m	$\Delta E_{\sigma_{tot}}$ , eV	Ref.
$\text{Li}_{1.3}\text{Al}_{0.3}\text{Ti}_{1.7}(\text{PO}_4)_3$	0.35	0.30	0.30			[17]
$\text{Li}_{1.3}\text{Al}_{0.2}\text{Y}_{0.1}\text{Ti}_{1.7}(\text{PO}_4)_3$	0.35	0.17	0.18	0.012	0.32	
$\text{Li}_{1.3}\text{Al}_{0.15}\text{Y}_{0.15}\text{Ti}_{1.7}(\text{PO}_4)_3$	0.22	0.26	0.26	0.0019	0.45	[18]
$\text{Li}_{1.3}\text{Al}_{0.1}\text{Y}_{0.2}\text{Ti}_{1.7}(\text{PO}_4)_3$	0.22	0.18	0.17	0.0073	0.31	
$\text{Li}_{1.3}\text{Y}_{0.3}\text{Ti}_{1.7}(\text{PO}_4)_3$	0.094	0.19	0.19			[17]

A good agreement between the activation energy of ionic migration process in grains,  $\Delta E_{\sigma_b}$ , and the activation energy of characteristic relaxation frequency,  $\Delta E_f$  is found. The activation energy  $\Delta E_f$  correlates with the activation energy of mobility of charge carriers in grains. As we found that the values of activation energies of the bulk ionic conductivities of investigated ceramics are similar to the activation energies of relaxation frequency, which can be attributed to migration of  $\text{Li}^+$  ions, the concentration of charge carriers remains constant with changing temperature. It is shown that the major role in the temperature dependence of bulk conductivity is played by the  $\text{Li}^+$  ion mobility, which increases as temperature increases.

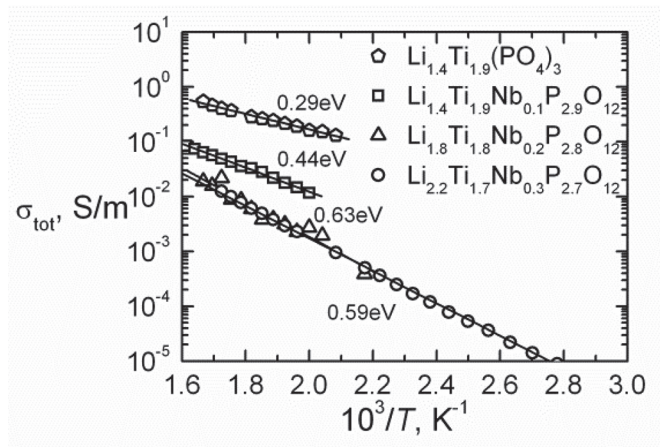


Figure 2.14. Temperature dependences of total conductivities of  $\text{Li}_{1+4x}\text{Ti}_{2-x}\text{Nb}_y\text{P}_{3-y}\text{O}_{12}$  ceramics

**Electrical properties of  $\text{Li}_{1+4x}\text{Ti}_{2-x}\text{Nb}_y\text{P}_{3-y}\text{O}_{12}$  ceramics** were investigated by using two probe methods. Two relaxation dispersions have been found in complex conductivity and impedance spectra of the studied  $\text{Li}_{1+4x}\text{Ti}_{2-x}\text{Nb}_y\text{P}_{3-y}\text{O}_{12}$  ceramics. The one in the high frequency region was attributed to  $\text{Li}^+$  ion relaxation in the bulk, and the intermediate frequency range dispersion was caused by ion blocking effect at grain boundaries of the ceramics [12]. Temperature dependences of  $\sigma_{tot}$  of  $\text{Li}_{1+4x}\text{Ti}_{2-x}\text{Nb}_y\text{P}_{3-y}\text{O}_{12}$  ( $x = 0.1, 0.2, 0.3$ ;  $y = 0, 0.1, 0.2, 0.3$ ) ceramics are shown in Fig. 2.14.  $\sigma_b$  and  $\sigma_{tot}$  of investigated ceramics

change according to Arrhenius law in the studied temperature range. The values of  $\sigma_b$  and  $\sigma_{tot}$ , their activation energies ( $\Delta E_b$ ) and ( $\Delta E_{tot}$ ) are summarized in Table 4. The comparison of the results of the XRD and conductivity investigations has shown that the increase of impurities of  $\text{LiTiPO}_5$  leads to the decrease of total and bulk conductivities and increase their activation energies. According to [19], the compound of  $\text{LiTiPO}_5$  exhibit very low electrical conductivity ( $(5-10) \cdot 10^{-4}$  S/m at 673 K, its activation energy  $\Delta E \approx 1$  eV).

Table 2.4.  $\sigma_b$  and  $\sigma_t$ , and their activation energies of  $\text{Li}_{1+4x}\text{Ti}_{2-x}\text{Nb}_y\text{P}_{3-y}\text{O}_{12}$  ceramics at temperature  $T = 530$  K

Compounds	$s_b, \text{S} \cdot \text{m}^{-1}$	$\Delta E_b, \text{eV}$	$s_t, \text{S} \cdot \text{m}^{-1}$	$\Delta E_t, \text{eV}$
$\text{Li}_{1.4}\text{Ti}_{1.9}\text{P}_3\text{O}_{12}$	2.07	0.18	0.244	0.29
$\text{Li}_{1.4}\text{Ti}_{1.9}\text{Nb}_{0.1}\text{P}_{2.9}\text{O}_{12}$	0.22	0.38	0.022	0.44
$\text{Li}_{1.8}\text{Ti}_{1.8}\text{Nb}_{0.2}\text{P}_{2.8}\text{O}_{12}$	0.05	0.4	0.004	0.59
$\text{Li}_{2.2}\text{Ti}_{1.7}\text{Nb}_{0.3}\text{P}_{2.7}\text{O}_{12}$	0.04	0.43	0.0038	0.59

$\text{Li}_{1+4x}\text{Ti}_{2-x}(\text{PO}_4)_3$  (where  $x = 0.2, 0.5$ ) ceramics measured in the frequency range from 10 Hz to 100 kHz were investigated by four probe method and in the microwave range the measurements were carried out by coaxial technique.

The temperature dependences of bulk ionic conductivities ( $\sigma_b$ ) have been found from complex plain plots of conductivity at different temperatures. The temperature dependences of  $\sigma_b$  and  $\sigma_{tot}$  of  $\text{Li}_{1+4x}\text{Ti}_{2-x}(\text{PO}_4)_3$  (where  $x = 0.2, 0.5$ ) of ceramic samples are shown in Fig. 2.15. The maximal value of  $\sigma_{tot}$  was found for compound with parameter  $x = 0.5$ . The increase of the parameter  $x$  leads to the increase of the value of  $\sigma_b$ . The activation energies of  $\sigma_b$  and  $\sigma_{tot}$  were found from the slopes of the Arrhenius plots.

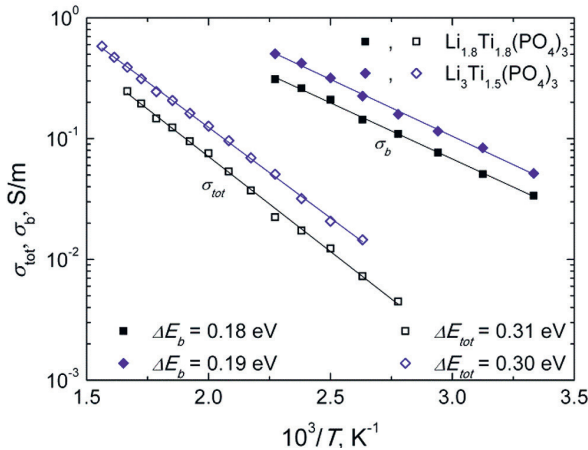


Figure 2.15. Arrhenius plots of total and bulk conductivities of  $\text{Li}_{1+4x}\text{Ti}_{2-x}(\text{PO}_4)_3$  (where  $x = 0.2, 0.5$ ) ceramics

## 2.5. Anomalies of electrical properties of $\text{LiFeP}_2\text{O}_7$ and $\text{Li}_{0.9}\text{Fe}_{0.9}\text{Ti}_{0.1}\text{P}_2\text{O}_7$ pyrophosphate ceramics

The characteristic frequency dependences of the real part of complex conductivity of the  $\text{LiFeP}_2\text{O}_7$  and  $\text{Li}_{0.9}\text{Fe}_{0.9}\text{Ti}_{0.1}\text{P}_2\text{O}_7$  ceramics were measured at temperatures 560 K and 660 K [15, 20]. The dispersion regions in spectra for both investigated ceramics were found. The processes are thermally activated and dispersion regions shift towards higher frequencies as temperature increases. This phenomenon is typical for relaxation-type dispersions, which are general in the solid electrolyte ceramics [21, 22]. It was not possible to distinguish grain boundary and bulk conductivities of the ceramics in the measured temperature and frequency ranges, as they were separated in the previous works [23, 24].

The total conductivities  $\sigma_{\text{tot}}$  of the ceramics were derived from frequency dependences at different temperatures and complex specific resistance. The temperature dependences of  $\sigma_{\text{tot}}$  of  $\text{LiFeP}_2\text{O}_7$  and  $\text{Li}_{0.9}\text{Fe}_{0.9}\text{Ti}_{0.1}\text{P}_2\text{O}_7$  ceramic samples are shown in Fig. 2.16.

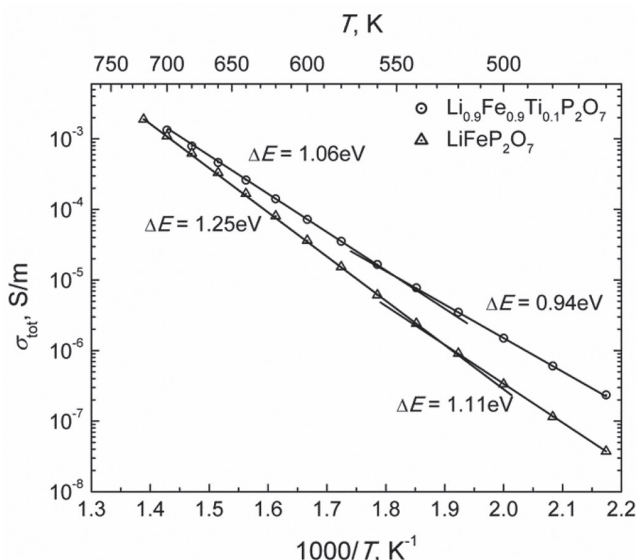


Figure 2.16. Total conductivity of  $\text{Li}_{0.9}\text{Fe}_{0.9}\text{Ti}_{0.1}\text{P}_2\text{O}_7$  and  $\text{LiFeP}_2\text{O}_7$  compound ceramics dependences on reciprocal temperature

The activation energies ( $\Delta E$ ) of  $\sigma_{\text{tot}}$  were found from the slopes of the Arrhenius plots. The partial changes of  $\text{Fe}^{3+}$  by  $\text{Ti}^{4+}$  in the compounds lead the increase of the value of  $\sigma_{\text{tot}}$  and decrease their activation energy of the investigated ceramics. The activation energy of  $\sigma_{\text{tot}}$  for  $\text{LiFeP}_2\text{O}_7$  and  $\text{Li}_{0.9}\text{Fe}_{0.9}\text{Ti}_{0.1}\text{P}_2\text{O}_7$  ceramics was found to be 1.11 eV and 0.94 eV respectively. At temperature  $T = 550 \text{ K}$  for  $\text{LiFeP}_2\text{O}_7$  and at  $T = 528 \text{ K}$  for  $\text{Li}_{0.9}\text{Fe}_{0.9}\text{Ti}_{0.1}\text{P}_2\text{O}_7$  compounds the change of activation energy of  $\sigma_{\text{tot}}$  was found. The values of  $\Delta E$  of  $\sigma_{\text{tot}}$  above 550 K for  $\text{LiFeP}_2\text{O}_7$  and above 528 K for  $\text{Li}_{0.9}\text{Fe}_{0.9}\text{Ti}_{0.1}\text{P}_2\text{O}_7$  were found to be 1.25 eV and 1.06 eV, respectively. The changes of activation energy of  $\sigma_{\text{tot}}$  of the investigated compounds are related to structure phase transitions detected by XRD measurements. The experimental results of the investigation of  $\sigma_{\text{tot}}$ , their activation energies and temperatures of the changes of  $\Delta E$  are summarized in Table 2.5.

Table 2.5. Summary of electrical properties: total conductivity ( $\sigma_{\text{tot}}$ ), activation energy ( $\Delta E_a$ ), Maxwell relaxation frequency ( $f_M$ ), dielectric permittivity ( $\epsilon'$ ), tangent loss ( $\tan\delta$ ) investigation at different temperatures ( $T$ )

Compound	$T$ , K	$\sigma_{\text{tot}}$ , S/m	$\Delta E_a$ , eV	$f_M$ , MHz	$\epsilon'$	$\tan\delta$
$\text{Li}_{0.9}\text{Fe}_{0.9}\text{Ti}_{0.1}\text{P}_2\text{O}_7$	460-550	$1.5 \cdot 10^{-6}$ (500 K)	0.94		6.63 (500 K)	0.0075 (500 K)
	550-700	$1.34 \cdot 10^{-3}$ (700 K)	1.06	3.28 (700 K)	7.35 (700 K)	0.049 (700 K)
$\text{LiFeP}_2\text{O}_7$	460-528	$3.33 \cdot 10^{-7}$ (500 K)	1.11		6.74 (500 K)	0.0074 (500 K)
	528-720	$1.09 \cdot 10^{-3}$ (700 K)	1.25	2.62 (700 K)	7.48 (700 K)	0.031 (700 K)

## 2.6. Influence of stoichiometry on the electrical properties of $\text{Li}_{4x}\text{Ti}_{1-x}\text{P}_2\text{O}_7$ pyrophosphate ceramics

$\text{Li}_{4x}\text{Ti}_{1-x}\text{P}_2\text{O}_7$  ( $x = 0, 0.06, 0.1, 0.2$ ) samples were obtained. The temperature dependences of total conductivities  $\sigma_{\text{tot}}$  of the ceramics were derived from complex impedance plots obtained at different temperatures [25]. The temperature dependences of  $\sigma_{\text{tot}}$  are presented in Fig. 2.17. The activation energies ( $\Delta E_{\text{tot}}$ ) of  $\sigma_{\text{tot}}$  were calculated according to Arrhenius law. The anomalies of activation energies of  $\sigma_{\text{tot}}$  of  $\text{Li}_{4x}\text{Ti}_{1-x}\text{P}_2\text{O}_7$  ( $x = 0.06, 0.1, 0.2$ ) compounds in the temperature range from 520 to 580 K were found. The changes of  $\Delta E_{\text{tot}}$  can be related to some disordering in the supercell associated with phase transitions.

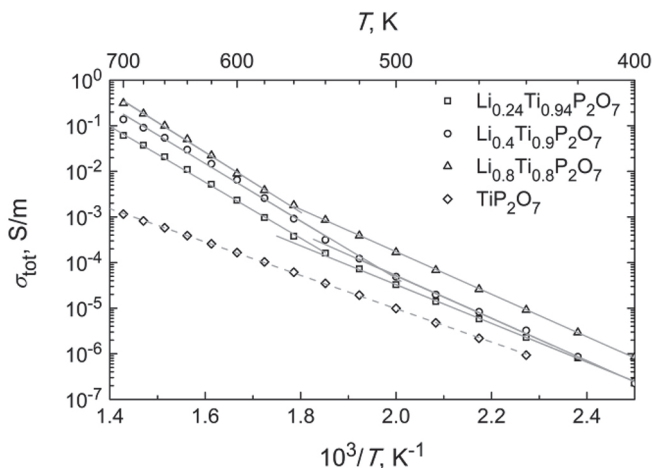


Figure 2.17. Temperature dependences of total conductivity of  $\text{Li}_{4x}\text{Ti}_{1-x}\text{P}_2\text{O}_7$  ( $x = 0, 0.06, 0.1, 0.2$ ) ceramics

The results of the investigation of  $\sigma_{\text{tot}}$  are summarized in Table 2.6. The values of total conductivity are higher for the samples with lithium ( $\text{Li}_{4x}\text{Ti}_{1-x}\text{P}_2\text{O}_7$ ,  $x = 0.06, 0.1, 0.2$ ) than for the host  $\text{TiP}_2\text{O}_7$  compound (see Table 2.6). With increasing amount of lithium in the samples,  $\sigma_{\text{tot}}$  values also increase. The increase of the values of total conductivity in  $\text{Li}_{4x}\text{Ti}_{1-x}\text{P}_2\text{O}_7$  ( $x = 0.06, 0.1, 0.2$ ) compared with  $\text{TiP}_2\text{O}_7$  can be caused by lithium ion transport contribution to  $\sigma_{\text{tot}}$ . The total proton conductivity of  $\text{TiP}_2\text{O}_7$  compound increases along with temperature according to Arrhenius law with activation energy  $\Delta E_{\text{tot}} = 0.73$  eV.

Table 2.6. Total conductivities and their activation energies of  $\text{Li}_{4x}\text{Ti}_{1-x}\text{P}_2\text{O}_7$  (where  $x = 0, 0.06, 0.1, 0.2$ ) ceramics

x in $\text{Li}_{4x}\text{Ti}_{1-x}\text{P}_2\text{O}_7$	Sintering duration	Total conductivity $\sigma_{\text{tot}}$ , S/m (440 K)	Activation energy $\Delta E_{\text{tot}}$ , eV	Total conductivity $\sigma_{\text{tot}}$ , S/m (600 K)	Activation energy $\Delta E_{\text{tot}}$ , eV
0	3 h	$9.34 \cdot 10^{-7}$	0.73 (440–720 K)	$1.66 \cdot 10^{-4}$	
0.06	1 h	$2.29 \cdot 10^{-6}$	0.85 (400–530 K)	$2.33 \cdot 10^{-3}$	1.23 (530–720 K)
0.1	1 h	$3.24 \cdot 10^{-6}$	0.93 (400–510 K)	$6.52 \cdot 10^{-3}$	1.26 (510–700 K)
0.2	1 h	$9.12 \cdot 10^{-6}$	0.93 (400–567 K)	$8.87 \cdot 10^{-3}$	1.31 (567–700 K)

## 2.7. Electrical properties of $\text{LiFePO}_4$ and $\text{LiFePO}_4/\text{C}$ ceramics in the broad frequency range

The characteristic frequency dependences of the real part of complex conductivity of the  $\text{LiFePO}_4$  ceramics measured at different temperatures (300, 350 and 400 K). The thermally activated dispersion regions in spectra for both investigated samples were found [26].

The dispersion regions shift towards higher frequencies as temperature increases. This phenomenon is typical for relaxation type dispersions [22]. The low frequency dispersion regions can be associated with relaxation processes in the grain boundary of the ceramics. The dispersion at high frequencies is caused by ionic transport in the bulk of the ceramics.

The temperature dependences of  $\sigma_b$  and  $\sigma_{\text{tot}}$  of the  $\text{LiFePO}_4$  ceramic and the  $\text{LiFePO}_4/\text{C}$  composite samples are shown in Fig. 2.18.

Table 2.7. Summary of the electrical characteristic at different temperatures for  $\text{LiFePO}_4$  and  $\text{LiFePO}_4/\text{C}$  samples

Compound	$\sigma_b$ , S/m (320 K)	$\Delta E_b$ , eV	$\sigma_{\text{tot}}$ , S/m (320 K)	$\Delta E_{\text{tot}}$ , eV	$\epsilon'$ (1 GHz) (320 K)	$\tan\delta$ (1 GHz) (320 K)	$f_M$ , MHz (420 K)	$\Delta E_{fb}$ , eV	$\Delta E_{fgb}$ , eV
$\text{LiFePO}_4$	$3.17 \cdot 10^{-5}$	0.60	$9.3 \cdot 10^{-6}$	0.66	15.09	0.14	5.92	0.55	0.61
$\text{LiFePO}_4/\text{C}$			$1.65 \cdot 10^{-6}$	0.49				0.54	

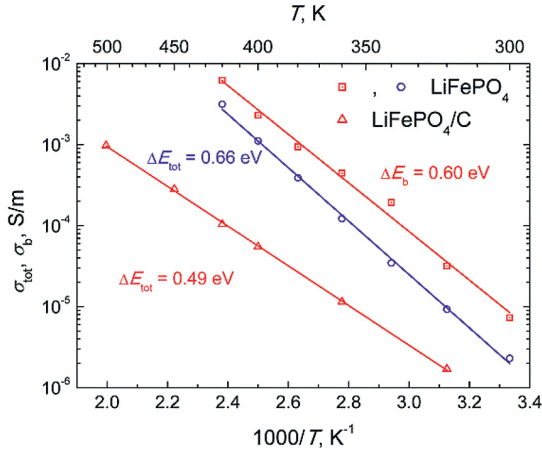


Figure 2.18. The temperature dependences of total and bulk conductivities of the  $\text{LiFePO}_4$  and the  $\text{LiFePO}_4/\text{C}$  ceramics

The activation energies of  $\sigma_{\text{tot}}$  ( $\Delta E_{\text{tot}}$ ) and of  $\sigma_b$  ( $\Delta E_b$ ) were found from the slopes of the Arrhenius plots. The experimental results of the investigation of  $\sigma_b$  and  $\sigma_{\text{tot}}$ , their activation energies are summarized in Table 2.7.

**2.8. Study of the  $\text{Li}_3\text{Fe}_{1.2}\text{Sc}_{0.75}\text{Y}_{0.05}(\text{PO}_4)_3$  ceramics by impedance and Mössbauer spectroscopy**

$\text{Li}^+$  conductive NASICON type  $\text{Li}_3\text{Fe}_{1.2}\text{Sc}_{0.75}\text{Y}_{0.05}(\text{PO}_4)_3$  compound has been synthesized by solid state reaction method [11, 27]. Ceramic samples were prepared for the study of electrical properties. Two and four probe methods were used for measurements of electrical impedance in the frequency range from 10 Hz to 1 MHz. Coaxial line was used for the investigation of impedance spectra in the frequency range from 1 MHz to 3 GHz. The electrical properties of the ceramics were studied in the temperature interval from room temperature (RT) to 600 K. The Mössbauer spectra were measured in the temperature interval (10–600) K (Fig. 2.19).

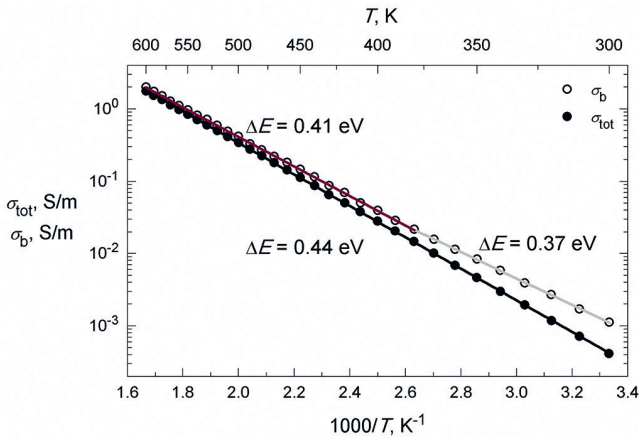


Figure 2.19. Total ( $\sigma_{\text{tot}}$ ) and bulk ( $\sigma_b$ ) conductivities of  $\text{Li}_3\text{Fe}_{1.2}\text{Sc}_{0.75}\text{Y}_{0.05}(\text{PO}_4)_3$  ceramics' dependences on reciprocal temperature

The results of the investigation of the structure parameters showed that  $\text{Li}_3\text{Fe}_{1.2}\text{Sc}_{0.75}\text{Y}_{0.05}(\text{PO}_4)_3$  compound was a single phase material and belonged to the monoclinic symmetry (space group  $\text{P}2_1/\text{n}$ ) with  $Z = 4$  formula units in the unit cell. The cell parameters  $a$ ,  $b$ ,  $c$  and volume ( $V$ ) of the cell were found to be  $8.715(4)$  Å,  $12.181(9)$  Å,  $8.684(3)$  Å and  $921.90$  Å<sup>3</sup>, respectively. The theoretical density ( $d_t$ ) of the compound was found to be  $2.956$  g/cm<sup>3</sup>.

The value of the of total conductivity of the  $\text{Li}_3\text{Fe}_{1.2}\text{Sc}_{0.75}\text{Y}_{0.05}(\text{PO}_4)_3$  ceramics at the room temperature is three times higher than the value for  $\text{Li}_3\text{Sc}_{2-x}\text{Fe}_x(\text{PO}_4)_3$  ( $x = 0.4$ ), and the value of grain conductivity is more than three orders of magnitude higher than that of  $\text{Li}_3\text{Sc}_2(\text{PO}_4)_3$  crystals. At temperature  $T = 380$  K, the change of  $\Delta E_b$  was found. In the temperature range  $T \geq 380$  K the value of  $\Delta E_b$  was found to be  $0.41$  eV. The  $\Delta E_b$  change at 380 K can be associated with  $\beta \rightarrow \gamma$  phase transition as previously was observed at higher temperatures in  $\text{Li}_3\text{Sc}_{2-x}\text{Y}_x(\text{PO}_4)_3$  ( $0.1 \leq x \leq 0.3$ ) system [28].

At temperature of around 380 K, the changes of activation energies of the grain conductivity, relaxation frequency were indicated also in quadrupole splitting of Mössbauer spectra (Fig. 2.20). The phenomenon can be related with  $\beta \rightarrow \gamma$  phase transition in the investigated compound.

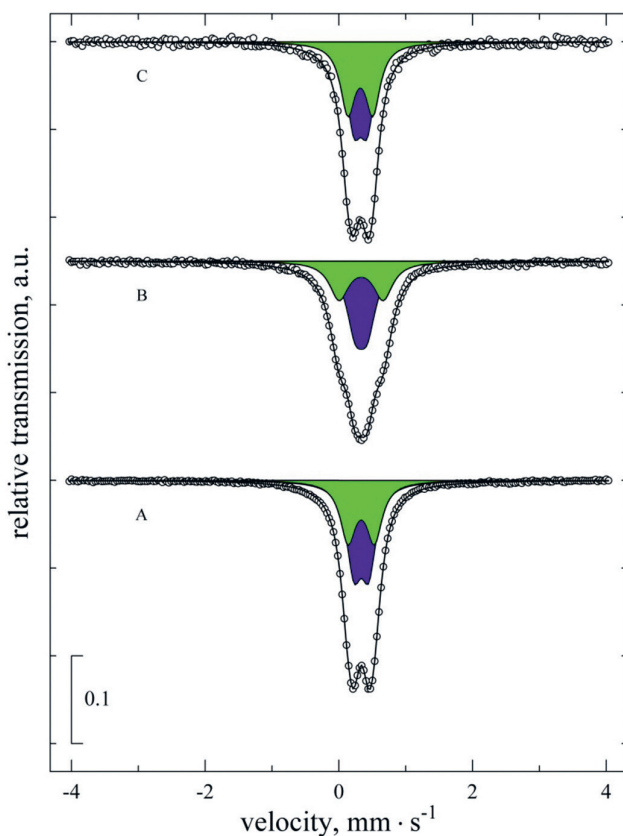


Figure 2.20. Mössbauer spectra measured at room temperature. A – as prepared sample; B – after heating up to 578 K; C – same as B, but cooled in liquid nitrogen

From Mössbauer spectroscopy (Fig. 2.20) it is evident that there exist two different ferric iron positions in the  $\text{Li}_3\text{Fe}_{1.2}\text{Sc}_{0.75}\text{Y}_{0.05}(\text{PO}_4)_3$  compound. Hyperfine parameters of iron ions are consistent with the octahedral coordination. The changes in quadrupole splitting at 380 K are in good agreement with the observed changes in the conductivity and activation energies. As the temperature is lowered, the system shows hysteresis-like behavior and undergoes the first-order phase transition.

## 2.9. NASICON-type $\text{Na}_3\text{M}_2(\text{PO}_4)_3$ (M = divalent metal) pyrophosphates

NASICON-type  $\text{Na}_3\text{M}_2(\text{PO}_4)_3$ , (M = Zn, Mn, Cu, Pb, etc.) and various pyrophosphates were proposed as potential candidates for sodium-ion battery cathode [30]. Among the pyrophosphates,  $\text{Li}_2\text{FeP}_2\text{O}_7$ ,  $\text{Na}_2\text{MnP}_2\text{O}_7$ ,  $\text{Na}_2\text{PbP}_2\text{O}_7$  and  $\text{Na}_2\text{ZnP}_2\text{O}_7$  compounds have been synthesized and investigated [7, 29]. Attempts to improve the properties of material involved various cationic substitutions in the above-mentioned double phosphates, new compounds such as  $\text{Na}_2\text{Fe}_{1-x}\text{Mn}_x\text{P}_2\text{O}_7$ ,  $\text{NaCsMnP}_2\text{O}_7$ ,  $\text{NaCsMn}_{0.35}\text{Cu}_{0.65}\text{P}_2\text{O}_7$ , Mn-doped  $\text{Na}_2\text{ZnP}_2\text{O}_7$  were synthesized. There were also attempts to improve the battery cathode by adding carbon nano tubes to sodium iron pyrophosphate

$\text{Na}_2\text{MnP}_2\text{O}_7$  is a promising sodium-ion battery cathode material. Electrical properties of  $\text{Na}_2\text{MnP}_2\text{O}_7$  ceramics were analysed by impedance spectroscopy in the broad frequency range from 10 Hz to 10 GHz. Temperature dependencies of conductivity indicated a phase transition taking place in the grains of ceramics at 663 K, which was also evidenced by differential thermal analysis and thermal X-ray diffraction. In addition, close to the room temperature protonic conductivity strongly influences the total conductivity of the ceramics. Both newly observed phenomena may be important for overall sodium battery performance.

Although the  $\text{Na}_2\text{MnP}_2\text{O}_7$  structure and electrochemical properties were studied, all the investigations on this compound were performed only at the room temperature. Consequently, the studies of high temperature behaviour of  $\text{Na}_2\text{MnP}_2\text{O}_7$  powder and ceramics were carried out.

$\text{Na}_2\text{MnP}_2\text{O}_7$  was synthesized by solid state reaction from stoichiometric amounts of  $\text{Na}_2\text{C}_2\text{O}_4$ ,  $\text{MnC}_2\text{O}_4 \cdot 2\text{H}_2\text{O}$ , and  $\text{NH}_4\text{H}_2\text{PO}_4$ . The initial compounds were mixed in ethyl alcohol for 3 h. The mixture was heated for 6 h at 300 °C in silicon carbide crucible in Ar/H<sub>2</sub> atmosphere, milled and pelletized (500 kg/cm<sup>2</sup>). Then the pellet was heated up to 620 °C (ramp rate of 10 °C/min), annealed for 6 h in a tubular furnace under a steady Ar/H<sub>2</sub> flow, and cooled down to room temperature in Ar/H<sub>2</sub> atmosphere. Finally, the pellet was heated at 700 °C for 6 h, cooled down to room temperature (in Ar/H<sub>2</sub> atmosphere) and milled. Differential thermal analysis and thermogravimetry (SDT Q600) was performed on heating and cooling the powder from room temperature to 620 °C with 10 K/min heating/cooling rate. Thermal X-ray powder diffraction (XRPD) has been performed at 30 °C, 100 °C, 300 °C, 400 °C and 500 °C in air with Cu K $\alpha$  radiation on a Panalytical Xpert MPD diffractometer equipped with the X' Celerator detector and an Anton Paar HTK 12 furnace. The diagrams were recorded in 2 $\theta$  range from 7 to 80° with a step of 0.017° and 100 s per step.

The temperature dependence of  $\text{Na}_2\text{MnP}_2\text{O}_7$  ceramics total conductivity suggested the phase transition taking place in this compound at 660 K. This phase transition has been approved by DTA and thermal XRPD experiments. To the best of our knowledge, it has never been reported before. Surprisingly, a significant decrease of conductivity was observed on heating ceramics up to 370 K. It was shown that a very small amount of water

in the sodium-manganese-pyrophosphates affects their room temperature conductivity, in this case,  $\text{Na}^+$  and  $\text{H}^+$  must be mixed at the same time. The high proton conductivity at the room temperature and humid ambient atmosphere can have a crucial impact on the performance of the studied material as a sodium battery cathode. The mixed  $\text{Na}^+$ -ionic and proton conductivity in  $\text{Na}_2\text{MnP}_2\text{O}_7$ , however, could possibly find another application in the future.

## 2.10. Preparation, structure, surface and impedance spectroscopy of $\text{Na}_2\text{Zn}_{0.5}\text{Mn}_{0.5}\text{P}_2\text{O}_7$ ceramics

For search new Na-based pyrophosphate materials for application in the secondary sodium ion batteries  $\text{Na}_2\text{Zn}_{0.5}\text{Mn}_{0.5}\text{P}_2\text{O}_7$  powder was synthesized by solid state reaction and ceramics were sintered [31]. The structure studies of the powder were conducted too.

The  $\text{Na}_2\text{Zn}_{0.5}\text{Mn}_{0.5}\text{P}_2\text{O}_7$  powder has been synthesized by solid-state reaction method from stoichiometric amounts of  $\text{Na}_2\text{CO}_3$ ,  $\text{ZnO}$  and  $\text{MnO}$  (all chemically pure). The precursor was mixed and then stoichiometric amount of 85%  $\text{H}_3\text{PO}_4$  (diluted with distilled water 1:1) was added very slowly, while mixing. The obtained mixture was heated in silica-carbon crucible at 393 K for 5 h and milled. After milling, the obtained powder was pressed into pellets at 50 MPa. The pellets were heated at 673 K for 4 h and subsequently at 923 K for 6 h. The tubular furnace with steady  $\text{Ar}/\text{H}_2$  flow was used in all heating steps. After the annealing, the pellet was cooled down to RT in  $\text{Ar}/\text{H}_2$  atmosphere. The obtained product was milled into ceramic powder.

The analysis of XRD patterns show that  $\text{Na}_2\text{Zn}_{0.5}\text{Mn}_{0.5}\text{P}_2\text{O}_7$  powder at RT consists of two phases:  $\text{Na}_2\text{MnP}_2\text{O}_7$  crystallizes in triclinic space group  $\text{P}\bar{1}$  (XRD card 074-2586) and  $\text{Na}_2\text{ZnP}_2\text{O}_7$  crystallizes in the tetragonal space group  $\text{P}4_2/\text{mmm}$  (XRD card 01-070-5836) The analysis showed that the obtained composite consists of 38.64 wt.%  $\text{Na}_2\text{MnP}_2\text{O}_7$  phase and 61.36 wt. %  $\text{Na}_2\text{ZnP}_2\text{O}_7$  phase. The lattice parameters, unit cell volume ( $V$ ), angles ( $\alpha$ ,  $\beta$ ,  $\gamma$ ), formula units in the unit cell ( $Z$ ) and theoretical density ( $d_t$ ) of both phases at RT are presented in Table 2.8 and Fig. 2.21.

Table 2.8. Summary of X-ray diffraction analysis of  $\text{Na}_2\text{Zn}_{0.5}\text{Mn}_{0.5}\text{P}_2\text{O}_7$  powder at room temperature

Phase	$a$ , Å	$b$ , Å	$c$ , Å	$\alpha$ , deg	$\beta$ , deg	$\gamma$ , deg	$V$ , Å <sup>3</sup>	$Z$	$d_t$ , g/cm <sup>3</sup>
$\text{Na}_2\text{MnP}_2\text{O}_7$	9.89(4)	11.08(5)	12.46(3)	148.48	121.98	68.35	595.18(15)	4	3.07
$\text{Na}_2\text{ZnP}_2\text{O}_7$	7.72(5)	10.27(4)	–	–	–	–	612.13(15)	4	3.10

In the temperature interval from 360 K to 700 K, the total electrical conductivity of  $\text{Na}_2\text{Zn}_{0.5}\text{Mn}_{0.5}\text{P}_2\text{O}_7$  increases with temperature according to Arrhenius law, but the activation energy change was found at about 630 K (Fig. 2.21). This change was associated with a phase transition taking place in  $\text{Na}_2\text{MnP}_2\text{O}_7$  phase. The temperature hysteresis of the total electrical conductivity value was found at heating and cooling of  $\text{Na}_2\text{Zn}_{0.5}\text{Mn}_{0.5}\text{P}_2\text{O}_7$  ceramics in the temperature from 300 K to 360 K. Non-Arrhenius behaviors of temperature dependence of conductivity can be associated with dehydration of the samples.

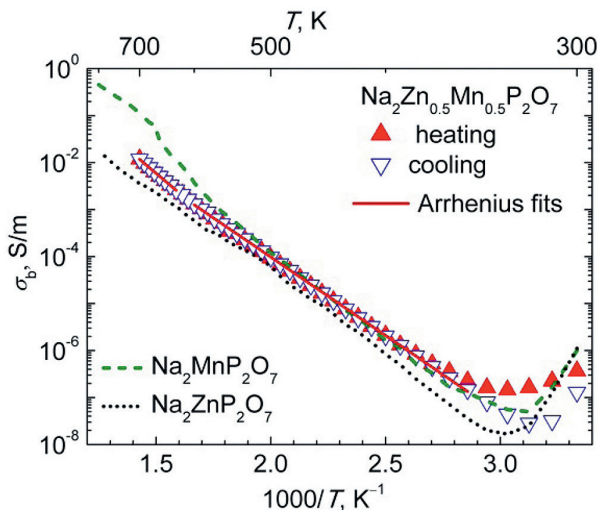


Figure 2.21. Temperature dependences of bulk electrical conductivity of  $\text{Na}_2\text{Zn}_{0.5}\text{Mn}_{0.5}\text{P}_2\text{O}_7$  ceramics during heating and cooling. Conductivities of  $\text{Na}_2\text{ZnP}_2\text{O}_7$  and  $\text{Na}_2\text{MnP}_2\text{O}_7$  phases are also presented for comparison

### 2.11. Synthesis, structure and impedance spectroscopy of $\text{NaCsZn}_{0.5}\text{Mn}_{0.5}\text{P}_2\text{O}_7$ pyro-phosphate ceramics

The evolution of  $\text{Na}^+$  ion batteries stimulates the search of new materials for such energy storage devices. In this study,  $\text{NaCsZn}_{0.5}\text{Mn}_{0.5}\text{P}_2\text{O}_7$  pyrophosphate powder was synthesized by solid state reaction and ceramics were sintered [8].

$\text{NaCsZn}_{0.5}\text{Mn}_{0.5}\text{P}_2\text{O}_7$  powders were prepared by a solid-state reaction method from stoichiometric mixture  $\text{Na}_2\text{CO}_3$ ,  $\text{ZnO}$ ,  $\text{MnO}$ ,  $\text{CsNO}_3$  (all precursors were chemically pure) in  $\text{Ar}/\text{H}_2$  atmosphere. The stoichiometric mixture was mixed and very slowly 85%  $\text{H}_3\text{PO}_4$  (diluted with distilled water 1:1) was added and mixed. The obtained product in silica crucibles was heated in  $\text{Ar}/\text{H}_2$  atmosphere at temperature 393 K for 4 h. After milling, the obtained powder was pressed into pellets with pressure of 50 MPa. The pellets were sintered at 673 K temperature for 6 h, and then at 923 K temperature for 4 h. Tubular furnace under a steady  $\text{Ar}/\text{H}_2$  flow was used for sintering. After annealing the obtained product in  $\text{Ar}/\text{H}_2$ , the atmosphere was cooled down to RT milled again and the obtained powder was heated at 993 K temperature for 4 h.

The results of XRD measurements show that  $\text{NaCsZn}_{0.5}\text{Mn}_{0.5}\text{P}_2\text{O}_7$  powder prepared by solid state reaction is a mixed phase solid solution. Three different phases were detected in the X-ray diffraction patterns of the powder.  $\text{NaCsZnP}_2\text{O}_7$  (65.61 wt.%),  $\text{NaCsMnP}_2\text{O}_7$  (15.35 wt.%) and  $\text{Cs}_2\text{MnP}_4\text{O}_{12}$  (19.04 wt.%) phases were found in the powder at the room temperature. We have not found the information about structure measurements of  $\text{NaCsZnP}_2\text{O}_7$  compound in the literature. The results of XRD patterns' analysis reveal that  $\text{NaCsZnP}_2\text{O}_7$  compound belongs to the monoclinic symmetry (space group  $\text{P}2_1/\text{n}$ ) with four formula units in the unit cell. The analysis of  $\text{NaCsMnP}_2\text{O}_7$  XRD patterns demonstrate that this phase crystallizes in the orthorhombic symmetry (space group  $\text{Cmc}2_1$ ) (PDF

01-089-5449). The  $\text{Cs}_2\text{MnP}_4\text{O}_{12}$  crystallizes in monoclinic structure (space group  $\text{P2}_1/\text{n}$ ). The lattice parameters, unit cell volume ( $V$ ), angle ( $\beta$ ), formula units in the unit cell ( $Z$ ) and theoretical density ( $d_t$ ) of the three phases at RT are presented in Table 2.9 below.

**Table 2.9. Summary of X-ray diffraction analysis of  $\text{NaCsZn}_{0.5}\text{Mn}_{0.5}\text{P}_2\text{O}_7$  powder at room temperature**

Phase	Space group	a, Å	b, Å	c, Å	$\beta$	V, Å <sup>3</sup>	Z	$d_t$ , g/cm <sup>3</sup>
$\text{NaCsMnP}_2\text{O}_7$	$\text{Cmc2}_1$	5.3203	15.0477	7.9974		784.37	4	3.534
$\text{NaCsZnP}_2\text{O}_7$	$\text{P2}_1/\text{n}$	13.0105	7.6912	7.4241	91.03	742.79	4	3.258
$\text{Cs}_2\text{MnP}_4\text{O}_{12}$	$\text{P2}_1/\text{n}$	7.9809	13.2416	11.5396	101.98	1192.91	4	3.545

The results of XRD measurements has shown anomalies of the lattice parameters in temperature range (400–500) K in orthorhombic  $\text{NaCsMnP}_2\text{O}_7$  and in temperature range (500–600) K in monoclinic  $\text{Cs}_2\text{MnP}_4\text{O}_{12}$ , but the symmetry group of above-mentioned compounds has not changed. It is possible that the detected anomalies of electrical properties are caused by disordering in the  $\text{NaCsMnP}_2\text{O}_7$  and  $\text{Cs}_2\text{MnP}_4\text{O}_{12}$  lattices.

Electrical properties of  $\text{NaCsZn}_{0.5}\text{Mn}_{0.5}\text{P}_2\text{O}_7$  ceramics were investigated by impedance spectroscopy in the temperature range of 300–700 K, and in the frequency range of 10 Hz – 3 GHz. In the temperature interval 420 K to 700 K, the total electrical conductivity of  $\text{NaCsZn}_{0.5}\text{Mn}_{0.5}\text{P}_2\text{O}_7$  increases with temperature according to Arrhenius law (Table 2.10). At 480 K and 590 K temperatures, the changes of activation energy of total electrical conductivity were found. In this case also it is possible that the detected anomalies of electrical properties are caused by disordering in the  $\text{NaCsMnP}_2\text{O}_7$  and  $\text{Cs}_2\text{MnP}_4\text{O}_{12}$  lattices.

**Table 2.10. Values of total electrical conductivity ( $\sigma_{10\text{Hz}}$ ) of  $\text{NaCsZn}_{0.5}\text{Mn}_{0.5}\text{P}_2\text{O}_7$  ceramic at various temperatures ( $T$ ) and its activation energies at heating ( $\Delta E_{\text{tot-h}}$ ) and cooling ( $\Delta E_{\text{tot-c}}$ )**

$T$ , K	Heating		Cooling	
	$\sigma_{10\text{Hz}}$ , S/m	$\Delta E_{\text{tot-h}}$ , eV	$\sigma_{10\text{Hz}}$ , S/m	$\Delta E_{\text{tot-c}}$ , eV
450	$1.19 \cdot 10^{-9}$	0.46	$4.14 \cdot 10^{-10}$	0.50
550	$3.17 \cdot 10^{-8}$	0.86	$1.3 \cdot 10^{-8}$	0.86
650	$8.88 \cdot 10^{-7}$	1.16	$5.42 \cdot 10^{-7}$	1.41

## 2.12. Conclusions

The following conclusions were obtained from the investigation:

1. X-ray diffraction analysis has shown that a partial substitution of  $\text{Al}^{3+}$  by  $\text{Y}^{3+}$  in  $\text{Li}_{1.3}\text{Al}_y\text{Y}_{x-y}\text{Ti}_{1.7}(\text{PO}_4)_3$  ( $x = 0.3$ ;  $y = 0.1, 0.2$ ), which belongs to NASICON-type compounds, causes an increase in the lattice parameters and theoretical density of

the compound. This variation can be caused by different values of the ionic radii of  $\text{Al}^{3+}$  by  $\text{Y}^{3+}$  ions.

2. The results of the investigation of electrical conductivities have shown that the increase of stoichiometric parameter  $y$  in  $\text{Li}_{1.3}\text{Al}_y\text{Y}_{x-y}\text{Ti}_{1.7}(\text{PO}_4)_3$  ( $x = 0.3; y = 0, 0.1, 0.15, 0.2, 0.3$ ) system leads to the increase of bulk conductivity ( $\sigma_b$ ) values.
3. The increase of the stoichiometric parameters  $x, y$  and amount of impurities  $\text{LiTiPO}_5$  in the  $\text{Li}_{1+4x}\text{Ti}_{2-x}\text{Nb}_y\text{P}_{3-y}\text{O}_{12}$  ( $x = 0.1, 0.2, 0.3; y = 0, 0.1, 0.2, 0.3$ ) compounds lead to the decrease of total and bulk conductivities and increase of their activation energies.
4. An increase of lithium content in  $\text{Li}_{1+4x}\text{Ti}_{2-x}(\text{PO}_4)_3$  (where  $x = 0.2, 0.5$ ) compounds leads to the increase of the volume of the lattice, the decrease of the theoretical density of the compounds, and the increase of total and bulk electrical conductivities.
5. The changes of activation energy of  $\sigma_{\text{tot}}$  ( $\Delta E_{\text{tot}}$ ) at 550 K and 528 K temperatures for  $\text{LiFeP}_2\text{O}_7$  and  $\text{Li}_{0.9}\text{Fe}_{0.9}\text{Ti}_{0.1}\text{P}_2\text{O}_7$ , respectively, can be related to the structure phase transitions detected by XRD measurements.
6. The anomalies of  $\Delta E_{\text{tot}}$  of  $\text{Li}_{4x}\text{Ti}_{1-x}\text{P}_2\text{O}_7$  ( $x = 0.06, 0.1, 0.2$ ) compounds in the temperature range from 520 to 580 K were found. The changes of  $\Delta E_{\text{tot}}$  can be related to some disordering in the supercell.
7. From Mössbauer spectroscopy it is evident that there exist two different ferric iron positions in the  $\text{Li}_3\text{Fe}_{1.2}\text{Sc}_{0.75}\text{Y}_{0.05}(\text{PO}_4)_3$  compound. The hyperfine parameters of iron ions are consistent with the octahedral coordination. Changes in quadrupole splitting at 380 K are in good agreement with observed changes in the conductivity and activation energies. Lowering the temperature, the system shows hysteresis-like behavior and undergoes the first-order phase transition.
8. The temperature dependence of  $\text{Na}_2\text{MnP}_2\text{O}_7$  ceramics' total conductivity suggested the phase transition taking place in this compound at 660 K. To the best of our knowledge, it has never been reported before. Surprisingly, a significant decrease of conductivity was observed on heating ceramics up to 370 K. A very small amount of water in the sodium-manganese-pyrophosphates affects their room temperature conductivity, in this case,  $\text{Na}^+$  and  $\text{H}^+$  must be mixed at the same time. The high proton conductivity at the room temperature and humid ambient atmosphere can have a crucial impact on the performance of the studied material as a sodium battery cathode. The mixed  $\text{Na}^+$  – ionic and proton conductivity in  $\text{Na}_2\text{MnP}_2\text{O}_7$ , however, can possibly find another application in the future.
9. The temperature hysteresis of total electrical conductivity value was found at heating and cooling of  $\text{Na}_2\text{Zn}_{0.5}\text{Mn}_{0.5}\text{P}_2\text{O}_7$  ceramics in the temperature from 300 K to 360 K. Non-Arrhenius behaviors of temperature dependence of conductivity can be associated with dehydration of the samples.
10.  $\text{NaCsZn}_{0.5}\text{Mn}_{0.5}\text{P}_2\text{O}_7$  powder is a mixed-phase solid solution, which consists of  $\text{NaCsZnP}_2\text{O}_7$  (65.61 wt.%),  $\text{NaCsMnP}_2\text{O}_7$  (15.35 wt.%) and  $\text{Cs}_2\text{MnP}_4\text{O}_{12}$  (19.04 wt.%) phases. The changes of lattice parameters with temperature were analysed for all three phases by XRD. The anomalies of lattice parameters were observed in the temperature region (400–500) K for  $\text{NaCsMnP}_2\text{O}_7$  and in the temperature range (500–600) K for  $\text{Cs}_2\text{MnP}_4\text{O}_{12}$ . These anomalies can be caused by structural disordering in these phases. It is possible that the detected anomalies of electrical properties are caused by disordering in the  $\text{NaCsMnP}_2\text{O}_7$  and  $\text{Cs}_2\text{MnP}_4\text{O}_{12}$  lattices.

## 2.13. References

1. Knauth, P. (2009) Inorganic solid Li ion conductors: An overview. *Solid State Ionics*, 180, 911–916.
2. Hagman, L. O., Kierkegaard, P. (1968) The Crystal Structure of  $\text{NaM}_2^{\text{IV}}(\text{PO}_4)_3$ ,  $\text{Me}^{\text{IV}} = \text{Ge, Ti, Zr}$ . *Acta Chem. Scand.*, 22, 1822–1832.
3. Arbi, K., Rojo, J. M., Sanz, J. (2007) Lithium mobility in titanium based Nasicon  $\text{Li}_{1+x}\text{Ti}_{2-x}\text{Al}_x(\text{PO}_4)_3$  and  $\text{LiTi}_{2-x}\text{Zr}_x(\text{PO}_4)_3$  materials followed by NMR and impedance spectroscopy. *J. Eur. Ceram. Soc.*, 27, 4215–4218.
4. Aono, H., Sugimoto, E., Sadaoka, Y., Imanaka, N., Adachi, G.-Y. (1991) Electrical property and sinterability of  $\text{LiTi}_2(\text{PO}_4)_3$  mixed with lithium salt ( $\text{Li}_3\text{PO}_4$  or  $\text{Li}_3\text{BO}_3$ ). *Solid State Ionics*, 47, 257–264.
5. Barpanda, P., Nishimura, S.-I., Yamada, A. (2012) High-voltage pyrophosphate cathodes. *Advanced Energy Materials*, 2, 841–859.
6. Shakoor, R. A., Park, C. S., Raja, A. A., Shin, J. and Kahraman, R. (2016) A mixed Iron-manganese based pyrophosphate cathode,  $\text{Na}_2\text{Fe}_{0.5}\text{Mn}_{0.5}\text{P}_2\text{O}_7$ , for rechargeable sodium ion batteries. *Phys. Chem. Chem. Phys.*, 18(5), 3929–3935.
7. Daugēla, S., Šalkus, T., Kežionis, A., Venckutė, V., Valdniece, D., Dindune, A., Barre, M., Orliukas, A. F. (2017) Anomalous temperature-dependent electrical properties of  $\text{Na}_2\text{MnP}_2\text{O}_7$ . *Solid State Ionics*, 302, 72–76.
8. Orliukas, A. F., Venckutė, V., Daugēla, S., Kežionis, A., Dindune, A., Valdniece, D., Ronis, J., Lelis, M., Mosiałek, M., Šalkus, T. (2017) Synthesis, structure and impedance spectroscopy of  $\text{NaCsZn}_{0.5}\text{Mn}_{0.5}\text{P}_2\text{O}_7$  pyrophosphate ceramics. *Solid State Ionics*, 302, 92–97.
9. Kežionis, A., Butvilas, P., Šalkus, T., et al. (2013) Four-electrode impedance spectrometer for investigation of solid ion conductors. *Rev. Sci. Instrum.*, 84, 013902-1-8.
10. Kežionis, A., Kazakevičius, E., Šalkus, T., Orliukas, A. F. (2011) Broadband high frequency impedance spectrometer with working temperatures up to 1200 K. *Solid State Ionics*, 188, 110–113.
11. Šalkus, T., Kazakevičius, E., Reklaitis, J., Venckute, V., Daugela, S., Davidonis, R., Baltrūnas, D., Dindune, A., Valdniece, D., Orliukas, A. F. (2017) Study of the  $\text{Li}_3\text{Fe}_{1.2}\text{Sc}_{0.75}\text{Y}_{0.05}(\text{PO}_4)_3$  ceramics by impedance and Mössbauer spectroscopy. *Solid State Ionics*, 302, 30–34.
12. Venckutė, V., Banytė, J., Kazlauskienė, V., Miškinis, J., Šalkus, T., Kežionis, A., Kazakevičius, E., Dindune, A., Kanepe, Z., Ronis, J., Orliukas, A. F. (2010) Preparation structure and electrical properties of  $\text{Li}_{1+4x}\text{Ti}_{2-x}\text{Nb}_y\text{P}_{3-y}\text{O}_{12}$  (where  $x = 0.1, 0.2, 0.3, y = 0, 0.1, 0.2, 0.3$ ) ceramics. *Lithuanian J. Phys.*, 50, 435–443.
13. Orliukas, A. F., Šalkus, T., Kežionis, A., Dindune, A., Kanepe, Z., Ronis, J., Venckutė, V., Kazlauskienė, V., Miškinis, J., Lukauskas, A. (2012) Structure and broadband impedance spectroscopy of  $\text{Li}_{1.3}\text{Al}_y\text{Y}_{x-y}\text{Ti}_{1.7}(\text{PO}_4)_3$  ( $x = 0.3, y = 0.1, 0.2$ ) solid electrolyte ceramics. *Solid State Ionics*, 225, 620–625.
14. Orliukas, A. F., Venckutė, V., Miškinis, J., et al. (2013) X-ray photoelectron and broadband impedance spectroscopy of  $\text{Li}_{1+4x}\text{Ti}_{2-x}(\text{PO}_4)_3$  (where  $x = 0.2, 0.5$ ) solid electrolyte ceramics. *Lithuanian J. Phys.*, 53, 244–254.
15. Venckutė, V., Miškinis, J., Kazlauskienė, V., et al. (2014) XRD, XPS, SEM/EDX and broadband impedance spectroscopy study of pyrophosphate ( $\text{LiFeP}_2\text{O}_7$  and  $\text{Li}_{0.9}\text{Fe}_{0.9}\text{Ti}_{0.1}\text{P}_2\text{O}_7$ ) ceramics. *Phase Transitions*, 87(5), 438–451.
16. Elbouaanani, L. K., Malaman, B., Gérardin, R. (1999) Structure refinement and magnetic properties of  $\text{C-Fe}(\text{PO}_3)_3$  studied by neutron diffraction and Mössbauer techniques. *Journal of Solid State Chemistry*, 148, 455–463.
17. Dindune, A., Kanepe, Z., Kazakevičius, E., Kežionis, A., Ronis, J., Orliukas, A. F. (2003) Synthesis and electric properties of  $\text{Li}_{1+x}\text{M}_x\text{Ti}_{2-x}(\text{PO}_4)_3$  (where  $\text{M} = \text{Sc, Al, Fe, Y, } x = 0.3$ ) superionic ceramics. *Journal of Solid State Electrochemistry*, 7, 113–117.
18. Salkus, T., Kazakevičius, E., Kežionis, A., et al. (2010) XPS and ionic conductivity studies on  $\text{Li}_{1.3}\text{Al}_{0.15}\text{Y}_{0.15}\text{Ti}_{1.7}(\text{PO}_4)_3$ . *Ceramics Ionics*, 16, 631–637.

19. Robertson, A., Fletcher, J. G., Skakle, J. M. S., West, A. R. (1994) Synthesis of  $\text{LiTiPO}_5$  and  $\text{LiTiAsO}_5$  with the  $\alpha\text{-Fe}_2\text{PO}_5$  Structure. *Journal of Solid State Chemistry*, 109, 53–59.
20. Venckutė, V., Miškinis, J., Kazlauskienė, V., et al. (2014) XRD, XPS, SEM/EDX and broadband impedance spectroscopy study of pyrophosphate ( $\text{LiFeP}_2\text{O}_7$  and  $\text{Li}_{0.9}\text{Fe}_{0.9}\text{Ti}_{0.1}\text{P}_2\text{O}_7$ ) ceramics. *Phase Transitions*, 87(5). <https://doi.org/10.1080/01411594.2013.857021>
21. Sobiestianskas, R., Dindune, A., Kanepė, Z., et al. (2000) Electrical properties of  $\text{Li}_{1+x}\text{Y}_y\text{Ti}_{2-y}(\text{PO}_4)_3$  (where  $x, y = 0.3, 0.4$ ) ceramics at high frequencies. *Materials Science and Engineering*, B76, 184–192.
22. Bogusz, W., Dygas, J. R., Krok, F., et al. (2001) Electrical conductivity dispersion in Co-doped NASICON samples. *Physica Status Solidi (a)*, 183, 323–330.
23. Orliukas, A. F., Bohnke, O., Kežionis, A., et al. (2012) Broadband impedance spectroscopy of some  $\text{Li}^+$  and  $\text{V}_0^{\bullet\bullet}$  conducting solid electrolytes. *Advanced Electromagnetics*, 1(1), 70–75.
24. Orliukas, A. F., Šalkus, T., Kežionis, A., et al. (2011) Structure and broadband impedance spectroscopy of  $\text{Li}_{1.3}\text{Al}_y\text{Y}_{x-y}\text{Ti}_{1.7}(\text{PO}_4)_3$  ( $x = 0.3, y = 0.1, 0.2$ ) solid electrolyte ceramics. 18<sup>th</sup> Int. Conf. Solid State Ionics, Warsaw, July 3–8, Abstracts, 240.
25. Venckutė, V., Dobrovolskis, P., Šalkus, T., et al. (2015) Preparation and Characterization of Solid Electrolytes Based on  $\text{TiP}_2\text{O}_7$  Pyrophosphate. *Ferroelectrics*, 479(1), 101–109.
26. Orliukas, A. F., Fung, K.-Z., Venckutė, V., et al. (2014) SEM/EDX, XPS and impedance spectroscopy of  $\text{LiFePO}_4$  and  $\text{LiFePO}_4/\text{C}$  ceramics. *Lithuanian J. Physics*, 54(2), 106–113.
27. Šalkus, T., Kazakevicius, E., Reklaitis, J., et al. (2016) Study of the  $\text{Li}_3\text{Sc}_{1.6}\text{Fe}_{0.4}(\text{PO}_4)_3$  and  $\text{Li}_3\text{Sc}_{0.75}\text{Y}_{0.05}\text{Fe}_{1.2}(\text{PO}_4)_3$  NASICON-type materials by impedance and Mössbauer spectroscopy. 12<sup>th</sup> Int. Symp. ISSFIT-12, July 3–7, 2016, Kaunas, Lithuania, Abstracts, 110.
28. Bykov, A. B., Chirkin, A. P., Demyanets, L. N., et al. (1990) Superionic conductors  $\text{Li}_3\text{M}_2(\text{PO}_4)_3$  ( $\text{M} = \text{Fe}, \text{Sc}, \text{Cr}$ ): Synthesis, structure and electrophysical properties. *Solid State Ionics*, 38, 31–52.
29. Daugėla, S., Šalkus, T., Kežionis, A., et al. (2016) Anomalous temperature-dependent electrical properties of  $\text{Na}_2\text{MnP}_2\text{O}_7$ . *Solid State Ionics*, 302, 72–76.
30. Palomares, V., Casas-Cabanas, M., Castillo-Martinez, E., Han, M. H., Rojo, T. (2013) Update on Na-based battery materials. A growing research path. *Energy Environ. Sci.*, 6, 2312–2337.
31. Venckutė, V., Dindune, A., Valdniece, D., et al. (2017) Preparation, structure, surface and impedance spectroscopy of  $\text{Na}_2\text{Zn}_{0.5}\text{Mn}_{0.5}\text{P}_2\text{O}_7$  ceramics. *Lith. J. Phys.*, 57(3), 183–193.

## 2.14. Kopsavilkums

Pētīti NASICON-a tipa tīklveida (vai karkasveida) fosfātu materiāli, kā arī fāžu veidošanās likumsakarības multikomponentās neorganisko fosfātu sistēmās, lai sintezētu jaunus savienojumus, noteiktu to struktūru un īpašības un perspektīvā izmantotu jaunu, alternatīvu, ekoloģiski tīru enerģijas avotu cieto elektrolītu (ar ātru jonu pārnesei) ieguvei un izstrādei (gāzu sensoros – vides monitoringā, baterijās – enerģētikā, akumulatoros). Litija jonu vadītājus (cietos elektrolītus) var izmantot arī jauna tipa katodu aizsargslāņa iegūšanā.

Pierādīts, ka NASICON-a tipa savienojumos, piemēram,  $\text{LiTi}_2^{\text{IV}}(\text{PO}_4)_3$ ,  $\text{Ti}^{\text{IV}}$ , aizvietojot ar trīsvērtīgajiem Sc, Al, Y u. c. joniem, var iegūt savienojumus ar ievērojami lielāku elektrovadītspēju (sevišķi istabas temperatūrā vai tuvu tai), jo tiek izmainīti režģa parametri un radīta iespēja palielinātai  $\text{Li}^+$  jonu mobilitātei, t. i., elektrovadītspējai. Tāpēc mūsu darba mērķis ir **jaunu**  $\text{Li}^+$  ( $\text{Na}^+$ ) neorganisko fosfora savienojumu sintēze un izpēte, pētot likumsakarības starp kristālu struktūru, elementārsastāvu un jonu vadītspēju šajos materiālos.

Pētījumus sadarbības projektā var iedalīt vairākās grupās.

1. NASICON-a tipa **litija jonu vadītāji** kā cietie elektrolīti litija jonu baterijās.

Kā zināms, kopējā un tilpuma vadītspēja  $\text{LiTi}_2(\text{PO}_4)_3$  keramikai ir  $2.5 \cdot 10^{-6}$  un  $6.3 \cdot 10^{-5} \text{ Scm}^{-1}$  atbilstoši. Lai palielinātu elektrovadītspēju, tika sintezēti modificēti NASICON-a tipa savienojumi:  $\text{Li}_{1+4x}\text{Ti}_{2-x}(\text{PO}_4)_3$  ( $x = 0.2, 0.5$ ),  $\text{Li}_{1.3}\text{Al}_y\text{Y}_{x-y}\text{Ti}_{1.7}(\text{PO}_4)_3$  ( $x = 0.3, y = 0.1, 0.2$ ),  $\text{Li}_{1+4x}\text{Ti}_{2-x}\text{Nb}_y\text{P}_{3-y}\text{O}_{12}$  ( $x = 0.1, 0.2, 0.3$  un  $y = 0, 0.1, 0.2, 0.3$ ),  $\text{Li}_3\text{Fe}_{1.2}\text{Sc}_{0.75}\text{Y}_{0.05}(\text{PO}_4)_3$ .

2. Iegūti arī vairāki katodu materiāli litija jonu baterijām. Jaunie **pirofosfāti** sintezēti cietfāžu reakcijās sistēmās  $\text{Li}_{1-x}\text{Fe}_{1-x}\text{Ti}_x\text{P}_2\text{O}_7$  ( $x = 0, 0.1$ ) un  $\text{Li}_{4x}\text{Ti}_{1-x}\text{P}_2\text{O}_7$  ( $x = 0, 0.06, 0.1, 0.2$ ), lai izmantotu kā perspektīvus elektrodu materiālus daudzkārtēji uzlādējamās baterijās. Iegūti arī  $\text{LiFePO}_4$  un  $\text{LiFePO}_4/\text{C}$  katodu materiāli ar olivīna struktūru.

3. Pēdējos gados atklāts, ka litija jonu baterijas sekmīgi aizstāj **Na-metāla pirofosfātu** tipa savienojumi, lai tos izmantotu nātrija jonu bateriju katodu materiāliem. Tāpēc tika sintezēti, pētīti un salīdzināti jauni fosfora savienojumi daudzkomponentu sistēmās  $\text{Na}_{2-x}\text{A}_x\text{MP}_2\text{O}_7$  ( $M = \text{Mn, Zn, A} = \text{Cs}$ ), lai perspektīvā tos izmantotu sadarbības projekta mērķiem. Cietfāžu reakcijās sintezēti un pētīti šādi savienojumi:  $\text{Na}_2\text{Zn}_{0.5}\text{Mn}_{0.5}\text{P}_2\text{O}_7$ ,  $\text{NaCsZn}_{0.5}\text{Mn}_{0.5}\text{P}_2\text{O}_7$ ,  $\text{Na}_2\text{MnP}_2\text{O}_7$ .

Izmantojot jaunākās pētniecības metodes, pētījumu rezultāti ļāva secināt, ka daļa iegūto fosfātu materiālu ir perspektīvi praktiskai izmantošanai.

Pētījumiem izmantota rentgendifrakcijas metode (XRD) struktūras parametru noteikšanai, impedances spektroskopija (IS) keramisko paraugu elektrovadītspējas mērīšanai, rentgenstaru fotoelektronu spektroskopija (XPS) vai elektronu spektroskopija (ESCA) ķīmiskai analīzei. Skenējošā elektronu mikroskopija (SEM) vai enerģijas dispersijas rentgenstaru spektroskopija (EDX) lietota kompozītu sastāva noteikšanai, Mesbauera spektrometrija – dzelzs jonu valences pētījumiem sintezētajos paraugos u. c.

## 3. Ionic liquids and their modification with lithium salts – synthesis and studies

### Jonu šķidrums un to modificēšana ar litija sāļiem – sintēze un pētījumi

Andris Zicmanis<sup>1</sup>, Sindija Briča<sup>1</sup> (3.2) and

Guntars Vaivars<sup>1,2</sup>, Einārs Sprūģis<sup>1,2</sup>, Juris Singatulovs<sup>1</sup> (3.3)

<sup>1</sup> Faculty of Chemistry, University of Latvia; Jelgavas iela 1, LV-1004, Riga, Latvia

<sup>2</sup> Institute of Solid State Physics, University of Latvia, Kengaraga iela 8, LV-1063, Riga, Latvia

E-mail: [guntars.vaivars@lu.lv](mailto:guntars.vaivars@lu.lv)

#### Contents

3. Ionic liquids and their modification with lithium salts. . . . .	54
3.1. Introduction. . . . .	55
3.2. <i>N, N'</i> – Dialkylimidazolium dimethyl phosphates – promising liquid media for different processes . . . . .	55
3.2.1. Introduction to ionic liquids . . . . .	55
3.2.2. Overview of imidazolium dimethyl phosphates and their manufacturing . . . . .	55
3.2.3. Summary on imidazolium dimethyl phosphates . . . . .	61
3.3. Ionic liquids with lithium salts. . . . .	61
3.3.1. Application of ionic liquids with Li salts. . . . .	61
3.3.2. Experimental part to ionic liquids with lithium salts . . . . .	62
3.3.3. Results and discussion about ionic liquid with Li salts . . . . .	63
3.3.4. Conclusions to ion liquids with Li salts . . . . .	66
3.4. References . . . . .	66
3.5. Kopsavilkums. . . . .	68

#### 3.1. Introduction

The lithium iron phosphate (LiFePO<sub>4</sub>) battery, which uses LiFePO<sub>4</sub> as a cathode material, and a graphitic carbon electrode as the anode, finds a number of roles in vehicle use and backup power because of low-cost, low-toxicity, well-defined performance, long-term stability, etc. Ionic liquids are electrolytes suitable for lithium batteries due to their high thermal stability and environment to dissolve the lithium salts. Ionic liquids form salts with inorganic acids, and it was reasonable to investigate phosphate salts for LiFePO<sub>4</sub> cells. Typical conductivity values for ionic liquids range from 10<sup>-5</sup> to 10<sup>-1</sup> S·cm<sup>-1</sup> at a room temperature, which is equivalent to the strong acid water solutions.

## 3.2. N, N' – Dialkylimidazolium dimethyl phosphates – promising liquid media for different processes (A. Zicmanis, S. Briča)

### 3.2.1. Introduction to ionic liquids

Development of smart technologies demands applications of advanced materials with properties allowing overrun of possibilities known till today. Ionic liquids (ILs) are among the materials of this kind. An IL (ethylammonium nitrate) was mentioned for the first time in the famous paper by Paul Walden in 1914 [1] as an interesting fact in author's systematic research of non-aqueous electrolytes, and this year is considered as the discovery of ionic liquids. The first publication was followed by wider investigations only years later, in the 1940s, when American authors proposed ILs as non-aqueous new solvents for use as battery electrolytes [2, 3]. The applications of ILs in electrochemistry continued for many years and remain topical today. However, the greatest boom in the research of ILs commenced in the middle of 1980s, when ILs were used as media in organic synthesis in place of traditional organic solvents – molecular liquids. Therefore, during the following thirty years chemistry of ILs has widely developed. Achievements and problems of synthesis, characterization and use of ILs are well recognized and described in numerous reviews [2–13], and new possibilities of ILs continue to be discovered and demonstrated.

Innumerable amounts of cations and anions may form ILs, and every combination of both these ions assign specific properties to their combination – the resulting IL. A group of ILs with 1,3-dialkylimidazolium cation and dimethyl phosphate anion create especially interesting ion pairs. These ILs are more thermally stable and resistant to the action of acids, bases, oxidizing and reducing reagents, etc. than the majority of ILs. Therefore, they may be used more extensively in chemical and technological processes. Promising properties of the mentioned imidazolium dimethyl phosphates (IA-DMPs) have encouraged us to seek further development of their applications in organic synthesis, modifications of membranes, extraction processes, etc., and the most important information about these materials with a high potential will be presented below.

Ammonium dialkyl phosphates that may be considered as remote relatives of IA-DMPs for the first time were mentioned in 1951 [14]. They were followed by alkylation products of pyridine with trialkyl phosphates that were described as salts with very low melting points in 1989 [15]. Later on, other authors have filed patents on the synthesis of imidazolium-based dialkyl phosphate ionic liquids [15, 16]. A comprehensive and detailed study of IA-DMPs was performed by Wasserscheid's group [17]. A variety of these ionic liquids have been synthesized and characterized in this work, paying particular attention to properties of practical relevance.

### 3.2.2. Overview of imidazolium dimethyl phosphates and their manufacturing

Today, there are two main ways for manufacturing the IA-DMP. The first, which has been known for more than thirty years, requires alkylation of 1-substituted imidazoles by trialkyl phosphates, mainly by trimethyl phosphate (route A, Fig. 3.1) [17–25]. This is the method for preparation of different 1-alkyl-3-methylimidazolium dimethyl phosphates (2).

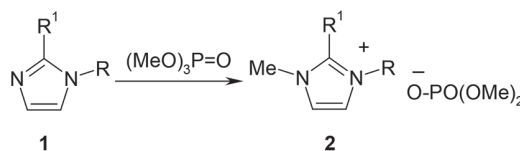


Figure 3.1. The most popular way for synthesis of ionic liquids with 1,3-dialkylimidazolium cation and dimethyl phosphate anion (route A)

Several organic solvents (toluene, ethyl acetate, acetonitrile, and others) are proposed for their synthesis. Various temperatures and reaction times up to 72 hours are successfully used. Reactions of 1-substituted imidazoles with trimethyl phosphate in boiling acetonitrile during 24 hours under nitrogen or argon are successfully applied for IA-DMP syntheses also in our laboratory (route A). The method allows obtaining practically colorless high quality ILs. A representative example of the method according to the route A is presented below.

**1,2,3-Trimethylimidazolium dimethyl phosphate (2a)** [26]. Trimethyl phosphate (8.41 g; 0.06 mol) was added drop by drop to the 1,2-dimethylimidazole (**1a**; 4.81 g; 0.05 mol), vigorously stirring in a round-bottom flask under argon. The mixture was stirred for 1 h at room temperature, then temperature was raised to 80 °C. 10 mL of acetonitrile was added after 30 minutes, and the content of the flask was stirred at 80 °C for 48 hours. The hot solution was poured into a conical flask and left at a room temperature for 24 hours. The precipitate formed was filtered, washed with ethyl acetate on the filter and dried in vacuum (0.5 mbar) during 6 hours after that. The IL (**2a**; 12.66 g; 91 %) was obtained as a white crystalline substance with m.p. 124-126 °C. <sup>1</sup>H NMR spectrum: (300 MHz, DMSO-d<sub>6</sub>, δ): 7.59 (2H, s, NCH=CHN); 3.75 (6H, s, CH<sub>3</sub>N-C(CH<sub>3</sub>)=NCH<sub>3</sub>); 3.23 (6H, d, P(OCH<sub>3</sub>)<sub>2</sub>); 2.55 (3H, s, NC(CH<sub>3</sub>)N) ppm.

The main limitation of the synthesis according to route A is the availability of the necessary raw materials – the corresponding 1-alkylimidazoles. Therefore, another method for obtaining IA-DMPs was recently developed in our laboratory – alkylation of 1,3-dialkylimidazolium chlorides by trimethyl phosphate (route B, Fig. 3.2) [25, 26].

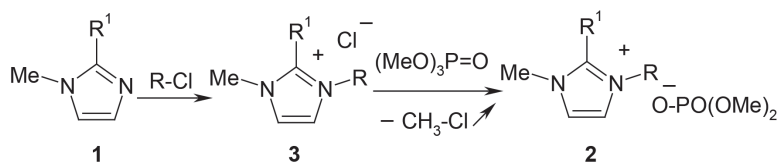


Figure 3.2. The alternative way for synthesis of ionic liquids with 1,3-dialkyl-imidazolium cation and dimethyl phosphate anion (route B)

In fact, route B represents an alkylation reaction of chloride anion. The driving force of the synthesis is the possibility to remove one of the reaction products (gaseous chloromethane) from the reaction area. The reaction demands elevated temperatures (80–110 °C) but takes quite a short time – only 2–4 hours. It is worth noting that raw materials for the aforementioned transformation – the corresponding 1,3-dialkylimidazolium chlorides – can be easily prepared according to the well-established protocol for the synthesis of ILs. We improved the old, well-investigated method with a slight modification – we performed the alkylation reaction in a tightly closed screw-top steel pressure tube. No inert gas is needed in this case for maintaining the quality of the product, and 1-chloroalkanes with low boiling temperatures can be used as alkylating reagents. 1-Methyl- and 1,2-dimethylimidazoles (**1**) were alkylated by 1-chloroalkanes in the mentioned steel pressure tube in our laboratory at 80 °C for the duration of 72 hours; the twofold molar excess of the alkylating reagent was applied. Expected imidazolium chlorides (**3**) formed in high yields, and the excess of the reagent was removed by

extracting the reaction mixture by ethyl acetate at the end. The obtained ILs with the chloride anion (**3**) were ready for further transformations after careful drying in high vacuum (0.5 mbar, 60 °C, 6 h) and analysis.

The second stage of the process according to route B – the exchange of the chloride ion for dimethyl phosphate anion (alkylation of chloride ion by trimethyl phosphate) was accomplished at temperatures 80–110 °C (Fig. 3.2), accompanied by the gas (CH<sub>3</sub>-Cl) release and providing the shift of the reaction equilibrium to the right. The negative AgNO<sub>3</sub> test together with the end of the evolution of gas allows fixing the end of the reaction. A complete conversion of the chloride ion can be ensured by using twofold molar excess of the alkylating reagent – trimethyl phosphate. There is no problem to dispose of the unreacted trimethyl phosphate; a simple extraction of the reaction mixture by ethyl acetate followed by drying of the obtained product in high vacuum (0.5 mbar, 70 °C, 8 h) is sufficient. A representative example of the method according to route B is shown below.

**1-Butyl-2,3-dimethylimidazolium chloride (3b)** [26] (the first stage of route B). 1,2-Dimethylimidazole (**1b**; 9.61 g; 0.10 mol), 1-chlorobutane (12.03 g; 0.13 mol), magnetic stirrer, and ethyl acetate (6 mL) were placed in a sealed screw-top home-made steel pressure tube. The airtight tube was placed in a glycerol bath, and the reaction mixture was stirred at 80 °C for 72 hours. Then the reaction mixture was poured in a round-bottom flask after cooling to room temperature and placed in the freezer for 24 hours. The obtained crystalline mass was filtered, washed with ethyl acetate (4 × 25 mL) on the filter, then dried under vacuum of rotary evaporator at 40°C and after that under high vacuum (0.5 mbar) at 60 °C for 6 hours. The IL (**3b**; 23.34 g; 89%) was obtained as a white crystalline substance with m.p. 93–94 °C. <sup>1</sup>H NMR spectrum (300 MHz, DMSO-d<sub>6</sub>, δ): 7.63 (2H, s, NCH=CHN); 4.11 (2H, t, NCH<sub>2</sub>-CH<sub>2</sub>-CH<sub>2</sub>-CH<sub>3</sub>); 3.74 (3H, s, CH<sub>3</sub>NCCH<sub>3</sub>); 2.58 (3H, s, CH<sub>3</sub>NCCH<sub>3</sub>); 1.68 (2H, m, NCH<sub>2</sub>-CH<sub>2</sub>-CH<sub>2</sub>-CH<sub>3</sub>); 1.29 (2H, m, NCH<sub>2</sub>-CH<sub>2</sub>-CH<sub>2</sub>-CH<sub>3</sub>); 0.92 (3H, t, NCH<sub>2</sub>-CH<sub>2</sub>-CH<sub>2</sub>-CH<sub>3</sub>) ppm.

**1-Butyl-2,3-dimethylimidazolium dimethyl phosphate (2b)** [26] (the second stage of the route B). 1-Butyl-2,3-dimethylimidazolium chloride (18.67 g; 10.0 mmol) and trimethyl phosphate (35.02 g; 25.0 mmol) were placed in a 50 mL round-bottomed flask equipped with a reflux condenser and CaCl<sub>2</sub> drying tube. The obtained mixture was stirred at the 110 °C for 24 h. Toluene (5 × 10 mL) was added to the crude product and the mixture was vigorously stirred and heated to reflux for 10 minutes. The toluene layer was then decanted while hot. The washing procedure was repeated further four times. Any remaining solvent was removed by rotary evaporation (10 mbar, 70 °C, 4 h). The pure product was dried under high vacuum (0.5 mbar, 70 °C, 8 h) and was subjected to AgNO<sub>3</sub> analysis to confirm the absence of a starting material. The ionic liquid with dimethyl phosphate anion (**2b**; 24, 13 g; 92%) was obtained as an oil that solidifies into a white crystalline substance with m.p. 92–93 °C during 24 h in a refrigerator. <sup>1</sup>H NMR spectrum (300 MHz, DMSO-d<sub>6</sub>, δ): 7.64 (2H, d, NCH=CHN); 4.13 (2H, t, NCH<sub>2</sub>-CH<sub>2</sub>-CH<sub>2</sub>-CH<sub>3</sub>); 3.74 (3H, s, CH<sub>3</sub>NCCH<sub>3</sub>); 3.23 (6H, d, P(OCH<sub>3</sub>)<sub>2</sub>); 2.58 (3H, s, CH<sub>3</sub>NCCH<sub>3</sub>); 1.67 (2H, m, NCH<sub>2</sub>-CH<sub>2</sub>-CH<sub>2</sub>-CH<sub>3</sub>); 1.29 (2H, m, NCH<sub>2</sub>-CH<sub>2</sub>-CH<sub>2</sub>-CH<sub>3</sub>); 0.92 (3H, t, NCH<sub>2</sub>-CH<sub>2</sub>-CH<sub>2</sub>-CH<sub>3</sub>) ppm.

1,3-Dialkylimidazolium dimethyl phosphates (**2**) prepared via both routes are colorless or slightly yellow oils. IA-DMPs with methyl group in their cations at C<sub>2</sub>-atom crystallize after being kept in a refrigerator for several days, while non-substituted at C<sub>2</sub>-atom substances remain in the form of thick oils. The yields of the second stage of the process – the alkylation of chloride ions – are high in all experiments (≥ 87 %) (Table 3.1).

Table 3.1. Some popular 1,3-dialkylimidazolium dimethyl phosphates [26]

No	Ionic liquid		route*	yield, %	m. p., °C	purity, %**	water, %***	T <sub>5%dec</sub> , °C****
	R	R <sup>1</sup>						
2a)	R = CH <sub>3</sub>	CH <sub>3</sub>	A	93	124–126	99.6	0.33	290
2b)	R = C <sub>4</sub> H <sub>9</sub>	CH <sub>3</sub>	B	92	92–93	99.4	0.55	297
2c)	R = C <sub>8</sub> H <sub>17</sub>	CH <sub>3</sub>	B	87	liquid	99.3	0.62	231
2d)	R = C <sub>12</sub> H <sub>25</sub>	CH <sub>3</sub>	B	92	113–114	99.2	0.71	218
2e)	R = CH <sub>3</sub>	H	A	93	liquid	99.5	0.44	302
2f)	R = C <sub>4</sub> H <sub>9</sub>	H	B	98	liquid	99.5	0.43	315
2g)	R = C <sub>8</sub> H <sub>17</sub>	H	B	93	liquid	99.4	0.45	286
2h)	R = C <sub>12</sub> H <sub>25</sub>	H	B	96	liquid	99.2	0.60	261
2i)	R = CH <sub>2</sub> CH <sub>2</sub> OH	H	B	97	liquid	99.4	0.46	284

where: \*route of synthesis; \*\*purity determined by potentiometric titration with perchloric acid in glacial acetic acid; \*\*\*water content (moisture) determined by Karl Fisher titration; \*\*\*\* decomposition temperatures (T<sub>5%dec</sub>) determined by TGA from onset to 5 wt % mass loss, heating at 10 °C min<sup>-1</sup> under air.

The previously discussed route B can be considered as an attractive alternative to route A, when problems arise with the preparation of 1-substituted imidazoles. Both aforementioned synthetic routes together allow preparing almost every imaginable IA-DMP, and both are successfully tested in our laboratory.

Every application of IA-DMP demands the necessary characterization of these materials after the synthesis and/or before use. Spectroscopic, titrimetric, and thermogravimetric methods were normally used for characterization of all the obtained ILs. <sup>1</sup>H NMR spectroscopy was the most useful tool for the qualitative analysis (confirmation of structures) of ILs. <sup>1</sup>H NMR spectra contained all the resonance signals characteristic to imidazolium salts, and the NMR data were consistent with literature data. The complete exchange of chloride ions for IA-DMP (prepared according to route B) was confirmed not only by the above-mentioned negative AgNO<sub>3</sub> test, but also by NMR data. The integral intensities of the resonance signals of protons of both O-CH<sub>3</sub> groups (6H) with  $\delta$  3.23–3.26 ppm that fully corresponded to those of protons C<sub>4</sub>-H and C<sub>5</sub>-H (2H) in the imidazolium cation ring with  $\delta$  7.63–7.67 ppm (an example in Fig. 3.3).

Like many other ILs, the ILs containing DMP anion are highly hygroscopic substances, and they should be stored in tightly closed containers. The Karl Fisher titration method was used for the control of moisture content in the obtained ILs. The water content did not exceed 1.0% in all the analysed correctly prepared samples (Table 3.1), but it is recommended to check the moisture content in ILs before their use, particularly in the samples stored over a longer time.

An important characteristic attesting to the quality of IA-DMP is their purity. Usually, it is tested by using chromatography. The HPLC/MS is usually used to determine the quality of prepared ILs. Only one signal can be observed in correctly made samples of IA-DMPs. The chromatogram of a frequently used IA-DMP – 1-butyl-3-methyl-imidazolium dimethyl phosphate [C<sub>4</sub>C<sub>1</sub>im] [DMP] is shown below for illustration (Fig. 3.4). Mass spectrum of the signal serves well to confirm the structure of IA-DMP (Fig. 3.5).

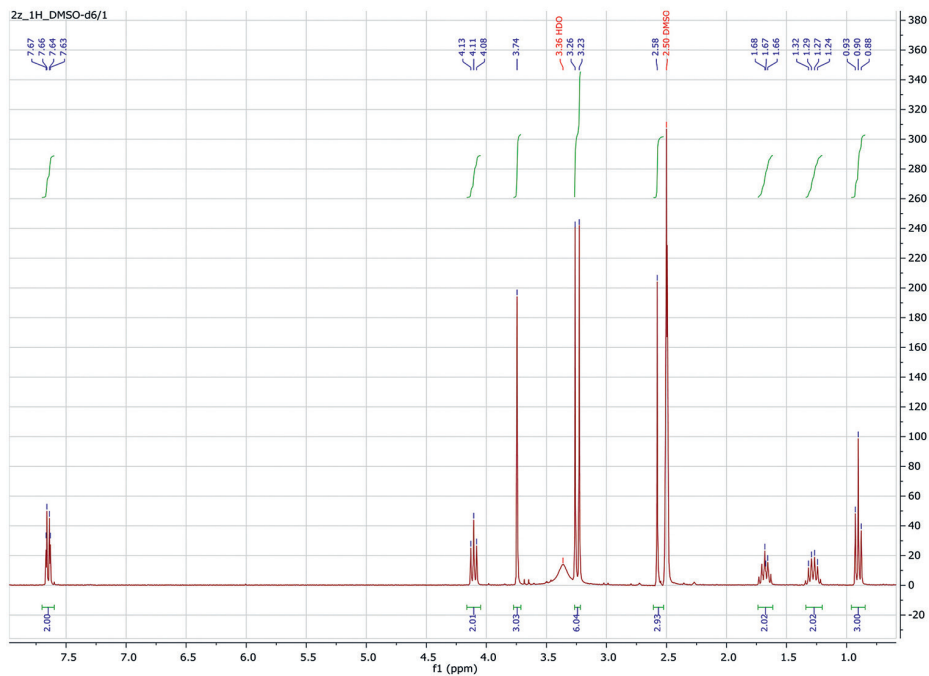


Figure 3.3.  $^1\text{H}$  NMR spectrum of 1-butyl-2,3-dimethylimidazolium dimethyl phosphate ( $[\text{C}_4\text{C}_1\text{im}][\text{DMP}]$ ) [26]

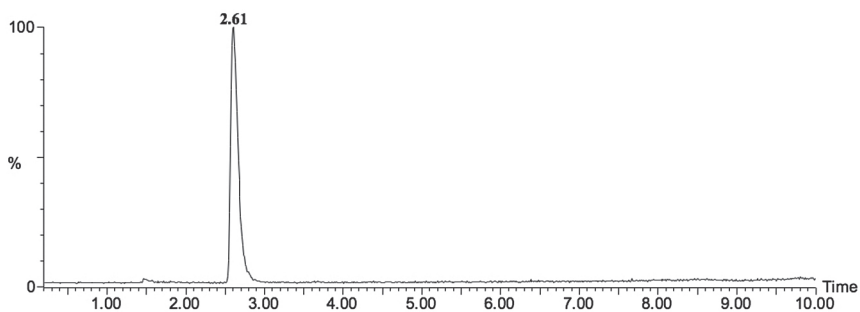


Figure 3.4. HPLC for 1-butyl-3-methylimidazolium dimethyl phosphate ( $[\text{C}_4\text{C}_1\text{im}][\text{DMP}]$ )

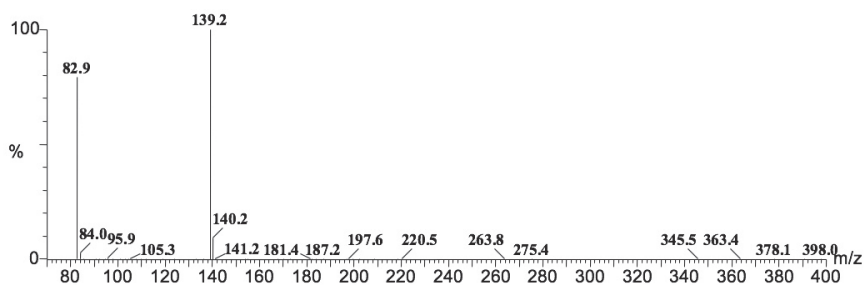


Figure 3.5. Mass spectrum for the peak at 2.61 min

Both NMR spectroscopy and chromatography are quite robust analytical methods. Very much more accurate data about the true quality of IA-DMP can be obtained using titrimetric methods. Titration of ILs containing DMP anion with perchloric acid in glacial acetic acid according to the recently published method [19, 26] was used for the quantitative analysis of ILs made in our laboratory. The method presents excellent titration curves, and all the obtained and carefully dried ILs have shown high purity (the content of the main substance in the product) – above 99 % (Table 3.1). A titration curve of 1-butyl-3-methylimidazolium dimethyl phosphate is shown below, again for the purposes for illustration (Fig. 3.6).

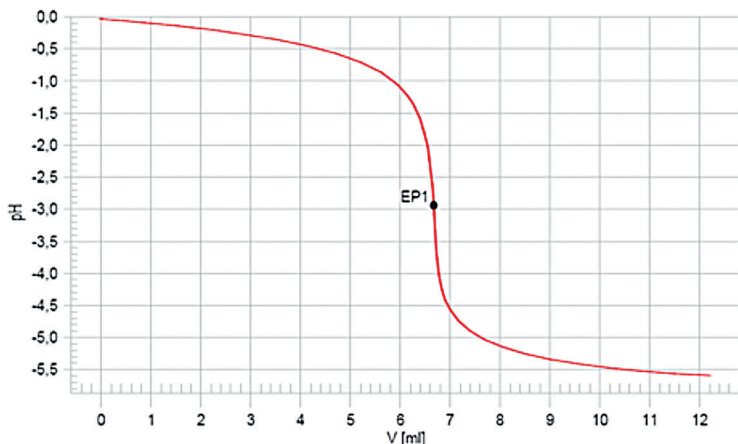


Figure 3.6. Titration curve of 1-butyl-3-methylimidazolium dimethyl phosphate ( $[\text{C}_4\text{C}_1\text{im}] [\text{DMP}]$ )

The performance of the quantitative analysis of IA-DMP is quite simple – just the traditional potentiometric non-aqueous titration.

#### Quantitative analyses of ionic liquids 1,3-dialkylimidazolium dimethyl phosphates.

A sample of an ionic liquid (2 or 4) (~100 mg) was dissolved in glacial acetic acid (50 mL) and titrated with the solution of perchloric acid in glacial acetic acid (0.05 mol/L) in the equipment of potentiometric titration. The purity (content of the main substance, %) of the sample was calculated from obtained titration curves and presented in Table 3.1.

An important characteristic of the quality of IA-DMP is their stability at elevated temperatures. The thermogravimetric analysis (TGA) is normally used for its determination. Our results have confirmed that IA-DMPs are highly stable ILs, disintegrating usually above 260 °C. Only IA-DMPs with long alkyl chains in their cations are a little bit less stable – their decomposition of 5 % was observed already at temperatures  $\geq 218$  °C. Hence, ILs with DMP anion are considerably more stable substances than similar ILs with carboxylate anions – even in cases, when their cation contains long alkyl groups ( $\text{C}_8$ – $\text{C}_{16}$ ) at nitrogen atom. These properties noticeably expands the available temperature interval for processes performed in these ILs and further expand their exploitation possibilities. A TGA curve of 1-butyl-3-methylimidazolium dimethyl phosphate ( $\text{C}_4\text{C}_1\text{im}$ ) [DMP] is presented below just for illustration of the thermal stability of IA-DMP (Fig. 3.7).

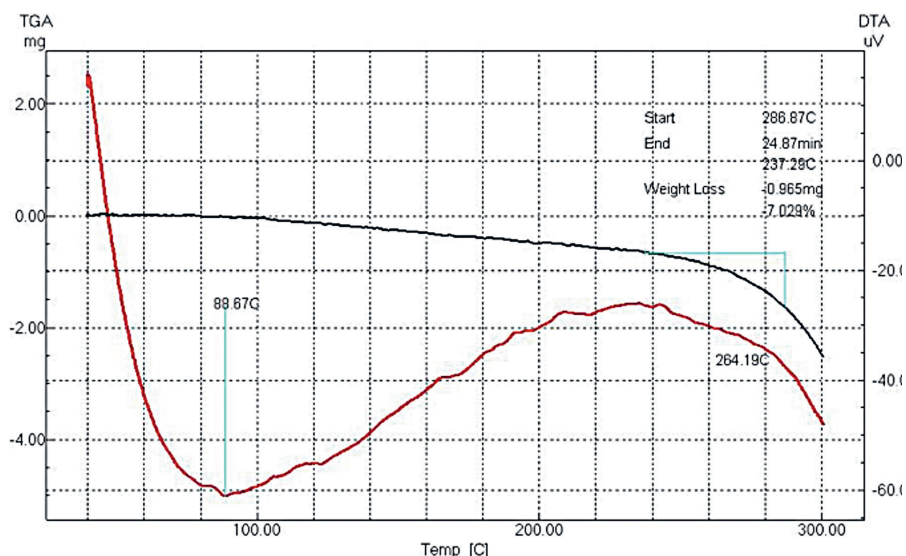


Figure 3.7. Curve of thermogravimetric analysis of 1-butyl-3-methylimidazolium dimethyl phosphate ( $C_4C_1im$ ) [DMP])

### 3.2.3. Summary on imidazolium dimethyl phosphates

Like other ILs, IA-DMPs most frequently are used as reaction media or/and catalysts in organic synthesis. This field of application has lately been also quite extensively investigated at the University of Latvia [19–26]. The use of IA-DMP in other research areas (electrochemistry, extraction processes, formation of composite materials, etc.) at the University of Latvia has started slightly later, and currently is in progress. This will be discussed hereafter.

## 3.3. Ionic liquids with lithium salts (G. Vaivars, E. Sprūģis, J. Singatulovs)

### 3.3.1. Application of ionic liquids with Li salts\*

Lithium-ion batteries are promoting the commercialization of electric car and home usage of local electric storage. However, safety issues are of the utmost importance. The lithium iron phosphate ( $LiFePO_4$ ) battery, which uses  $LiFePO_4$  as a cathode material, and a graphitic carbon electrode as the anode is finding a number of roles in vehicle use and backup power because of low-cost, low-toxicity, well-defined performance, long-term stability, etc. Ionic liquids (IL) are suitable electrolytes for lithium batteries due to high thermal stability and environment to dissolve the lithium salts [27]. Ionic liquids form salts with inorganic acids and it was reasonable to investigate phosphate salts for  $LiFePO_4$  cells. Typical conductivity values for ionic liquids range from  $10^{-5}$  to  $10^{-1}$   $S \cdot cm^{-1}$  at a room temperature [28], which is equivalent to the strong acid water solutions.

In the study, two ionic liquids were chosen for tests and synthesized: 1-butyl-3-methylimidazolium dimethylphosphate and 1, 3-dimethylimidazolium dimethylphosphate.

\* Corresponding author. Tel.: +371-20242643. E-mail address: [Guntars.Vaivars@cfi.lu.lv](mailto:Guntars.Vaivars@cfi.lu.lv) (G. Vaivars)

The structure of lithium nitrate solutions in a protic ionic liquid due to interactions between lithium ion and other species is of higher importance, because the electric conductivity will depend on it [29]. Méndez-Morales, et al. [30] studied solvation of lithium salts. It was concluded that the lithium cations were solvated by embedding them in the polar nanodomains of the solution formed by the anions, where they coordinated with the latter in a solid-like fashion reminiscent of a pseudolattice structure. This coordination led to interaction and increase of viscosity, which would determine the charge transfer properties [29–32]. The increase of viscosity would decrease the lithium ion mobility and therefore lithium ion conductivity [33].

One of the limitations when working with ionic liquids is to obtain these components with a high and known purity [34]. The most problematic are those that have high affinities with ionic liquids, such as water with hydrophilic ionic liquids. The most striking example is the viscosity that dramatically decreases only with traces of water. It was observed that 1% of water changes viscosity by 30%. However, the water molecules will adsorb on electrode surface, and the impact on electric double layer formation might be reasonable. It will influence the electrochemical stability of the system and the electrode potential, which is important for lithium batteries. Literature on ionic liquids often shows non-reproducible values or important deviations between different sets of data for a number of properties, in particular viscosity and density. These discrepancies mainly result from (i) the purity of the samples, (ii) inappropriate measurement methods [35]. Typically, ionic liquids melt at temperatures below 100 C [36–38]. Their partial vapour pressure is close to zero, they are not flammable and therefore are suitable for application in different devices. The high hygroscopicity limits the usage of ILs. They also physically absorb CO<sub>2</sub> gas [39], which is a physical absorption and might be used to remove the gas from environment. The process is slow [39], but the volume of absorbed gas could be reasonable [39–43]. The nature of ionic liquid is important. However, the length of hydrocarbon chain was less important [43].

### **3.3.2. Experimental part to ionic liquids with lithium salts**

The used ionic liquids were synthesized, as follows (Fig. 3.8): 1-methylimidazolium and trimethyl phosphate was mixed at a room temperature and molar ratio 1:1. The resulting mixture was intensively stirred and heated up to 80 C under argon. The mixture was stirred for 24 hours. The product was extracted using diethyl ether and dried at 0.5 Torr pressure for 4 hours at 80 C. 1-butyl-3-methylimidazolium dimethyl phosphate was produced by replacing 1-methylimidazolium with 1-butylimidazolium. 0.1 mol/kg (or 0.5 mol/kg) of lithium nitrate was dissolved in IL providing lithium ion conductivity.

Conductivity and electrochemical stability dependence of temperature were determined for pure ionic liquids and ionic liquid – lithium nitrate electrolytes. Detection methodology of conductivity dependence on temperature was designed. The factors affecting conductivity were identified with impedance spectroscopy. AUTOLAB potentiostat/galvanostat with a FRA was used for electrochemical and impedance measurements. The frequency range was from 3.5 to 20 kHz (signal amplitude 10 mV). The electrochemical stability window was obtained in a range from –3.5 to +3.5 V. A small glass vessel (2.5 mL) with stainless steel electrodes was used for measurements. The temperature control was realized using glycerol bath.

The thermal stability of ionic liquids was characterized using DTG-60 series from Shimadzu thermogravimetric equipment with aluminium crucibles (heating rate 10 deg/min).

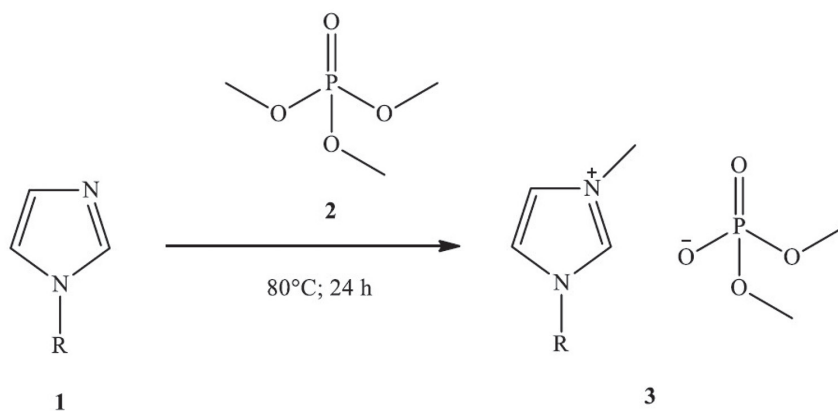


Figure 3.8. Synthesis procedure for the used ionic liquids

### 3.3.3. Results and discussion about ionic liquid with Li salts

Ionic liquids are stable up to 200 C (Fig. 3.9, 1-buthyl-3-methylimidazolium dimethyl phosphate). The stability was controlled before and after impedance measurements. The thermal stability was just slightly influenced by adding lithium nitrate.

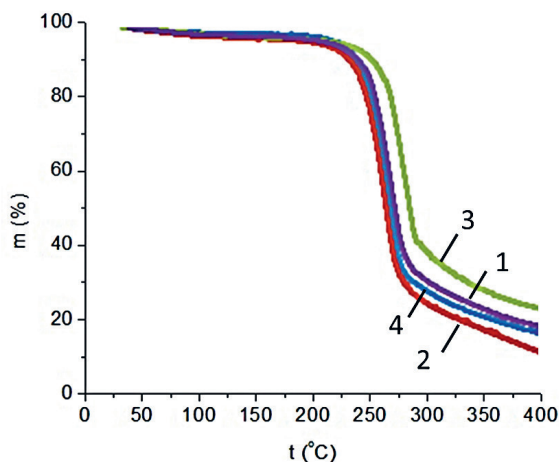


Figure 3.9. Thermal stability of 1-buthyl-3-methylimidazolium dimethyl phosphate: 1) freshly prepared; 2) after impedance measurements; 3) with 0.1 mol/kg lithium nitrate added; 4) with 0.5 mol/kg lithium nitrate added

The electrochemical stability window ( $\pm 3V$ ) was established from voltamperic curves measured in a two-electrode system. It was sufficient for current research. After drying under argon, the IL contains some impurities of water and they are narrowing the electrochemical stability window (see Table 3.2). At higher temperatures, the electrochemical stability window is also reduced.

**Table 3.2. IL and IL- lithium nitrate electrolyte electrochemical stability window at different temperatures**

T, °C	1,3-dimethylimidazolium dimethyl phosphate			1-butyl-3-methylimidazolium dimethyl phosphate		
		+ 0,5 mol/kg LiNO <sub>3</sub>	+ 0,1 mol/kg LiNO <sub>3</sub>		+ 0,1 mol/kg LiNO <sub>3</sub>	+ 0,5 mol/kg LiNO <sub>3</sub>
	25	6 V	6 V	6 V	7 V	7 V
50	6 V	6 V	6 V	7 V	7 V	7 V
100	5 V	5 V	5.5 V	6 V	6 V	6 V
150	5 V	5 V	5.5 V	4 V	4 V	5 V

The impedance of two-electrode cell containing IL was measured, stabilizing the cell before measurement for 20 minutes at each temperature. The cell was stabilized in order to achieve the same results for both heating and cooling cycle. The cell resistance  $R$  was obtained from the Nyquist plot extrapolating to the higher frequencies. The cell constant  $K$  was obtained using standard KCl solution at a room temperature. Both parameters were used to calculate the electrolyte conductivity  $\sigma$  ( $\sigma = K/R$ ). Arrhenius plot revealed non-linear behaviour from room temperature up to 150 C (Fig. 3.10), which is characteristic for ILs.

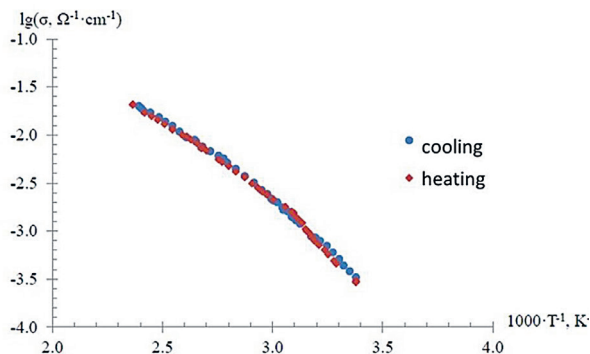


**Figure 3.10. Arrhenius plot of conductivity for 1-butyl-3-methylimidazolium dimethyl phosphate (both heating and cooling cycles)**

After dissolving lithium nitrate, the temperature dependence of electrolyte was measured and plotted in Arrhenius coordinates. The plot (Fig. 3.11) revealed that the conductivity values practically not increases by adding lithium salt.

Analogous behaviour was observed also for the second investigated IL – 1,3- dimethylimidazolium dimethyl phosphate (Fig. 3.12). Most likely, the reason is the increase of viscosity by adding lithium salt and subsequent decrease of lithium ion mobility as it was discussed before. The conductivity most strongly was influenced by increasing the length of the hydrocarbon chain. The dimethyl group replacing by butyl decreased the conductivity by 0.5 units in Arrhenius coordinates.

The IL temperature stability is higher than 200 °C. However, by adding lithium salt, the chemical interaction was observed at temperatures higher than 170 °C, which resulted in a reasonable decrease of conductivity (Fig. 3.13).

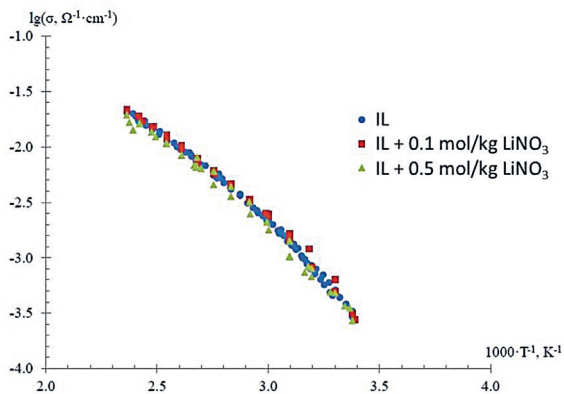


Figure 3.11. Arrhenius plot of conductivity for 1-butyl-3-methylimidazolium dimethyl phosphate with and without adding lithium nitrate

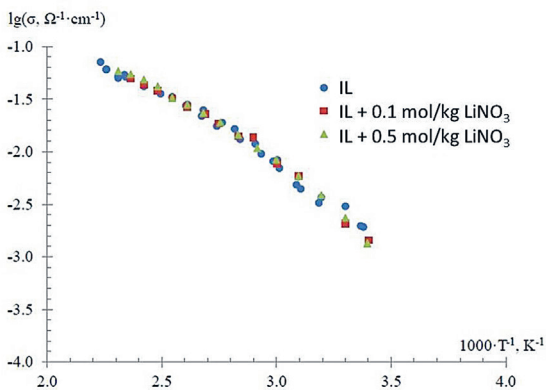


Figure 3.12. Arrhenius plot of conductivity for 1,3-dimethylimidazolium dimethyl phosphate with and without adding lithium nitrate

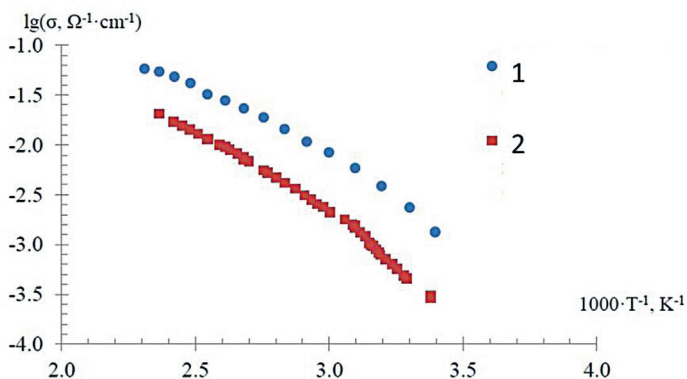


Figure 3.13. Arrhenius plot of conductivity for 1,3-dimethylimidazolium dimethyl phosphate (1) and 1-butyl-3-methylimidazolium dimethyl phosphate (2)

### 3.3.4. Conclusions to ion liquids with Li salts

This research confirmed that the ILs such as imidazolium dimethyl phosphates are an excellent environment to dissolve the lithium salts. It will change ion equilibrium, but it is not possible to reach higher conductivity values. Investigated electrolyte system was designed to be used in lithium-ion batteries with a lithium iron phosphate electrode. It was assumed that the saturation of electrolyte with the phosphate-based ions will stabilize the interface with the phosphate-based electrode. More stability tests for batteries are planned in a future.

### 3.4. References

1. Walden, P. (1914) Ueber die Molekulargröße und elektrische Leitfähigkeit einiger geschmolzenen Salze. *Bull. Acad. Imper. Sci. St. Petersburg*, 405–422.
2. Wasserscheid, P., Welton, T. (eds.). (2008) *Ionic Liquids in Synthesis*. 2nd ed. Wiley-VCH: Weinheim, Vol. 1, Vol. 2, 721.
3. Wilkes, J. S. (2002) A Short History of Ionic Liquids – from Molten Salts to Neoteric Solvents. *Green Chem.* 4, 73–80.
4. Hallet, J. P., Welton, T. (2011) Room-temperature ionic liquids: solvents for synthesis and catalysis. *Chem. Rev.* 111, 3508–3576.
5. Yue, C., Fang, D., Liu, L., Yi, T.-F. (2011) Synthesis and application of task-specific ionic liquids used as catalysts and/or solvents in organic unit reactions. *J. Molecular Liquids*, 163, 99–121.
6. Olivier-Bourbigou, H., Magna, M., Morvan, D. (2010) Ionic liquids and catalysis: recent progress from knowledge to applications. *Appl. Catal. A: General*, 373, 1–56.
7. Petkovic, M. A., Seddon, K. R., Rebelo, L. P. N., Pereira, C. S. (2010) Ionic liquids: a pathway to environmental acceptability. *Chem. Soc. Rev.*, 40, 1383–1403.
8. Anastas, P. T. (ed.). (2010) *Handbook of Green Chemistry – Green Solvents*. Vol. 6: Ionic Liquids; Wiley-VCH: Weinheim, 352.
9. Kirchner, B. (2009) *Ionic Liquids*. Springer: Heidelberg, 341.
10. Plechkova, N. V., Seddon, K. R. (2008) Applications of ionic liquids in the chemical industry. *Chem. Soc. Rev.*, 37, 123.
11. Mikami, K. (2005) *Green Reaction Media in Organic Synthesis*; Wiley-Blackwell: Oxford, 187.
12. Dinarès, I., de Miguel, C. G., Ibáñez, A., Mesquida, N., Alcalde, E. (2009) Imidazolium ionic liquids: A simple anion exchange protocol. *Green Chem.*, 11, 1507–1510.
13. Branco, L. C., Rosa, J. N., Moura Ramos, J. J., Afonso, C. A. M. (2002) Preparation and Characterization of New Room Temperature Ionic Liquids. *Chem. Europ. J.*, 8, 3671–3677.
14. Wernitz, J. H. (1951) Quaternary ammonium salts of phosphorus acid esters. USA patent 2,563,506.
15. Modro, A. M., Modro, T. A. (1989) Alkylating properties of phosphate esters. 4. Medium effects on methylation of pyridines by trimethyl phosphate. *Journal of Physical Organic Chemistry*, 2, 377–382.
16. Zhou, Y., Robertson, A. J., Hillhouse, J. H., Baumann, D. (2006) Phosphonium and imidazolium salts and methods of their preparation. USA patent US 2006/0264645.
17. Finkelstein, M., Dunkl, F. S., Ross, S. D. (1980) Non-aqueous electrolytic capacitor electrolyte. USA patent 4,189,761.
18. Kuhlmann, E., Himmler, S., Giebelhaus, H., Wasserscheid, P. (2007) Imidazolium dialkylphosphates – a class of versatile, halogen-free and hydrolytically stable ionic liquids. *Green Chem.*, 9, 233–242.
19. Zicmanis, A., Antaina, L. (2014) Dialkylimidazolium dimethyl phosphates as solvents and catalysts for the Knoevenagel condensation reaction. *Tetrahedron Lett.*, 55, 2027–2028.

20. Anteina L., Gaidule A., Zicmanis A. (2014) 1,3-Dialkylimidazolium dimethyl phosphates – effective solvents and catalysts for condensation reactions. *Latvian J. Chem.*, 41–48.
21. Priede, E., Nakurte, I., Zicmanis, A. (2014) Structure effect of imidazolium-based dicationic ionic liquids on Claisen rearrangement. *Synth. Commun.*, 44, 1803–1809.
22. Priede, E., Brica, S., Udris, N., Zicmanis, A. (2015) Designing highly efficient solvents for the Knoevenagel condensation: two novel dicationic dimethyl phosphate ionic liquids. *Arkivoc*, 7, 243–252.
23. Priede, E., Zicmanis, A. (2015) One-pot three-component synthesis of Hantzsch 1,4-dihydropyridines promoted by dimethyl phosphate ionic liquids. *Helv. Chim. Acta*, 98, 1095–1103.
24. Priede, E., Brica, S., Bakis, E., Udris, N., Zicmanis, A. (2015) Ionic liquids as solvents for the Knoevenagel condensation: understanding the role of solvent-solute interactions. *New J. Chem.*, 39, 9132–9142.
25. Priede, E., Bakis, E., Zicmanis, A. (2014) When chlorides are the most reactive: a simple route towards diverse mono- and dicationic dimethyl phosphate ionic liquids. *SYNLETT*, 2447–2450.
26. Brica, S., Freimane, L., Kulikovska, L., Zicmanis, A. (2017) *N,N'*-Dialkylimidazolium dimethyl phosphates – promising media and catalysts at the same time for condensation reactions. *Chem. Sci. Internat. J.*, 19(4), 1–9.
27. Wongittharom, N., Wang, C.-H., Wang, Y.-C., Fey, G. T.-K., Li, H.-Y., Wu, T.-Y., Lee, T.-C., Chang, J.-K. (2014) Charge-Storage Performance of Li/LiFePO<sub>4</sub> Cells with Additive-Incorporated Ionic Liquid Electrolytes at Various Temperatures. *Journal of Power Sources*, 260, 268–275.
28. Stejskal, J., Dybal, J., Trchová, M. (2014) The Material Combining Conducting Polymer and Ionic Liquid: Hydrogen Bonding Interactions between Polyaniline and Imidazolium Salt. *Synthetic Metals*, 197, 168–174.
29. Fotouhi, A., Auger, D. J., Propp, K., Longo, S., Wild, M. (2016) A Review on Electric Vehicle Battery Modelling: From Lithium-Ion toward Lithium–Sulphur. *Renewable and Sustainable Energy Reviews*, 56, 1008–1021.
30. Méndez-Morales, T. et al. (2014) Solvation of Lithium Salts in Protic Ionic Liquids: A Molecular Dynamics Study. *J. Phys. Chem. B*, 118(3), 761–770.
31. Voroshlylova, I. V., Smaga, S. R., Lukinova, E. V., Chaban, V. V., Kalugin, O. N. (2015) Conductivity and Association of Imidazolium and Pyridinium Based Ionic Liquids in Methanol. *Journal of Molecular Liquids*, 203, 7–15.
32. Wohde, F., Bhandary, R., Moldrickx, J. M., Sundermeyer, J., Schönhoff, M., Roling, B. (2016) Li<sup>+</sup> Ion Transport in Ionic Liquid-Based Electrolytes and the Influence of Sulfonate-Based Zwitterion Additives. *Solid State Ionics*, 284, 37–44.
33. Scheers, J., Fantini, S., Johansson, P. (2014) A Review of Electrolytes for Lithium–sulphur Batteries. *Journal of Power Sources*, 255, 204–218.
34. Andanson, J.-M., Traïkia, M., Husson, P. (2014) Ionic Association and Interactions in Aqueous Methylsulfate Alkyl-Imidazolium-Based Ionic Liquids. *The Journal of Chemical Thermodynamics*, 77, 214–221.
35. Andanson, J.-M., Meng, X., Traïkia, M., Husson, P. (2016) Quantification of the Impact of Water as an Impurity on Standard Physico-Chemical Properties of Ionic Liquids. *The Journal of Chemical Thermodynamics*, 94, 169–176.
36. Abdelhamid, H. N. (2016) Ionic Liquids for Mass Spectrometry: Matrices, Separation and Microextraction. *TrAC Trends in Analytical Chemistry*, 77, 122–138.
37. Reinert, L., Batouche, K., Lévêque, J.-M., Muller, F., Bény, J.-M., Kebabi, B., Duclaux, L. (2012) Adsorption of Imidazolium and Pyridinium Ionic Liquids onto Montmorillonite: Characterisation and Thermodynamic Calculations. *Chemical Engineering Journal*, 209, 13–19.
38. Efimova, A., Pfützner, L., Schmidt, P. (2015) Thermal Stability and Decomposition Mechanism of 1-Ethyl-3-Methylimidazolium Halides. *Thermochimica Acta*, 604, 129–136.

39. Dai, Z., Noble, R. D., Gin, D. L., Zhang, X., Deng, L. (2016) Combination of Ionic Liquids with Membrane Technology: A New Approach for  $\{CO_2\}$  Separation. *Journal of Membrane Science*, 497, 1–20.
40. Hiremath, V., Jadhav, A. H., Lee, H., Kwon, S., Seo, J. G. (2016) Highly Reversible  $\{CO_2\}$  Capture Using Amino Acid Functionalized Ionic Liquids Immobilized on Mesoporous Silica. *Chemical Engineering Journal*, 287, 602–617.
41. Lv, B., Xia, Y., Shi, Y., Liu, N., Li, W., Li, S. (2016) A Novel Hydrophilic Amino Acid Ionic Liquid [C2OHmim][Gly] as Aqueous Sorbent for  $\{CO_2\}$  Capture. *International Journal of Greenhouse Gas Control*, 46, 1–6.
42. Bazargani, Z., Sabzi, F. (2016) Prediction of  $\{CO_2\}$  Solubility in Ionic Liquids with [HMIM] and [OMIM] Cations by Equation of State. *Journal of Molecular Liquids*, 216, 87–93.
43. Zoubeik, M., Henni, A. (2014) Experimental and Thermodynamic Study of  $\{CO_2\}$  Solubility in Promising [TF<sub>2</sub>N and DCN] Ionic Liquids. *Fluid Phase Equilibria*, 376, 22–30.

### 3.5. Kopsavilkums

Tāpat kā citi jonu šķidrums (JŠ), arī imidazolijs dimetilfosfāti (IA-DMP) visbiežāk tiek izmantoti kā reakcijas vide un/vai katalizatori organiskajā sintēzē. Tie iegūti, vai nu alkilējot 1-aizvietotos imidazolus ar trimetilfosfātu, vai hlorīda jona metatēzēs atbilstošajos imidazolijs sāļos. Izveidotas minēto JŠ kvalitatīvās un kvantitatīvās analīzes metodes. Gan JŠ sintēze, gan to pielietojumi ir plaši pētīti arī Latvijas Universitātē dažādās jomās: elektroķīmija, organiskā sintēze, ekstrakcijas procesi, kompozītmateriālu veidošanās. Darbā dots pārskats par imidazolijs dimetilfosfātu jonu šķidrumu sintēzes metodēm un struktūras pētījumiem. Jonu šķidrumus 1914. gadā atklājis Pauls Valdēns, pēc tam tie tika aizmirsti līdz 1940. gadiem, kad amerikāņu pētnieki ierosināja izmantot JŠ kā nešķīstošu šķīdinātāju akumulatora elektrolītiem. Litija jonu akumulatori veicināja elektrisko automobiļu komercializāciju un mājsaimniecību pašu saražotās elektriskās enerģijas uzglabāšanu vēlākai izmantošanai. Tomēr drošības jautājumi ir vissvarīgākie. Litija dzelzs fosfāta (LiFePO<sub>4</sub>) akumulators, kas kā katoda materiālu izmanto LiFePO<sub>4</sub> un kā anodu – oglekļa elektrodu, pēdējos gados ir atradis plašu pielietojumu transportlīdzekļos – mazs svars, liels enerģijas blīvums, zema cena, zema toksicitāte, laba veiktspēja, ilglaicīga stabilitāte utt. Jonu šķidrums ir piemēroti elektrolīti litija baterijām savas augstās termiskās stabilitātes un vides draudzīguma dēļ. JŠ veido sāļus ar neorganiskām skābēm, tādēļ mūsu darbā pētīti JŠ fosfātu sāļi LiFePO<sub>4</sub> šūnām. Jonijas šķidrumu tipiskās vadītspējas vērtības istabas temperatūrā svārstās no 10<sup>-5</sup> līdz 10<sup>-1</sup> S · cm<sup>-1</sup>, kas ir ekvivalenta stipriem skābes ūdens šķīdumiem.

## 4. Selection and modification of microorganisms and substrates for acquiring and separation of energy carriers

### Mikroorganismu un substrātu atlase un modifikācija energonesēju ieguvei un atdalīšanai

**Ilze Dimanta, Matiss Paiders, Artūrs Gruduls, Vizma Nikolajeva**

Faculty of Biology, University of Latvia, Jelgavas iela 1, Rīga, LV-1004, Latvia,  
E-mail: [ilze.dimanta@gmail.com](mailto:ilze.dimanta@gmail.com)

#### Contents

4. Selection and modification of microorganisms and substrates for acquiring and separation of energy carriers . . . . .	69
4.1. Biological hydrogen production and storage research . . . . .	69
4.1.1. Hydrogen gas as renewable energy carrier . . . . .	70
4.1.2. Biohydrogen production processes. . . . .	70
4.1.3. Microbial strains and optimal substrates for hydrogen production . . . . .	72
4.1.4. Crude glycerol fermentation process . . . . .	73
4.1.5. Feasibility of biohydrogen production processes. . . . .	74
4.1.6. Metal hydride alloy usage in storing hydrogen . . . . .	75
4.1.7. Biohydrogen isolation experiments in hydride-forming metals and alloys. . . . .	76
4.2. Microbial fuel cells for production of energy carriers . . . . .	82
4.2.1. Introduction. . . . .	82
4.2.2. Applicability of 3D-printed graphene electrodes in MBFC. . . . .	84
4.2.3. Anodic biofilm vitality during operation of MBFC. . . . .	87
4.2.4. Benthic MBFC. . . . .	92
4.3. Summary. . . . .	93
4.4. References . . . . .	93
4.4. Kopsavilkums . . . . .	99

#### 4.1. Biological hydrogen production and storage research

Hydrogen is regarded as a sustainable energy carrier for various reasons:

- 1) high energy conversion efficiencies;
- 2) production from water with no emissions;
- 3) abundance;
- 4) different forms of storage (e. g. gaseous, liquid, or in together with metal hydrides);
- 5) long distance transportation;
- 6) ease of conversion to other forms of energy;
- 7) higher heating value (HHV) and lower heating value (LHV) than most of the conventional fossil fuels.

Hydrogen usage as an energy carrier is the most important stone in hydrogen economy as it can store the energy from fossil domestic resources (natural gas, coal, oil), biomass and intermittently available renewables such as wind and Sun for use in stationary and mobile applications [1]. The information in this chapter is obtained from PhD thesis of Ilze Dimanta, defended in June, 2016, at the University of Latvia [2], MSc thesis of Sintija Valucka, defended in June 2015, Faculty of Biology, the University of Latvia [3], Bachelor's thesis of Zane Kleinmane, defended in June 2016, Faculty of Biology, the University of Latvia [4], Bachelor's thesis of Matīss Paiders defended in June 2017, Faculty of Biology, the University of Latvia [5], which to some extent is reflected in publications [6–11].

#### **4.1.1. Hydrogen gas as renewable energy carrier**

Hydrogen is a flammable, colourless and odourless gas with low solubility in water, discovered in 1766 by Henry Cavendish. Its melting point is  $-259.2\text{ }^{\circ}\text{C}$  and its boiling point is  $-252.8\text{ }^{\circ}\text{C}$ . The density of hydrogen gas at conditions of  $0\text{ }^{\circ}\text{C}$  and  $101.3\text{ kPa}$  is  $0.08987\text{ kg/m}^3$ , which is about 14 times less than air under same conditions [12]. Hydrogen is the most abundant element in the Universe, making up about three quarters of all matter, though scarcely available on the Earth in a molecular (dihydrogen,  $\text{H}_2$ ) form. The atmosphere contains trace amounts of it (0.07%), while the Earth's surface contains about 0.14% [13]. Hydrogen can be found in many substances in nature, for example, in sea/fresh water and biomass. Nevertheless, hydrogen can be produced from many different sources (oil, natural gas, water, biomass rich in carbohydrates and more). Currently, hydrogen covers about 2% of the world energy demand [14] and worldwide production exceeds 1 billion  $\text{m}^3/\text{day}$  of which 48% is produced from natural gas, 30% from oil, 18% from coal, and the remaining 4% is produced from water electrolysis, currently the most basic industrial process for almost pure hydrogen generation [15]. Most commonly used and the least expensive hydrogen production process is natural gas steam reforming, but it produces heavy greenhouse gas emissions [16]. Water electrolysis is more environmentally friendly. Technologies of most significance for electrochemical hydrogen production are:

- 1) polymer membrane [voltage efficiency (VE) 67–82%, with current density (CD)  $0.6\text{--}2.0\text{ A/cm}^2$ ];
- 2) alkaline membrane (VE 62–82%, CD  $0.2\text{--}0.4\text{ A/cm}^2$ ); and
- 3) solid oxide electrolyzers (VE 81–86%, CD  $0.3\text{--}1.0\text{ A/cm}^2$ ) [17].

Apart from electrolysis, different hydrogen production methods have been developed, including photolysis, thermolysis, biophotolysis, photoelectrochemical process, photocatalysis and thermochemical water splitting, as well as thermochemical conversion of biomass, gasification, biofuel reforming and others [13]. Every physical or chemical method of hydrogen production requires energy input, which is not always environment-friendly.

On the contrary, biological processes of hydrogen recovery and collection from organic resources such as municipal wastewater and sludge facilitate recycling of sewage and are environmentally benign [18].

#### **4.1.2. Biohydrogen production processes**

Bacteria have their own hydrogen fuel cycle. Hydrogen production by dark fermentation is restricted by the incomplete degradation of organic matter into volatile fatty acids, hydrogen and carbon dioxide. In nature, low partial pressure of hydrogen is maintained by the presence of hydrogen consumers in syntrophic association with hydrogen producers

[19]. Estimates are that microorganisms annually form approximately 150 million tons of hydrogen. The combustion of 150 million tons of hydrogen yields  $18 \times 10^{18}$  J of energy that is equivalent to 3.75% of the primary energy consumed by world population [20].

Hydrogen production using microbial fermentation process is acknowledged from the 1920s (photosynthesis in microalgae). Biological processes for hydrogen production and collection from organic resources such as municipal wastewater and sludge facilitate recycling of sewage are environmentally benign [21]. Biohydrogen generation via dark fermentation process is widely studied due to higher production rates and treatment capacity for organic waste products. Many institutions and universities worldwide are involved in the research of hydrogen production using bacteria or/and algae [22].

Biohydrogen production is divided in five broader groups: direct photolysis, indirect photolysis, photofermentation, dark fermentation and coupled or hybrid systems and there are vast group of organisms that can produce hydrogen in various environmental conditions [23]. A more detailed description is provided in Table 4.1.

Table 4.1. Processes of biohydrogen production (modified from [24–27])

Process	Description	Organisms
Direct biophotolysis	Hydrogen from water and the sun through photosynthesis, genetic modifications necessary for maintaining higher efficiency	Green algae ( <i>Chlamydomonas reinhardtii</i> )
Indirect biophotolysis	$6\text{H}_2\text{O} + 6\text{CO}_2 + \text{light} \rightarrow \text{C}_6\text{H}_{12}\text{O}_6 + 6\text{O}_2$ $\text{C}_6\text{H}_{12}\text{O}_6 + 6\text{H}_2\text{O} + \text{light} \rightarrow 12\text{H}_2 + 6\text{CO}_2$	Cyanobacteria ( <i>Anabaena variabilis</i> )
Photo-fermentation	Conversion of organic substrate by using light energy with photosynthetic purple non-sulphur bacteria in anaerobic environment	Photosynthetic bacteria ( <i>Rhodobacter</i> spp.)
Dark fermentation	By using different substrates, including organic waste in anaerobic environment produces hydrogen	Anaerobic and facultative anaerobic bacteria ( <i>Enterobacter</i> spp.)
Hybrid systems	Firstly, via fermentation process acetate, $\text{CO}_2$ and $\text{H}_2$ are produced. Secondly, in a photo-bio-reactor, acetate is turned into $\text{H}_2$ and $\text{CO}_2$	Association of photosynthetic and fermentative bacteria

All biohydrogen production ways depend on either a hydrogenase or nitrogenase enzyme for hydrogen evolution and derive energy either directly from light energy or indirectly by consuming photosynthetically derived carbon compounds. Each approach has positive and negative aspects, and each has serious technical barriers that need to be overcome before it could become practical [28]. There is a natural consequence of the fact that fermentations have been optimized by evolution to produce cell biomass and not hydrogen. Thus, a portion of the substrate is used in both cases to produce ATP giving a product that is excreted. In many anaerobic microorganisms, the actual hydrogen generation yields are reduced by hydrogen recycling due to the presence of one or more uptake hydrogenases, which consume the hydrogen that is produced [29].

Hydrogen production by fermentation of carbohydrate-containing substrates (glucose, cellulose, starch and organic waste materials) is frequently preferred to photolysis, because it does not rely on the availability of light sources [24]. Hydrogenases are enzymes that catalyse the oxidation of hydrogen to protons and the reduction of protons to hydrogen. They can be distributed into three classes: the [Fe]-H<sub>2</sub>ases, the [NiFe]-H<sub>2</sub>ases, and the metal-free hydrogenases. Hydrogenases may interact with membrane-bound electron transport systems in order to maintain redox balance, particularly in some photosynthetic microorganisms such as cyanobacteria [30]. One of the pyruvate oxidation products, alongside with acetyl-CoA, is a formate, which is produced by pyruvate formate lyase and is the sole source of hydrogen in these bacteria. The formate is split into CO<sub>2</sub> and H<sub>2</sub> by formate hydrogen lyase (FHL) complex, which comprises seven proteins, six of them being encoded *hyc* operon. Five *hyc* operon encoded proteins are membrane-embedded electron transporters. The HycE protein is one of the three *E. coli* NiFe hydrogenases (also referred to as Hyd-3) [27].

The HycE and FDH-H components of FHL complex are soluble periplasmic proteins. The hydrogen evolved from FHL is consumed by *E. coli* uptake hydrogenases Hyd-1 and Hyd-2. In contrast to enterobacteria, strictly anaerobic fermenters, e.g. clostridia, use a reduced ferredoxin (required to oxidize pyruvate to acetyl-CoA) for H<sub>2</sub> production by the hydrogenase that generates ferredoxin in the oxidized form and releases electrons as molecular hydrogen [24]. Glucose fermentation by enteric bacteria yields the maximum of 2 mol H<sub>2</sub>/ mol glucose [31]. To enhance the hydrogen production and utilize the substrate in the full measure for complete conversion, synergy of biological processes (two-stage/ hybrid ones) should be applied. Anaerobic fermentations with *Escherichia coli* and *Clostridium* spp. are the most thoroughly investigated hydrogen bioprocesses, which offer hydrogen yields from glucose up to 2 or 4 moles per mol of glucose [32]. The end products of fermentation process are mainly volatile organic acids and spirits that are produced depending on microbial metabolic pathways and substrate used.

#### 4.1.3. Microbial strains and optimal substrates for hydrogen production

Various microorganisms have the ability to produce hydrogen under certain conditions – starting from microalgae that use light energy, cyanobacteria, but the major hydrogen yielding biocatalysts are heterotrophs in the fermentation process – facultative and obligate anaerobes. Here are listed some of active hydrogen producers: green algae (*Scenedesmus obliquus*, *Chlamydomonas reinhardtii*, *C. moewusii*), cyanobacteria heterocystous (*Anabaena azollae*, *A. variabilis*, *A. cylindrica*, *Nostoc muscorum*, *N. spongiaeforme*, *Westiellopsis prolifica*), cyanobacteria non-heterocystous (*Plectonema boryanum*, *Oscillatoria* sp. Miami BG7, *O. limnetica*, *Synechococcus* sp., *Aphanothece halophytico*, *Mastidocladus laminosus*, *Phormidium valderianum*), photosynthetic bacteria (*Rhodobater sphaeroides*, *R. capsulatus*, *Rhodopseudomonas palustris*, *Rhodospirillum rubrum*, *Rhodovulum sulfidophilum*, *Chromatium* sp. Miami PSB 1071, *Chlorobium limicola*, *Chloroflexus aurantiacus*, *Thiocapsa roseopersicina*, *Halobacterium halobium*) and fermentative bacteria [*Klebsiella (Enterobacter) aerogenes*, *E. cloacae*, *Clostridium butyricum*, *C. pasteurianum*, *Desulfovibrio vulgaris*, *Megasphaera elsdenii*, *Citrobacter intermedius*, *Escherichia coli*] [24, 33, 34].

Thermophiles are the closest for hydrogen production to the theoretical yield by overwhelming thermodynamic barrier, but these strains have to be cultivated at elevated temperature with high energy requirements [33]. Hydrogen research strategies organism-wise

stated that productive pure cultures were used with defined substrate as the carbon source, but mixed cultures are preferred for operational ease and process stability [35]. When wastewater or agricultural waste is used as the substrate, a mixed microbial population is more favorable and practical [36]. Regardless of the research goal, the key requirement for every biological hydrogen production research is a proper choice of hydrogen production system and understanding of the biochemical and biophysical characteristics of this system [37, 38].

The substrate plays an important role in the H<sub>2</sub> yield, H<sub>2</sub> production rate and the overall economy of the process. Carbohydrate rich substrates have been extensively used in biohydrogen production studies [39]. Glucose and sucrose are the most commonly used pure substrates in both batch and continuous processes due to their simple structures and ease of biodegradability [40]. Renewable biohydrogen production requires the substrate or feedstock to come from renewable resources. Second generation biomass sources, such as waste biomass, are abundant and thus can support the supply of renewable substrates and fermentation process offers biological treatment of the organic waste [39]. In order to reach sustainable production and also waste management, various agriculture and industrial waste materials as feedstock may be used [41]. Substantial factors like availability and cost are highly important in the selection of waste materials to be used in hydrogen production with fermentative bacteria [40].

#### 4.1.4. Crude glycerol fermentation process

One of the substrates that can be effectively used for microbial hydrogen production is crude glycerol, which is a by-product from the process of biodiesel production. Because large quantities of crude glycerol are available and the highly reduced nature of carbon in glycerol per se, microbial conversion of it in hydrogen is an economically and environmentally viable possibility, especially because over the last several years the demand and production of biodiesel has remarkably increased [42]. Glycerol (C<sub>3</sub>H<sub>8</sub>O<sub>3</sub>) is a trihydroxyl (sugar alcohol) compound, the energy content of pure glycerol is 19.0 MJ/kg, but for crude glycerol the energy content is 25.30 MJ/kg, that most probably is due to presence of methanol and traces of biodiesel. Energy content of crude glycerol indicates its high potential to be an effective substrate for biological hydrogen production, especially because it does not require additional pre-treatment to make it available for the hydrogen-producing microorganisms [43]. About 10 billion litres (L) of crude glycerol per year are a by-product of biodiesel generation from plant oils, giving 1 L of glycerol for every 10 L of biodiesel [44, 45]. Biodiesel is mainly produced from the transesterification of vegetable oils or animal fats with methanol catalysed by alkalis, such as NaOH and KOH. After the transesterification process, two layers are formed: the top layer is the desired product, i. e., biodiesel, and the bottom layer is the raw/unrefined crude glycerol [46, 47]. One of the major challenges for the utilization of crude glycerol is the inconsistency of its composition since it varies with the feedstock, production processes, and post-treatments involved in the biodiesel production. Upgrading or refining crude glycerol to technical grade glycerol (>98% glycerol content) makes its composition more consistent, but currently this is not economically viable, especially for small and/or medium-sized biodiesel plants [48].

Reungsang et al. [49] for hydrogen production with *Enterobacter aerogenes* KKU-S1 used crude glycerol with glycerol concentration of 441.3 g/L, methanol 230 g/L, NaCl 10 g/L. Mangayil et al. (2012) [50] used Savon Siemen Oy manufactory glycerol, that contained 45% (v/v) glycerol and 30% (v/v) methanol. Valuable compounds can be

produced from crude glycerol such as hydrogen, and 1,3-propanediol as main products, methane, ethanol and succinic acid in smaller amounts [50]. Hydrogen production comparing to production of 1,3-propanediol is more valuable, hydrogen has a higher energy content (142.9 kJ/g) and it results in higher yield and productivity [43]. Various bacterial strains are considered promising for glycerol utilization because of possibility to ferment crude glycerol, and H<sub>2</sub> is one of the end-products of this process [51]. The most productive microorganisms that grow anaerobically on glycerol as the sole carbon and energy source are *Rhodospseudomonas palustris*, *Enterobacter aerogenes*, *Escherichia coli*, *Thermotoga neapolitana* and others [43, 51].

There are two ways of glycerol metabolism – oxidative and reductive. In the reducing pathway glycerol is converted in 1,3-propanediol. In the oxidative pathway glycerol is firstly converted in dihydroxyacetone using catalytic activity by glycerol dehydrogenase, then dihydroxyacetone is phosphorylated by the glycolytic enzyme dihydroxyacetone kinase and the phosphorylated product is metabolized through glycolysis. Pyruvate may be further converted to various end-products depending on microorganism. In most of glycerol bioconversion pathways hydrogen is produced along with other metabolites (e. g. butyrate, ethanol, butanol, acetate, acetone, lactate) [43, 50].

Optimal conditions are pH 6.5; 40 °C for hydrogen production using crude glycerol with microbial consortium mainly dominated by *Clostridium* species. Environmental conditions like medium pH and temperature are the major parameters to be controlled in the hydrogen production, because they affect qualitative and quantitative content and hydrogen yield and rate of bacterial produced gas. Hydrogen production using glycerol is 1.5-fold higher at pH 5.5 than at pH 6.5 [52] using *E. coli*. Anaerobic conditions have to be maintained during the hydrogen production process, which are ensured by barbotage media with reducing agent or inert gas such as nitrogen or argon [40, 53].

Guillaume and Patrick [53] have reported hydrogen production using photo-fermentation of pure and crude glycerol by *Rhodospseudomonas palustris* with maximum of 6 mol of hydrogen per mole of glycerol, that is 75% of theoretical maximum 8 mol hydrogen production per mole glycerol, meaning that intermediate products such as acetic acid, ethanol and butyric acid were further metabolized to hydrogen, which is otherwise accumulated during dark fermentation [43]. *Enterobacter aerogenes* have an ability to convert glycerol in a fermentative process to yield hydrogen and ethanol as the main by-products. Yields of 0.86 mol H<sub>2</sub>/mol glycerol and 0.75 mol ethanol/mol glycerol were reported by Jitrwung and Yargeau (2015) [54]. Dharmadi et al. (2006) [55] reported that glycerol can be fermented also by *E. coli* at slightly acidic pH (pH 6.3). [56] have reported production of hydrogen from crude glycerol with anaerobic sludge.

#### 4.1.5. Feasibility of biohydrogen production processes

In order to achieve higher overall volumetric hydrogen production co-culture employing gives a possibility to maintain anaerobic conditions for strict anaerobes and eliminate the need for a reducing agent – facultative anaerobes consume oxygen in medium [57]. Biohydrogen price could compete with current fuel prices, when fermentation process outcome is 10 H<sub>2</sub> moles per glucose mol (it is close to maximally theoretically possible outcome – 12 moles) and glucose price is approximately 0.05 USD for one glucose dry matter pound. Dark fermentation – 2.4 \$/kg. Comparatively, more developed method costs for hydrogen gas – fossil fuel reforming (0.75 \$/kg), plasma arc decomposition (0.85 \$/kg) and coal gasification (0.92 \$/kg) [17, 58].

#### 4.1.6. Metal hydride alloy usage in storing hydrogen

Research activity in hydrogen storage field has increased substantially due to practical need for hydrogen storage possibilities. Hydrogen is a low density gas in atmospheric pressure and room temperature, for example, 1 kg of hydrogen occupies a volume of 11 m<sup>3</sup>. Various methods are used to increase hydrogen density:

- 1) Hydrogen storage in high-pressure gas cylinders with a maximum pressure up to 80 MPa and therefore the hydrogen gas can reach a volumetric density of 36 kg/m<sup>3</sup>; current state of art storage tanks in electric/hydrogen passenger vehicles (Toyota, Hyundai) hold hydrogen at pressures up to 70 MPa, which allows the storage of 5.4 kg of hydrogen in a 260 L tank and travel 600 km without refilling;
- 2) Liquid hydrogen storage in cryogenic tanks at -252 °C. The volumetric density of liquid hydrogen is 70.8 kg/m<sup>3</sup>;
- 3) Adsorbed hydrogen on materials with a large specific surface area [59], e.g. carbon nanotubes and nanofibers [60];
- 4) Hydrogen absorption on interstitial sites in a host metal (metal hydrides);
- 5) Chemically bonded hydrogen in covalent and ionic compounds (such as sodium tetrahydroborate (NaBH<sub>4</sub>) and ammonia borane (NH<sub>3</sub>BH<sub>3</sub>), which stores 19.6 wt% or 145 kg/m<sup>3</sup>).

Hydrogen storage in solid-state materials is an alternative way to store hydrogen at low pressure and ambient temperatures, and may be a very promising potential solution. Reversible hydrogen storage materials tend to be hydrides or microporous materials. The most extensively known metal forming hydride is palladium – white, silver like metal that soaks up hydrogen like a sponge – at a room temperature and atmospheric pressure, palladium can absorb up to 900 times its own volume of hydrogen; it was first noted by T. Graham in 1866. Material that can reversibly absorb or adsorb hydrogen in atomic (H) or molecular (H<sub>2</sub>) form is used to compress hydrogen (chemically or physically) to high storage densities (Fig. 4.1).

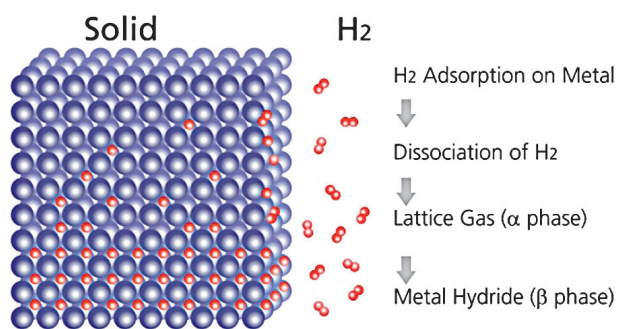


Figure 4.1. Metal hydride formation [61]

In standard practices, biohydrogen is synthesized in the fermentation medium, but collected from the headspace of the flask or fermenter after diffusion into gaseous phase. Theoretically, dissolved hydrogen is in equilibration with the gas phase and tends to release from the liquid phase, if partial pressure of H<sub>2</sub> decreases [62]. Nevertheless, during dark fermentation, biohydrogen oversaturation in the liquid phase takes place [6]

and inhibits further synthesis of the gas. To optimize biohydrogen production, it must be removed from the liquid phase by, e. g. barbotage  $N_2$  or Ar through the fermentation medium, and afterwards purified, collected and stored from gaseous phase. Absorption of biohydrogen from gaseous phase by alloys and metals that can form hydrides is a safe and efficient method to collect the gas, but will it work also in liquid phase?

Metals and alloys can be “charged” with hydrogen from gas phase under pressure, they release hydrogen when heated or subjected to evacuation [63]. It is reported that the presence of moisture in the hydrogen gas decreases the efficiency of its sorption by metals and alloys, e.g.  $LaNi_5$  in 300 ppm of water vapour loses its hydrogen absorption capacity [64].  $LaNi_5$  is one of the most widely used intermetallic alloys for hydrogen storage, due to its sorption capacity, reversibility of absorption and desorption and quick charge–discharge kinetics under room temperature and atmospheric pressure.

Metals and alloys can be “charged” with hydrogen also from liquid (electrolyte). Already for decades hydride-forming alloys are used as the cathode material in alkaline Ni/Me hydride batteries (see, for example, [65]). Hydrogen ion (proton) is inserted in metal hydride cathode through overvoltage applied to the battery in the process of charging and is ejected due to the difference of electrode potentials in the battery.

#### 4.1.7. Biohydrogen isolation experiments in hydride-forming metals and alloys

Our innovative idea in this research is that absorption of the biohydrogen directly from the medium of cultivation would increase the efficiency of the gas production due to

- 1) removing of its inhibitory over-saturated concentration from the medium;
- 2) more simple construction of the fermenter since the inert gas barbotage appliances will become superfluous;
- 3) collection of the gas would occur directly during the fermentation process, not afterwards with additional treatment of the gas phase.

The purpose of the study was to explore if the hydride-forming metals and alloys are able to adsorb and desorb biohydrogen directly from the fermentation solution. The mass-spectrometry was used to characterize the composition of the headspace gases in fermentation process and the thermogravimetric weight loss (TG) method was used to estimate the amount of gases and volatile substances absorbed in powdered Pd and  $LaNi_5$ ,  $AB_5$  and  $AB_2$  alloys. Nobuyuki Nishimiya et al. [66] found that ZrVFe encapsulated in polymer is an effective material to enhance hydrogen produced by *Anabaena* in argon atmosphere: the total amounts of hydrogen increased 6-7 times compared to normal hydrogen production in the absence of the alloy.

*Klebsiella (Enterobacter) aerogenes* MSCL 758 and *Escherichia coli* BW25113 *hyaB hybC hycA fdoG frdC aceE ldhA:kan* (kindly provided by Prof. T.K. Wood, Texas A&M University, USA) were used for fermentation experiments. Strains were grown on modified anaerobic growth medium (AM, g/L): tryptone 1.0, yeast extract 2.5, cysteine 0.5. Growth medium components were suspended in sterile water and supplemented with glycerol source 6 g/L of analytical grade glycerol (Stanlab LLC, Poland) or crude glycerol (Delta Riga Ltd., Latvia and the biofuel factory in Naukšēni, Latvia). The nutritional medium was sterilized by autoclaving for 15 minutes at 121 °C. The bacterial strains were cultivated overnight aerobically in Petri dishes on solid Luria-Bertani (LB) medium at 37 °C. The overnight cultures were adjusted to 1 OD (600 nm) in sterile distilled water and the OD-adjusted cultures used as inoculum for further cultivation anaerobically in 50 mL serum bottles (Supelco Analytical, USA) containing 35 mL AM medium and 1 mL

bacteria suspension. Inoculated serum bottles were closed with butyl rubber stoppers sealed with aluminium caps and flushed with argon gas to obtain anaerobic environment. The serum bottles were incubated in Biosan RS-24 programmable rotator in a thermostat at  $37 \pm 2$  °C.

Pd and LaNi<sub>5</sub>, AB<sub>5</sub>, AB<sub>2</sub> alloy powders that were tested for the capacity to remove bio-hydrogen from the liquid phase in fermentation are listed in Table 4.2.

**Table 4.2. Materials tested for hydrogen absorption capacity from the liquid phase of fermentation**

No.	Metal or alloy	Origin	Composition, grain size
1	Pd	Aldrich	Microcrystalline powder, <10 μm
2	LaNi <sub>5</sub>	Treibacher Industrie AG, Austria	Crystalline powder, <500 μm
3	AB <sub>5</sub>	Gesellschaft fur Elektrometallurgie; Nurnberg; Germany	Microcrystalline powder <75 μm; A = Mm = La, Ce, Nd, Pr; B = Co, Mn, Al; Mm(Co, Mn, Al) <sub>5</sub>
4	AB <sub>2</sub>	Gesellschaft fur Elektrometallurgie; Nurnberg; Germany	Microcrystalline powder <75 μm; A = Zr, Y; B = Ni, Al, Fe, Mn (Zr, Y)(Ni, Al, Fe, Mn) <sub>2</sub>

10–12 g of powders were activated before use: simultaneously heated up to 170 °C and evacuated up to ~0.01 bar in ca 8 cm<sup>3</sup> cylindrical stainless steel hydrogen adsorption/desorption reactor built in the Institute of Solid State Physics (University of Latvia), then exposed to hydrogen gas (2 bar) for 30 min and cooled down to room temperature in hydrogen atmosphere in the reactor; this process was repeated three times until rapid hydrogen absorption in alloy powder was observed. Finally, the absorbed hydrogen was removed by simultaneous heating and evacuation process. Argon gas was used to preserve activated alloys until their contact with the fermentation medium. One g of each alloy and 0.5 g of Pd powder was used for 30 mL of fermentation medium. Serum bottles with microorganisms, medium and metal hydride powder were rotated for 18, 24 and 36 hours in 37 °C temperature. Metal hydride powders were washed with 96% ethanol and dried in 4 °C temperature for at least 12 hours.

Gas analysis and thermogravimetry was done using equipment from Institute of Solid State Physics (University of Latvia). Qualitative analysis of evolved gases was performed with RGA Pro-100 mass spectrometer. Data was assessed by SR Residual Gas Analyzer with RGA 3.0 software. The volume of produced gas was measured by puncturing rubber stoppers of the serum bottles with a 20 mL syringe. If there was an elevated pressure in the serum bottle, the gas entered the syringe, making it possible to read the volume of produced gas.

By measuring the composition of gaseous phase of growth media using mass spectrometry after 24-hour incubation (Fig. 4.2), highest proportion of hydrogen was found in

sample 4, which consisted of growth medium, glycerol, *K. aerogenes* and multicomponent AB<sub>5</sub> alloy – maximum hydrogen concentration measured was 23.1%. Control samples without added bacteria showed insignificant hydrogen concentration (0.0–0.2%).

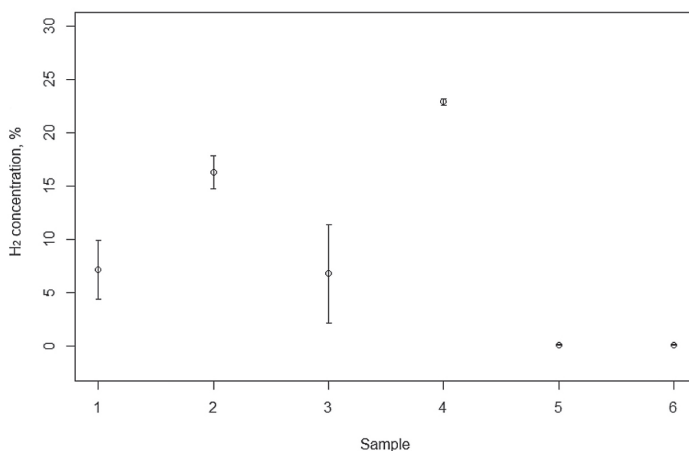


**Figure 4.2. Average amount of hydrogen (%) in the gas phase sample of growth media after 24 h of cultivation. Components of samples: 1 – *K. aerogenes*, growth medium; 2 – *K. aerogenes*, growth medium, glycerol; 3 – *K. aerogenes*, growth medium, glycerol, LaNi<sub>5</sub>; 4 – *K. aerogenes*, growth medium, glycerol, multicomponent AB<sub>5</sub> alloy; 5 – growth medium, glycerol; 6 – growth medium, glycerol, LaNi<sub>5</sub> [5]**

By comparing samples 1 and 2 in Fig. 4.2, statistically significant effect for addition of glycerol on the proportion of hydrogen in gas phase of growth media was determined ( $p = 0.0195$ ). The sample, which did not contain glycerol, showed an average hydrogen concentration of 7.1%, whereas for the sample containing glycerol it was 16.3%. By comparing the samples 2 and 3, it was determined that addition of LaNi<sub>5</sub> alloy statistically significantly decreased the proportion of hydrogen in gas phase of growth media ( $p = 0.00016$ ). The sample containing LaNi<sub>5</sub> showed an average hydrogen concentration of 6.7%. Multicomponent AB<sub>5</sub> alloy statistically significantly increased the proportion of hydrogen ( $p = 4.7 \times 10^{-6}$ ) by comparison with the sample 2, which did not contain multicomponent AB<sub>5</sub> alloy. The average hydrogen concentration in the sample with multicomponent AB<sub>5</sub> alloy was 22.9%. The sample with LaNi<sub>5</sub> powder showed a reduced concentration of H<sub>2</sub> and CO<sub>2</sub>, which suggests inhibitory effect of LaNi<sub>5</sub> for the growth of bacteria (Ni is known as an inhibitor of metabolic pathway, in which H<sub>2</sub> and CO<sub>2</sub> is produced [67]). Conversely, the addition of multicomponent AB<sub>5</sub> alloy showed a positive effect on H<sub>2</sub> and CO<sub>2</sub> production.

Differential TG of the Pd or alloy grains upon heating after the incubation in the fermentation media was performed using DTG-60 device (Shimadzu). The amount of gas absorbed by the hydrogen-absorbing materials was tested by removing 1.5–2.0 cm<sup>3</sup> medium containing 5–15 mg of the Pd or alloy grains from the bottle with the large gauge syringe. Before the TG measurements, the grains were washed with 98% ethanol and dried at room temperature for 24 hours in argon atmosphere. The temperature of the crucible in TG experiments was increased with a constant rate –10 °C per minute. Selected hydride-forming metals and alloys were compared for their H<sub>2</sub> absorption capacity from

fermentation broth with H<sub>2</sub>-producing *E. coli*. TG measurements disclosed that H<sub>2</sub> was absorbed most efficiently by powdered Pd, followed by AB<sub>5</sub>, AB<sub>2</sub> and LaNi<sub>5</sub> alloys (Fig. 4.3).

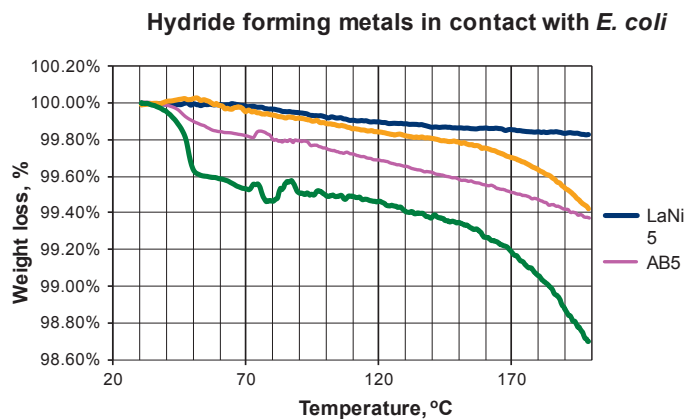


Figure 4.3. TG assessment of H<sub>2</sub> release from different hydrides formed during 72-h incubation in *E. coli* fermentation medium containing crude glycerol [2]

H<sub>2</sub> absorption by alloys during fermentation was analysed by TG in separate experiments by removing 5–15 mg of granulated material from the serum flask at regular intervals. Three parallel tests were conducted. Table 4.3 illustrates that the highest amount of H<sub>2</sub> was absorbed after 18 h of fermentation.

Table 4.3. H<sub>2</sub> absorption by AB<sub>5</sub> alloy during 42 h *K. aerogenes* fermentation of crude glycerol

Time after the beginning of fermentation, h	Weight loss (30–100 °C), wt%
6	0.41 ± 0.07
18	1.61 ± 0.72
24	0.38 ± 0.16
36	0.12 ± 0.01

The utilization of glycerol at bacterial fermentation was measured by HPLC on Agilent 1290 Infinity device (Agilent Technologies, Germany) using the *Atlantis dC18 3 μm, 2.1x150mm* (Waters) column. The aliquots from the fermentation media were passed through 0.45 μm filters (Nonpyrogenic Sterile-R, Sarstedt) and 1 μL of the solution was injected into the liquid chromatography system. All the experiments were performed in triplicate. The relative standard deviation was determined to be less than 1%. Data analyses were performed using MassHunter version B05.00 software (Agilent Technologies). Glycerol utilization by bacteria was not impaired by alloy grains in the medium. HPLC-MS demonstrated that glycerol was degraded completely within 24 h of fermentation with or without alloy grains in the medium (Fig. 4.4).



The surfaces of alloy grains after incubation in fermentation medium were examined by SEM. Fig. 4.5 shows that bacteria cells are present on the surfaces of alloy grains, thus being in close contact with H<sub>2</sub>-absorbing material. It also appeared that contact with alloy grains stimulates bacteria growth. More colony-forming units (CFU 10<sup>7</sup>/mL medium) of *K. aerogenes* were found on AB<sub>5</sub> alloy (Fig. 4.5 C). Although this field with metal hydride usage for bacteria produced hydrogen storage is novelty, it has been investigated that ability to grow on special carrier or substrate stimulates hydrogen production [68].

The first attempts were made for hydrogen collection from bacteria fermentation broth using metal hydrides [2, 3, 5]. Various powdered metals and alloys (Pd, LaNi<sub>5</sub>, AB<sub>5</sub>, AB<sub>2</sub>) forming hydrides were investigated to collect hydrogen directly from liquid phase. Vacuum extraction measurements were accomplished to ascertain the measured gas weight changes in thermogravimetry experiments were regarding to hydrogen and not water from broth or thermal decomposition changes of organic materials. As per LaNi<sub>5</sub>, a similar behaviour was seen with metal hydrides immersed in fermentation medium and hydrated metal hydride: similar weight losses occurred according to temperature changes. This could be considered as evidence that hydride-forming metals absorb H<sub>2</sub> not only from the gas phase but also from dissolved gas. Hydrated metal hydride weight losses with LaNi<sub>5</sub> are accordingly reported elsewhere [69]. All the materials in these experiments are known to release H<sub>2</sub> at low temperature: Pd at 70 °C, AB<sub>2</sub> at 50 °C, LaNi<sub>5</sub> and AB<sub>5</sub> at 25 °C [69, 70]. Weight loss of material at heating within the 30–100 °C range approximates the amount of adsorbed H<sub>2</sub>. At temperatures exceeding 150 °C, the organic substances from microorganisms and fermentation broth begin to decompose and can elicit additional weight losses not related to H<sub>2</sub> desorption. Thermal decomposition of organic materials is most active at around 200 °C [71].

In comparing weight loss, Pd and the 3 hydride alloys tested could be listed according to the amount of stored H<sub>2</sub> in the following order (starting with the highest amount): Pd, AB<sub>5</sub>, AB<sub>2</sub> and LaNi<sub>5</sub>. This could be explained by Pd's greater stability in corroding environments, as all the experiments were carried out in fermentation broth and with smaller size particles. It appears that, if the samples contained metals that absorbed H<sub>2</sub> released in fermentation, H<sub>2</sub> concentration in the gaseous phase at the end of the process would be lower. This was also confirmed by MS analysis. Each molecule that is produced inside the bottle, increases H<sub>2</sub> temperature release in metal hydrides [65] with 1.4% being the maximum (Inspection Certificate from GfE Gesellschaft für Elektrometallurgie mbH).

Our findings showed that less H<sub>2</sub> was detected in the gaseous phase owing to the presence of metal hydrides in all samples, except for AB<sub>2</sub>. Vacuum extraction measurements concurred with our hypothesis that weight changes in the TG experiments were due to H<sub>2</sub> and not organic decomposition. Also, if some H<sub>2</sub> was produced by organic decomposition, CO<sub>2</sub> and other carbon (C)-containing gas levels would increase.

The analysis of H<sub>2</sub> absorption dynamics in alloys during fermentation determined that the largest amount of soak-up H<sub>2</sub> occurred after 18 h from the beginning of fermentation. It coincides well with the analysis of consumed glycerol – all the results indicated that crude glycerol was completely expended within 24 h of fermentation. Incidentally, this may also explain the results of the first fermentation experiments with relatively small, bonded H<sub>2</sub> in hydride metals – because they were removed from the fermentation bottles after 72 h.

## Conclusions

1. The studies show that hydride-forming materials – Pd, AB<sub>5</sub>, AB<sub>2</sub> – can be successfully exploited for H<sub>2</sub> collection from the liquid phase in crude glycerol fermentation by *E. coli* and *Klebsiella aerogenes* (previously known as *Enterobacter aerogenes*) MSCL 758. The inhibitory effect of LaNi<sub>5</sub> was established for the growth of bacteria or inhibition of metabolic pathway, in which H<sub>2</sub> and CO<sub>2</sub> is produced. Conversely, Pd and multicomponent alloys AB<sub>2</sub> and AB<sub>5</sub> showed a positive effect on H<sub>2</sub> and CO<sub>2</sub> production. Attachment of bacteria to the metal alloys was demonstrated and hydrogen accumulation from fermentation media containing AB<sub>5</sub> alloy powder was proved by vacuum extraction and MS analysis.
2. H<sub>2</sub> concentration in the gaseous phase after 72 h of fermentation was lower in cultivation medium loaded with hydride-forming materials than in unloaded controls, while total calculated amount of H<sub>2</sub> absorbed in hydrides and the gas phase exceeded the control level.
3. TG data ranked the tested hydride-forming materials by their H<sub>2</sub> sorption capacity in the fermentation broth in the following order (highest to lowest): Pd, AB<sub>5</sub>, AB<sub>2</sub> and LaNi<sub>5</sub>.
4. The presence of powdered Pd or hydride-forming alloys in cultivation medium did not impede glycerol consumption: it was fully degraded during 24 h of fermentation. Concomitantly, the highest amount of absorbed H<sub>2</sub> was measured by the weight loss of hydride-forming materials in TG experiments after 18 h of glycerol fermentation.

## 4.2. Microbial fuel cells for production of energy carriers

### 4.2.1. Introduction

**Microbial electrolysis cells** (MBECs) are a technique used to produce H<sub>2</sub> from a wide variety of substrates. MBECs are adapted microbial fuel cells (MBFCs). Using the MBECs as an alternative electrically driven hydrogen production process results in the conversion of a wide range of organic substrates into hydrogen under applied external potential [15]. The MBEC technology resembles an MBFC in which the primary difference is the necessity of a small input of external voltage. Based on thermodynamics, a potential higher than 0.110 V, in addition to that generated by microorganisms (–0.300 V), will produce H<sub>2</sub>. The MBECs are capable of more than 90% efficiency in the production of H<sub>2</sub>. The performance of MBECs is determined by the type of microorganism, electrode materials, type of the membrane used, applied potential range, composition and concentration of the substrate, and design of the MBEC [72]. Babu et al. [73] reported usage of two-stage process integrating the MBEC process with the dark fermentation in order to convert the acid-rich dark fermentation effluents into substrates for additional hydrogen gas production. MBECs were operated with a small range of varying applied potential (0.2–1.0 V) using an anaerobic mixed consortium as a biocatalyst. The process produced hydrogen with rate 0.53 mmol/h and high substrate conversion efficiency (90%) (Fig. 4.6).

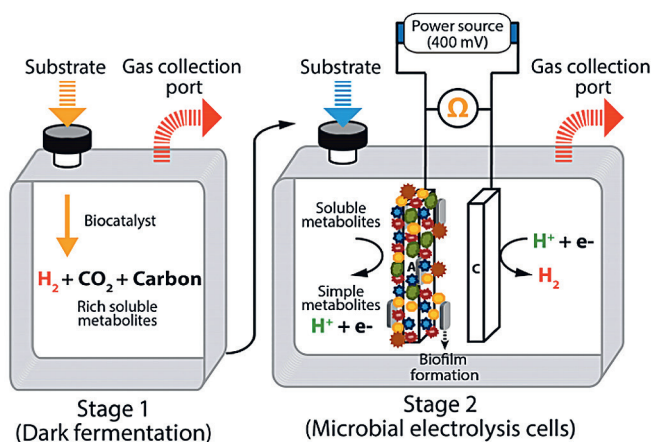


Figure 4.6. Two-stage process integrating the MBEC process with the dark fermentation. Green, orange, brown, and blue symbols represent a mixed microbial population. In stage 1, complex substrates are used for  $H_2$  production in dark fermentation, and in stage 2, acid-rich effluents were used as substrates in MBECs for further  $H_2$  production (adapted from [15, 73])

**Microbial fuel cells** (MBFCs) are devices that convert chemical energy of organic compounds to electrical energy by the catalytic reactions of microorganisms under anaerobic conditions (reviewed in [74]). MBFCs generate electricity directly from biodegradable materials [75]. Almost any biodegradable organic substance can be used to operate an MBFC device and generate electricity. Examples include domestic and industrial wastewater and agricultural pollution, as well as sugars, proteins, starch and cellulose [76]. MBFCs are promising future technology for alternative renewable power sources. Simultaneous wastewater treatment and energy production are one example of the effective operation of MBFCs [77]. Bacteria obtain energy in two steps. The first step involves the removal of electrons from an organic material (oxidation), and the second step is to give these electrons to the final electron acceptor (reduction), such as oxygen or nitrate or sulphate ions. If bacteria grow under anaerobic conditions, they can return electrons to a carbon electrode (anode). The electrons travel through the external resistance (the consumer) to the cathode, where they are combined with protons and oxygen. When electrons move from anode to a cathode, they generate current and voltage [78]. For most of the microorganisms, the outer surface consists of electricity non-conductive substances, lipid membranes, peptidoglycan and lipopolysaccharides, which prevent direct transport of electrons to anode [74]. The activity of MBFC is provided by microorganisms capable of carrying out electron transport outside the cell. They are called exoelectrogenic microorganisms, because they have the ability to directly transport electrons outside the cell [76] with conductive pili or nanowires [79]. Some of the bacterial species found in biofilms improve the function of MBFC and can produce and excrete soluble compounds acting as mediators to shuttle electrons to the surfaces [80].

Two different types of MBFC technologies are available – single and dual chamber MBFC [75]. A traditional MBFC consists of anode and cathode compartments that connects the proton exchange membrane (PEM) or the salt bridge [74, 81]. A single-chamber MBFC eliminates the need for a separate cathode chamber, putting the cathode

outside the cell in contact with airborne oxygen. Dual-chamber MBFCs are typically chosen to avoid mixing electron acceptors and electron donors that would lead to electron losses [75]. Nafion membranes (Dupont Co., USA) are the most commonly used PEM, but the agar-salt bridge is the simplest and cheapest solution [82]. Increased voltages or power can be achieved by connecting some MBFC circuits, or in parallel. Power generation using MBFC is influenced by several factors such as the type of microorganisms, the type and concentration of fuel biomass, ion strength, pH, temperature and reactor configuration [74]. In today's research, mixed cultures and microbial isolates are used. Often the use of mixed cultures shows better results than experiments with pure cultures [76]. However, there is a lack of information about MBFC potential in natural environments and usage of natural sludge as an inoculum.

#### 4.2.2. Applicability of 3D-printed graphene electrodes in MBFC

The choice of anode material is very important for MBFC's efficient operation. Graphite electrodes are most often applied, but their hydrophobic and antimicrobial properties reduce biocompatibility. Graphene materials are less hydrophobic and have good conductivity, thus exhibiting potentially better biocompatibility [83]. Providing favourable conditions for microorganisms it is possible to improve the functioning of the MBFC.

The aim of this study was to test the applicability of the graphene-PLA composite for the production of 3D-printed electrodes for MBFC. The pure culture of *Pseudomonas aeruginosa* and natural mixed inoculum was used to evaluate wild habitat response to MBFC technology. *P. aeruginosa* is a wide distributed Gram-negative rod-shaped bacterium which produces pyocyanin, a compound which acts as an electrochemical extracellular mediator and promotes electron transport to the anode [84].

Sandwich-type dual-chamber MBFCs were built in our laboratory. Each MBFC consisted of two hermetically sealed polycarbonate containers, which were interconnected with a bridge (Fig. 4.7). Anode chamber (100 mL) was separated from cathode chamber (100 mL) with Nafion® 212 membrane or agar-salt bridge. The active surface of Nafion membrane was 25 cm<sup>2</sup>. The conductive part of agar-salt bridge (4% agar, 2% NaCl) has diameter 18 mm and length 40 mm. Four different anodes (5x5 cm, Fig. 4.8) were used:

- 1) graphite paper (Sidrabe JSC, Latvia);
- 2) plain 3D-printed graphene-PLA composite (BlackMagic3D, Graphene 3D Lab, USA);
- 3) sponge-like 3D-printed graphene-PLA composite;
- 4) self-made pressed graphene powder electrode.

Electrochemically (0.00384 A/cm<sup>2</sup>) platinum-coated stainless steel wire mesh, 5 × 5 cm, was used as a cathode.

In total, 16 MBFCs were constructed, of which eight operated with natural substratum and inoculum, and eight operated with pure culture of *Pseudomonas aeruginosa* MSCL 331 in MH medium (glucose 5 g/L). The anode chamber was filled with a natural lake sediment (particle size less than 5 × 5 mm) or suspension of *P. aeruginosa* in medium. After filling with an inoculum/ substrate, an MBFC anode chamber was flushed with argon gas for 5 minutes (2 L/min). The cathode chamber was filled with tap water. MBFC operated at a room temperature of 20±2 °C. The measurements were taken with potentiostat Voltalab PGZ301 (Radiometer Analytical) and software VoltaMaster4 after a 96-hours adaptation period in the case of sediment and after 12 hours in the case of *P. aeruginosa*.

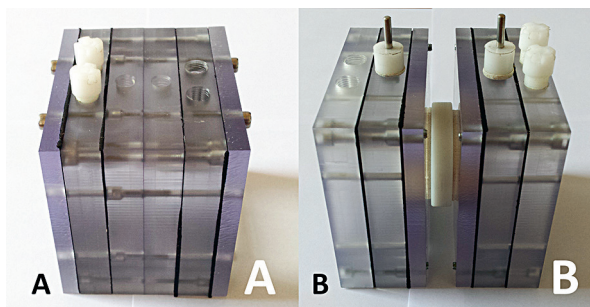


Figure 4.7. Two-chamber MBFCs. A – with Nafion 212 membrane; B – with agar-salt bridge

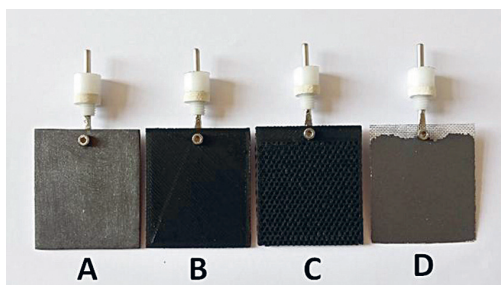


Figure 4.8. Anodes made from A – graphite paper, B – plain 3D-printed graphene-PLA composite, C – sponge-like 3D-printed graphene-PLA composite, and D – pressed graphene powder

MBFCs with agar bridges showed three times lower power densities than MBFCs with Nafion membranes because the bridge had a higher internal resistance. MBFCs with a lake sludge and plain printed graphene-PLA electrode showed a similar maximum power density ( $11.6 \text{ mW/m}^2$ ) as a graphite paper ( $12.4 \text{ mW/m}^2$ ) (Fig. 4.9).

However, the MBFCs with *P. aeruginosa* culture (Fig. 4.10) and plain printed graphene-PLA electrodes showed a significantly higher power density ( $35.8 \text{ mW/m}^2$ ) than graphite electrodes ( $6.5 \text{ mW/m}^2$ ). The best result showed printed sponge-like electrodes, which had three times larger surface area than plain graphene-PLA electrodes. The highest power densities obtained by *P. aeruginosa* point to a much more efficient MBFC performance than a natural system. However, such MBFCs proved to be unstable as they did not work after 36 h. The pressed graphene powder electrodes also showed good power density ( $15.7\text{--}28.5 \text{ mW/m}^2$ ) however, the electrodes were mechanically unstable. The open circuit potential increased from 0.45 V to 0.75 V in MBFCs with graphene-PLA electrodes (Fig. 4.11, 4.12), which could indicate a better biocompatibility however the output power was limited by increased material resistance. The obtained maximum power density was 10 times smaller than for MBFCs with graphene electrodes mentioned in the literature [85, 86], which could be explained by the limiting function of the cathode. The properties of the platinum-coated stainless steel cathode were significantly different from the catalytic properties of pure platinum (Fig. 4.13).

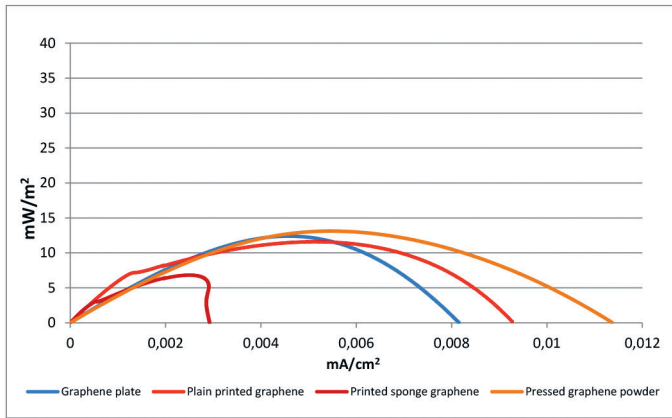


Figure 4.9. Power curves of MBFC after 96 hours' operation with lake sediment

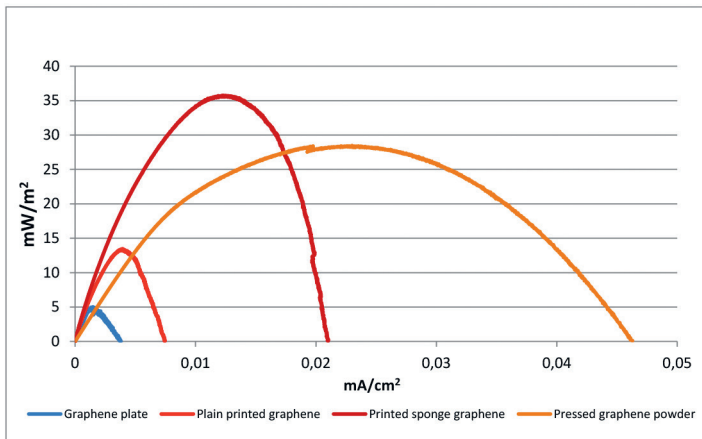


Figure 4.10. Power curves of MBFC after 12 hours' operation with *P. aeruginosa*

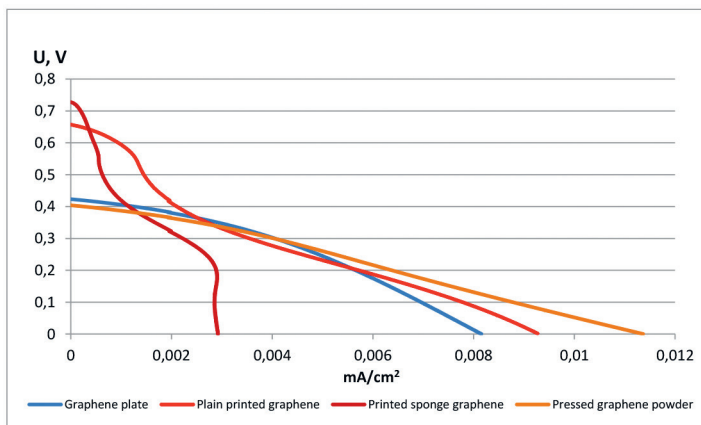


Figure 4.11. Polarization curves of MBFC after 96 hours operation with lake sediment

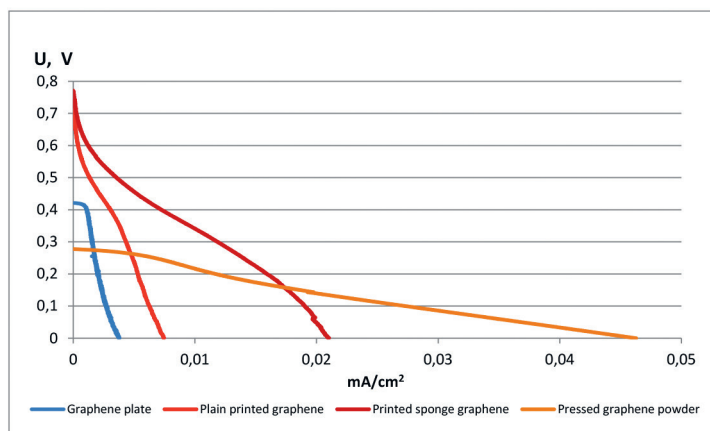


Figure 4.12. Polarization curves of MBFC after 12 hours operation with *P. aeruginosa*

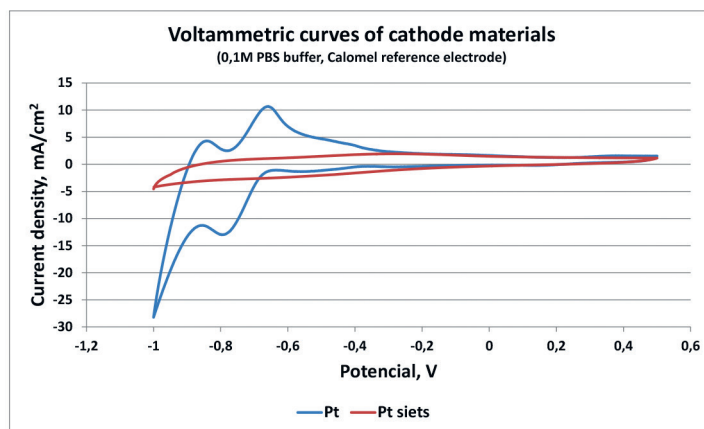


Figure 4.13. Voltammetric curves of cathode materials

The voltammetry of graphene-PLA composite electrodes showed worse electrochemical performance than graphite, but electrodes worked equally well or better than graphite, indicating better biocompatibility. However, the increased MBFC potential may also indicate a better biodegradability of the electrode. With 3D printable material, it is possible to produce any form of MBFC electrodes quickly. An innovative anode configuration is required to reduce the spatial conductivity resistance of the graphene-PLA composite. The long-term operation of MBFC was more efficient with lake sediment as a substrate/ inoculum than with a bacterial pure culture.

#### 4.2.3. Anodic biofilm vitality during operation of MBFC

Freshwater and marine sediments, landfill leachate, wastewaters, activated sludge and other substrates serve as organic-rich nutrients and sources of microorganisms for sustainable energy production in MBFCs (reviewed in [87]). Bacteria are looking for electron

acceptors such as nitrate or sulphate ions during decomposition of organic materials under anaerobic conditions. They can return electrons also to an anode which usually contains carbon-based materials. It has been discovered that it does many bacteria using several electron transfer mechanisms. Exoelectrogenic bacteria transfer the electrons either directly to the anode surface via specialized protein-based nanowires and/or mediate them by secreting different soluble electron shuttles (reviewed by [88]). Bacteria form biofilms on the anode (reviewed by [89]). Correlation between increasing bacterial biomass on the anode and current is proven. There is no decrease in cell viability as current increases. Reguera et al. [90] studied biofilm development and energy production by pilin-deficient *Geobacter sulfurreducens* mutant and showed that the live population was preferentially located in direct contact with the anode surface, and that the dead cells were present primarily in the upper biofilm layers. Situation with mixed-species biofilms is more complicated because it is not known which species or strains may be conductive and contribute to the transfer of electrons [91]. Read et al. [92] demonstrated that biofilm viability was maintained highest nearer the anode during closed circuit operation, but viability was highest on the top of the biofilms in open circuit. Other authors have noted that development of biofilms is influenced by startup performance of MBFC under different external resistances and that compact biofilm resulted in a poor mass transfer [93].

The aim of this study was to determine the vitality and succession of microorganisms in MBFCs fed with organic-rich lake sediment during operation at various load conditions.

Three sandwich-type dual-chamber MBFC was built in our laboratory. Each MBFC consisted of two hermetically sealed 1 L polycarbonate containers (Cambro, USA), which were interconnected with a bridge. The conductive part of agar-salt bridge (4% agar, 2% NaCl), made from POM plastic (Industriplasts Ltd., Latvia) cylinder with threads at both ends, has the diameter of 18 mm and the length of 40 mm. The anode chamber was filled with 0.7 L of natural organic-rich sediment obtained from watercourse near lake Jugla in Riga (Latvia). After insertion of sediment, anode was placed into the anode chamber. The anode was made from graphite paper (Sidrabe JSC, Latvia), 13 × 6 cm, and it was fixed in a stainless steel mesh frame (Severstallat JSC, Latvia). The cathode chamber was filled with 0.7 L of cold tap water. Platinum-coated stainless steel wire mesh, 13 × 6 cm, was used as a cathode. After filling, an MBFC anode chamber was flushed with argon gas for 10 minutes (2 L/min).

After providing an anaerobic environment, the open circuit potential was measured and MBFC1 was connected to a supercapacitor system (Kamcap, 2.6 V 10 F) with a total capacity of 30 farads (F) and a portable pH-meter PH-208 (Lutron, USA). Supercapacitor system consisted of three parallel-connected 10 F supercapacitors. A 500 kΩ external resistance and a portable pH-meter were connected between the MBFC2 outputs and the MBFC2 was operating at this low load. The third MBFC (MBFC3) was load-free, without external consumer. Voltage readings were taken with a multimeter DPM (Solid Polska, Poland) every day. Super capacitor charging was monitored in time with Arduino based data acquisition system. When the MBFC1 supercapacitor system voltage approached the open circuit voltage, the supercapacitor system was discharged and reconnected. MBFCs operated at a room temperature of  $20 \pm 2$  °C.

Samples for chemical and microbiological analyses were taken at the beginning and after 14 and 42 days since the beginning of the experiment. Liquid (anolyte) was mixed to obtain homogeneous structure. 25 mL and 50 mL of liquid was removed from each MBFC with

a sterile spoon and placed in 50 mL polypropylene tubes for determination of BOD. One mL of liquid was taken for the determination of COD and one mL for the determination of bacterial colony-forming units (CFU). Measurements of biochemical oxygen demand (BOD<sub>5</sub>) were made, using OxiDirect (Lovibond, Germany). Measurements of chemical oxygen demand (COD) were conducted using Lovibond thermoreactor RD125 and COD VARIO photometer MD200.

Biofilm was removed from the anodes by scraping of one cm<sup>2</sup> surface area of each anode under sterile conditions. Biofilm was suspended in one mL of sterile water in 1.5 mL tube for the determination of bacterial CFU. For microscopy, the piece of each anode in size of 0.5 × 0.5 cm was cut and placed in sealed 1.5 mL tubes. After sampling, MBFC was hermetically closed and argon gas was blown with a flow rate 2 L/min for 10 min.

The amount of culturable bacteria was analysed in the samples of liquid and anode biofilms. Serial dilutions of each suspension were plated in duplicate in the medium R2A (Bio-Rad, France). Equal amount of plates was incubated aerobically and anaerobically at 21°C for 3–10 days. Anaerobic growth was provided in GasPak™ EZ Anaerobe Pouch System (BD, USA). The number of CFU was estimated and expressed as CFU per mL of liquid or per cm<sup>2</sup> of anode surface. Based on colony and cell morphology, predominant bacterial species were isolated from the highest dilutions of samples. These bacteria were purified and identified with BBL® Crystal™ ID kits (BD, USA). Viability of bacteria was determined with LIVE/DEAD BacLight Bacterial Viability kit L7007 (Molecular Probes, USA).

**Performance indicators of MBFCs.** Electrical performance of MBFCs was confirmed by monitoring of open circuit voltage and supercapacitor charging. Results of measurements showed that lake sediment used as inoculum and feed for the fuel cells had an initial COD and BOD<sub>5</sub> value of 51720 mg/L and 223 mg/L, respectively. The ratio of BOD<sub>5</sub>/COD, which characterizes the biological stability of substrate, was low, i. e. 0.43% which points to the fact that the sediment contains many difficult to break down or non-biodegradable organic compounds, or toxic substances. High COD and low BOD/COD-ratio is a common feature of landfill leachate [94] and indicates that there is a low concentration of volatile fatty acids and relatively higher amount of recalcitrant humic substances [95]. During operation of MBFCs, BOD<sub>5</sub> decreased by 28.3–42.2% (Fig. 4.14 A). COD decreased by 539 mg/L, 171 mg/L and 34 mg/L per day in MBFC1, MBFC2 and MBFC3, respectively, or by 43.8% (MBFC1), 13.9% (MBFC2) and 2.8% (MBFC3) after 42 days (Fig. 4.14 B). COD removal showed that MBFC should operate under maximally high load conditions for optimal performance in bioremediation. MBFCs open circuit voltage measurements showed that 24-hours adaptation period is needed for natural sediment based MBFC to gain highest voltage. After this period, voltage stayed stable at about 0.57 V. Supercapacitor charging results showed that under high load conditions MBFC adapts and works better with each next cycle. However, results from 4th week showed worse but it can be explained with detected air-tightness problems of particular MBFC.

**Characteristics of microbial communities.** The amount of culturable microorganisms in the anolyte decreased from 6.7 log CFU/mL for aerobic growing bacteria and 7.9 log CFU/mL for anaerobic growing bacteria in the beginning of the experiment to 5.1 log CFU/mL (MBFC1) for aerobic and anaerobic bacteria after six weeks. The biggest decrease was detected in MBFC1 while the bacterial concentration on the anode surface increased in all MBFCs and reached 4.8–5.6 log CFU/cm<sup>2</sup> for aerobic growing bacteria and 4.3–4.9 log CFU/cm<sup>2</sup> for anaerobic growing bacteria after six weeks without significant difference between MBFCs.

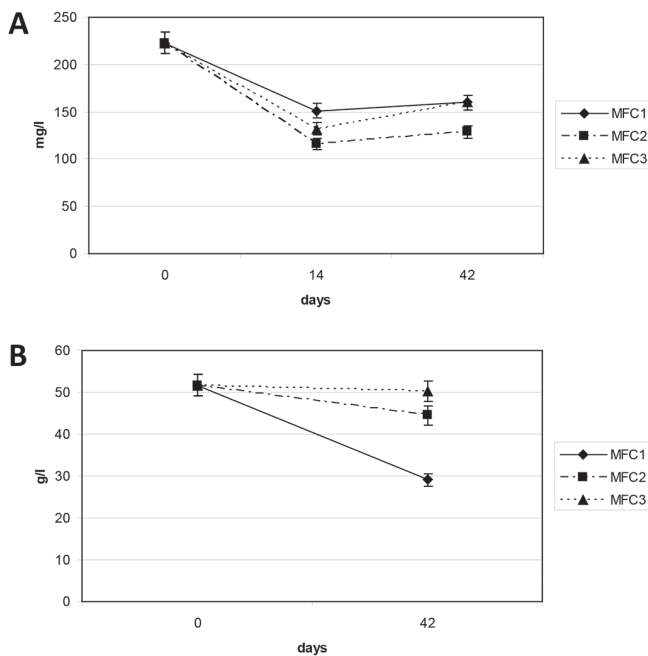


Figure 4.14. Changes of BOD<sub>5</sub> (A) in mg/L and COD (B) in g/L during operation of MBFCs

From 15 isolated predominant species of culturable bacteria, seven belonged to phylum *Firmicutes* (*Bacillus*, *Clostridium* species), five belonged to *Bacteroidetes* (*Bacteroides*, *Empedobacter*, *Prevotella* species), and one species belonged to *Actinobacteria* (*Leifsonia aquatica*), *Fusobacteria* (*Fusobacterium necrophorum*) and *Proteobacteria* (*Sphingomonas paucimobilis*) (Table 4.5). *Bacteroidetes* (*Bacteroides eggerthii*, *B. uniformis*, *Prevotella buccae*), *Firmicutes* (*Clostridium clostridioforme*, *C. perfringens*), as well as *Actinobacteria* (*Leifsonia aquatica*) were isolated directly from the anode biofilms. *Clostridium* spp. did not appear between the predominant at the beginning (day 0) but were enriched in MBFCs. Electrochemical activity of *Clostridium butyricum* has been recognized [96]. Taxonomic analysis provided by Kiseleva et al. [97] also showed that three bacterial phyla, *Proteobacteria*, *Firmicutes* and *Bacteroidetes* constitute the core of microbiomes in MBFCs in distinct climatic zones. Study provided by Read et al. [92] indicated a synergistic or mutualistic relationship between Gram-positive bacterium *Enterococcus faecium* and Gram-negative bacteria in current generation.

After 42 days, biofilms were formed around anodes of all three MBFCs. Graphite paper of MBFC1 had the most durable and best immobilized biofilm. This can be explained by the positive effect of the increased load on bacterial metabolism due to the availability of a solid final electron acceptor, i.e. anode. The MBFC2 electrode biofilm was thinner than the biofilm of MBFC1 electrode. The MBFC3 biofilm was the weakest and it was easily rinsed with water. This indicates that bacteria did not have favourable growth conditions on the surface of the electrode, if the MBFC was not connected to an electricity consumer. Bacteria have different respiration strategies in environments containing multiple electron acceptors [98]. It is possible that there was a lack of suitable chemical electron acceptors on the anaerobic anode of MBFC3.

Table 4.5. Predominant culturable bacteria isolated from anolyte and anode biofilms and identified biochemically with BBL Crystal ID kits

Day	Substratum	Aerobic/ anaerobic cultivation	Species		
			Phylum	Name	Confidence
0	Anolyte	Aerobic	<i>Firmicutes</i>	<i>Bacillus pumilus</i>	0.9500
			<i>Bacteroidetes</i>	<i>Empedobacter brevis</i>	0.7121
			<i>Proteobacteria</i>	<i>Sphingomonas paucimobilis</i>	0.9999
		Anaerobic	<i>Firmicutes</i>	<i>Bacillus mycoides</i>	0.9500
			<i>Bacteroidetes</i>	<i>Bacteroides uniformis</i>	0.9170
42	Anolyte	Aerobic	<i>Firmicutes</i>	<i>Bacillus subtilis</i>	0.9930
		Anaerobic	<i>Firmicutes</i>	<i>Clostridium butyricum</i>	0.9246
			<i>Firmicutes</i>	<i>Clostridium clostridioforme</i>	0.9940
			<i>Fusobacteria</i>	<i>Fusobacterium necrophorum</i>	0.7878
	Anodes	Aerobic	<i>Actinobacteria</i>	<i>Leifsonia aquatica</i>	0.8976
		Anaerobic	<i>Bacteroidetes</i>	<i>Bacteroides eggerthii</i>	0.8048
			<i>Bacteroidetes</i>	<i>Bacteroides uniformis</i>	0.6845
			<i>Firmicutes</i>	<i>Clostridium clostridioforme</i>	0.9927
			<i>Firmicutes</i>	<i>Clostridium perfringens</i>	0.8704
	<i>Bacteroidetes</i>	<i>Prevotella buccae</i>	0.8771		

Fluorescent staining results showed that after 42 days most of all live bacteria are visible in MBFC1 anodic biofilm which operated under high load conditions. Lake sediment COD removal also indicated the highest biological activity in MBFC1 in comparison with MBFC2 and MBFC3 (Fig. 4.14 B). It means that a 500 k $\Omega$  external resistance was too small to provide biofilm bacteria with sufficient electron removal. Without the load, MBFC3 acted as a storage vessel and bacterial viability on the surface of the electrode should have been unaffected. However, the possible lack of a solid electron acceptor and/or the difficulty in getting nutrients in the depth of biofilm led to cell death. It coincides with results obtained by Ieropoulos et al. (2005) that MBFC biofilms can store electrons when the device was left in open circuit for an extended period of time [99]. Also, Wrighton et al. [100] revealed a greater percentage of viable cells and a higher cell density associated with electrode surface. Right bacterial cytochromes are those that act as electron sinks [100]. No differences were observed between investigated MBFCs in viability of planktonic cells (in the liquid).

**Conclusions.** Dual-chamber MBFCs were operated under different external load conditions with high COD and low BOD/COD-ratio lake sediment as a substrate and inoculum. Fluorescent staining and count of CFU were used for evaluation of anodic biofilm vitality. 24-hours' adaptation period was needed to gain the highest voltage. COD removal showed that MBFC should operate under maximally high load conditions for optimal performance in bioremediation. Number of culturable bacteria on the anode surface increased in all MBFCs and after six weeks reached 4.8-5.6 log CFU/cm<sup>2</sup> without significant difference between MBFCs. Predominant species of culturable bacteria

belonging to phyla *Bacteroidetes*, *Firmicutes* and *Actinobacteria* were isolated directly from the anode biofilms. No differences were observed between MBFCs in viability of bacterial cells in anolyte but there was better viability in anode biofilms in case of high load conditions than without external resistance. COD removal also indicated the highest biological activity under high load conditions. This can be explained by the availability of anode as additional electron acceptor.

#### 4.2.4. Benthic MBFC

Sediment or benthic MBFC is a special type of MBFC that that can be deployed in a natural water body for energy production [102]. It means that anode is embedded, for example in a pond, lake or marine sediment but the cathode is placed in the upper layer of water to get access to atmospheric oxygen. Power generation results from oxidation of sedimentary organic carbon catalysed by microorganisms [103].

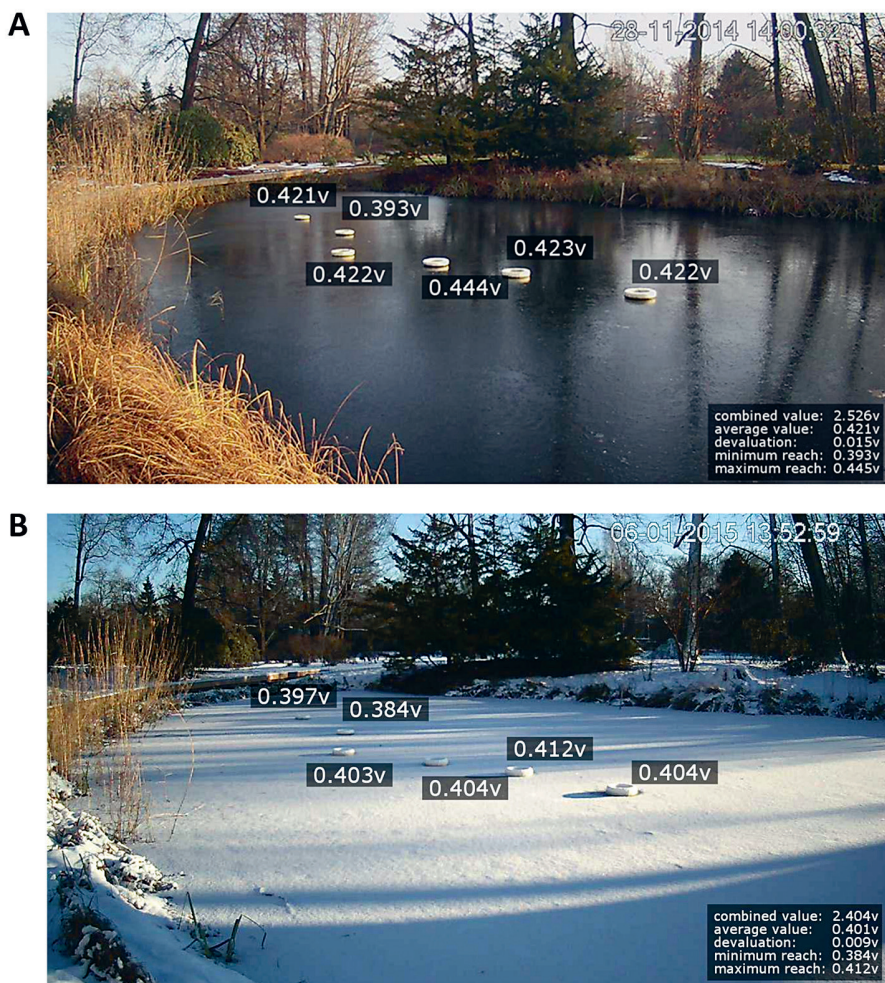


Figure 4.15. “Pond Battery” installation in the Botanical Garden of the University of Latvia: A – screen-shot from November 11, 2014; B – screen-shot from January 6, 2015

Sediment MBFCs are particularly promising for the bioremediation purposes. Our team, Artūrs Gruduls et al. in cooperation with artists Rasa Šmite and Raitis Šmits (RIXC) has developed a “Pond Battery” installation in the Botanical Garden of the University of Latvia in 2014/2015 (Figure 4.15). This battery consisted of six MBFCs and was installed in August 2014 and operated up to April, 2015, both in the summer and in the winter seasons. It has been found that benthic MBFCs have been operated for several years with no remarkable decrease in power output [104].

### 4.3. Summary

Researchers of the Faculty of Biology in close cooperation with Institute of Solid State Physics of University of Latvia (Laboratory of Materials for Energy Harvesting and Storage) studied the microbiological production of hydrogen ( $H_2$ ) in dark fermentation reactions and storage possibilities in hydride-forming materials, constructed and developed laboratory-scale bioreactors, and researched possibilities to generate electrical energy with microbial fuel cells (MBFC) or bacterial batteries.

The studies show that hydride-forming materials – Pd,  $AB_5$ ,  $AB_2$  – can be successfully exploited for  $H_2$  collection from the liquid phase in crude glycerol fermentation by *E. coli* and *Klebsiella aerogenes* (previously known as *Enterobacter aerogenes*) MSCL 758. The inhibitory effect of  $LaNi_5$  was established for the growth of bacteria or inhibition of metabolic pathway, in which  $H_2$  and  $CO_2$  is produced. Conversely, Pd and multicomponent alloys  $AB_2$  and  $AB_5$  showed positive effect on  $H_2$  and  $CO_2$  production.

Dual-chamber MBFCs were operated under different external load conditions with high COD and low BOD/COD-ratio lake sediment as a substrate and inoculum. Fluorescent staining and count of CFU were used for evaluation of anodic biofilm vitality. 24-hours adaptation period was needed to gain the highest voltage. COD removal showed that MBFC should operate under maximally high load conditions for optimal performance in bioremediation. Number of culturable bacteria on the anode surface increased in all MBFCs and after six weeks reached 4.8–5.6 log CFU/cm<sup>2</sup> without significant difference between MBFCs. Predominant species of culturable bacteria belonging to phyla *Bacteroidetes*, *Firmicutes* and *Actinobacteria* were isolated directly from the anode biofilms. No differences were observed between MBFCs in viability of bacterial cells in anolyte but there was better viability in anode biofilms in case of high load conditions than without external resistance. COD removal also indicated the highest biological activity under high load conditions. This can be explained by the availability of anode as additional electron acceptor.

It has been found that benthic MBFCs have been operated for several years with no remarkable decrease in power output.

### 4.4. References

1. Hydrogen Tech Roadmap (2015). Available at [https://www1.eere.energy.gov/hydrogenand-fuelcells/pdfs/h2\\_tech\\_roadmap.pdf](https://www1.eere.energy.gov/hydrogenand-fuelcells/pdfs/h2_tech_roadmap.pdf) (accessed on December 4, 2018).
2. Dimanta, I. (2016) Biohydrogen Production from Crude Glycerol, Lactose and Hydrogen Storage Possibilities with Metalhydrides from Fermentation Broth. PhD thesis. Available at <https://dspace.lu.lv/dspace/handle/7/31856> (accessed on December 4, 2018).
3. Valucka, S. (2015) Ūdeņraža mikrobioloģiska producēšana tumsas fermentācijā un uzkrāšana metālhidrīdos (Microbial hydrogen production by dark fermentation and its storage in metal

- hydrides). MSc thesis. Available at <https://dspace.lu.lv/dspace/handle/7/29440> (accessed on December 4, 2018).
- Kleinmane, Z. (2016) Dažādu oglekļa bāzētu materiālu elektrodu pielietojamība mikroorganismu degvielas šūnās (Application of different carbon-based electrodes in microbial fuel cells). Bch thesis. Available at <https://dspace.lu.lv/dspace/handle/7/32186> (accessed on December 4, 2018).
  - Paiders, M. (2017) Ūdeņraža mikrobioloģiska producēšana, izmantojot *Enterobacter aerogenes*, un uzkrāšana AB<sub>5</sub> tipa sakausējumā (Microbial hydrogen production using *Enterobacter aerogenes* and its storage in AB<sub>5</sub> type alloy). Bachelor's thesis. Available at <https://dspace.lu.lv/dspace/handle/7/35181> (accessed on December 4, 2018).
  - Kleperis, I., Muiznieks, I., Kleperis, J. (2010). A bacterial hydrogen production test system for measuring H<sub>2</sub> concentrations in liquids and gases. *Latvian Journal of Physics and Technical Sciences*, 2, 60–68.
  - Dimanta, I., Nikolajeva, V., Gruduls, A., Muiznieks, I. (2013). Assessment of bio-hydrogen production from glycerol and glucose by fermentative bacteria. *Enerģetika*, 59, 124–128.
  - Nikolajeva, V., Neibergs, M., Valucka, S., Dimanta, I., Kleperis, J. (2015) Application of pretreatment, bioaugmentation and biostimulation for fermentative hydrogen production from maize silage. *The Open Biotechnology Journal*, 9, 39–48.
  - Dimanta, I., Kleperis, J., Nakurte, I., Valucka, S., Nikolajeva, V., Rutkovska, Z., Muiznieks, I. (2016) Metal hydride alloys for storing hydrogen produced by anaerobic bacterial fermentation. *International Journal of Hydrogen Energy*, 41, 9394–9401.
  - Kleinmane, Z., Gruduls, A., Nikolajeva, V., Kleperis, J. (2016) Anodic biofilm vitality during operation of microbial fuel cells at various load conditions. *Journal of Biotechnology*, 231, S105–S106.
  - Paiders, M., Gruduls, A., Kalnina, L., Valucka, S., Kleperis, J., Dimanta, I., Nikolajeva, V. (2017) Biogas and hydrogen production from glycerol by *Enterobacter aerogenes* and anaerobic microbial communities. *Agronomy Research*, 15, 256–269.
  - Wiberg, E., Wiberg, N., Holleman, A.F. (2001) *Inorganic Chemistry*. San Diego, CA: Academic Press, 1884 pp.
  - Goswami, D. Y., Kreith, F. (2007). *Handbook of Energy Efficiency and Renewable Energy*. CRC Press.
  - Suleman, F., Dincer, I., Agelin-Chaab, M. (2016) Comparative impact assessment study of various hydrogen production methods in terms of emissions. *International Journal of Hydrogen Energy*, 41, 8364–8375.
  - Chandrasekhar, K., Lee, Y. J., Lee, D. W. (2015) Biohydrogen production: Strategies to improve process efficiency through microbial routes. *International Journal of Molecular Sciences*, 16, 8266–8293.
  - Abánades, A. (2012) The challenge of hydrogen production for the transition to a CO<sub>2</sub>-free economy. *Agronomy Research*, 10, 11–16.
  - Dincer, I., Acar, C. (2015). Review and evaluation of hydrogen production methods for better sustainability. *International Journal of Hydrogen Energy*, 40, 11094–11111.
  - Das, D., Khanna N., Dasgupta, C. (2008) *Biohydrogen Production: Fundamentals and Technology Advances*. CRC Press, 408 pp., Boca Raton, Florida.
  - Madigan, M. T., Martinko, J. M. (2006). *Brock Biology of Microorganisms*. 11th ed. Pearson Prentice Hall (USA), 118–119.
  - Thauer, R. K., Kaster, A. K., Goenrich, M., Schick, M., Hiromoto, T., Shima, S. (2010) Hydrogenases from methanogenic archaea, nickel, a novel cofactor, and H<sub>2</sub> storage. *Annual Review of Biochemistry*, 79, 507–536.
  - Das, D., Veziroglu, T. (2008) Advances in biological hydrogen processes. *International Journal of Hydrogen Energy*, 33, 6046–6057.
  - Ghimire, A., Frunzo, L., Pirozzi, P., Trably, E., Escudie, R., Lens, P. N. L., Esposito, G. (2015) A review on dark fermentative biohydrogen production from organic biomass: Process parameters and use of by-products. *Applied Energy*, 144, 73–95.

23. Manish, S., Banerjee, R. (2008) Comparison of biohydrogen production processes. *International Journal of Hydrogen Energy*, 33, 279–286.
24. Das, D., Veziroglu, T. N. (2001) Hydrogen production by biological processes: a survey of literature. *International Journal of Hydrogen Energy*, 26, 13–28.
25. Hallenbeck, P. C., Benemann, J. R. (2002) Biological hydrogen production: fundamentals and limiting processes. *International Journal of Hydrogen Energy*, 27, 1185–1193.
26. Levin, D. B., Pitt, L., Love, M. (2004) Biohydrogen production: prospects and limitations to practical application. *International Journal of Hydrogen Energy*, 29, 173–185.
27. Maeda, T., Sanchez-Torres, V., Wood, T. K. (2008) Enhanced hydrogen production from glucose by metabolically engineered *Escherichia coli*. *Applied Microbiology and Biotechnology*, 77, 879–890.
28. Hallenbeck, P. C. (2009) Fermentative hydrogen production: Principles, progress, and prognosis. *International Journal of Hydrogen Energy*, 34, 7379–7389.
29. Rogner, M., Igarashi, Y., Asada, Y., Miyake, J. (2002) Biohydrogen III: Renewable Energy System by Biological Solar Energy Conversion. Elsevier Science. 1 ed. AIST/METI, 187 pp.
30. Vignais, P. M., Colbeau, A. (2004) Molecular biology of microbial hydrogenases. *Current Issues in Molecular Biology*, 6, 159–188.
31. Nath, K., Muthukumar, M., Kumar, A., Debabrata, D. (2008) Kinetics of two-stage fermentation process for the production of hydrogen. *International Journal of Hydrogen Energy*, 33, 1195–1203.
32. Nath, K., Das, D. (2004) Improvement of fermentative hydrogen production: various approaches. *Applied Microbiology and Biotechnology*, 65, 520–529.
33. Hallenbeck, P. C. (2012) Hydrogen production by cyanobacteria. *Microbial Technologies in Advanced Biofuels Production*. Springer: New York, NY, USA, 15–28.
34. Boichenko, V. A., Greenbaum, E., Seibert, M. (2004) Hydrogen production by photosynthetic microorganisms. In: *Molecular to Global Photosynthesis*. Imperial College Press: London, UK, 397–451.
35. Pachapur, V. L., Sarma, S. J., Brar, S. K., Bihan, Y. E., Buelna, G., Verma, M. (2015) Biological hydrogen production using co-culture versus mono-culture system. *Environmental Technology Reviews*, 4, 55–70.
36. Mohan V. S., Chandrasekhar, K., Chiranjeevi, P., Babu, P. S. (2013) Biohydrogen production from wastewater. In: *Biohydrogen*. Pandey, A., Chang, J.-S., Hallenbeck, P. C., Larroche, C. (eds.), Elsevier: Amsterdam, The Netherlands, 223–257.
37. Angenent, L. T., Karim, K., Al-Dahhan, M. H., Domiguez-Espinosa, R. (2004) Production of bioenergy and biochemicals from industrial and agricultural wastewater. *Trends in Biotechnology*, 22, 477–485.
38. Wang, J., Wan, W. (2009) Factors influencing fermentative hydrogen production: a review. *International Journal of Hydrogen Energy*, 34, 799–811.
39. Zhang, Y.-H. P. (2010) Renewable carbohydrates are a potential high-density hydrogen carrier. *International Journal of Hydrogen Energy*, 35, 10334–10342.
40. Kapdan, I. K., Kargi, F. (2006) Bio-hydrogen production from waste materials. *Enzyme and Microbial Technology*, 38, 569–582.
41. Hawkes, F. R., Dinsdale, R., Hawkes, D. L., Hussy, I. (2002) Sustainable fermentative hydrogen production: challenges for process optimisation. *International Journal of Hydrogen Energy*, 27, 1339–1347.
42. Raghunandan, K., McHunu, S., Kumar, A., Kumar, K. S., Govender, A., Permaul, K., Singh, S. (2014) Biodegradation of glycerol using bacterial isolates from soil under aerobic conditions. *Journal of Environmental Science and Health, Part A, Toxic/Hazardous Substances & Environmental Engineering*, 49, 85–92.
43. Sarma, S. J., Brar, S. K., Sydney, E. B., Bihan, Y. L., Buelna, G., Soccol, C. R. (2012) Microbial hydrogen production by bioconversion of crude glycerol: a review. *International Journal of Hydrogen Energy*, 37, 6473–6490.

44. Adhikari, S., Fernando, S. D., Haryanto, A. (2009) Kinetics and reactor modelling of hydrogen production from glycerol via steam reforming process over Ni/CeO<sub>2</sub> catalysts. *Chemical Engineering & Technology*, 32, 541–547.
45. Mane, R. B., Rode, C. V. (2013) Catalytic recycling of glycerol formed in biodiesel production. In: Grohens, Y., Kumar, S.K., Boudenne, A., Weimin Y. (eds.), *Recycling and reuse of materials and their products*, Advances in materials science. Oakville, Apple Academic Press, 9–24.
46. Hu, S., Luo, X., Wan, C., Li, Y. (2012) Characterization of crude glycerol from biodiesel plants. *Journal of Agricultural and Food Chemistry*, 60, 5915–5921.
47. Hajek, M., Skopal, F. (2010) Treatment of glycerol phase formed by biodiesel production. *Bioresource Technology*, 101, 3242–3245.
48. Manosak, R., Limpattayanate, S., Hunsom, M. (2011) Sequential-refining of crude glycerol derived from waste used-oil methyl ester plant via a combined process of chemical and adsorption. *Fuel Processing Technology*, 92, 92–99.
49. Reungsang, A., Sittijunda, S., Angelidaki, I. (2013) Simultaneous production of hydrogen and ethanol from waste glycerol by *Enterobacter aerogenes* KKU-S1. *International Journal of Hydrogen Energy*, 38, 1813–1825.
50. Mangayil, R., Aho, T., Karp, M., Santala, V. (2012) Bioconversion of crude glycerol from biodiesel production to hydrogen. *International Journal of Hydrogen Energy*, 37, 12198–12204.
51. Ito, T., Nakashimada, Y., Senba, K., Matsui, T., Nishio, N. (2005) Hydrogen and ethanol production from glycerol-containing wastes discharged after biodiesel manufacturing process. *Journal of Bioscience and Bioengineering*, 100, 260–265.
52. Trchounian, K., Sanchez-Torres, V., Wood, T. K., Trchounian, A. (2011) *Escherichia coli* hydrogenase activity and H<sub>2</sub> production under glycerol fermentation at a low pH. *International Journal of Hydrogen Energy*, 36, 4323–433.
53. Guillaume, S. P., Patrick, C. H. (2009) High yield conversion of a crude glycerol fraction from biodiesel production to hydrogen by photofermentation. *Bioresource Technology*, 100, 3513–3517.
54. Jitrwung, R., Yargeau, V. (2015) Biohydrogen and bioethanol production from biodiesel-based glycerol by *Enterobacter aerogenes* in a continuous stir tank reactor. *International Journal of Molecular Sciences*, 16, 10650–10664.
55. Dharmadi, Y., Murarka, A., Gonzalez, R. (2006) Anaerobic fermentation of glycerol by *Escherichia coli*: a new platform for metabolic engineering. *Biotechnology and Bioengineering*, 94, 821–829.
56. Bruna, S. F., Guilherme, P., Fernanda, R. A., Nora, K., Saavedra, A., Marcelo, Z. (2010) Potential to produce biohydrogen from various wastewaters. *Energy for Sustainable Development*, 14, 143–148.
57. Elsharnouby, O., Hafez, H., Nakhla, G., El Naggat M. H. (2013) A critical literature review on biohydrogen production by pure cultures. *International Journal of Hydrogen Energy*, 38, 4945–4966.
58. Kotay, S. M., Das, D. (2008) Biohydrogen as a renewable energy resource – prospects and potentials. *International Journal of Hydrogen Energy*, 33, 258–263.
59. Zuttel, A. (2004) Hydrogen storage methods. *Naturwissenschaften*, 91, 152–157.
60. Sakintuna, B., Lamari-Darkrim, F., Hirscher, M. (2007) Metal hydride materials for solid hydrogen storage: a review. *International Journal of Hydrogen Energy*, 32, 1121–1140.
61. Fraunhofer Institute for Manufacturing Technology and Advanced Materials IFAM, Department Hydrogen Technology, Dresden, Germany (2018) Available at <https://www.ifam.fraunhofer.de/en/Profile/Locations/Dresden/HydrogenTechnology/hydrides.html> (accessed on December 22, 2018).
62. Pray, H. A., Schweickert, C. E., Minnic, B. H. (1952) Solubility of hydrogen, oxygen, nitrogen, and helium in water at elevated temperatures. *Industrial and Engineering Chemistry*, 44, 1146–1151.

63. Kleperis, J., Grinberga, L. (2008) Laboratorijas darba materiāli (Materials of Laboratory Work), Rīga, LU CFI.
64. Sandrock, G. D., Goodell, P. D. (1980) Surface poisoning of LaNi<sub>5</sub>, FeTi and (Fe, Mn) Ti by O<sub>2</sub>, CO and H<sub>2</sub>O. *Journal of the Less Common Metals*, 73, 161–168.
65. Kleperis, J., Wójcik, G., Czerwinski, A., Skowronski, J., Kopczyk, M., Beltowska-Brzezinska, M. (2001) Electrochemical behavior of metal hydrides. *Journal of Solid State Electrochemistry*, 5, 229–224.
66. Nishimiya, N., Kojima, Y., Toyama, T. (2014) Encapsulation of Hydrogen Storage Alloys by Softened Sol-Gel Method and Recovery of Hydrogen from Gas Mixtures, IDHE meeting, Nantes, France.
67. Macomber, L., Hausinger, R. P. (2011) Mechanisms of nickel toxicity in microorganisms. *Metalomics*, 3, 1153–1162.
68. Wongthanate, J., Polprasert, C. (2015) Immobilized biofilm in thermophilic biohydrogen production using synthetic versus biological materials. *Brazilian Archives of Biology and Technology*, 58, 124–130.
69. Broom, D. P. (2011) Hydrogen Storage Materials: The Characterization of Their Storage Properties, Springer, 260 pp.
70. Chen, P., Zhu, M. (2008) Recent progress in hydrogen storage. *Materials Today*, 11, 36–43.
71. Wicinska, P. (2016) Thermal degradation of organic additives used in colloidal shaping of ceramics investigated by the coupled DTA/TG/MS analysis. *Journal of Thermal Analysis and Calorimetry*, 123, 1419–1430.
72. Cheng, S., Logan, B. E. (2007) Sustainable and efficient biohydrogen production via electrohydrogenesis. *Proceedings of the National Academy of Sciences of the United States of America*, 104, 18871–18873.
73. Babu, M. L., Subhash, G. V., Sarma, P. N., Mohan, S. V. (2013) Bio-electrolytic conversion of acidogenic effluents to biohydrogen: An integration strategy for higher substrate conversion and product recovery. *Bioresource Technology*, 133, 322–331.
74. Du, Z., Li, H., Gu, T. (2007) A state of the art review on microbial fuel cells: a promising technology for wastewater treatment and bioenergy. *Biotechnology Advances*, 25, 464–482.
75. Deval, A., Dikshit, A. K. (2013) Construction, Working and Standardization of Microbial Fuel Cell. *APCBEE Procedia*, 5, 59–63.
76. Logan, B. E. (2008) Microbial Fuel Cells. Hoboken, NJ: John Wiley & Sons, 213 pp.
77. Liu, H., Cheng, S., Logan, B. E. (2005) Production of electricity from acetate or butyrate using a single-chamber microbial fuel cell. *Environmental Science & Technology*, 39, 658–662.
78. Rabaey, K., Boon, N., Siciliano, S. D., Verhaege, M., Verstraete, W. (2004) Biofuel cells select for microbial consortia that self-mediate electron transfer. *Applied and Environmental Microbiology*, 70, 5373–5382.
79. Reguera, G., McCarthy, K. D., Mehta, T., Nicoll, J. S., Tuominen, M. T., Lovley, D. R. (2005) Extracellular electron transfer via microbial nanowires. *Nature*, 435, 1098–1101.
80. Picioreanu, C., van Loosdrecht, M. C., Katuri, K. P., Scott, K., Head, I. M. (2008) Mathematical model for microbial fuel cells with anodic biofilms and anaerobic digestion. *Water Science & Technology*, 57, 965–971.
81. Mohan, Y., Kumar, S. M. M., Das, D. (2008) Electricity generation using microbial fuel cells. *International Journal of Hydrogen Energy*, 33, 423–426.
82. Min, B., Cheng, S., Logan, B. E. (2005) Electricity generation using membrane and salt bridge microbial fuel cells. *Water Research*, 39, 1675–1686.
83. El Mekawy, A., Hegab, H. M., Losic, D., Saint, C. P., Pant, D. (2017) Applications of graphene in microbial fuel cells: the gap between promise and reality. *Renewable and Sustainable Energy Reviews*, 72, 1389–1403.
84. Gomes, A. S., La Rotta, C. E., Nitschke, M., González, E. R. (2011) Evaluation of current output in *Pseudomonas aeruginosa* microbial fuel cells using glycerol as substrate and Nafion 117 as proton exchange membrane. *ECS Transactions*, 41, 2011–2017.

85. Hou, J., Liu, Z., Li, Y., Yang, S., Zhou, Y. (2015) A comparative study of graphene-coated stainless steel fiber felt and carbon cloth as anodes in MBFCs. *Bioprocess & Biosystems Engineering*, 38, 881–888.
86. Zhang, Y., Mo, G., Li, X., Zhang, W., Zhang, J., Ye, J., Huang, X., Yu, C. (2011) A graphene modified anode to improve the performance of microbial fuel cells. *Journal of Power Sources*, 196), 5402–5407.
87. Pant, D., Van Bogaert, G., Diels, L., Vanbroekhoven, K. (2009) A review of the substrates used in microbial fuel cells (MBFCs) for sustainable energy production. *Bioresource Technology*, 101, 1533–1543.
88. Kumar, R., Singh, L., Zularisam, A. W. (2016) Exoelectrogens: recent advances in molecular drivers involved in extracellular electron transfer and strategies used to improve it for microbial fuel cell applications. *Renewable and Sustainable Energy Reviews*, 56, 1322–1336.
89. Schechter, M., Schechter, A., Rozenfeld, S., Efrat, E., Cahan, R. (2014) Anode Biofilm. In: Wang, C.T. (Ed.), *Technology and Application of Microbial Fuel Cells*. InTech: 57–74.
90. Reguera, G., Nevin, K. P., Nicoll, J. S., Covalla, S. F., Woodard, T. L., Lovley, D. R. (2006) Biofilm and nanowire production leads to increased current in *Geobacter sulfurreducens* fuel cells. *Applied and Environmental Microbiology*, 72, 7345–7348.
91. Malvankar, N. S., Lau, J., Nevin, K. P., Franks, A. E., Tuominen, M. T., Lovley, D. R. (2012) Electrical conductivity in a mixed-species biofilm. *Applied and Environmental Microbiology*, 78, 5967–5971.
92. Read, S. T., Dutta, P., Bond, P. L., Keller, J., Rabaey, K. (2010) Initial development and structure of biofilms on microbial fuel cell anodes. *BMC Microbiology*, 10, 98.
93. Zhang, L., Li, J., Zhu, X., Ye, D., Fu, Q., Liao, Q. (2017) Startup performance and anodic biofilm distribution in continuous-flow microbial fuel cells with serpentine flow fields: effects of external resistance. *Industrial & Engineering Chemistry Research*, 56, 3767–3774.
94. Greenman, J., Gálvez, A., Giusti, L., Ieropoulos, L. (2009) Electricity from landfill leachate using microbial fuel cells: comparison with a biological aerated filter. *Enzyme and Microbial Technology*, 44, 112–119.
95. Kjeldsen, P., Barlaz, M. A., Rooker, A. P., Braun, A., Ledin, A., Christensen, T. H. (2002) Present and long-term composition of MSW landfill leachate: a review. *Critical Reviews in Environmental Science and Technology*, 32, 297–336.
96. Park, H. S., Kim, B. H., Kim, H. S., Kim, H. J., Kim, G. T., Kim, M., Chang, I. S., Park, Y. K., Chang, H.I. (2001) A novel electrochemically active and Fe(III)-reducing bacterium phylogenetically related to *Clostridium butyricum* isolated from a microbial fuel cell. *Anaerobe*, 7, 297–306.
97. Kiseleva, L., Garushyants, S. K., Ma, H., Simpson, D. J., Fedorovich, V., Cohen, M. F., Goryanin, I. (2015) Taxonomic and functional metagenomic analysis of anodic communities in two pilot-scale microbial fuel cells treating different industrial wastewaters. *Journal of Integrative Bioinformatics*, 12, 273.
98. Yang, Y., Xiang, Y., Sun, G., Wu, W.-M., Xu, M. (2015) Electron acceptor-dependent respiratory and physiological stratifications in biofilms. *Environmental Science & Technology*, 49, 196–202.
99. Ieropoulos, I., Greenman, J., Melhuish, C., Hart, J. (2005) Energy accumulation and improved performance in microbial fuel cells. *Journal of Power Sources*, 145, 253–256.
100. Wrighton, K. C., Thrash, J. C., Melnyk, R. A., Bigi, J. P., Byrne-Bailey, K. G., Remis, J. P., Schichnes, D., Auer, M., Chang, C. J., Coates, J. D. (2011) Evidence for direct electron transfer by a Gram-positive bacterium isolated from a microbial fuel cell. *Applied and Environmental Microbiology*, 77, 7633–7639.
101. Esteve-Núñez, A., Sosnik, J., Visconti, P., Lovley, D. R. (2008) Fluorescent properties of c-type cytochromes reveal their potential role as an extracytoplasmic electron sink in *Geobacter sulfurreducens*. *Environmental Microbiology*, 10, 497–505.
102. Hong, S. W., Kim, H. J., Choi, Y. C., Chung, T. H. (2008) Field experiments on bioelectricity production from lake sediment using microbial fuel cell technology. *Bulletin of the Korean Chemical Society*, 29, 2189–2194.

103. Tender, L. M., Reimers, C.E., Stecher III, H. A., Holmes, D. E., Bond, D. R., Lowy, D. A., Pilobello, K., Fertig, S. J., Lovley, D. R. (2002) Harnessing microbially generated power on the seafloor. *Nature Biotechnology*, 20, 821–825.
104. Tender, L. M., Gray, S. A., Groveman, E., Lowy, D. A., Kauffman, P., Melhado, J., Tyce, R. C., Flynn, D., Petrecca, R., Dobarro, J. (2008) The first demonstration of a microbial fuel cell as a viable power supply: powering a meteorological buoy. *Journal of Power Sources*, 179, 571–575.

#### 4.4. Kopsavilkums

Bioloģijas fakultātes pētnieki ciešā sadarbībā ar LU CFI Dr. phys. Jāni Kleperi un viņa grupu pētīja ūdeņraža (H<sub>2</sub>) mikrobioloģisku producēšanu tumsas fermentācijas reakcijās un uzkrāšanas iespējas hidrīdus veidojošos materiālos, konstruēja un pilnveidoja laboratorijas mēroga bioreaktorus, kā arī pētīja elektriskās enerģijas ieguvu, strādājot ar mikroorganismu degvielas šūnām (MBFC) jeb baktēriju baterijām.

Pētījumi parādīja, ka hidrīdus veidojoši materiāli – pallādijs (Pd) un sakausējumi AB<sub>2</sub>, AB<sub>5</sub> un LaNi<sub>5</sub> – ir izmantojami H<sub>2</sub> saistīšanai baktēriju *Escherichia coli* un *Klebsiella (Enterobacter) aerogenes* fermentācijas šķidrā fāzē. Kultivēšanas laikā novērota barotnes sastāvdaļu un baktēriju adsorbēcija uz materiālu daļiņām. LaNi<sub>5</sub> inhibējoši iedarbojās uz baktēriju augšanu un/vai metabolisma ceļiem, kuros veidojas H<sub>2</sub> un ogļskābā gāze (CO<sub>2</sub>), turpretim jaukta sastāva AB<sub>5</sub> sakausējuma pulvera (La, Ce, Nd un Pr pozīcijā A un Co, Mn un Al pozīcijā B) pievienošana barotnei ievērojami palielināja H<sub>2</sub> un CO<sub>2</sub> daudzumu. Vakuuma ekstrakcija un masspektrometrijas analīze pierādīja H<sub>2</sub> uzkrāšanos AB<sub>5</sub> pulverī. Pēc termogravimetrijas datiem, hidrīdus veidojošie materiāli pēc to H<sub>2</sub> sorbcijas kapacitātes fermentācijas šķīdumā ierindojās šādā secībā (no lielākās uz mazāko): Pd, AB<sub>5</sub>, AB<sub>2</sub> un LaNi<sub>5</sub>.

Pētīta baktēriju tīrkultūru un asociāciju spēja izmantot dažādus oglekļa barības avotus, tai skaitā ražošanas blakusproduktus, piemēram, jēlglicerīnu, lai producētu ūdeņradi. Izsekota dominējošo kultivējamo aerobo un anaerobo mikroorganismu sugu un grupu un metabolītu dinamika dažādos fermentācijas procesa režīmos. Hidrīdus veidojošu materiālu pievienošana kultivēšanas barotnei netraucēja glicerīna izmantošanu. Vienlaikus ar glicerīna koncentrācijas samazināšanos palielinājās baktēriju producētā H<sub>2</sub> daudzums.

Tika izstrādāts divkameru MBFC prototips, izmantojot jauna oglekļa materiāla elektrodus un pētot to biosaderību un efektivitāti. Ir novērtēta grafīta, grafēna un grafēna-PLA kompozīta elektrodu pielietojamība. Par substrātu izmantotas gan mikrobioloģiskās barotnes, gan dabiskas ezeru dūņas, par mikroorganismu avotu – baktēriju tīrkultūras un dūņu mikroorganismu asociācijas. No pētītajiem materiāliem maksimālo jaudas blīvumu uzrādīja 3D printēta grafēna-PLA kompozīts, kam bija arī labāka biosaderība nekā grafītam. Dūņām bija nepieciešams 24 h adaptācijas periods. MBFC ilgtermiņa darbība bija vieglāk kontrolējama, izmantojot ezera dūņas kā mikroorganismu avotu, nevis baktēriju tīrkultūras. Asociāciju papildināšana ar eksoelektrogēno baktēriju *Shewanella* sp. tīrkultūru neietekmēja MBFC darbības rezultātus.

Tika pētīta bioplēves veidošanās un tās sastāvā esošo mikroorganismu dzīvotspēja divkameru MBFC, kas darbojās dažādos elektriskās slodzes apstākļos ar ezera dūņām kā mikroorganismu un barības avotu. Dūņas saturēja daudz organisko vielu, ko raksturo liels ķīmiskais skābekļa patēriņš jeb COD, bet tajās bija maza mikroorganismiem viegli izmantojamu substrātu koncentrācija (mazs bioķīmiskais skābekļa patēriņš jeb BOD). Organisko vielu noārdīšanās (COD samazināšanās) visātrāk noritēja MBFC, kas darbojās

vislielākās elektriskās slodzes režīmā. Uz visu MBFC anodiem izveidojās bioplēves. Visblīvākā un noturīgākā bioplēve bija MBFC ar vislielāko slodzi, bet vismazākā – MBFC, kura bija atvērtas elektriskās ķēdes režīmā (bez slodzes).

Dzīvo un bojāgājušo baktēriju fluorescentās iekrāsošanas un kolonijas veidojošo vienību (kvv) noteikšanas rezultāti ļāva novērtēt anoda bioplēves veidojošo baktēriju dzīvotspēju. Kultivējamo baktēriju daudzums līdzīgi palielinājās uz visu MBFC anodiem un pēc sešām nedēļām sasniedza 4.8–5.6 log kvv/cm<sup>2</sup>. Anodu bioplēvēs dominējošās kultivējamās baktērijas piederēja pie *Bacteroidetes*, *Firmicutes* un *Actinobacteria* tipiem. Netika konstatētas nozīmīgas atšķirības starp baktēriju dzīvotspēju dažādu MBFC anolītos (anoda kamerās), bet anodu bioplēvēs vairāk dzīvo baktēriju bija lielas slodzes apstākļos nekā bez ārējas elektriskās slodzes. Arī COD samazināšanās norādīja uz lielāku bioloģisko aktivitāti lielas slodzes gadījumā. To var izskaidrot ar anoda kā papildu elektronu akceptora pieejamību. Rezultāti liecina, ka MBFC ir jādarbojas ar maksimālu slodzi, lai nodrošinātu optimālu bioremediāciju.

Nogulšņu jeb bentosa MBFC ir īpašs MBFC veids, ko var izmantot enerģijas ieguvei dabiskās ūdenstilpēs. Tas nozīmē, ka anods ir novietots, piemēram, dīķa, ezera vai jūras nogulumos, bet katodu novieto augšējā ūdens slānī, lai tam piekļūtu atmosfēras skābeklis. Elektroenerģija rodas no mikroorganismu katalizētās nogulsnēto organisko oglekļa savienojumu oksidēšanas. Mūsu grupa, Artūrs Gruduls un kolēģi sadarbībā ar māksliniekus Rasu Šmiti un Raiti Šmitu (jauno mediju kultūras centrs RIXC) 2014. gadā izveidoja instalāciju “Dīķa baterija” LU Botāniskajā dārzā. Šī baterija sastāvēja no sešām MBFC un darbojās gan vasarā, gan ziemā. Ir noskaidrots, ka bentosa MBFC var darboties vairākus gadus bez jaudas samazināšanās.

## 5. Nanostructured materials and their thin films for Li-ion battery electrodes: synthesis, research and performance

### Nanostrukturēti materiāli un to plānās kārtiņas Li-jonu bateriju elektrodiem: sintēze, pētījumi un darbība

Gints Kučinskis, Kaspars Kaprāns, Gunārs Bajārs

Institute of Solid State Physics, University of Latvia, Ķengaraga iela 8, Rīga, LV-1063, Latvia  
E-mail: [gunars.bajars@cfi.lu.lv](mailto:gunars.bajars@cfi.lu.lv)

#### Contents

5. Nanostructured materials and their thin films for Li-ion battery electrodes: synthesis, research and performance. . . . .	101
5.1. Review of materials for Li-ion battery electrodes. . . . .	101
5.2. Methods for synthesizing materials and obtaining thin/thick films used in this research. . . . .	102
5.3. Characterization methods of synthesized materials and devices. . . . .	103
5.4. Thin film LiFePO <sub>4</sub> cathodes for Li ion batteries: characterisation, structure and composition, electrochemical properties. . . . .	104
5.5. Electrophoretically deposited graphene and $\alpha$ -Fe <sub>2</sub> O <sub>3</sub> /TiO <sub>2</sub> /GO anode for lithium ion batteries. . . . .	111
5.5. Summary. . . . .	119
5.6. References. . . . .	119
5.7. Kopsavilkums. . . . .	122

#### 5.1. Review of materials for Li-ion battery electrodes

After commercialization of Li-ion battery with metallic lithium anode and numerous self-ignition cases in hands of consumers, carbon-based anode for rechargeable batteries has been the preferred choice for the anode [1]. Here, carbon porous/layered structures are reversibly absorbing/desorbing lithium ions at low electrochemical potentials. Graphite can intercalate one Li atom per carbon ring:  $\text{Li}^+ + \text{e}^- + \text{C}_6 \rightarrow \text{LiC}_6$  corresponding to 372 mAh/g theoretically (comparing to about 3800 mAh/g for Li metal). Li can intercalate at an even higher capacity with some amorphous carbons, corresponding to a stoichiometry of LiC<sub>3</sub>. Therefore, by replacing Li metal anodes with carbon nanomaterials in Li batteries, there is a 90% decrease of anode capacity, but the advantages are an increased stability and a prolonged cycle life [2].

The most important cathode materials for commercially available Li-ion batteries are layered oxides with 3.4–4 V potential (versus Li electrode) LiCoO<sub>2</sub>, as well as LiMn<sub>2</sub>O<sub>4</sub> [3], LiFePO<sub>4</sub> [4] and LiMn<sub>x</sub>Li<sub>y</sub>Co<sub>z</sub>O<sub>2</sub> [5] with practically achievable capacities of 150, 120, 155 and 160 mAh/g, respectively.

As a rule, the electrodes are formed by mixing active material with various nanostructured carbon materials to improve the electrical and heat conductivities, as well as mechanical strength. In the last few decades, the number of the research articles on “nanostructured carbon materials” has grown exponentially. Nanoporous carbon materials (NCM) can be classified as various carbon allotropes in 0D (amorphous carbon black and graphitized carbon black), 1D (polymer chains), 2D (graphene) and 3D (diamond) scale. There are up to 100 review articles about their research in different applications (see, for example, [1, 6]). By assembling carbon nanomaterials with functional metal or oxide nanocrystals, composites with new functions in electrical, physical, or chemical properties are obtained. In this chapter our research results have been summarized based on the publications [1, 7–9] about the role and properties of nanostructured carbon materials in lithium ion batteries, electrodes for supercapacitors and hydrogen storage materials.

## 5.2. Methods for synthesizing materials and obtaining thin/thick films used in this research

A thin film is a thin layer of material, which has been obtained by depositing single atoms, molecules or ions [10]. A thin film is different from a thick film, which is obtained by reducing the size of a thick material or depositing readily-made grains or big clusters of atoms, molecules and ions. There are chemical and physical thin film deposition techniques. Physical techniques include mechanical, electromechanical or thermodynamic processes, while chemical thin film deposition techniques usually involve a liquid precursor that forms a thin solid film as a result of a chemical reaction or indifferent solution with dispersed nanopowder of material. The most popular physical thin film deposition techniques are physical vapour deposition (resistive, inductive, electron beam, pulsed laser, arc-discharge, etc.) and sputtering techniques (direct current, alternating current, impulse, etc.). The most typical thick film growth techniques include electrochemical anodation and deposition, electrophoretic deposition, spray pyrolysis, electrostatic spinning, spin coating and more. Below, we will describe the methods used in this study in greater detail. The thickness of the films was evaluated by using a Veeco Dektak 150 profilometer.

**Pulsed laser deposition (PLD)** is based on a target located in a vacuum chamber being irradiated with a high energy pulsed laser. As a result, the target atoms are being excited. Target ablation, surface exfoliation and plasma formation take place [11]. The products of pulsed laser – target interaction form a directed flow of particles towards the substrate. Part of the particles are deposited on the substrate and form a thin film. This technique is relatively easy to optimize and therefore is very popular for scientific purposes. In this research [9], pulsed laser deposition (PLD) ArF excimer laser with a wavelength of 248 nm was used for LiFePO<sub>4</sub> thin film deposition by PLD. The energy of the laser beam in front of the lens of the vacuum chamber was 70–90 mJ, the area of the target irradiated by the laser – 4.5 mm<sup>2</sup>. Laser frequency – 5 Hz, pulse length – 25 ns. The target material was LiFePO<sub>4</sub> tablet that was prepared as described before. The initial vacuum in the vacuum chamber was 3·10<sup>-6</sup> mBar. The chamber was then filled with argon to a pressure of 0.2 mBar, gas flow – 3 sccm/s. During the thin film deposition, the target rotation speed was 0.5 Hz. Before the thin film deposition, the target was pre-ablated with 600 laser pulses. During the thin film deposition, the substrate temperature was 500–530 °C. Thin films were deposited on Nb doped SrTiO<sub>3</sub> (Nb:STO) monocrystals, Nb content – 0.5 wt.%, polished from one side, crystallographic orientation (100), size: 5 × 5 mm.

**Magnetron sputtering** is another popular physical vapour deposition technique [10]. Contrary to PLD, magnetron sputtering can easily be used to coat large surfaces. The technique is based on collisions between an inert gas and a target, which is made either from a pressed powder or a monolithic metal or alloy. We used a device made by Sidrabe, Inc. in direct current (DC) or radio frequency (RF) modes. Thin  $\text{LiFePO}_4$  films were obtained in RF mode with frequency 13.56 MHz and discharge power 300 W. Target was prepared by pressing  $\text{LiFePO}_4$  powder (two different materials were used – synthesized at Institute of Inorganic Chemistry (RTU) and commercial powder obtained from Linyi Gelon (New Battery Materials Co.) with 3.9 mPa pressure. The diameter of the target – 15 cm, distance between the target and substrate in sputtering chamber – 15 cm. Before deposition a pressure of  $5 \cdot 10^{-5}$  mBar was obtained in the vacuum chamber. Argon was used as a sputtering gas, the target was presputtered for at least 10 min. In some cases, substrate was heated to 500 °C. Thin films were deposited on stainless steel, silicon monocrystals and glass substrates. In some cases, thin film recrystallization for 1 h at 600 °C in Ar was performed.

**Electrophoretic deposition (EPD).** EPD method is a highly beneficial, low-cost and eco-friendly technique for the preparation of required films and multi-layer coatings [8, 11]. For the electrophoretic growth two  $3 \times 3 \text{ cm}^2$  stainless steel (grade 316) electrodes were used. Distance between electrodes was 1 cm. A constant voltage of 100 V was applied between the electrodes by DC Power Supply (Agilent Technologies N5772A) and held for 10 min. EPD ensures colloidal particle deposition on substrate from electrically conductive electrolyte, in this case isopropanol. The process begins when applied electric field makes dispersed colloidal particles migrate to the electrode, where particles stay intact after losing charge. The deposited coatings were gradually heated (5 °C/min) and annealed at 500 °C for 2 h.

### 5.3. Characterization methods of synthesized materials and devices

**Analysis of material composition, structure and morphology.** The structure of research materials was analysed by XRD (Cu K $\alpha$  radiation), morphology was studied by two different SEM (table-top device Phenom Pro; Zeiss Merlin; Tescan Lyra). Atomic force microscopy (AFM) was used in a contact mode, silicon needle with a radius smaller than 10 nm was used. Thin film thickness was determined by breaking the thin film and analysing the cross-section by SEM or by a focused ion beam (FIB) – gallium ions were used to etch a part of the thin film, the cross-section was then studied by SEM. To determine composition of samples the EDAX (Eagle 3) XRF spectrometer was used. Sample excitation by X-rays (Rh tube) focused by poly capillary fibre lens, minimum spot size 50 microns (fwhm). Energy dispersive liquid N<sub>2</sub>-cooled Si detector with Be window, suitable for detecting of XRF of chemical elements ranging from Na to U. The composition of selected samples was analysed by ICP-OES. Thin film stoichiometry on the surface and in the bulk of the thin film was analysed by secondary ion mass spectroscopy (SIMS) by using 15 keV Ga<sup>+</sup> ion gun. Selected samples (powders, thin films) were studied by X-ray photoelectron spectroscopy (XPS, PHI 5000 Versaprobe) the spectra were obtained in a vacuum chamber with a pressure under  $2 \cdot 10^{-10}$  Torr by using Al K $\alpha$  X-rays with 1486.6 eV energy.

From spectroscopical methods to determine the structure, Raman spectroscopy was used (Renishaw InVia instrument with green laser (514 nm, max power 20 mW), objective  $\times 100$ , laser power used 100%, 30–4000  $\text{cm}^{-1}$  exposure time 10 s; red laser (633 nm, max power 12.5 mW) objective  $\times 100$ , laser power used 100%, 30–4000  $\text{cm}^{-1}$  exposure time 10 s).

**Electrochemical measurements.**  $\text{LiFePO}_4$  thin film electrodes were measured in Swagelok-type two electrode electrochemical cells with a metallic lithium counter

electrode that was at the same time used also as a reference electrode. 1 M  $\text{LiPF}_6$  in ethylene carbonate (EC) and dimethyl carbonate (DMC) in volume ratio 1 : 1 was used as an electrolyte. Whatman GF/F glass microfiber separator was also used. Electrochemical impedance spectroscopy for  $\text{LiFePO}_4$  thin films deposited with magnetron sputtering was carried out in a cell containing 1 M  $\text{LiClO}_4$  in propylene carbonate as an electrolyte. Electrochemical cells were assembled in an argon-filled glove box. Electrochemical measurements were carried out with potentiostat Voltalab PGZ-301 and Solartron 1287A in combination with frequency analyser Solartron 1255. For  $\text{LiFePO}_4$  thin films deposited by PLD, the electrolyte used was 1 M  $\text{LiPF}_6$  in EC and diethylene carbonate (DEC) in volume ratio 1 : 1. Celgard 2500 polypropylene (PP) separator was also used. Electrochemical cells were assembled in an argon-filled glove box with  $\text{O}_2$  and  $\text{H}_2\text{O}$  content lower than 1 ppm. Electrochemical measurements were performed by using potentiostats Voltalab PGZ-301, Voltalab PGZ-402, Autolab PGSTAT101 and Solartron 1287A in combination with frequency analyser Solartron 1255.

#### 5.4. Thin film $\text{LiFePO}_4$ cathodes for Li ion batteries: characterisation, structure and composition, electrochemical properties

$\text{LiFePO}_4$  is one of the most researched lithium ion battery cathode materials and considered to be a model material that serves to understand many basic phenomena taking place in lithium insertion materials. The prospects of improving the  $\text{LiFePO}_4$  electrodes is still being actively studied [12–16]. However, several fundamental properties of the material, such as its particle-by-particle (de)lithiation behavior and phase-separation within the  $\text{LiFePO}_4$  have remained elusive [12]. This chapter is based on ref. [9] and for more details the reader can be referred to the said work.

##### Thin films deposited by pulsed laser deposition

The XRD analysis of the prepared PLD target (Fig. 5.1.) indicates that the material is pristine  $\text{LiFePO}_4$ . This is additionally confirmed by ICP-OES measurements which corroborate that the target material is stoichiometric  $\text{LiFePO}_4$  within the margin of error.

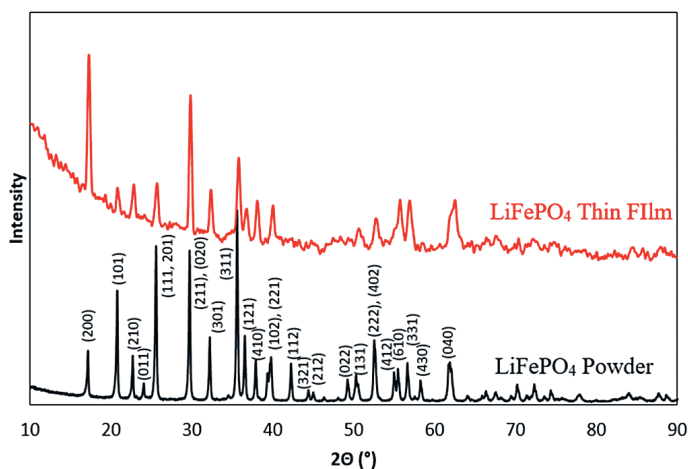


Figure 5.1. XRD pattern of  $\text{LiFePO}_4$  powder and thin film deposited with PLD.

The XRD data for the obtained  $\text{LiFePO}_4$  thin films also display only peaks characteristic to  $\text{LiFePO}_4$ . ICP-OES results show stoichiometry  $\text{Li}_{0.94}\text{Fe}_{1.01}\text{P}_{0.99}\text{O}_{3.96}$ , indicating a slight lithium loss during the thin film deposition.

The SEM images of the thin films (Fig. 5.2) indicate that the obtained thin films are composed of longitudinal particles with an average diameter of 5  $\mu\text{m}$ . These particles are composed of smaller grains with diameter of 50–500 nm as shown in Fig. 5.2. (b). The color of the grains in Fig. 5.2 is different due to variations in the crystallographic orientations. A few cracks can also be observed. Most likely, they are formed as a result of the substrate heating due to different thermal expansion coefficients of Nb:STO and  $\text{LiFePO}_4$  [17–19].

Cross-sections of  $\text{LiFePO}_4$  thin films can be seen in Fig. 5.2. (c) and (d). They indicate that the thin film is dense, with no significant pores and with a smooth surface. This is also confirmed by AFM. The roughness analysis by using AFM indicates the actual surface and projected surface of the sample to differ by only 2%. Thin film deposition rate was determined to be 200 nm/h.

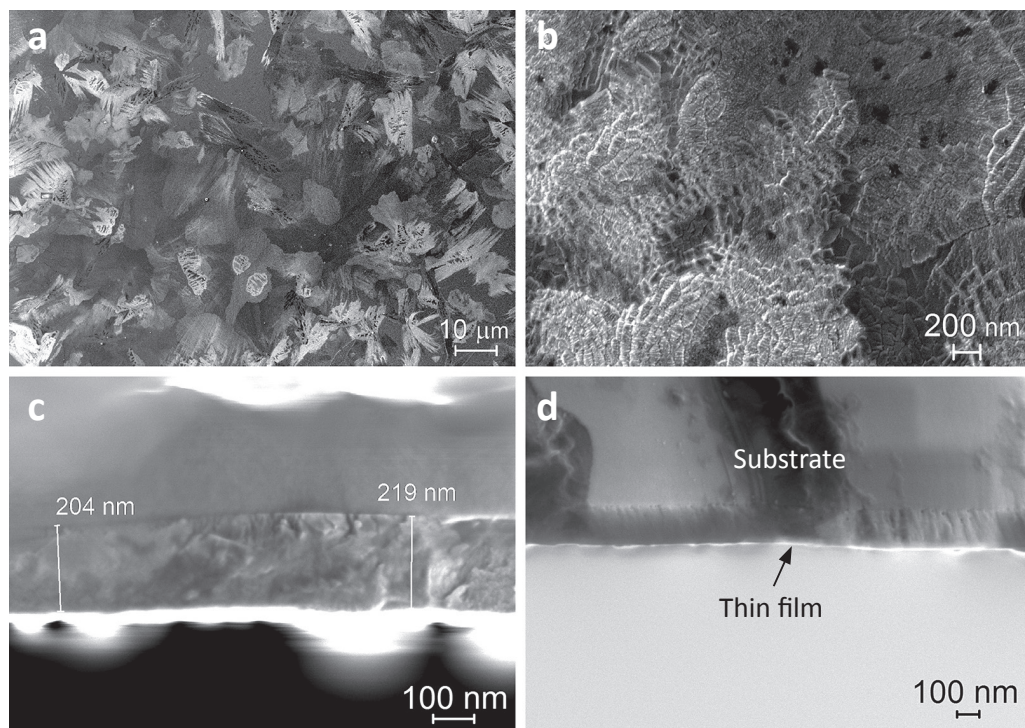


Figure 5.2.  $\text{LiFePO}_4$  thin film SEM (a), (b) surface and (c), (d) cross-section images

The discharge capacities of the obtained thin films are up to 118 mAh/g for the 100 nm thin film and slightly less for thicker thin films (see Fig. 5.3). 118 mAh/g constitute around 70% of the 170 mAh/g theoretical capacity of  $\text{LiFePO}_4$ . The capacities are very high when compared with other  $\text{LiFePO}_4$  thin film studies [20–30]. All electrochemical measurements have been performed in two electrode electrochemical cells that were modified in order to avoid undesired side reactions connected with the electrolyte decomposition. At sufficiently small mass of active material the signal from such side reactions becomes significant.

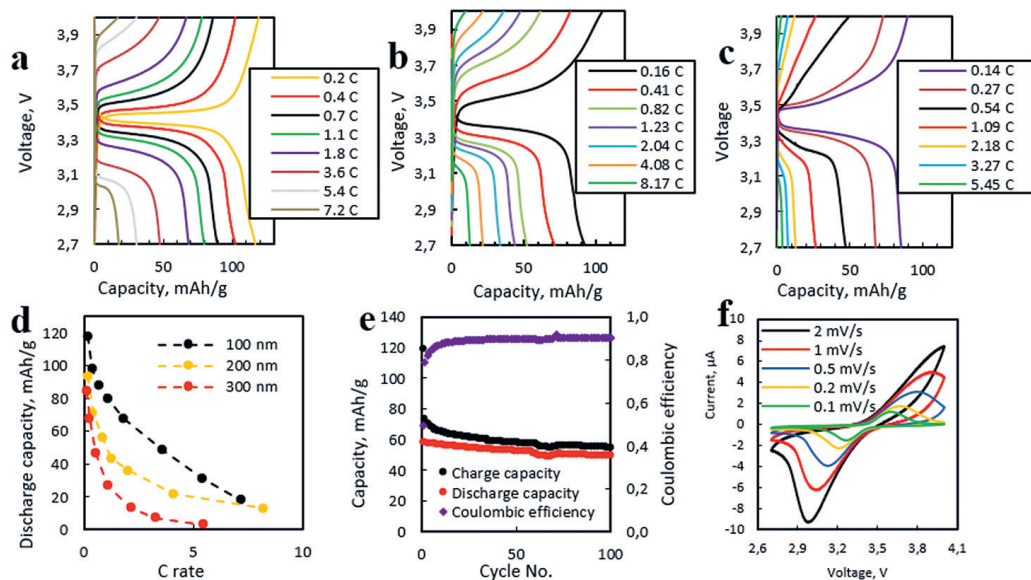


Figure 5.3. Galvanostatic charge and discharge experiments for: (a) 100 nm, (b) 200 nm and (c) 300 nm thick  $\text{LiFePO}_4$  thin films; (d) rate capabilities, (e) cyclability of a 200 nm thin film, (f) cyclic voltammetry curve, 1 C = 170 mA/g

The cyclability of the obtained  $\text{LiFePO}_4$  thin films is very good – 85% of the initial discharge capacity of a 200 nm thin film is retained after 100 charge and discharge cycles at 0.7 C rate (Fig. 5.3 (e)). Cyclic voltammetry (CV) curves display the peaks characteristic to lithium insertion and extraction (Fig. 5.3 (f)).

Electrochemical impedance spectroscopy (EIS) was performed for several  $\text{LiFePO}_4$  thin films – see Fig. 5.4 (b). The charge transfer resistance increases with increasing  $\text{LiFePO}_4$  thin film thickness, and the values of the charge transfer resistance are close to those of the expected electronic resistance of the thin film.

By using EIS and galvanostatic intermittent titration technique (GITT), the effective chemical diffusion coefficients of  $\text{LiFePO}_4$  thin films were determined. Their values can be seen in Fig. 5.4. (b) and (c). For stoichiometries that are close to  $\text{Li}_{0.5}\text{FePO}_4$ , the effective chemical lithium diffusion coefficient  $D_{\text{Li}}$  is approximately  $10^{-17}$   $\text{cm}^2/\text{s}$ . At higher and lower lithium concentrations the determined diffusion coefficients are larger. The effective chemical diffusion coefficients of lithium calculated from GITT data in intermediate states of charge are approximately  $10^{-17}$   $\text{cm}^2/\text{s}$  and  $10^{-16}$   $\text{cm}^2/\text{s}$  for calculations done by using charge and discharge data, respectively. The diffusion coefficients calculated from charge and discharge measurements differ because the thin film de-lithiation process has larger resistance (higher overvoltage) due to the electronic conductivity of  $\text{FePO}_4$  being lower than for  $\text{LiFePO}_4$  [31]. Additionally, since the thin film was deposited in a stoichiometry that is close to  $\text{LiFePO}_4$  (and not  $\text{FePO}_4$ ), during de-lithiation additional mechanical strains can develop, thus hindering lithium transport in the de-lithiated state. Diffusion coefficients calculated both from EIS and GITT data are close and also in agreement with the values determined from the CV curves by using Randles – Sevcik equation ( $10^{-18}$ – $10^{-17}$   $\text{cm}^2/\text{s}$ ).

Interpreting the calculated effective chemical diffusion coefficients, one has to take into account that, firstly, the model which is used for calculation of  $D_{Li}$  assumes that all particles are lithiating and de-lithiating at the same time, which might not be the case with  $LiFePO_4$  [32]. Secondly, the aforementioned methods for calculating  $D_{Li}$  are intended for solid solutions and not for two-phase materials such as  $LiFePO_4$ . Therefore, the change in the free energy that comes from the separation of lithium rich and lithium poor phases is not taken into account [33]. Due to aforementioned reasons, the calculated results are called effective (or apparent) chemical diffusion coefficients, and they characterize not only the diffusion but also the overall lithium kinetics in the  $LiFePO_4$  electrode.

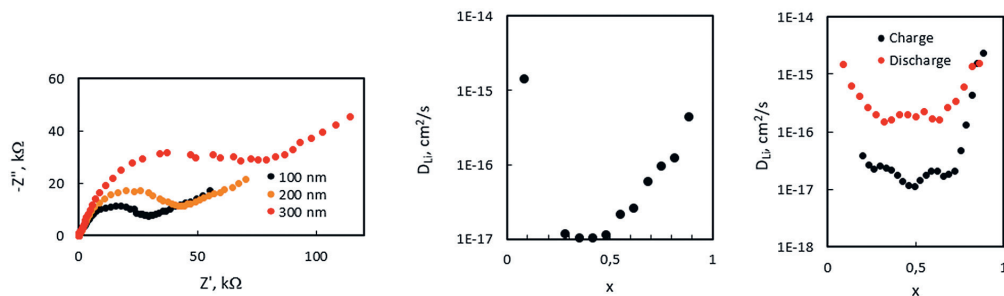


Figure 5.4. (a) EIS results for  $LiFePO_4$  thin films with various thicknesses; effective chemical lithium diffusion coefficients for a 200 nm  $LiFePO_4$  thin film obtained by using (b) EIS and (c) GITT

### Thin films deposited by magnetron sputtering

The  $LiFePO_4$  thin films deposited by radio frequency magnetron sputtering are also composed of crystalline  $LiFePO_4$ . Fig. 5.5 shows SEM images of  $LiFePO_4$  thin films obtained by magnetron sputtering. Distinct grains can be observed in the thin film with a size of 1–10  $\mu m$ . Although the grains are packed densely, grain boundaries can be clearly distinguished. No cracks are formed during the deposition, the surface adhesion is sufficient for the thin film to adhere to the substrate.

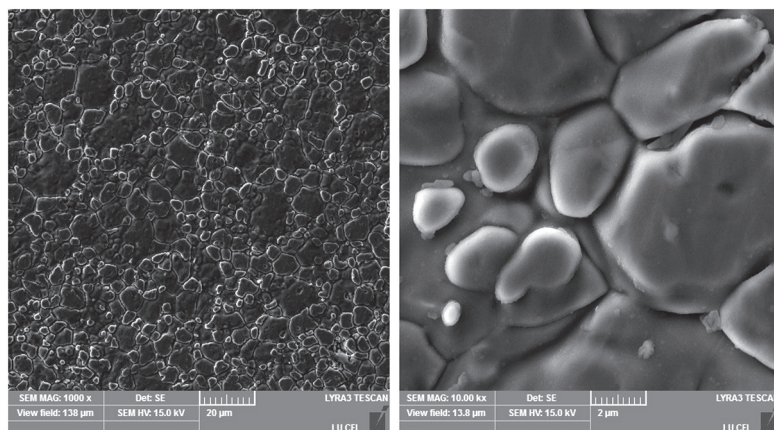


Figure 5.5. SEM images of  $LiFePO_4$  thin films obtained by magnetron sputtering

CV curves in Fig. 5.6. (a) indicate that the best electrochemical properties can be obtained by annealing the thin film after its deposition. Annealing is important because the particles reaching the substrate during the deposition may not have sufficient energy to form ordered crystalline structures. The obtained capacities are up to 61 mAh/g at 0.1C rate (17 mA/g) for a 1000 nm film (see Fig. 5.6. (b)). The capacities measured at higher charge and discharge rates are 30 mAh/g at 0.2 C, 19 mAh/g at 0.3 C and 10 mAh/g at 1 C.

Effective chemical diffusion coefficients of lithium are shown in Fig. 5.6. (c). The determined diffusion coefficients are by several orders of magnitude higher than the ones obtained for thin films deposited by PLD. However, these values are also in agreement with those reported in literature (in the range of  $10^{-18}$  to  $10^{-10}$  cm<sup>2</sup>/s [20, 34–36]). It must be noted again that the values of effective chemical diffusion coefficients are determined not only by lithium diffusion, but also by differences in electrode morphology, grain structure and composition.

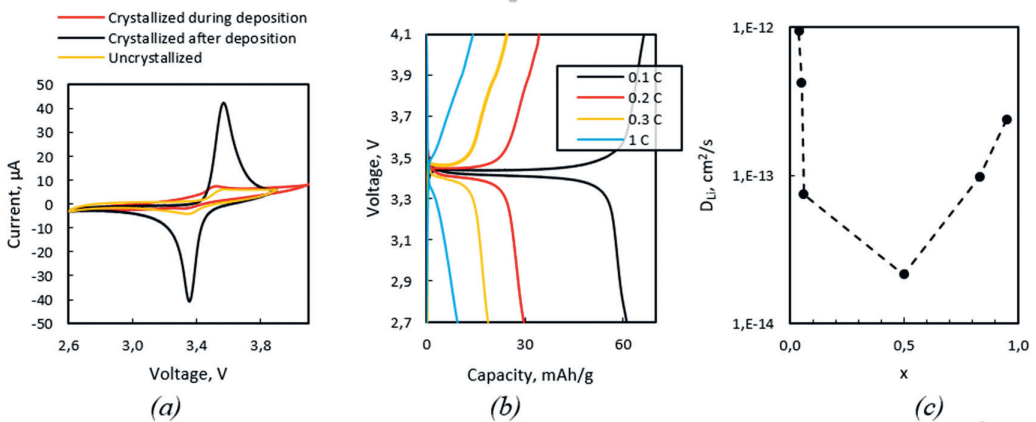


Figure 5.6. (a) CV curves for various  $\text{LiFePO}_4$  thin films ( $v = 1$  mV/s), (b) galvanostatic charge and discharge curves for 1000 nm thin film,  $1\text{ C} = 170$  mA/g, (c) effective chemical diffusion coefficient of lithium in a  $\text{LiFePO}_4$  thin film at various states of charge

### Sequential particle charging and discharging in $\text{LiFePO}_4$ thin films

Measurements of voltage hysteresis were performed for  $\text{LiFePO}_4$  thin films deposited by PLD. The measurements are based on a galvanostatic charge and discharge experiments in a limited charge interval. Open circuit voltage (OCV) is being measured between galvanostatic measurements. Voltage hysteresis measurements for  $\text{Li}_x\text{FePO}_4$  were conducted in the lithium concentration range  $0.1 < x < 0.9$ , where  $\text{LiFePO}_4$  is expected to separate in lithium-rich and lithium-poor phases. The experimental procedure is schematically shown in Fig. 5.7. The measurement cycle demonstrated in the figure was repeated several times, the low currents used for hysteresis measurements were varied.



Figure 5.7. Experimental procedure for a single voltage hysteresis measurement

Voltage hysteresis measurements were conducted with four  $\text{LiFePO}_4$  thin film samples. Sample LFP-H1 is 100 nm thick, LFP-H2 and LFP-H3 – 200 nm thick, LFP-H3L is the thin film from batch LFP-H3 coated with a 400 nm thick LiPON layer. The electrochemically active mass of the thin films were normalized based on their rate capabilities. Voltage hysteresis graphs and Butler – Volmer type dependence or overvoltage versus current are shown in Fig. 5.8.

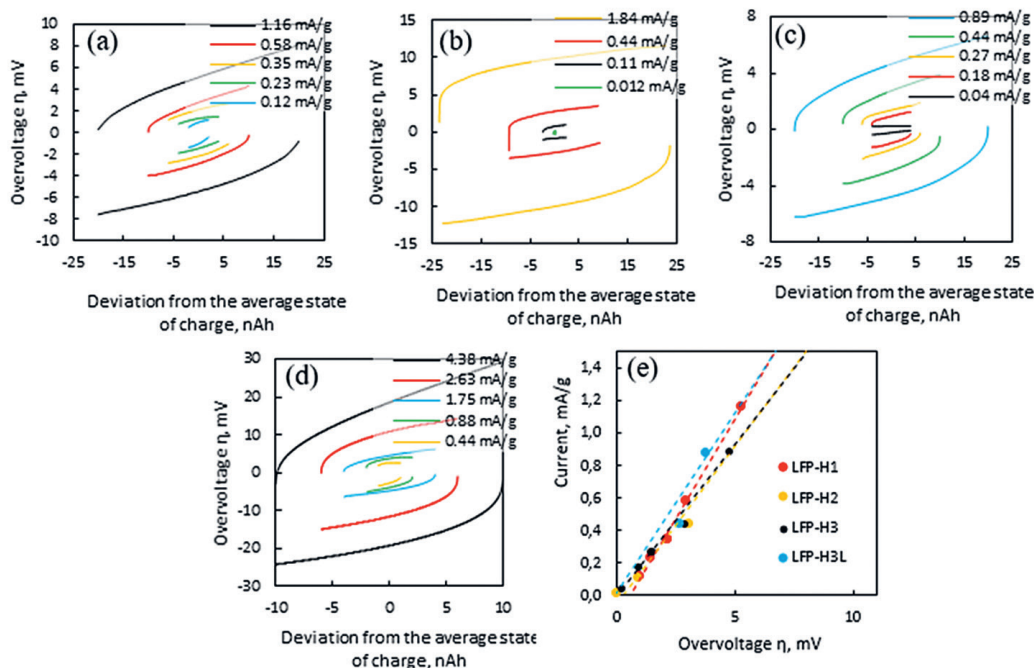


Figure 5.8. Voltage hysteresis obtained at several currents for samples (a) LFP-H1, (b) LFP-H2, (c) LFP-H3, (d) LFP-H3L; (e) Butler – Volmer type dependence between overvoltage and specific currents

The results indicate that, if 1–5% galvanostatic charge and discharge would be performed at intermediate SOC with infinitely low currents, there would be no voltage hysteresis or the observed voltage hysteresis would be extremely small. Even if voltage and current dependence at very small currents cannot be fitted with a linear line, there are still several data points indicating voltage hysteresis below 2 mV, which is at least an order of magnitude lower than reported in literature for  $\text{LiFePO}_4$  bulk material [37].

The results contradict the expectations according to the current model, which predicts a non-vanishing voltage hysteresis due to non-monotonic lithium chemical potential – concentration dependence and sequential particle charging and discharging [37]. The disappearance of voltage hysteresis indicates that the sequential charging and discharging of  $\text{LiFePO}_4$  particles in thin film can occur in a significantly different way than in bulk material. It is suspected that (de)lithiation could take place via a solid solution route, where instead of two phases (lithium-rich  $\text{Li}_{1-x}\text{FePO}_4$  and lithium-poor  $\text{Li}_y\text{FePO}_4$ ) only single phase  $\text{Li}_x\text{FePO}_4$  is present with lithium distributed relatively homogeneously throughout the

thin film. This is feasible, since the grains in a thin film are tightly packed and they are not separated by a layer of carbon coating or electrolyte, and thus mass transfer between the grains can take place more efficiently. It must be noted that the voltage hysteresis measurements were performed within a relatively narrow state-of-charge range where on average amount of lithium corresponding to about 1% of the total capacity is removed and inserted in the  $\text{LiFePO}_4$  thin film electrode.

Two more electrochemical phenomena have been observed for  $\text{LiFePO}_4$  thin films. Firstly, at the first galvanostatic charging curve of a  $\text{LiFePO}_4$  thin film an uncharacteristically high local electric potential maximum can be observed (see Fig. 5.9. (a)). Secondly, the memory effect has been observed in  $\text{LiFePO}_4$  thin film, the results are shown in Fig. 5.9. (b), (c) and (d). The reader can learn more about the origins of the memory effect in the reference [37].

A precondition to being able to observe the memory effect (Fig. 5.9. (b), (c) and (d)) is the fact that a sequential particle-by-particle (de)lithiation takes place. The experimental procedure for memory effect measurements is shown in Fig. 5.10.

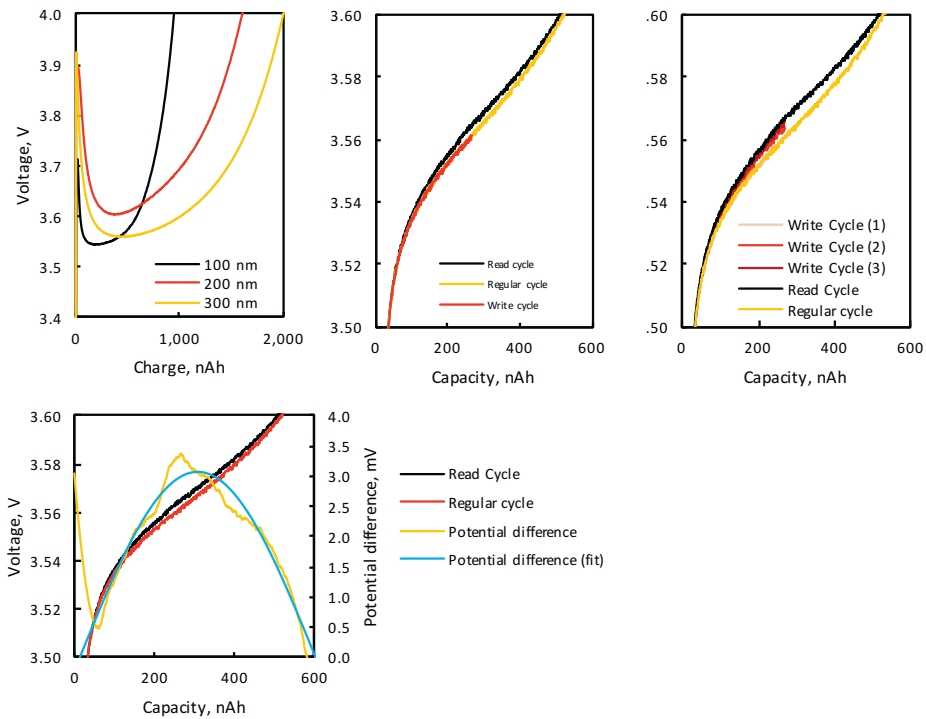


Figure 5.9. Electrochemical effects observed in  $\text{LiFePO}_4$  thin films: (a) a local maximum of the electric potential at the beginning of the charge (200 nA current), (b) and (c) memory effect with one and three write cycles and (d) potential difference due to the memory effect

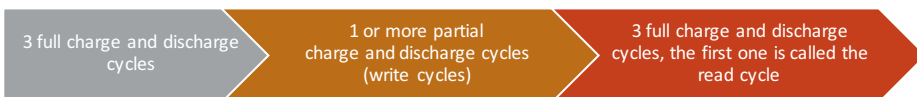


Figure 5.10. The experimental procedure for memory effect measurements

The memory effect [37] is thought to arise when during a partial charge and discharge cycle only a part of the electrode is being (de)lithiated. After this partial charge and discharge cycle, some particles of the electrode are in a metastable state which leads to an increased electrode overpotential during a part of the next full charge or discharge. When comparing the results obtained for thin films with those seen for bulk material, the overpotential in the read cycle is more stretched out and not as localized as for bulk electrodes. This is likely explained by the different electrode of the thin film as compared to the bulk electrode.

Although slight voltage maximum has been observed for bulk materials before [37–41], it has never been as pronounced as in  $\text{LiFePO}_4$  thin films obtained in this work (Fig. 5.9 a). We hypothesize that this is due to increased mechanical strain in the thin film when compared to the bulk material.

### 5.5. Electrophoretically deposited graphene and $\alpha\text{-Fe}_2\text{O}_3/\text{TiO}_2/\text{GO}$ anode for lithium ion batteries

Graphite is commonly used as an anode material for LIBs because of its high columbic efficiency, acceptable specific capacity and cyclic performance by forming intercalation compounds  $\text{LiC}_6$  [42]. However theoretical specific capacity of graphite is  $372 \text{ mAh}\cdot\text{g}^{-1}$  because of the limited Li-ion storage sites within the  $\text{sp}^2$  carbon structure [43]. One alternative to graphite has recently been reported – graphene nanosheets (GNS) obtained by various fabrication routes [7, 44]. Electrophoretic deposition (EPD) is an economical and versatile processing technique that has been applied for deposition of coatings and films. It has many advantages in the preparation of thin films from suspensions, such as high deposition rate and throughput, good uniformity and controlled thickness of the obtained films, no need of binders, and simplicity of scaling up [45]. Fabrication of graphene and CNT/graphene composite nanosheets by electrophoretic deposition technique was demonstrated before [45, 46]. However, the specific capacity values of graphene nanosheets obtained by EPD using a suspension in isopropanol have been dramatically reduced after the first discharge. In this study, the direct EPD method is used to prepare free standing porous graphene sheets from a suspension of graphene oxide (GO) in water, followed by a thermal reduction of as-deposited multilayers.

Among various transition metal oxides, hematite ( $\alpha\text{-Fe}_2\text{O}_3$ ) is among the most promising anode materials because of its non-toxicity, excellent stability and low cost [47, 48]. The incorporation of metal oxide nanoparticles will produce a porous network, and make excellent electron-conducting pathways. Hence, the nanostructured metal oxides loaded onto graphene can act as spacers to prevent the re-stacking of anode material layers during charge/discharge process. Therefore, graphene–metal oxide composites become an attractive issue to increase the cycling performance and rate capabilities of LIBs [48]. Among the transition metal oxides iron oxide, especially hematite ( $\alpha\text{-Fe}_2\text{O}_3$ ), is environmentally friendly and widely available, and an important industrial product. As the most stable iron oxide,  $\alpha\text{-Fe}_2\text{O}_3$  has been widely investigated in the fields of gas sensors, catalysis, energy storage, etc. [48, 49].

$\text{TiO}_2$  has been studied for application in large-scale energy storage because it is a high-capacity and high-current rate tolerance material [8, 50, 51]. It has various nanostructure forms, such as nanorods, nanotubes, nanofibers and nano squares. However, low electronic conductivity and relatively low theoretical capacity ( $380 \text{ mAhg}^{-1}$ ) limit the applications of  $\text{TiO}_2$ . In addition,  $\text{TiO}_2$  nanostructures collapse after electrochemical cycling, causing decreased charge capacity.

The use of nanostructured TiO<sub>2</sub>-based materials may be an efficient approach to deal with the main problems of Li-ion batteries [50, 51].

Practical applications of TiO<sub>2</sub> in LIBs are limited by poor electrical conductivity and low chemical diffusivity of lithium – key factors for lithiation insertion in electrode materials. Therefore, it is highly desirable to develop new strategies for improve lithium kinetics in TiO<sub>2</sub>. There have been some research efforts in developing TiO<sub>2</sub> based nanomaterials for high performance energy conversion and storage devices [51]. Here, we report a novel  $\alpha$ -Fe<sub>2</sub>O<sub>3</sub>/TiO<sub>2</sub>/graphene oxide composite anode prepared by electrophoretic deposition.

### Fabrication of graphene sheet and metal oxide composite electrodes

Water suspension of graphene oxide was used for electrophoretic deposition of films under potentiostatic mode. GO was dispersed in de-ionized water at the concentration 10 mg·mL<sup>-1</sup> and diluted to the concentration 1 mg·mL<sup>-1</sup> afterwards. Before the EPD process GO suspension was sonicated for 1 h in order to ensure homogenous dispersion. Electrodes used for EPD process were 1 mm thick 316 stainless steel substrates with a size of 1 × 4 cm. The distance between the two electrodes was 10 mm, and the applied electric field was 30 V·cm<sup>-1</sup> (DC power supply Agilent Technologies N5772A). Under the applied voltage, the negatively charged graphene oxide particles migrated toward the positive electrode and were subsequently orderly deposited on it. Thermal reduction of as-deposited GO films was performed by heating at 700 °C in argon/hydrogen flow (Ar: H<sub>2</sub> volume ratio – 95 : 5). The thickness of the graphene films was tuned ranging from several nanometers to a few micrometers by varying the deposition conditions, including the concentration of graphene oxide, the applied voltage, and the deposition time.

Composites of two metal oxides,  $\alpha$ -Fe<sub>2</sub>O<sub>3</sub> and anatase phase TiO<sub>2</sub> with a particle diameter 50 nm and 21 nm respectively (Sigma-Aldrich) were dissolved in 20 ml graphene oxide water suspension (BGT Materials, concentration 1mg/ml, flake size 1–20  $\mu$ m). Electrophoretic deposition under potentiostatic mode was performed. Mass ratio of materials was 16.4 mg of  $\alpha$ -Fe<sub>2</sub>O<sub>3</sub> and 8.2 mg of TiO<sub>2</sub>. Metal oxide powder before suspension was prepared and mixed in a ball mill (Retsch MM 200) for 20 minutes at 30 Hz. In order to obtain homogenous dispersion before EPD process, the suspension was sonicated one hour.

In order to apply electrodes within coin-type electrochemical cell thin film was electrophoretically deposited on a flat stainless steel discs (1 mm thick and 10 mm in diameter). Schematic illustration of electrode setup is presented in Fig. 5.11.

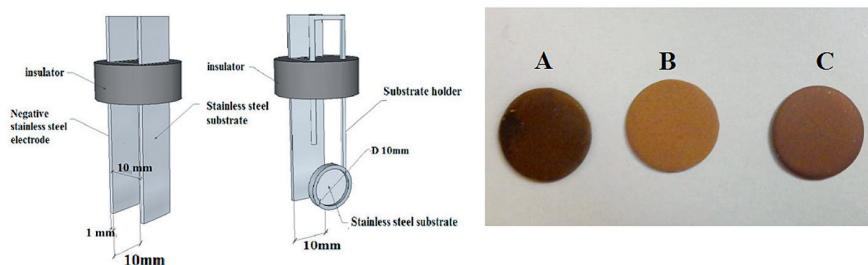


Figure 5.11. Structural model of electrode setup during anodic EPD and photographs of obtained thin films of different composites. (A)-FTGO, (B)-TGO, (C)-FGO

During deposition process, the negatively charged particles under the applied voltage migrate toward the positive electrode and subsequently deposit on it. Thermal reduction of as-deposited thin films was performed by heating for two hours at 580 °C in argon/hydrogen flow (Ar : H<sub>2</sub> volume ratio was 95:5) [51]. Important parameters of as-prepared thin film are listed in Table 5.1.

Table 5.1. Parameters and preparation conditions of sample

Sample name	Composition	Ratio of mass, %	Thickness of film, μm	Weight of sample, mg
TGO	TiO <sub>2</sub> /rGO	29/71	3 ± 0,2	1.1 ± 0,1
FGO	Fe <sub>2</sub> O <sub>3</sub> /rGO	45/55	2 ± 0,2	1.7 ± 0,1
TFGO	TiO <sub>2</sub> /Fe <sub>2</sub> O <sub>3</sub> /rGO	18/36/46	5 ± 0,2	2.3 ± 0,1

### Structure and morphology of graphene sheet and oxide composite electrodes

Results of XRD showed the presence of α-Fe<sub>2</sub>O<sub>3</sub>, rutile and anatase phases of TiO<sub>2</sub> (Fig. 5.12.). No detectable diffraction peaks from possible impurities are observed suggesting highly crystalline and purity of the as prepared films. The XRD patterns of samples are shown in Fig. 5.12. It is noteworthy to mention that the XRD pattern exhibits the typical diffraction peaks of few layer graphene (FLG) (002) at the peak position 26°. It means that most of the graphene oxide was successfully converted to rGO by thermal reduction and it has an interplanar distance of  $d = 0.34$  nm calculated on the basis of Bragg's equation [52].

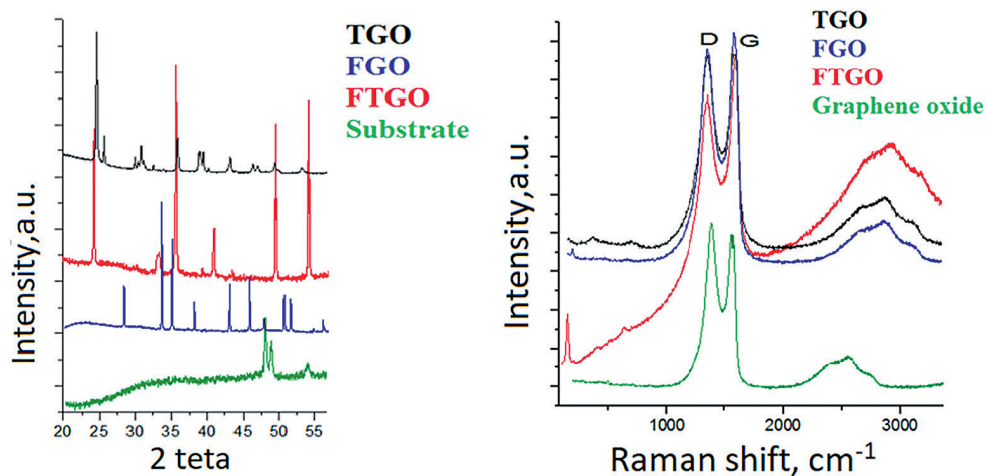


Figure 5.12. XRD pattern and Raman spectra of TGO, FGO and FTGO composites (for interpretation of the references to color in this figure, reader is referred to the web version of this article)

Raman spectroscopy is an effective technique to detect the significant structural changes of graphene nanosheets based on the location and intensity of the relative peaks [53]. Raman spectroscopy was performed to indicate the structures of as-prepared thin films and structure of rGO by analyzing carbon D and G bands, see Fig. 5.12. The D band at  $1350\text{ cm}^{-1}$  is ascribed to defects and disordered carbon, while G band at  $1580\text{ cm}^{-1}$  arises from the zone centre  $E^{2g}$  mode, corresponding to ordered  $sp^2$  bonded carbon [53–57]. The Raman spectrum of all samples shows well referred documented D band peak due to the  $sp^3$  defects and another peak of G band corresponded to the inplane vibrations of  $sp^2$  carbon atoms and a doubly degenerated phonon mode at the Brillouin zone centre [56]. Raman spectra of obtained samples are plotted in Fig. 5.12. and shows relative intensities of D and G bands. It was observed that G band has a higher intensity than D band, it indicates an ordered  $sp^2$  bonded carbon and a successful reduction of GO to rGO.

It is clearly visible that the peak at  $100\text{ cm}^{-1}$  indicates the presence of  $\alpha\text{-Fe}_2\text{O}_3$  in both samples depicted in Fig. 5.12 (curves marked as red and blue). Two flat peaks ( $420\text{ cm}^{-1}$  and  $715\text{ cm}^{-1}$ ) of  $\text{TiO}_2$  sample indicate the presence of titanium dioxide [51].

The observed peaks of Raman shift for all the samples within Raman shift range of  $0\text{--}1000\text{ cm}^{-1}$  reveal the characteristic peaks of  $\text{TiO}_2$  and  $\alpha\text{-Fe}_2\text{O}_3$ . As can be seen, all curves contains a very broad reflection peak at the range of  $2500\text{--}3500\text{ cm}^{-1}$ , indicating the presence of multilayered reduced graphene oxide. The change of 2D band peak intensity and location further proves that  $\text{Fe}_2\text{O}_3/\text{TiO}_2/\text{rGO}$  nanocomposites were successfully prepared. The second order of zone boundary phonons or 2D band, which is related to the stacking nature of graphene layers, was observed at  $2700\text{ cm}^{-1}$ . The peak was broadened for the  $\alpha\text{-Fe}_2\text{O}_3/\text{TiO}_2/\text{rGO}$  nanocomposite as a consequence of multilayer rGO sheets stacking caused by decrease of functional groups attached to the rGO, which prevents the sheets from restacking together. Raman analysis further confirmed that  $\alpha\text{-Fe}_2\text{O}_3$  and  $\text{TiO}_2$  nanoparticles were effectively loaded among rGO sheets [55–57].

The morphology of graphene sheets obtained by EPD with the electric field  $30\text{ V}\cdot\text{cm}^{-1}$  was characterized by SEM, and their images are shown in Fig. 5.13. SEM images of graphene sheets exhibit a nanocrystalline structure with the particle size in the range of  $200\text{--}400\text{ nm}$ . Such nanocrystalline structure has been obtained due to the water decomposition during the EPD process at a high voltage, followed by the intensive evolution of gases on the electrodes. Therefore, the obtained graphene films possess not only layered but also nanocrystalline structure, which is advantageous for enhanced Li-ion transport in films. SEM images of oxide composite layers in Fig. 5.13 (B, C) clearly depict the uniform wrapping of metal oxide particles by crinkled graphene sheets. As shown, the image indicates that  $\text{TiO}_2$  and  $\text{Fe}_2\text{O}_3$  nanoparticles were evenly anchored between the thin-layered rGO sheets (C). The layered graphene sheets accommodate the volume expansion of  $\text{TiO}_2$  and  $\text{Fe}_2\text{O}_3$  nanoparticles during the lithiation/delithiation process. The image (D) displays metal oxide grains intercalated by the flexible and ultrathin wrinkled rGO sheets with a few layers to form a sandwich structure.

Intercalation of metal oxide nanoparticles between graphene sheets plays a vital role to accumulate a large amount of lithium ion during charge/discharge process of the electrode. Furthermore, this unique morphology is beneficial to inhibit the aggregation of the graphene sheets [57, 58].

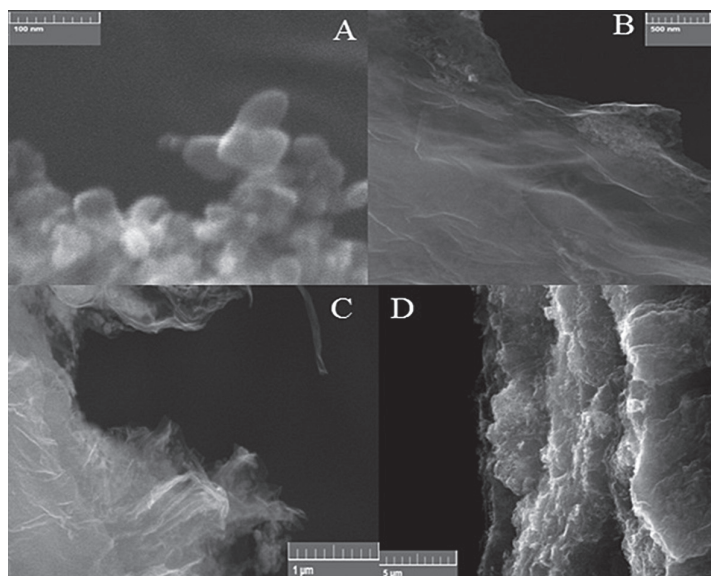


**Figure 5.13.** SEM images of thin films. (A) Fe<sub>2</sub>O<sub>3</sub> nanograins with an average size of about 50 nm, (B, C) Fe<sub>2</sub>O<sub>3</sub> and TiO<sub>2</sub> nanograins anchored on rGO layers, (D)-cross section of layered thin film structure

### Electrochemical performance of electrodes from graphene sheets and oxide composites

Electrochemical properties of graphene sheets were first characterized by CV method. Typical cyclic voltammogram of GS electrode at 1 mV·s<sup>-1</sup> from 0.01 to 4 V vs. Li/Li<sup>+</sup> is shown in Fig. 5.14 on the left. The CV profile is almost similar to the graphitic carbon with two cathodic and two anodic peaks [56, 57]. The wide reductive peak at around 1.2 V can be attributed to the formation of SEI film. The visible cathodic peak observed at around the potential 0.5 V and corresponding anodic peak at around 1.8 V complies to the Li-ion intercalation and deintercalation during the potential scan. This result is consistent with the charge-discharge voltage profiles (Fig. 5.14 on the right). The gravimetric charge capacity dependence on discharge current is shown in Fig. 5.15 on the right. At a slow discharge rate ( $I = 0.8$  mA), gravimetric charge capacity of obtained GS anode reaches a high value  $\sim 1120$  mAh·g<sup>-1</sup> which is comparable or even higher than reported by other authors [44, 53, 54]. Increasing of discharge rate causes the gradual decrease of capacity. At much higher discharge rate ( $I = 2$  mA), capacity falls to  $\sim 620$  mAh·g<sup>-1</sup>. The cycling behaviour of obtained GS electrodes at  $I = 2$  mA within the voltage range of 0.01 to 4 V is shown in Fig. 5.15 on the left. It was found that after 50 cycles the reversible capacity of GS electrode still remains  $\sim 530$  mAh·g<sup>-1</sup>. The Coulombic efficiency for the first 50 cycles of GS electrode exceeded 85%. The further decrease of capacity during the cycling is negligible.

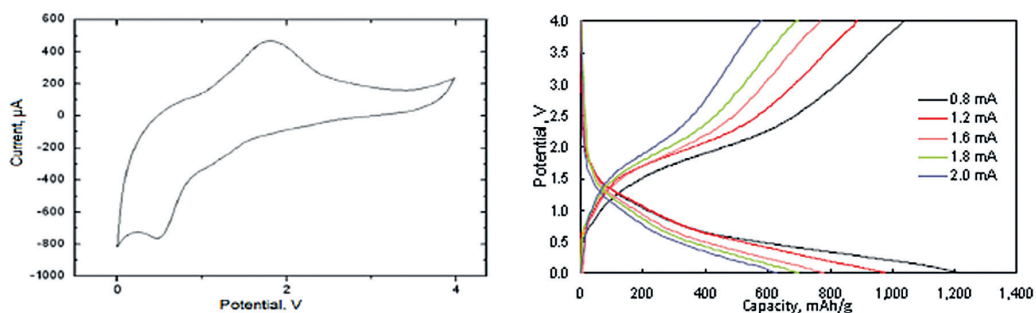


Figure 5.14. CV curve of graphene sheet electrode at the potential scan rate  $1 \text{ mV}\cdot\text{s}^{-1}$  (left); galvanostatic charge-discharge profiles of graphene sheet electrode at the potential range  $0.01\text{--}4 \text{ V}$  (right)

Graphene sheets were fabricated by electrophoretic deposition method followed by thermal reduction. The results of scanning electron microscopy, X-ray diffraction and Raman spectroscopy confirm the formation of nanocrystalline graphene sheet films. The profile of voltammetric curves indicated smooth lithiation and delithiation processes of obtained graphene films. The initial discharge capacity was about  $1120 \text{ mAh}\cdot\text{g}^{-1}$  at a constant current density of  $1 \text{ mA}\cdot\text{cm}^{-2}$ . Extended cycling was performed that demonstrated good reversibility of lithium intercalation and deintercalation in graphene sheet film with capacity retention over 85% after 50 cycles. The results show that nanocrystalline graphene sheets prepared by EPD exhibited a great potential for application as an anode material in lithium ion batteries because of the very nanocrystalline structure of GS, which promotes the Li-ion intercalation through the graphene layers. The use of lightweight graphene and lithium metal provides a high gravimetric capacity and energy density. The experimental results indicate that EPD is a highly powerful tool for the deposition of nanocrystalline graphene films from water suspension of graphene oxide.

The cycling performance of composite oxide samples is shown in Fig. 5.15 on the left. It was carried out in the voltage window of  $0.01\text{--}3.8 \text{ V}$  (vs.  $\text{Li}/\text{Li}^+$ ) at a constant discharge rate of  $100 \text{ mA}\cdot\text{g}^{-1}$  up to 150 cycles at ambient temperature (RT). The discharge capacity of FTGO is  $\sim 790 \text{ mAh}\cdot\text{g}^{-1}$  that is higher than the capacity of TGO  $\sim 95 \text{ mAh}\cdot\text{g}^{-1}$  and FGO  $\sim 240 \text{ mAh}\cdot\text{g}^{-1}$ . This can be attributed to the large electrochemical active surface of well-dispersed rGO and synergic effect of  $\text{TiO}_2$  and  $\alpha\text{-Fe}_2\text{O}_3$  nanoparticles anchored on rGO and to the large area of SEI. Without the spacer of  $\text{TiO}_2$  and  $\alpha\text{-Fe}_2\text{O}_3$  nanoparticles, rGO sheets easily stack together, therefore providing a small host area for lithium ions [58].

The initial capacity loss is 12% for FTGO, 21% for FGO, 15% for TGO after 150 cycles, and mainly resulted from diverse irreversible processes, such as interfacial lithium storage, inevitable formation of SEI layer, organic conductive polymer and electrolyte decomposition, which are common for most anode materials [36]. During cycling, it is clearly visible that after 40 cycles the capacity of TGO is decreased drastically, and then at the point when 140 cycles occurred, the capacity returns to the initial condition. For FGO electrode, the capacity slightly decreases within all the range of cycles. However, paradoxically, FTGO electrodes have shown a different electrochemical behaviour. At the first 50 cycles, the capacity slowly decreases and then begins to rise, finally even surpassing the initial value. This clearly demonstrates the improved reversibility of FTGO thin film electrode.

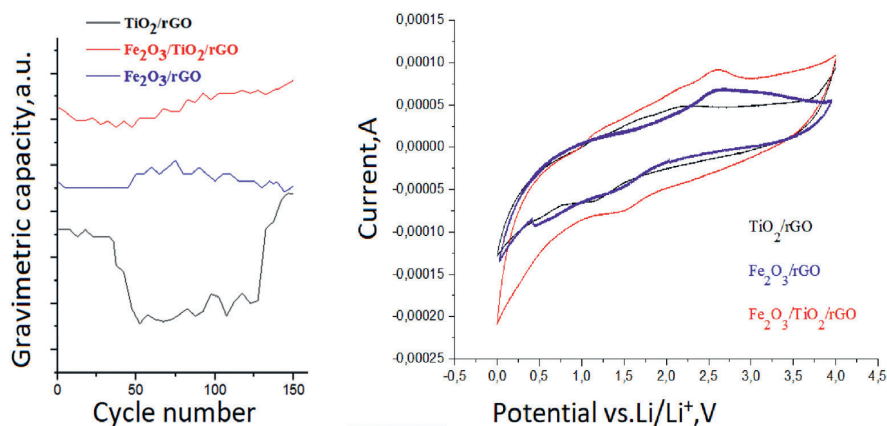


Figure 5.15. Reversible lithium storage capacities vs. cycle number (left) at a current density  $100 \text{ mA}\cdot\text{g}^{-1}$  ( $0.1 \text{ C}$ ) and CV curves (right) at a scan rate  $4 \text{ mV}\cdot\text{s}^{-1}$  of FGO, TGO and FTGO

The decay of reversible capacities of the FTGO during the first 50 cycles can be attributed to the pulverization of original TiO<sub>2</sub> and Fe<sub>2</sub>O<sub>3</sub> *in situ* formed Fe and Ti nanoparticles during Li insertion and extraction process, which lead to the loss of electrical connectivity between neighbouring particles. In the initial cycles, the pulverized particles did not contact well with each other, as a result, the reversible capacity decreased. However, the Fe and Ti nanoparticles began to shrink and pulverize into small particles, when Li was extracted. With Li insertion and extraction, the formed Fe and Ti nanoparticles became smaller and smaller due to electrochemical milling effects and formed a strong attachment to the graphene sheets.

The excellent reversible capacities are also attributed to the critical size of Fe and Ti nanoparticles, where a smaller particle size can help to prevent the gradual aggregation into large clusters.

CV measurements were conducted to identify the electrochemical reactions occurred during lithiation/delithiation process of the TGO, FGO and FTGO hybrid films. Fig. 5.15 (right) shows three CV curves of the as-prepared electrodes at the scan rate of  $4 \text{ mV}\cdot\text{s}^{-1}$  within a cutoff voltage 0.005 and 4.0 V (vs. Li<sup>+</sup>/Li).

Charge storage behaviours of all samples were carried out, and a visible cathodic peak can be clearly observed at 1.5 V for FGO, 1.2 for TGO and 1.6 V for FTGO, and a corresponding anodic peak at 2.2 V for TGO, 2.6 V for FGO and 2.7 V for FTGO, respectively, which could be ascribed to the Li-ion intercalation and deintercalation during the potential scan. This result is consistent with the charge-discharge voltage profiles (Fig. 5.16).

Voltage versus capacity profiles as well as rate performance are illustrated in Fig. 5.16 A. The specific capacities and current densities of FGO, TGO and FTGO electrodes were figured out on the basis of the total weight  $\alpha\text{-Fe}_2\text{O}_3$ , TiO<sub>2</sub> and rGO.

The increase of discharge rate causes the gradual decrease of gravimetric capacity. At the highest value of discharge rate ( $I = 500 \text{ mA}$ ), the capacity falls to  $\sim 42 \text{ mAh}\cdot\text{g}^{-1}$  for TGO,  $\sim 65 \text{ mAh}\cdot\text{g}^{-1}$  for FGO and  $\sim 390 \text{ mAh}\cdot\text{g}^{-1}$  for FTGO, respectively. The first discharge (lithiation)/charge (delithiation) capacities of the electrodes at the current density of  $0.05 \text{ A/g}$  and initial Coulombic efficiencies are listed in Table 5.2.

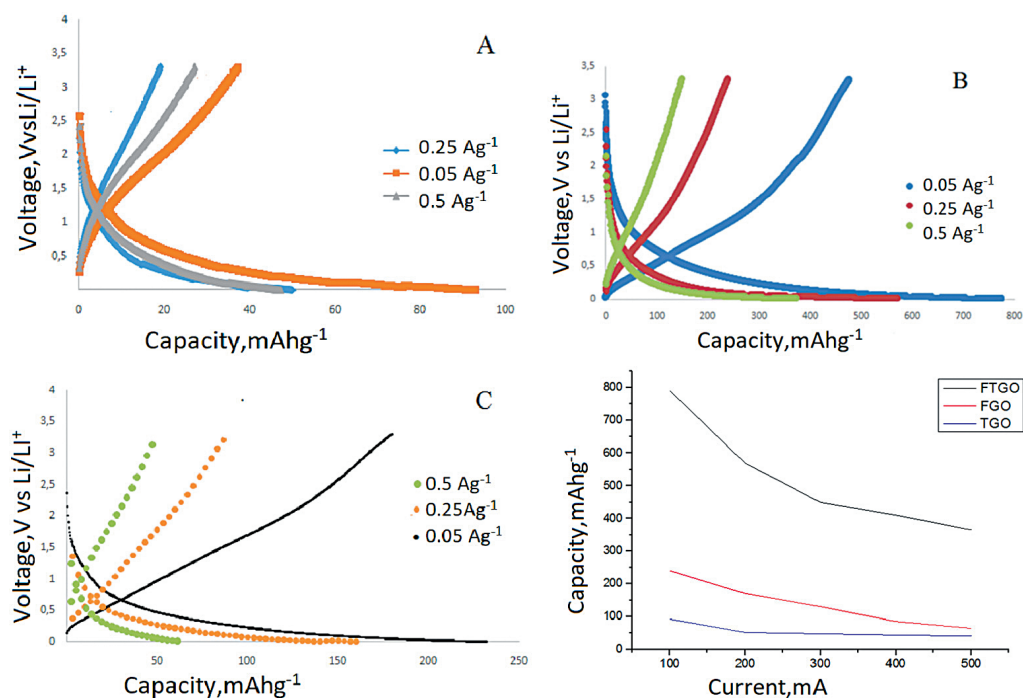


Figure 5.16. Galvanostatic charge-discharge profiles of (A) – TGO, (B) – FTGO, (C) – FGO composite electrodes at the potential range 0.03–3.6 V and discharge rate performance

Table 5.2. Gravimetric capacities and Coulombic efficiencies of samples

	TGO/mAh·g <sup>-1</sup>	FGO/mAh·g <sup>-1</sup>	FTGO/mAh·g <sup>-1</sup>
Lithiation	95	240	790
Delithiation	40	190	520
CE/%	42	79	66
Theoretical capacities	661	879	765

FTGO composite shows the best performance among three composites, and it may further prove the synergistic interaction between the rGO sheets,  $\alpha$ -Fe<sub>2</sub>O<sub>3</sub> and TiO<sub>2</sub> nanoparticles. The specific capacity was calculated by using complete mass of composite material.

However, the pure  $\alpha$ -Fe<sub>2</sub>O<sub>3</sub> and TiO<sub>2</sub> nanoparticles tend to agglomerate, hence providing a much smaller surface area for the transportation of lithium ions. Finally, the layered structure of reduced graphene facilitates the rapid Li-ion diffusion at both the electrode/electrolyte interface and within the bulk electrode, leading to enhanced electrochemical reaction kinetics and excellent cycle performance.

## 5.5. Summary

Both the cathode and anode materials for LIBs were developed during the project. Remarkable electrode improvements have been achieved by designing nanostructured materials, composites and thin films. The use of nanomaterials results in operating parameters close to their theoretical values and increases the charge capacity and cyclability of the Li-ion cells. The enhanced surface of nanomaterials also increases the charge transfer at the electrode – electrolyte interface. Additionally, lowering the particle size of active electrode material reduces the diffusion path of Li-ions and decreases the polarization of the electrodes. Nanostructured electrodes improve the structural stability and stabilize the solid electrolyte interface. Nanosized particles exhibit unique Li-ion storage mechanisms involving intercalation processes and/or conversion reactions.

Thin films of  $\text{LiFePO}_4$  were obtained by PLD and magnetron sputtering techniques. The electrochemical performance of obtained cathode films was studied as a function of preparation technique, and the obtained electrode morphology, grain structure and composition. The discharge capacity of the thin films obtained by PLD reach  $118 \text{ mAh}\cdot\text{g}^{-1}$ , which is slightly higher than that of the films obtained by magnetron sputtering ( $61 \text{ mAh}\cdot\text{g}^{-1}$  at 0.1 C rate). However, the effective diffusion coefficients of PLD thin films ( $10^{-18} - 10^{-17} \text{ cm}^2/\text{s}$ ) are lower than those of the films obtained by magnetron sputtering ( $10^{-14} - 10^{-12} \text{ cm}^2/\text{s}$ ), and besides the diffusion, they also generally characterize the overall lithium kinetics in the  $\text{LiFePO}_4$  electrode. Voltage hysteresis was not observed for  $\text{LiFePO}_4$  thin films deposited by PLD. The disappearance of voltage hysteresis indicates that the sequential charging and discharging of  $\text{LiFePO}_4$  particles in thin film can occur in a significantly different way than in bulk material.

Reduced graphene oxide (rGO) sheets and composite thin films  $\text{TiO}_2/\text{rGO}$ ,  $\text{Fe}_2\text{O}_3/\text{rGO}$  and  $\text{TiO}_2/\text{Fe}_2\text{O}_3/\text{rGO}$  obtained by electrophoretic deposition were studied as anode material for LIBs. Intercalation of metal oxide nanoparticles between reduced graphene oxide sheets plays a vital role to accumulate a large amount of lithium ion during charge/discharge process of the electrode. Furthermore, this unique morphology is beneficial to inhibit the aggregation of the graphene sheets. At a slow discharge rate, the gravimetric charge capacity of obtained graphene sheet anode reaches a high value  $\sim 1120 \text{ mAh}\cdot\text{g}^{-1}$ , which is comparable to or even higher than that reported by other authors. The gravimetric charge capacity of  $\alpha\text{-Fe}_2\text{O}_3/\text{TiO}_2/\text{rGO}$  films reaches  $790 \text{ mAh}\cdot\text{g}^{-1}$  that is much higher than the capacity of a single metal oxide composite with rGO, and exhibits excellent cyclability. The improved electrochemical properties were due to the rGO uniform dispersion in the inter-space of  $\alpha\text{-Fe}_2\text{O}_3$  and  $\text{TiO}_2$ , as well as the synergic effect between metal oxides and rGO.

## 5.6. References

1. Kucinskis, G., Bajars, G., and Kleperis, J. (2013) Graphene in lithium ion battery cathode materials: A review. *Journal of Power Sources*, 240, 66–79.
2. Ibrahim, H., Ilinca, A., and Perron, J. (2008) Energy storage systems – characteristics and comparisons. *Renewable and Sustainable Energy Reviews*, 12(5), 1221–1250.
3. Whittingham, M. S. (2004) Lithium Batteries and Cathode Materials. *Chemical Reviews*, 104(10), 4271–4302.
4. Goodenough, J. B. (2007) Cathode materials: A personal perspective. *Journal of Power Sources*, 174(2), 996–1000.

5. Fergus, J. W. (2010) Recent developments in cathode materials for lithium ion batteries. *Journal of Power Sources*, 195(4), 939–954.
6. Yang, Z., Ren, J., Zhang, Z., Chen, X., Guan, G., Qiu, L., et al. (2015) Recent Advancement of Nanostructured Carbon for Energy Applications. *Chemical Reviews*, 115(11), 5159–5223.
7. Kaprants, K., Bajars, G., Kucinskis, G., Dorondo, A., Mateuss, J., Gabrusenoks, J., et al. (2015) Electrophoretic Nanocrystalline Graphene Film Electrode for Lithium Ion Battery. *IOP Conference Series: Materials Science and Engineering*, 77(1), 012042.
8. Kaprants, K., Mateuss, J., Dorondo, A., Bajars, G., Kucinskis, G., Lesnicenoks, P., et al. (2018) Electrophoretically deposited  $\alpha$ -Fe<sub>2</sub>O<sub>3</sub> and TiO<sub>2</sub> composite anchored on rGO with excellent cycle performance as anode for lithium ion batteries. *Solid State Ionics*, 319, 1–6.
9. Kucinskis, G. (2015) The study of nanostructured bulk and thin film LiFePO<sub>4</sub> cathode materials for lithium-ion batteries. Summary of Doctoral Thesis, University of Latvia, 2015.
10. Wasa, K., Kitabatake, M., and Adachi, H. (2004) Thin Film Materials Technology, Sputtering of Compound Materials. William Andrew, Inc.,
11. Ohring, M. (2002) Materials Science of Thin Films. Elsevier.
12. Malik, R., Abdellahi, A., and Ceder, G. (2013) A Critical Review of the Li Insertion Mechanisms in LiFePO<sub>4</sub> Electrodes. *Journal of the Electrochemical Society*, 160(5), A3179–A3197.
13. Tian, R., Liu, G., Liu, H., Zhang, L., Gu, X., Guo, Y., et al. (2015) Very high power and superior rate capability LiFePO<sub>4</sub> nanorods hydrothermally synthesized using tetraglycol as surfactant. *RSC Adv.*, 5(3), 1859–1866.
14. Lung-Hao Hu, B., Wu, F.-Y., Lin, C.-T., Khlobystov, A.N., and Li, L.-J. (2013) Graphene-modified LiFePO<sub>4</sub> cathode for lithium ion battery beyond theoretical capacity. *Nature Communications*, 4, 1687.
15. Wang, J. and Sun, X. (2015) Olivine LiFePO<sub>4</sub>: the remaining challenges for future energy storage. *Energy Environ. Sci.*, 8(4), 1110–1138.
16. Zaghbi, K., Guerfi, A., Hovington, P., Vijh, A., Trudeau, M., Mauger, A., et al. (2013) Review and analysis of nanostructured olivine-based lithium rechargeable batteries: Status and trends. *Journal of Power Sources*, 232, 357–369.
17. McCready, D. E., Liang, Y., Shutthanandan, V., Wang, C. M., and Thevuthasan, S. (2006) Thermal Lattice Expansion in Epitaxial SrTiO<sub>3</sub>(100) on Si(100). *Advances in X-Ray Analysis*, ISSN 1097, 175–179.
18. de Ligny, D. and Richet, P. (1996) High-temperature heat capacity and thermal expansion of SrTiO<sub>3</sub> and SrZrO<sub>3</sub> perovskites. *Physical Review B.*, 53(6), 3013–3022.
19. Chen, Z., Ren, Y., Qin, Y., Wu, H., Ma, S., Ren, J., et al. (2011) Solid state synthesis of LiFePO<sub>4</sub> studied by in situ high energy X-ray diffraction, *Journal of Materials Chemistry*, 21, 5604.
20. Tang, K., Yu, X., Sun, J., Li, H., and Huang, X. (2011) Kinetic analysis on LiFePO<sub>4</sub> thin films by CV, GITT, and EIS. *Electrochimica Acta.*, 56(13), 4869–4875.
21. Palomares, V., Ruiz de Larramendi, I., Alonso, J., Bengoechea, M., Goñi, a., Miguel, O., et al. (2010) LiFePO<sub>4</sub> thin films grown by pulsed laser deposition: Effect of the substrate on the film structure and morphology. *Applied Surface Science*, 256(8), 2563–2568.
22. Köhler, M., Berkemeier, F., Gallasch, T., and Schmitz, G. (2013) Lithium diffusion in sputter-deposited lithium iron phosphate thin-films. *Journal of Power Sources*, 236, 61–67.
23. Chiu, K.-F. (2007) Optimization of Synthesis Process for Carbon-Mixed LiFePO<sub>4</sub> Composite Thin-Film Cathodes Deposited by Bias Sputtering. *Journal of the Electrochemical Society*, 154(2), A129.
24. Hong, J., Wang, C., Dudney, N. J., and Lance, M. J. (2007), Characterization and Performance of LiFePO<sub>4</sub> Thin-Film Cathodes Prepared with Radio-Frequency Magnetron-Sputter Deposition. *Journal of The Electrochemical Society*, 154(8), A805.
25. Xie, J., Imanishi, N., Zhang, T., Hirano, A., Takeda, Y., and Yamamoto, O. (2009) Li-ion diffusion kinetics in LiFePO<sub>4</sub> thin film prepared by radio frequency magnetron sputtering. *Electrochimica Acta*, 54(20), 4631–4637.
26. Zhu, X.-J., Cheng, L.-B., Wang, C.-G., Guo, Z.-P., Zhang, P., Du, G.-D., et al. (2009) Preparation and Characteristics of LiFePO<sub>4</sub> Thin Film by Radio Frequency Magnetron

- Sputtering for Lithium Microbatteries. *The Journal of Physical Chemistry C*, 113(32), 14518–14522.
27. Lu, Z. G., Lo, M. F., and Chung, C. Y. (2008) Pulse Laser Deposition and Electrochemical Characterization of LiFePO<sub>4</sub> - C Composite Thin Films. *J. Phys. Chem. C*, 112, 7069–7078.
  28. Sauvage, F., Baudrin, E., Gengembre, L., and Tarascon, J. (2005) Effect of texture on the electrochemical properties of LiFePO<sub>4</sub> thin films. *Solid State Ionics*, 176(23-24), 1869–1876.
  29. Yada, C., Iriyama, Y., Jeong, S.-K., Abe, T., Inaba, M., and Ogumi, Z. (2005) Electrochemical properties of LiFePO<sub>4</sub> thin films prepared by pulsed laser deposition. *Journal of Power Sources*, 146(1-2), 559–564.
  30. Song, S.-W., Reade, R. P., Kostecki, R., and Striebel, K. A. (2006) Electrochemical Studies of the LiFePO<sub>4</sub> Thin Films Prepared with Pulsed Laser Deposition. *Journal of The Electrochemical Society*, 153(1), A12.
  31. Zhu, C., Weichert, K., and Maier, J. (2011) Electronic Conductivity and Defect Chemistry of Heterosite FePO<sub>4</sub>. *Advanced Functional Materials*, 21(10), 1917–1921.
  32. Li, Y., El Gabaly, F., Ferguson, T. R., Smith, R. B., Bartelt, N. C., Sugar, J. D., et al. (2014) Current-induced transition from particle-by-particle to concurrent intercalation in phase-separating battery electrodes. *Nature Materials*, 13(12), 1149–1156.
  33. Zhu, Y. and Wang, C. (2010) Galvanostatic Intermittent Titration Technique for Phase-Transformation Electrodes. *The Journal of Physical Chemistry C*, 114(6), 2830–2841.
  34. Prosini, P. P., Lisi, M., Zane, D., and Pasquali, M. (2002) Determination of the chemical diffusion coefficient of lithium in LiFePO<sub>4</sub>. *Solid State Ionics*, 148(1–2), 45–51.
  35. Churikov, A. V., Ivanishchev, A. V., Ivanishcheva, I. A., Sycheva, V. O., Khasanova, N. R., and Antipov, E. V. (2010) Determination of lithium diffusion coefficient in LiFePO<sub>4</sub> electrode by galvanostatic and potentiostatic intermittent titration techniques. *Electrochimica Acta*, 55(8), 2939–2950.
  36. Bajars, G., Kucinskis, G., Smits, J., Kleperis, J., and Lasis, A. (2012) Characterization of LiFePO<sub>4</sub> /C Composite Thin Films Using Electrochemical Impedance Spectroscopy. *IOP Conference Series: Materials Science and Engineering*, 38(1), 012019.
  37. Sasaki, T., Ukyo, Y., and Novák, P. (2013) Memory effect in a lithium-ion battery. *Nature Materials*, 12(6), 569–575.
  38. Kang, B. and Ceder, G. (2009) Battery materials for ultrafast charging and discharging. *Nature*, 458(7235), 190–3.
  39. Shang, W., Kong, L., and Ji, X. (2014) Synthesis, characterization and electrochemical performances of LiFePO<sub>4</sub>/graphene cathode material for high power lithium-ion batteries. *Solid State Sciences*, 38, 79–84.
  40. Li, J., Wu, J., Wang, Y., Liu, G., Chen, C., and Liu, H. (2014) Synthesis of LiFePO<sub>4</sub>/C composite with high rate capability using spheniscidite as a facile precursor. *Materials Letters*, 136, 282–285.
  41. Kim, K.M., Lee, Y.-G., Kang, K.-Y., Yang, Y.S., and Kim, J. (2012) A simple method for solving the voltage overshoots of LiFePO<sub>4</sub>-based lithium-ion batteries with different capacity classes. *RSC Advances*, 2(9), 3844.
  42. Goriparti, S., Miele, E., De Angelis, F., Di Fabrizio, E., Proietti Zaccaria, R., and Capiglia, C. (2014) Review on recent progress of nanostructured anode materials for Li-ion batteries. *Journal of Power Sources*, 257, 421–443.
  43. Nitta, N., Wu, F., Lee, J.T., and Yushin, G. (2015) Li-ion battery materials: present and future. *Materials Today*, 18(5), 252–264.
  44. Dao, T.D., Hong, J.-E., Ryu, K.-S., and Jeong, H.M. (2014) Super-tough functionalized graphene paper as a high-capacity anode for lithium ion batteries. *Chemical Engineering Journal*, 250, 257–266.
  45. Wu, Z.-S., Pei, S., Ren, W., Tang, D., Gao, L., Liu, B., et al. (2009) Field Emission of Single-Layer Graphene Films Prepared by Electrophoretic Deposition. *Advanced Materials*, 21(17), 1756–1760.

46. Seo, S.-D., Hwang, I.-S., Lee, S.-H., Shim, H.-W., and Kim, D.-W. (2012) 1D/2D carbon nanotube/graphene nanosheet composite anodes fabricated using electrophoretic assembly. *Ceramics International*, 38(4), 3017–3021.
47. Chen, D., Ji, G., Ma, Y., Lee, J.Y., and Lu, J. (2011) Graphene-Encapsulated Hollow Fe<sub>3</sub>O<sub>4</sub> Nanoparticle Aggregates As a High-Performance Anode Material for Lithium Ion Batteries. *ACS Applied Materials & Interfaces*, 3(8), 3078–3083.
48. Yan, Y., Tang, H., Li, J., Wu, F., Wu, T., Wang, R., et al. (2017) Self-assembly synthesis of a unique stable cocoon-like hematite @C nanoparticle and its application in lithium ion batteries. *Journal of Colloid and Interface Science*, 495, 157–167.
49. Wu, Z.-S., Zhou, G., Yin, L.-C., Ren, W., Li, F., and Cheng, H.-M. (2012) Graphene/metal oxide composite electrode materials for energy storage. *Nano Energy*, 1(1), 107–131.
50. Yu, Y., Sun, D., Wang, H., and Wang, H. (2016) Electrochemical Properties of Rutile TiO<sub>2</sub> Nanorod Array in Lithium Hydroxide Solution. *Nanoscale Research Letters*, 11(1), 448.
51. Wen, Z., Ci, S., Mao, S., Cui, S., He, Z., and Chen, J. (2013) CNT@TiO<sub>2</sub> nanohybrids for high-performance anode of lithium-ion batteries. *Nanoscale Research Letters*, 8(1), 499.
52. Van Meveren, M. M. (2017) Graphene-Based “Hybrids” as High-Performance Electrodes with Tailored Interfaces for Alternative Energy Applications: Synthesis, Structure and Electrochemical Properties. Western Kentucky University, 2017.
53. Bai, L.-Z., Zhao, D.-L., Zhang, T.-M., Xie, W.-G., Zhang, J.-M., and Shen, Z.-M. (2013) A comparative study of electrochemical performance of graphene sheets, expanded graphite and natural graphite as anode materials for lithium-ion batteries. *Electrochimica Acta*, 107, 555–561.
54. Guo, P., Song, H., and Chen, X. (2009) Electrochemical performance of graphene nanosheets as anode material for lithium-ion batteries. *Electrochemistry Communications*, 11(6), 1320–1324.
55. Wu, Q.-H., Qu, B., Tang, J., Wang, C., Wang, D., Li, Y., et al. (2015) An Alumina-Coated Fe<sub>3</sub>O<sub>4</sub>-Reduced Graphene Oxide Composite Electrode as a Stable Anode for Lithium-ion Battery. *Electrochimica Acta*, 156, 147–153.
56. Zhou, X., Zhang, J., Su, Q., Shi, J., Liu, Y., and Du, G. (2014) Nanoleaf-on-sheet CuO/graphene composites: Microwave-assisted assemble and excellent electrochemical performances for lithium ion batteries. *Electrochimica Acta*, 125, 615–621.
57. Wang, D., Choi, D., Li, J., Yang, Z., Nie, Z., Kou, R., et al. (2009) Self-Assembled TiO<sub>2</sub>-Graphene Hybrid Nanostructures for Enhanced Li-Ion Insertion. *ACS Nano*, 3(4), 907–914.
58. Wei, D., Liang, J., Zhu, Y., Zhang, J., Li, X., Zhang, K., et al. (2013) Facile formation of graphene-encapsulated  $\alpha$ -Fe<sub>2</sub>O<sub>3</sub> nanorice as enhanced anode materials for lithium storage. *Electrochimica Acta*, 114, 779–784.

## 5.7. Kopsavilkums

Projekta laikā tika izstrādāti jauni katoda un anoda materiāli litija jonu baterijām ar uzlabotām elektroķīmiskajām īpašībām, kas tika panāktas, veidojot nanostrukturētus materiālus, kompozītmateriālus un plānās kārtiņas. Nanomateriālu izmantošana dod iespēju sasniegt darbības parametrus, kas ir tuvi to teorētiskajām vērtībām un palielina litija jonu elektroķīmisko šūnu lādiņietilpību un ciklējāmību. Nanomateriālu palielinātā aktīvā virsma samazina arī lādiņu pārnese pretestību caur elektroda-elektrolīta robežvirsmu. Turklāt elektrodu materiāla daļiņu izmēra samazināšana saīsina litija jonu difūzijas ceļu un samazina elektrodu polarizāciju. Nanostrukturētie elektrodi uzlabo arī struktūras stabilitāti un stabilizē elektroda robežvirsmu ar cieto elektrolītu. Nanoizmēru daļiņas uzrāda arī unikālus litija jonu uzkrāšanas mehānismus, kas ietver interkalācijas procesus un/vai konversijas reakcijas.

Plānās  $\text{LiFePO}_4$  kārtiņas tika iegūtas, izmantojot impulsa lāzera nogulsnešanas (PLD) un magnetrona izputināšanas metodi. Iegūto katodmateriālu kārtiņu elektroķīmiskās īpašības tika pētītas atkarībā no to iegūšanas metodes, elektrodu morfoloģijas, graudu struktūras un sastāva. PLD plāno kārtiņu lādiņietilpība sasniedz  $118 \text{ mAh}\cdot\text{g}^{-1}$ , kas ir nedaudz lielāka nekā kārtiņām, kuras iegūtas magnetrona izputināšanas rezultātā ( $61 \text{ mAh}\cdot\text{g}^{-1}$  pie  $0.1 \text{ C}$  uzlādes/izlādes ātruma). Tomēr PLD plāno kārtiņu efektīvie difūzijas koeficienti ( $10^{-18}$ – $10^{-17} \text{ cm}^2/\text{s}$ ) ir zemāki nekā ar magnetrona izputināšanas metodi iegūtajām kārtiņām ( $10^{-14}$ – $10^{-12} \text{ cm}^2/\text{s}$ ), un vairumā gadījumu tie raksturo ne tikai difūzijas procesus, bet arī kopējo litija kinētiku  $\text{LiFePO}_4$  elektrodā. Ar PLD metodi iegūtajās  $\text{LiFePO}_4$  plānajās kārtiņās netika novērota sprieguma histerēze. Sprieguma histerēzes trūkums liecina, ka  $\text{LiFePO}_4$  daļiņu uzlāde un izlāde plānās kārtiņas gadījumā var notikt ievērojami atšķirīgā veidā nekā pulverveida materiālā.

Vairākslāņu reducētā grafēna oksīda (rGO) un kompozītu  $\text{TiO}_2/\text{rGO}$ ,  $\text{Fe}_2\text{O}_3/\text{rGO}$  un  $\text{TiO}_2/\text{Fe}_2\text{O}_3/\text{rGO}$  plānās kārtiņas, kas iegūtas ar elektroforētiskās nogulsnešanas metodi, tika pētītas kā anoda materiāls litija jonu baterijām. Metāla oksīdu nanodaļiņu interkalācijai starp reducētā grafēna oksīda slāņiem ir svarīga loma, lai akumulētu lielu daudzumu litija jonu elektroda uzlādes/izlādes procesā. Turklāt šī unikālā morfoloģija kavē rGO slāņu agregāciju. Vairākslāņu rGO anoda gravimetriskā lādiņietilpība, kas iegūta pie maza izlādes ātruma, sasniedz augstu vērtību  $\sim 1120 \text{ mAh}\cdot\text{g}^{-1}$  un ir salīdzināma vai pat augstāka, nekā ziņots citu autoru pētījumos.  $\alpha\text{-Fe}_2\text{O}_3/\text{TiO}_2/\text{rGO}$  gravimetriskā lādiņietilpība sasniedz  $790 \text{ mAh}\cdot\text{g}^{-1}$ , kas ir daudz lielāka nekā viena atsevišķa metāla oksīda kompozīta ar rGO lādiņietilpība. Turklāt tas uzrāda izcilu ciklējāmību. Uzlabotās elektroķīmiskās īpašības ir saistītas ar rGO viendabīgu dispersiju tilpumā starp  $\alpha\text{-Fe}_2\text{O}_3$  un  $\text{TiO}_2$ , kā arī sinerģisku efektu starp metāla oksīdiem un rGO.

## 6. Nanostructured TiO<sub>2</sub>-based materials with photocatalytic properties

### Nanostrukturēti TiO<sub>2</sub> materiāli un kompozīti ar fotokatalītiskām īpašībām

**Ainārs Knoks, Līga Grīnberga, Jānis Kleperis, Ineta Liepiņa, Gunārs Bajārs**

Institute of Solid State Physics, University of Latvia

Ķengaraga iela 8, Rīga, LV-1063, Latvia

E-mail: [ainars.knoks@cfi.lu.lv](mailto:ainars.knoks@cfi.lu.lv)

#### Contents

6. Nanostructured TiO <sub>2</sub> -based materials with photocatalytic properties . . . . .	124
6.1. Review of photocatalytic materials for water splitting . . . . .	124
6.2. Methods applied to synthesize and research photocatalytic materials . . . . .	127
6.3. Discussion about structure, composition and photo-electrochemical properties of TiO <sub>2</sub> -based materials . . . . .	128
6.4. Conclusions . . . . .	134
6.5. References . . . . .	135
6.6. Kopsavilkums . . . . .	137

#### 6.1. Review of photocatalytic materials for water splitting

In order to reduce global climate change by limiting CO<sub>2</sub> emissions, it is necessary to switch from continuous power production by burning fossil fuels (coal, oil, gas) to the unsteady energy generation from local renewable energy sources. Wind, sun and rivers are the most popular renewable energy sources, but they are available occasionally or seasonally, which doesn't always coincide with required consumption. It is especially important for countries in Northern latitudes with dark and short days in winter, and sunny, long days in summer, like Latvia. Therefore, reliable energy storage systems are critically needed to store and supply power in continuous manner. Electricity and hydrogen are two comparable energy carriers, and in order to be able to meet humanity's demand for energy storage in the form of electricity and/or hydrogen, appropriate materials are researched [1]. In hydrogen economics, the production of hydrogen from renewables is very important.

TiO<sub>2</sub> has attracted high interest of industry and scientific communities. Following the discovery by Honda and Fujishima [2] of TiO<sub>2</sub> photocatalytic properties, it has been used

and investigated for wide variety of applications, such as, self-cleaning surfaces [3, 4] which was attributed to the size difference of the starting materials. The film with only 2 wt % TiO<sub>2</sub> maintained higher contact angle than the film without TiO<sub>2</sub> after 1800-h outdoor exposure, the accumulation of stain being avoided due to TiO<sub>2</sub> photocatalysis. The films prepared in this study are the first ones that satisfy the requirements of transparency, superhydrophobicity, and long lifetime simultaneously. Transparent superhydrophobic thin films with TiO<sub>2</sub> photocatalyst were prepared by utilizing a sublimation material and subsequent coating of a fluoroalkyl, water and air purification [5–9] scanning electron microscope-energy dispersive analysis of X-ray (SEM-EDAX) at the same time looking into the safety of TiO<sub>2</sub> [10] particularly under ultraviolet (UV) and as a viable energy harvesting solution via hydrogen production from water [11–13].

Due to its photocatalytic capability, low cost and chemically inert properties, TiO<sub>2</sub> is a promising material for water and air contamination treatment technologies [9, 14–16]. Most of investigations have been devoted to the pure TiO<sub>2</sub> films because of its reusability. However, practical application of such films is limited by fast recombination of photo-induced hole-electron pairs. Coupling TiO<sub>2</sub> with other inorganic oxides such as SiO<sub>2</sub> [17], SnO<sub>2</sub> [18], WO<sub>3</sub> [19], In<sub>2</sub>O<sub>3</sub>, (Sr, La)TiO<sub>3</sub>, ZnFe<sub>2</sub>O<sub>4</sub>, and Fe<sub>2</sub>O<sub>3</sub> [20] can increase the photon energy range of photo-excitation and this will change the photocatalytic efficiency [21].

Unfortunately, quantum yield for pristine TiO<sub>2</sub> is low, thus making photocatalytic hydrogen production from water not viable. To tackle this problem various modifications are performed. This chapter contains overview of used methods and practices of TiO<sub>2</sub> modifications.

TiO<sub>2</sub> has wide band gap that varies for polymorph phases, anatase has 3.2 eV, rutile 3.05 eV and brookite 3.4 eV [22]. Thus, TiO<sub>2</sub> can be excited only by UV light, that constitute about 10% of sun radiation, but only 5% reaches the surface of the Earth [23]. Indicating that either the quantum yield must be increased immensely, or absorption edge must be moved deeper into visible (VIS) range. Both directions are in the process of exploration due to benefits and downfalls.

Lowering the band gap of TiO<sub>2</sub> can be done through creation of heterostructure with narrow gap materials or doping with various materials. It has been reported that WO<sub>3</sub> increase of absorption in VIS region as shown by various research papers [19, 24–28].

Viable materials to lower TiO<sub>2</sub> band gap, for example nanowire TiO<sub>2</sub> wrapped with ZnO, reported lowering of band gap up to 2.6 eV [29] the impact of angstrom thick atomic layer deposited (ALD), or decorating TiO<sub>2</sub> nanotubes with Cu<sub>2</sub>O particles shifting band gap into region of 1.5 to 3.3 eV [30]. Of course, other photoanode materials can be used to lower band gap and increase photocatalytic activity such as Fe<sub>2</sub>O<sub>3</sub> thin film on anodized TiO<sub>2</sub> thus, enabling absorption of VIS light and increasing photocatalytic activity [31].

Doping of TiO<sub>2</sub> often brings increase of quantum yield at the same time changing band gap. Increase in yield can be due to additional levels that dopants bring or increase in generated charge carrier lifetime. Deposited CdS quantum dots increased charge carrier separation though additional conduction band (CB) electrons above CB edge of TiO<sub>2</sub> [32] or gold nanoparticle increase photocatalytic activity though localised surface plasmonic resonance and charge transfer kinetics [33]. Anionic and cationic doping is prominent choice for modifying TiO<sub>2</sub>. N [34] and F [35] change the unit cell and crystallite size of anatase and rutile in addition to change of band gap. Combining S and N doping with graphene quantum dots modification increase hydrogen production, but again the proper

ratio is of great importance as showed by Xie et al. [36], where they investigated P25 doping with S,N-GQDs. At 3wt% providing highest yield.

Fe, C, V, and other dopants are possible [4]. Computational modelling of various dopants such as work by Lisovski et al. on various atom dopant influence on  $\text{TiO}_2$  [37].

It is noteworthy that synthesis and treatment of  $\text{TiO}_2$  is important, because various types of oxide perform differently. Anodized  $\text{TiO}_2$  photocatalytic properties are annealing dependent, not only amorphous in comparison to crystalline but also annealing temperature dependent as it was shown by Macak [38].

All abovementioned efforts are to promote hydrogen generation through photocatalytic process. Change in band gap is important due to reduction dependency on the potential of generated charge carriers. Generated electrons in conduction band and hole in valence band then have to migrate to surface and interact with water molecule. This means band edge position can be crucial for efficient hydrogen production.

A detailed review by Jafari et al. shows that modifying  $\text{TiO}_2$  brings various results for photocatalysis, from Pt, Cr, Ta doped  $\text{TiO}_2$  producing  $11.7 \mu\text{mol h}^{-1}$  to  $647 \text{ mmol h}^{-1}$  on Au- $\text{TiO}_2$  [39], thus, the investigation of sustainable and accessible photocatalyst is still in progress.

Thus,  $\text{WO}_3$  is a suitable photo-electron storing material to couple with  $\text{TiO}_2$  because  $\text{WO}_3$  has narrower band gap (2.7 eV [40]) than that of  $\text{TiO}_2$  to allow the transfer of photogenerated electrons from  $\text{TiO}_2$  to ensure effective charge separation as shown in Fig. 6.1. As reported by [41] the ratio of  $\text{WO}_3$  to  $\text{TiO}_2$  is critical for higher photocatalytic activity with existing threshold of  $\text{WO}_3$  coverage of  $\text{TiO}_2$  surface for acquired photocurrent increase. Existence of threshold is set by generated charge carrier interfacial transfer, but over the threshold most of the light will be absorbed by  $\text{WO}_3$  and as material with lower photocurrent values the result shows lower overall photocurrent. Authors suggest that generated e-h pairs go through charge interfacial transfer, hole from VB of  $\text{WO}_3$  to VB of  $\text{TiO}_2$  and  $e^-$  from  $\text{TiO}_2$  CB to  $\text{WO}_3$  CB [41].

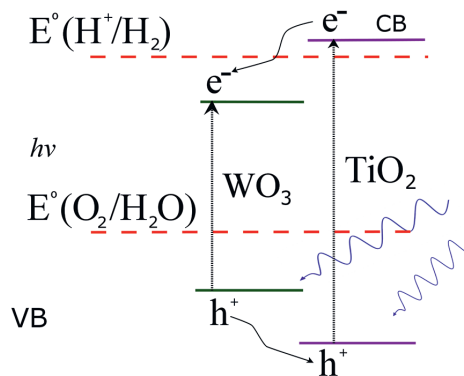


Figure 6.1. Band structure of  $\text{TiO}_2/\text{WO}_3$  heterosystem, optical absorption edge shift to VIS region

In this chapter our research results on the role and properties of nanostructured  $\text{TiO}_2$ -based materials with photocatalytic properties have been summarized based on publications [28].

## 6.2. Methods applied to synthesize and research photocatalytic materials

There are chemical and physical thin film deposition techniques. Physical techniques include mechanical, electromechanical or thermodynamic processes, while chemical thin film deposition techniques usually involve a liquid precursor that forms a thin solid film as a result of a chemical reaction or indifferent solution with dispersed nanopowder of material. The most popular physical thin film deposition techniques are physical vapour deposition (resistive, inductive, electron beam, pulsed laser, arc-discharge, etc.) and sputtering techniques (direct current, alternating current, impulse, etc.). The most typical thick film growth techniques are electrochemical oxidation and deposition, electrophoretic deposition, spray pyrolysis, electrostatic spinning, spin coating and more. More detailed description of material synthesis methods used in this study will be described further.

**Electrophoretic deposition (EPD)** method is a highly beneficial, low-cost and eco-friendly technique for the preparation of required films and multi-layer coatings [42, 43]. For the electrophoretic growth two 3 × 3 cm<sup>2</sup> stainless steel (grade 316) electrodes were used. Distance between electrodes was 1 cm. A constant voltage of 100 V was applied between the electrodes by DC Power Supply (Agilent Technologies N5772A) and held for 10 min. EPD ensures colloidal particle deposition on substrate from electrically conductive electrolyte, in this case isopropanol. The process begins when applied electric field makes dispersed colloidal particles migrate to the electrode, where particles stay intact after losing charge. The deposited coatings were gradually heated (5 °C/min) and annealed at 500 °C for 2 h.

Electrophoretic deposition from suspension of TiO<sub>2</sub> : WO<sub>3</sub> mixtures (molar ratio in suspension 1 : 0, 1 : 1, 2 : 1, 3 : 1 and 1 : 2) in isopropanol (Fluka Analytical, 97%). To improve conductivity of dispersion media, pH of the suspension was adjusted with 1 mL HCl (Fluka Analytical, 98%). Each suspension was sonicated for 30 min. For the electrophoretic growth two 3 × 3 cm<sup>2</sup> stainless steel (grade 316) electrodes were used with distance 1 cm between them. A constant voltage of 100 V was applied to electrodes by DC Power Supply (Agilent Technologies N5772A) and held for 10 min. The deposited coatings were gradually heated (5 °C/min) and annealed at 500 °C for 2 h.

**Electrochemical anodization.** Coating of TiO<sub>2</sub> nanotube arrays were synthesized in electrochemical anodization using Ti foil (99.98% pure) and water-based electrolyte dissolving H<sub>3</sub>PO<sub>4</sub> (Enola 96%) in deionized water. For anodization process to occur NaF was dissolved in electrolyte so that F<sup>-</sup> ion wt% = 0.3, pH = 4 was adjusted by adding NaOH. Anodization was performed in two electrode cell (working electrode Ti foil, counter electrode – platinum plate, distance between electrodes 2.5 cm). Potential of 5 V was applied for 10 minutes, then anodization process was initiated at 20 V. After anodization samples were rinsed with deionized water and annealed in a muffle furnace at 500 °C for 120 minutes for crystallization of amorphous oxide. Then WO<sub>3</sub> was electro-phoretically deposited on TiO<sub>2</sub> surface from dispersed WO<sub>3</sub> in isopropanol/HCl using constant 120V potential with electrode separation of 2 cm. WO<sub>3</sub> was deposited on anodized samples at various stages before annealing and after annealing.

**Analysis of material composition, structure and morphology.** The structure of research materials was analysed by XRD (Diffractometer X'Pert Pro MPD, Cu anode, λ = 0.154 nm), morphology was studied by two different SEM systems (table-top device Phenom Pro up to 95000× magnification at 10 kV and SEM-FIB Tescan Lyra up to 30kV).

In addition, Raman spectroscopy was used (Renishaw InVia instrument with green laser (514 nm, max power 20 mW), objective ×100, laser power used 10%, 30–4000 cm<sup>-1</sup> exposure time 10 s; red laser (633 nm, max power 12.5 mW) objective ×100, laser power used 10%, 30–4000 cm<sup>-1</sup> exposure time 10 s).

**Photocatalytic measurements** were carried out using methylene blue (MB) solution under UV irradiation [28]. Each sample was placed in 80 mL of 0.43 mg/L MB solution in a quartz beaker and illuminated with Hg lamp from 30 cm distance. Each composite was used to obtain MB solution sample series after 0; 0.5; 1; 3 and 6 hours of photodegradation. Light absorption measurements (spectrophotometer Jenway 6300, 1 cm quartz cell) were used to calculate MB concentration after photodegradation had occurred.

Electrochemical photoactivity was determined using three electrode cell, where sample was used as working electrode, platinum (Pt) and calomel (SCE) respectively used as auxiliary and reference electrodes. Data were collected by potentiostat VoltaLab 40 (PGZ301 Radiometer analytical) in photoactivity measurements where the light source with 150 W xenon lamp, 10 mW/cm<sup>2</sup> was used. Photocurrent response (PCR), open circuit potential (OCP) measurements were performed in three electrode cell, sample as working electrode, Pt as auxiliary electrode and calomel as the reference electrode (SCE) was used in 1M NaOH.

### 6.3. Discussion about structure, composition and photo-electrochemical properties of TiO<sub>2</sub> – based materials

In this work multiple samples were created, Table 6.1 shows all samples discussed in this work.

Table 6.1. Synthesized samples and synthesis parameters

Mixed anodic/EPD samples					
Names	Composi-tion	Low voltage, V	Time, min	High voltage, V	Time, min
T1	TiO <sub>2</sub>	5	15	20	90
TW1	TiO <sub>2</sub> /WO <sub>3</sub>	0	0	120	0
TW2	Ti/WO <sub>3</sub>	0	0	120	6
T3	TiO <sub>2</sub>	5	10	20	90
TW3	TiO <sub>2</sub> /WO <sub>3</sub>	0	0	120	6
T4	TiO <sub>2</sub>	5	10	30	90
TW4	TiO <sub>2</sub> /WO <sub>3</sub>	0	0	0	0
T5	TiO <sub>2</sub>	7	10	20	90
TW5	TiO <sub>2</sub> /WO <sub>3</sub>	0	0	120	8
TW6	TiO <sub>2</sub>	0	0	120	6
TW7	TiO <sub>2</sub> /WO <sub>3</sub>	0	0	125	20
T8	TiO <sub>2</sub>	5	15	20	90
TW8	TiO <sub>2</sub> /WO <sub>3</sub>	0	0	120	5
Samples obtained with EPD only					
Names	<i>m</i> (TiO <sub>2</sub> ), g	<i>m</i> (WO <sub>3</sub> ), g	<i>n</i> (TiO <sub>2</sub> ), mol	<i>n</i> (WO <sub>3</sub> ), mol	<i>n</i> (TiO <sub>2</sub> ): <i>n</i> (WO <sub>3</sub> )
a	1.55	4.52	0.019	0.019	1 : 1
b	3.07	4.52	0.038	0.019	2 : 1
c	4.71	4.52	0.059	0.019	3 : 1
d	1.51	8.96	0.019	0.039	1 : 2

### Structure and morphology:

Phase composition and crystallinity were determined using XRD and Raman measurements. As shown in Fig. 6.2, EPD synthesized samples contain TiO<sub>2</sub> anatase peaks at  $2\theta = 25^\circ$  (101) and  $2\theta = 25^\circ$  (200). Similarly, anodic TiO<sub>2</sub> shows  $2\theta=25^\circ$  (101) and well known three WO<sub>3</sub> peaks at 23.2 (002), 23.7 (020), and 24.5 (200). WO<sub>3</sub> crystallite size was determined to be from 35 to 64 nm, it was estimated using  $2\theta = 23^\circ$ , whereas TiO<sub>2</sub> crystallite size was estimated to be 20 nm using  $2\theta = 25^\circ$ , it done by using Scherrer equation [44].

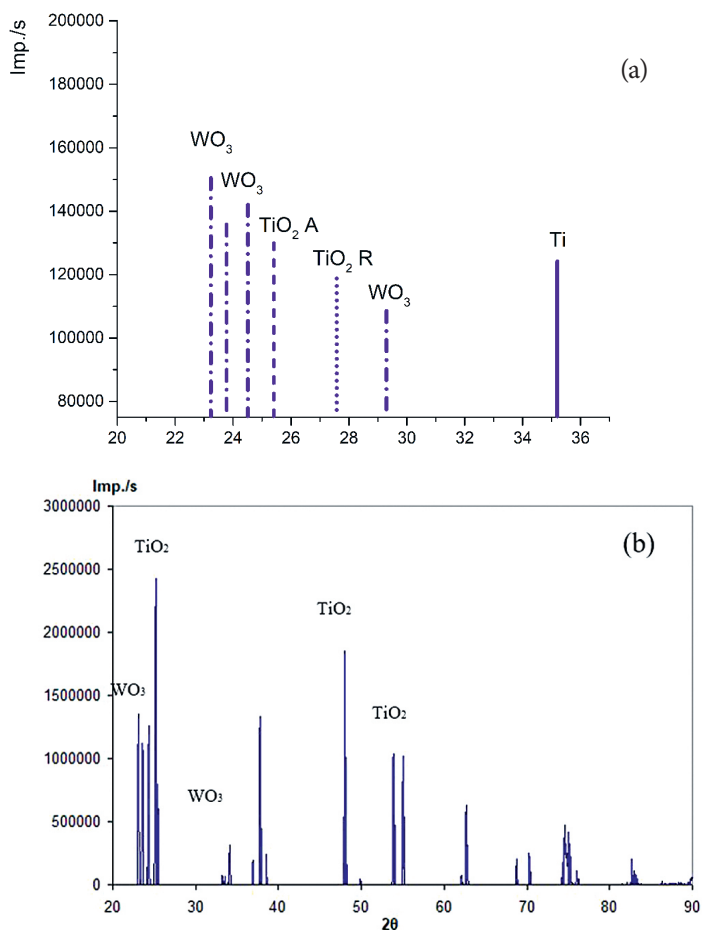
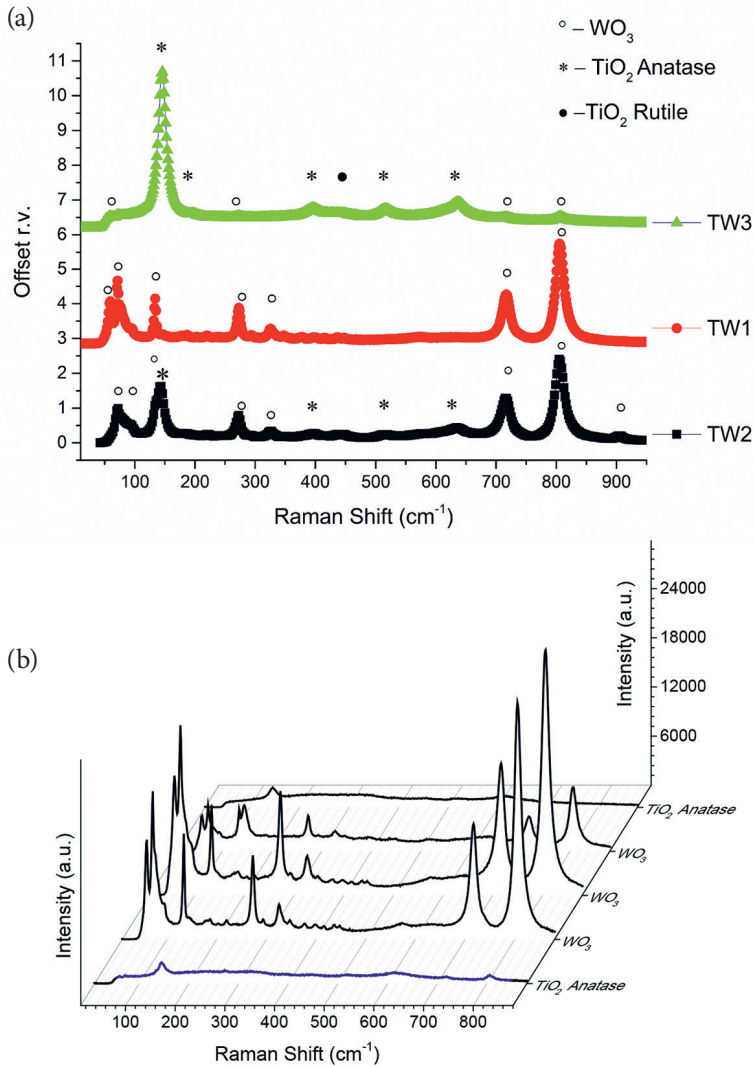


Figure 6.2. XRD data for TiO<sub>2</sub>/WO<sub>3</sub> samples a) anodic TiO<sub>2</sub> with EPD WO<sub>3</sub> sample TW8  
 b) EPD TiO<sub>2</sub>/WO<sub>3</sub> sample d.

Raman spectra indicates TiO<sub>2</sub> anatase and WO<sub>3</sub> presence, as seen in Fig. 6.3. EPD TiO<sub>2</sub>/WO<sub>3</sub> showed anatase TiO<sub>2</sub> and WO<sub>3</sub> as expected, with bands at 150, 400, 515 and 633 cm<sup>-1</sup> for TiO<sub>2</sub> and 274, 327, 716 and 806 cm<sup>-1</sup> for WO<sub>3</sub>. Though anodic TiO<sub>2</sub> with EPD WO<sub>3</sub> indicated bands at 144, 395, 516, 635 cm<sup>-1</sup> and 57, 70, 132, 273, 716, 806 cm<sup>-1</sup> for WO<sub>3</sub>. Additionally, performing Raman mapping of the anodic/EPD sample surface for WO<sub>3</sub> particle distribution.



**Figure 6.3.** Raman investigation of anodic TiO<sub>2</sub> with EPD WO<sub>3</sub>. Clear anatase phase and WO<sub>3</sub> are present, as seen in image a), TW3 shows clear TiO<sub>2</sub>, TW1 and TW2 is standard WO<sub>3</sub>. Image b) Raman surface mapping of sample TW1, low intensity TiO<sub>2</sub> and higher intensity WO<sub>3</sub> bands indicate WO<sub>3</sub> particles on surface

After comparison of results with known Raman band positions, it was noted that some TiO<sub>2</sub> and WO<sub>3</sub> bands are shifted compared to known values. That indicates a change in particle size after the heat treatment, thus, a probable change in band gap. Full comparison of measured band positions with known values is depicted in Table 6.2.

Table 6.2. Characteristic Raman bands in vibration spectra of WO<sub>3</sub>

Band position, cm <sup>-1</sup>	Vibrations*	Source
949	$\nu_s$ (W = O ter.)	[45]
806	$\nu_a$ (W-O-W)	[45]
801	" "	[46]
805	" "	[46]
806	" "	[47]respectively, of well-defined W(VI
806	" "	This work, sample TW1
806	" "	Sample b
695	$\nu$ (W <sub>2</sub> O <sub>6</sub> &W <sub>3</sub> O <sub>8</sub> )	[45]
710	" "	[45]
715	" "	[46]
712	" "	[47]respectively, of well-defined W(VI
716	" "	This work, Sample TW1
716	" "	Sample b
518	(O-Lattice)	[45]
316	(WO <sub>3</sub> )	[45]
322	" "	[46]
324	" "	[46]
256	$\nu$ (O-W-O) $\delta$ (O-W-O)	[45]
262	" "	[48]
270	" "	[46]
270	" "	[47]respectively, of well-defined W(VI
274	" "	Sample b
272	" "	This work, Samples TW1, TW2
194	W-W	[45]
180	" "	[46]
130	" "	[46]
76	" "	Sample b
65	" "	[45]

From SEM images self-organized TiO<sub>2</sub> tubes (Fig. 6.4 (a) and (b)) can be seen as well as deposited WO<sub>3</sub> on the surface as seen in Fig. 6.4 (c) and (d). In EPD samples, WO<sub>3</sub> showed 200 to 400 nm particles and similar results were gained for anodic/EPD samples.

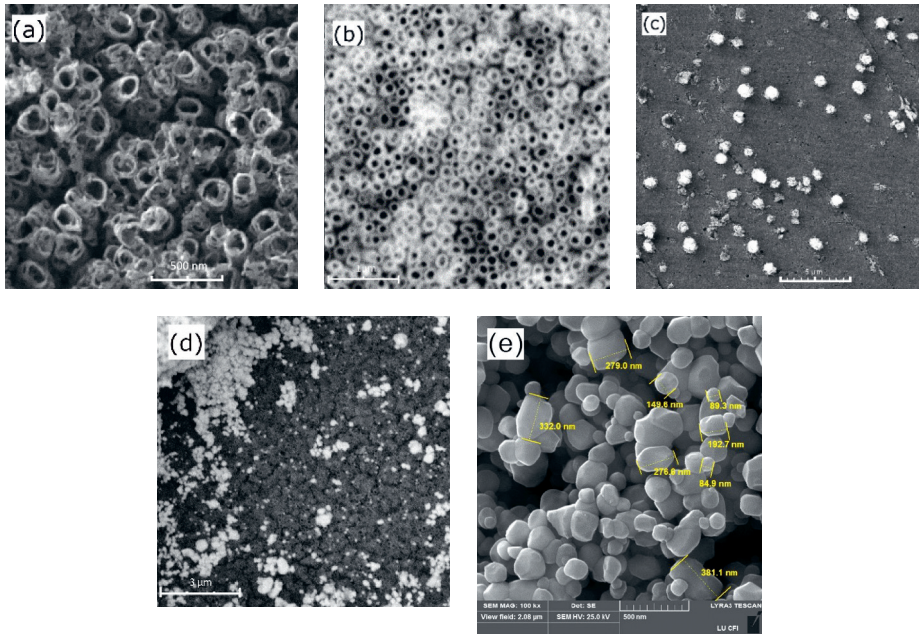


Figure 6.4. SEM images of sample surface. (a) and (b) Anodic  $\text{TiO}_2$  in tubular form, (d) and (c)  $\text{TiO}_2$  surface after deposited  $\text{WO}_3$ , (e) EPD synthesized sample surface

Photocatalytic activity was determined through MB degradation and photoelectrochemical properties such as photocurrent response, open circuit potential, EPD samples showed slower initial MB degradation as showed in Fig. 6.5 indicating that absorption and dissociation of water in contact with oxygen bridges, that is followed by oxide and superhydroxide species that performs the degradation of MB molecules. From MB degradation samples with resulting  $\text{WO}_3$  content of 17.8%. With higher concentration  $\text{WO}_3$  (19.9 wt%) MB degradation rate was lowest, thus showing that proper  $\text{TiO}_2/\text{WO}_3$  ratio is crucial for highest photocatalytic properties.

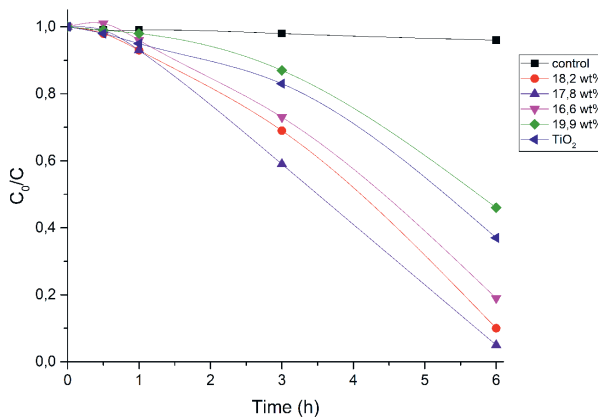


Figure 6.5. MB degradation by EPD  $\text{TiO}_2/\text{WO}_3$  mixture. Clear indication that proper ratio of  $\text{WO}_3$  to  $\text{TiO}_2$  for increase in photocatalytic activity

Anodic samples also provided similar results, proper ratio is necessary for higher photocatalytic activity as indicated in Fig. 6.6 (a) and (c). Secondary heat treatment can lower photocatalytic activity, as seen in Fig. 6.6 (b), due to change in crystallite size and band gap as well as possible defect creation. Fig. 6.6 (c) show OCP comparison between various anodic TiO<sub>2</sub> with EPD WO<sub>3</sub>, as one can see, the sample TW2 shows the highest potential in comparison to other samples.

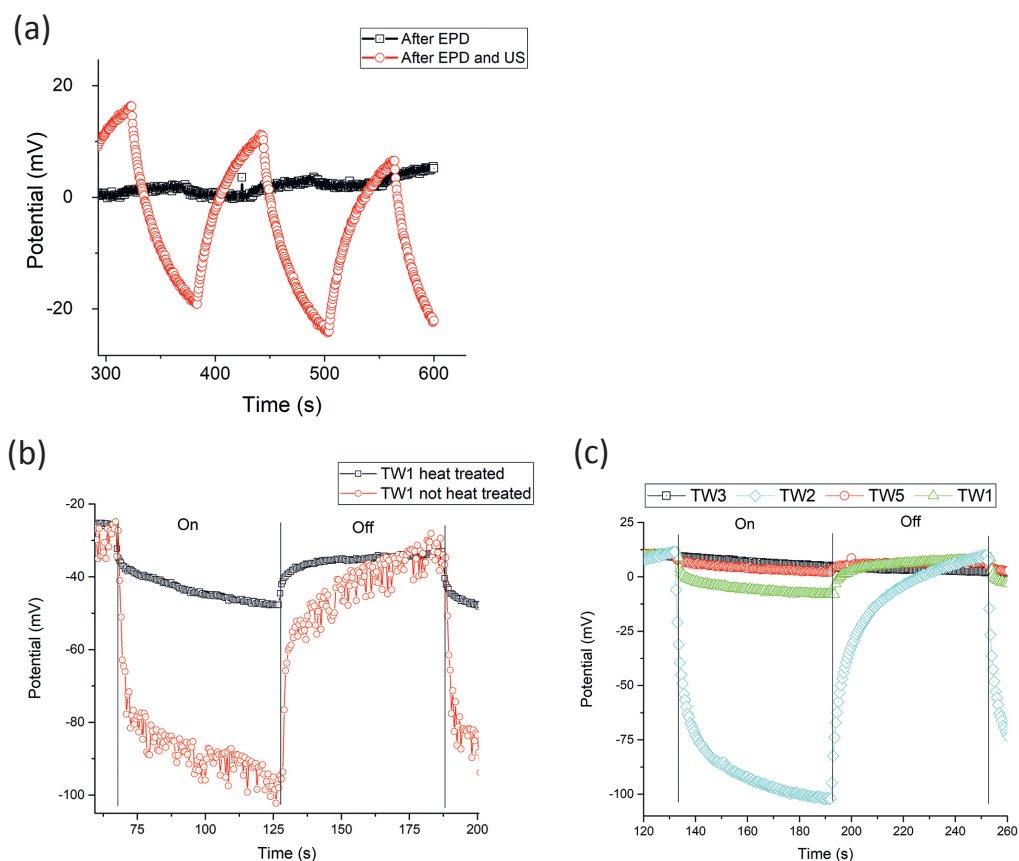


Figure 6.6. OCP comparison for anodic TiO<sub>2</sub> samples with EPD WO<sub>3</sub>.

(a) proper TiO<sub>2</sub>/WO<sub>3</sub> ratio is necessary (b) additional heat treatment lowers OCP and thus photocatalytic activity (c) various anodic/EPD samples, sample with proper TiO<sub>2</sub>/WO<sub>3</sub> ratio shows highest OCP value

Investigation of optical band gap can be performed by finding absorption coefficient. Due to TiO<sub>2</sub> and WO<sub>3</sub> being deposited on non-transparent substrates absorption coefficient and optical band gap can be found from reflectance spectra using Kubelka-Munk transformation [49, 50]. As seen in Fig. 6.7, samples with WO<sub>3</sub> has lower optical absorption edge in comparison to only TiO<sub>2</sub> samples.

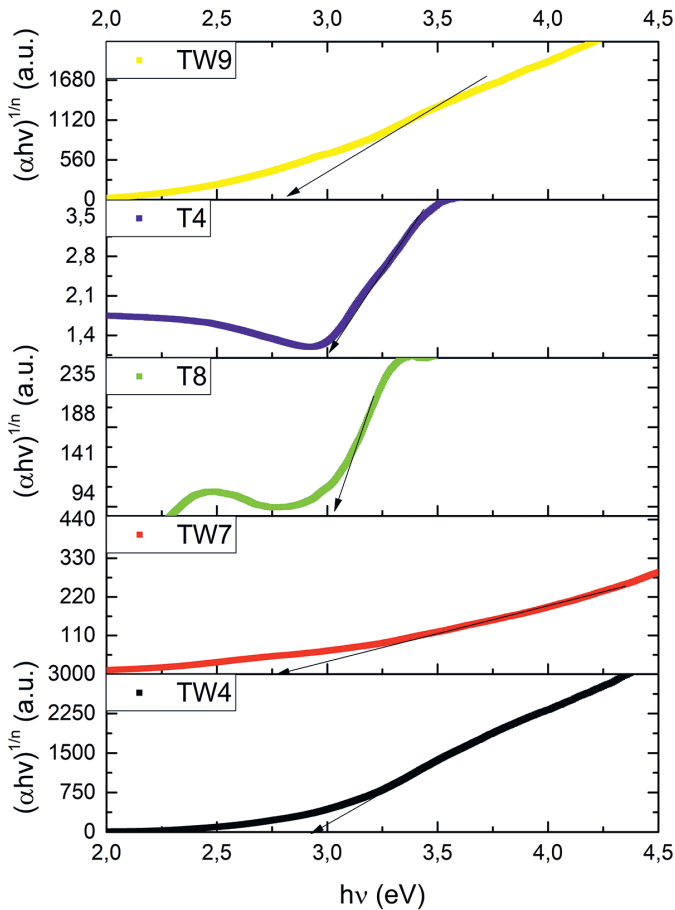


Figure 6.7. Optical absorption edge determination through Kubelka-Munk transformation of reflectance spectra

#### 6.4. Conclusions

Investigation of two methodologies of photoanode synthesis was done through electrochemical anodization and electrophoretic deposition. Structural investigation indicated that after secondary heat treatment  $\text{TiO}_2$  and  $\text{WO}_3$  do not undergo phase transition. Upon further investigation Raman spectroscopy showed band position shifts that indicate change in particle size. Optical band gap investigation showed that combination of  $\text{TiO}_2$  with  $\text{WO}_3$  lowers band gap of material, coinciding with literature data. Secondary heat treatment might influence band gap size, but the influence is rather small.

Photocatalytic activity measurements clearly showed that  $\text{TiO}_2/\text{WO}_3$  ratio directly influences photoactivity as by increasing of the  $\text{WO}_3$  content photocatalytic activity also increases but after certain point it starts to decrease. Anodic  $\text{TiO}_2$  with  $\text{WO}_3$  showed similar results. In addition, secondary heat treatment lowered photoactivity, probably due to increased grain boundary or crystallite size change.

## 6.5. References

1. Züttel, A., Borgschulte, A. and Schlapbach, L. (eds.). (2008) Hydrogen as a future energy carrier. *Journal of Applied Electrochemistry*, 38(10), Wiley-VCH.
2. Fujishima, A. and Honda, K. (1972) Electrochemical Photolysis of Water at a Semiconductor Electrode. *Nature*, 238, 37–38.
3. Nakajima, A., Hashimoto, K., Watanabe, T., Takai, K., Yamauchi, G. and Fujishima, A. (2000) Transparent superhydrophobic thin films with self-cleaning properties. *Langmuir*, 16, 7044–7047.
4. Grimes, C. A. and Mor, G. K. (2009) *TiO<sub>2</sub> Nanotube Arrays*. Boston, MA: Springer US.
5. Oza, G., Pandey, S., Gupta, A., Shinde, S., Mewada, A., Jagadale, P., Sharon, M. and Sharon, M. (2013) Photocatalysis-assisted water filtration: using TiO<sub>2</sub>-coated vertically aligned multi-walled carbon nanotube array for removal of Escherichia coli O157:H7. *Mater. Sci. Eng. C. Mater. Biol. Appl.*, 33, 4392–4400.
6. Jamil, T. S., Ghaly, M. Y., Fathy, N. A., Abd El-Halim, T. A. and Österlund, L. (2012) Enhancement of TiO<sub>2</sub> behavior on photocatalytic oxidation of MO dye using TiO<sub>2</sub>/AC under visible irradiation and sunlight radiation. *Sep. Purif. Technol.*, 98, 270–279.
7. Tang, Y., Luo, S., Teng, Y., Liu, C., Xu, X., Zhang, X. and Chen, L. (2012) Efficient removal of herbicide 2,4-dichlorophenoxyacetic acid from water using Ag/reduced graphene oxide co-decorated TiO<sub>2</sub> nanotube arrays. *J. Hazard. Mater.*, 241–242, 323–330.
8. Houas, A. (2001) Photocatalytic degradation pathway of methylene blue in water. *Appl. Catal. B. Environ.*, 31, 145–157.
9. Pichat, P. (2013) *Photocatalysis and Water Purification: From Fundamentals to Recent Applications*. Wiley, 438 pages, ISBN: 978-3-527-33187-1
10. Sayes, C. M., Wahi, R., Kurian, P. A., Liu, Y., West, J. L., Ausman, K. D., Warheit, D. B. and Colvin, V. L. (2006) Correlating nanoscale titania structure with toxicity: A cytotoxicity and inflammatory response study with human dermal fibroblasts and human lung epithelial cells. *Toxicol. Sci.*, 92, 174–185.
11. Fujishima, A., Zhang, X. and Tryk, D. (2008) TiO<sub>2</sub> photocatalysis and related surface phenomena. *Surf. Sci. Rep.*, 63, 515–582.
12. Fujishima, A., Rao, T. N. and Tryk, D. A. (2000) Titanium dioxide photocatalysis 1, *Journal of Photochemistry and Photobiology C Photochemistry Reviews*, 1–21.
13. Young, K. J., Martini, L., Milot, R. L., Snoeberger, R. C., Batista, V. S., Schmuttenmaer, C., Crabtree, R. H., Brudvig, G. W., (2012) Light-driven water oxidation for solar fuels. *Coord. Chem. Rev.*, 256, 2503–2520.
14. Ilie, M., Cojocaru, B., Parvulescu, V. I. and Garcia, H. (2011) Improving TiO<sub>2</sub> activity in photo-production of hydrogen from sugar industry wastewaters. *Int. J. Hydrogen Energy*, 36, 15509–15518.
15. Serrano, B. and de Lasa, H. (1997) Photocatalytic Degradation of Water Organic Pollutants. Kinetic Modeling and Energy Efficiency. *Ind. Eng. Chem. Res.*, 36, 4705–4711.
16. Rajeshwar, K., Osugi, M. E., Chanmanee, W., Chenthamarakshan, C. R., Zaroni, M. V. B., Kajitvichyanukul, P. and Krishnan-Ayer, R. (2008) Heterogeneous photocatalytic treatment of organic dyes in air and aqueous media. *J. Photochem. Photobiol. C Photochem. Rev.*, 9, 171–192.
17. Wang, J., Yang, G., Lyu, W. and Yan, W. (2016) Thorny TiO<sub>2</sub> nanofibers: Synthesis, enhanced photocatalytic activity and supercapacitance. *J. Alloys Compd.*, 659, 138–145.
18. Abdullah, H., Khan, M. M. R., Ong, H. R. and Yaakob, Z. (2017) Modified TiO<sub>2</sub> photocatalyst for CO<sub>2</sub> photocatalytic reduction: An overview. *J. CO<sub>2</sub> Util.*, 22, 15–32.
19. Li, X. Z., Li, F. B., Yang, C. L. and Ge, W. K. (2001) Photocatalytic activity of WO<sub>x</sub>-TiO<sub>2</sub> under visible light irradiation. *J. Photochem. Photobiol. A Chem.*, 141, 209–217.
20. Šutka, A., Vanags, M., Joost, U., Šmits, K., Ruža, J., Ločs, J., Kleperis, J. and Juhna, T. (2018) Aqueous synthesis of Z-scheme photocatalyst powders and thin-film photoanodes from earth abundant elements. *J. Environ. Chem. Eng.*, 6, 2606–2615.

21. Georgieva, J., Valova, E., Armyanov, S., Philippidis, N., Poullos, I. and Sotiropoulos, S. (2012) Bi-component semiconductor oxide photoanodes for the photoelectrocatalytic oxidation of organic solutes and vapours: A short review with emphasis to TiO<sub>2</sub>-WO<sub>3</sub> photoanodes. *J. Hazard. Mater.*, 211–212, 30–46.
22. Edelmánová, M., Lin, K. Y., Wu, J. C. S., Troppová, I., Čapek, L. and Kočí, K. (2018) Photocatalytic hydrogenation and reduction of CO<sub>2</sub> over CuO/ TiO<sub>2</sub> photocatalysts. *Appl. Surf. Sci.*, 454, 313–318.
23. Nunez, M., Forgan, B. and Roy, C. (1994) Estimating ultraviolet radiation at the earth's surface. *Int. J. Biometeorol.*, 38, 5–17.
24. Nazari, M., Golestani-Fard, F., Bayati, R. and Eftekhari-Yekta, B. (2015) Enhanced photocatalytic activity in anodized WO<sub>3</sub>-loaded TiO<sub>2</sub> nanotubes. *Superlattices and Microstruct.*, 80, 91–101.
25. Kmentova, H., Kment, S., Wang, L., Pausova, S., Vaclavu, T., Kuzel, R., Han, H., Hubicka, Z., Zlamal, M., Olejnicek, J., Cada, M., Krysa, J. and Zboril, R. (2016) Photoelectrochemical and structural properties of TiO<sub>2</sub> nanotubes and nanorods grown on FTO substrate: Comparative study between electrochemical anodization and hydrothermal method used for the nanostructures fabrication. *Catal. Today*, 287, 130–136.
26. Ashokkumar, M. (1998) An overview on semiconductor particulate systems for photoproduction of hydrogen. *Int. J. Hydrogen Energy*, 23, 427–438.
27. Anandan, S., Sivasankar, T. and Lana-Villarreal, T. (2014) Synthesis of TiO<sub>2</sub>/WO<sub>3</sub> nanoparticles via sonochemical approach for the photocatalytic degradation of methylene blue under visible light illumination. *Ultrason. Sonochem.*, 21, 1964–1968.
28. Liepina, I., Bajars, G., Rublans, M., Kleperis, J., Lusiš, A. and Pentjuss, E. (2015) Structure and Photocatalytic Properties of TiO<sub>2</sub> -WO<sub>3</sub> Composites Prepared by Electrophoretic Deposition. *IOP Conf. Ser. Mater. Sci. Eng.*, 77, 012039.
29. Ghobadi, A., Ulusoy, T. G., Garifullin, R., Guler, M. O. and Okyay, A. K. (2016) A heterojunction design of single layer hole tunneling ZnO passivation wrapping around TiO<sub>2</sub> nanowires for superior photocatalytic performance. *Sci. Rep.*, 6, 30587.
30. Jagminas, A., Kovger, J., Rėza, A., Niaura, G., Juodkazytė, J., Selskis, A., Kondrotas, R., Šebeka, B. and Vaičiūnienė, J. (2014) Decoration of the TiO<sub>2</sub> nanotube arrays with copper suboxide by AC treatment. *Electrochim. Acta*, 125, 516–523.
31. Cong, Y., Li, Z., Zhang, Y., Wang, Q. and Xu, Q. (2012) Synthesis of Fe<sub>2</sub>O<sub>3</sub>/TiO<sub>2</sub> nanotube arrays for photoelectro-Fenton degradation of phenol. *Chem. Eng. J.*, 191, 356–363.
32. Zhao, D. and Yang, C.-F. (2016) Recent advances in the TiO<sub>2</sub>/CdS nanocomposite used for photocatalytic hydrogen production and quantum-dot-sensitized solar cells. *Renew. Sustain. Energy Rev.*, 54, 1048–1059.
33. Haro, M., Abargues, R., Herraiz-Cardona, I., Martínez-Pastor, J. and Giménez, S. (2014) Plasmonic versus catalytic effect of gold nanoparticles on mesoporous TiO<sub>2</sub> electrodes for water splitting. *Electrochim. Acta*, 144, 64–70.
34. Rumaiz, A. K., Woicik, J. C., Cockayne, E., Lin, H. Y. and Jaffari, G. H. (2009) Oxygen vacancies in N doped anatase TiO<sub>2</sub>: Experiment and first-principles calculations. *Applied Physics Letters*, 95(26), Article ID 262111, 6–9.
35. Samsudin, E. M. and Abd Hamid, S. B. (2017) Effect of band gap engineering in anionic-doped TiO<sub>2</sub> photocatalyst. *Appl. Surf. Sci.*, 391, 326–336.
36. Wang, W., Zhou, Q., Fei, X., He, Y., Zhang, P., Zhang, G., Peng, L. and Xie, W. (2010) Synthesis of CuO nano- and micro-structures and their Raman spectroscopic studies. *Cryst. Eng. Comm.*, 12, 2232–2237.
37. Lisovski, O., Chesnokov, A., Piskunov, S., Bocharov, D., Zhukovskii, Y. F., Wessel, M. and Spohr, E. (2016) Ab initio calculations of doped TiO<sub>2</sub> anatase (101) nanotubes for photocatalytical water splitting applications. *Mater. Sci. Semicond. Process.*, 42, 138–141.
38. Macak, J. M., Gong, B. G., Hueppe, M. and Schmuki, P. (2007) Filling of TiO<sub>2</sub> nanotubes by self-doping and electrodeposition. *Adv. Mater.*, 19, 3027–3031.

39. Jafari, T., Moharreri, E., Amin, A., Miao, R., Song, W. and Suib, S. (2016) Photocatalytic Water Splitting – The Untamed Dream: A Review of Recent Advances. *Molecules*, 21, 900.
40. González-Borrero, P. P., Sato, F., Medina, A. N., Baesso, M. L., Bento, A. C., Baldissera, G., Persson, C., Niklasson, G. A., Granqvist, C. G. and Ferreira Da Silva, A. (2010) Optical band-gap determination of nanostructured WO<sub>3</sub> film. *Appl. Phys. Lett.*, 96, 4–6.
41. Qamar, M., Drmosh, Q., Ahmed, M. I., Qamaruddin, M. and Yamani, Z. H. (2015) Enhanced photoelectrochemical and photocatalytic activity of WO<sub>3</sub>-surface modified TiO<sub>2</sub> thin film. *Nanoscale Res. Lett.*, 10, 54.
42. Besra, L. and Liu, M. (2007) A review on fundamentals and applications of electrophoretic deposition (EPD). *Prog. Mater. Sci.*, 52, 1–61.
43. Djošić, M. S., Miskovic-Stankovic, V. B., Janačković, D. T., Kačarević-Popović, Z. M. and Petrović, R. D. (2006) Electrophoretic deposition and characterization of boehmite coatings on titanium substrate. *Colloids Surfaces A Physicochem. Eng. Asp.*, 274, 185–191.
44. Patterson, A. L. (1939) The Scherrer Formula for X-Ray Particle Size Determination. *Phys. Rev.*, 56, 978–982.
45. Díaz-Reyes, J., Dorantes-García, V., Pérez-Benítez, A. and Balderas-López, J. A. (2008) Obtaining of films of tungsten trioxide (WO<sub>3</sub>) by resistive heating of a tungsten filament. *Superf. y Vacío*, 21, 12–17.
46. Diaz-Reyes, J., Flores-Mena, J. E., Gutierrez-Arias, J. M., Morin-Castillo, M. M., Azucena-Coyotecatl, H., Galván, M., Rodriguez-Fragoso, P. and Mendez-López, A. (2010) Optical and structural properties of WO<sub>3</sub> as a function of the annealing temperature. In: Frazao, O. (ed.). *Sensig Materials. Proceedings of the 3rd WSEAS International Conference on Advances in Sensors, Signals and Materials*, 99–104.
47. Ross-Medgaarden, E. I. and Wachs, I. E. (2007) Structural Determination of Bulk and Surface Tungsten Oxides with UV-vis Diffuse Reflectance Spectroscopy and Raman Spectroscopy. *J. Phys. Chem. C*, 111, 15089–15099.
48. Choi, H. C., Jung, Y. M. and Kim, S. Bin. (2005) Size effects in the Raman spectra of TiO<sub>2</sub> nanoparticles. *Vib. Spectrosc.*, 37, 33–38.
49. Kubelka, P. (1948). *New Contributions to the Optics of Intensely Light-Scattering Materials Part I. J. Opt. Soc. Am.*, 38, 448.
50. Kubelka, P. (1954) *New Contributions to the Optics of Intensely Light-Scattering Materials Part II: Nonhomogeneous Layers. J. Opt. Soc. Am.*, 44, 330.

## 6.6. Kopsavilkums

Lai risinātu pasaules enerģijas iegūšanas un izmantošanas problēmas, kā arī pārietu uz ilgtspējīgiem un videi draudzīgiem risinājumiem, tiek meklēti atjaunojami energoresursi un jaunas tehnoloģijas. Kā viens no daudzsoļiem risinājumiem ir fotokatalītisku materiālu izmantošana gaisa, ūdens attīrīšanai, kā arī enerģijas iegūšanai un uzglabāšanai ūdeņraža formā, kur ūdeņradi iespējams iegūt, fotokatalītiski sadalot ūdeni. Tiek meklēti dažādi materiāli šīs funkcijas veikšanai, piemēram, titāna dioksīds (TiO<sub>2</sub>), volframa trioksīds (WO<sub>3</sub>), dzelzs oksīdi, kadmija selenīds (CdS), vara oksīdi, cinka oksīds un citi. Fotokatalīzes procesā svarīgu vietu ieņem materiāla aizliegtās zonas platums, tam jābūt pēc iespējas šaurākam, lai iekļautos redzamās gaismas diapazonā, jo līdz Zemes virsmai nonāk 3–5% no UV starojuma (kurā darbojas lielākā daļa fotokatalītiski aktīvo materiālu), bet redzamā gaisma ir 40%. TiO<sub>2</sub> ir viens no daudzsoļiem fotokatalizatoriem, tas ir fotoķīmiski izturīgs, relatīvi vienkārši iegūstams, bet tā absorbcijas mala ir UV diapazonā.

Kombinējot dažādus materiālus, iespējams iegūt fotokatalizatoru ar mazāku absorbcijas malu un lielāku fotokatalītisko aktivitāti, piemēram, TiO<sub>2</sub>/WO<sub>3</sub>. Šajā darbā tiek dots pārskats par heterostruktūru un tās fizikālajām un fotoķīmiskajām īpašībām.

Tika izveidotas divas paraugu sērijas – viena, lietojot  $\text{TiO}_2$  un  $\text{WO}_3$  pulverus dažādās attiecībās (a, b, c, d paraugs). Otra – elektroķīmiski audzētas  $\text{TiO}_2$  nanostruktūras, kurām uzklāts  $\text{WO}_3$  pulveris. Pulveru uzklāšanu veikta ar elektroforēzes metodi (EPD).

Paraugu morfoloģija tika pētīta ar skenējošo elektronu mikroskopu (SEM). Strukturālās īpašības tika noteiktas, lietojot rentgenstaru difrakciju (XRD) un Ramana spektroskopiju. Optiskās īpašības pētītas, lietojot difūzo atstarošanu un Kubelkas–Munka transformāciju. Savukārt fotokatalītiskās īpašības noteiktas, izmantojot atvērtās ķēdes potenciāla (OCP), fotostrāvas (PCR) un metilēnzilā sadalīšanās mērījumus.

Morfoloģijas pētījumi atklāja, ka, izmantojot EPD metodi,  $\text{WO}_3$  (redzami 6.4. e attēlā) ir uzklāts vienmērīgā kārtā uz  $\text{TiO}_2$  virsmas ar daļiņu izmēru 200 līdz 400 nm, savukārt anodēts  $\text{TiO}_2$  (redzams 6.4. a attēlā) atklāja pašorientētu nanocauruļu morfoloģiju ar daudz lielāku aktīvo virsmu. Gan tikai EPD metodē iegūtās  $\text{TiO}_2/\text{WO}_3$  kārtiņas, gan arī anodēts  $\text{TiO}_2$  ar EPD metodē uzklātu  $\text{WO}_3$  uzrāda abu oksīdu esamību uz virsmas, pirmajā gadījumā – vienmērīgs daļiņu sadalījums uz pamatnes un otrajā gadījumā – atsevišķas  $\text{WO}_3$  daļiņas uz virsmas. SEM mērījumi pierāda, ka  $\text{WO}_3$  uznešanas laikā iespējams pārklāt visu  $\text{TiO}_2$  virsmu, samazinot kopējo aktīvās virsmas laukumu, tādējādi samazinot kompozīta fotoaktivitāti. Šie mērījumi apliecina, ka fotokatalītisko īpašību uzlabošanai nepieciešams izmantot optimālu oksīdu attiecību.

Struktūras pētījumi uzrādīja, ka visi paraugi satur kristāliskās fāzes  $\text{TiO}_2$  un  $\text{WO}_3$ . Pārsvārā  $\text{TiO}_2$  tika iegūts anatāza fāzē, ko apstiprina zinātniskās literatūras un empīriskie dati – karsējot  $\text{TiO}_2$  līdz 500 °C, fāžu pāreja anatāzs-rutils vēl nenotiek. Novērtējot XRD datus, tika noteikts raksturīgais kristalītu izmērs –  $\text{WO}_3$  35 līdz 64 nm un  $\text{TiO}_2$  ap 20 nm. Tika novērots, ka atkārtotas karsēšanas gadījumā  $\text{WO}_3$  notiek Ramana piķu pārbīde (skatīt apkopotos rezultātus 2. tabulā). Nobīde var būt saistīta ar kristalītu lieluma izmaiņu vai karsēšanas rezultātā iegūtiem skābekļa nestehiometrijas defektiem. Precīza mehānisma noskaidrošanai jāveic tālāka izpēte.

Fotokatalītisko īpašību pētījumi skaidri parāda, ka ir optimāla oksīdu daudzumu attiecība, pie kuras iegūst fotokatalītiskās aktivitātes pieaugumu. Nesasniedzot un pārsniedzot šo lielumu, aktivitāte pie noteiktiem apstākļiem, piemēram, aizsegta  $\text{TiO}_2$  virsmas vai liela robežvirsmas laukuma, kļūst mazāka nekā tīram  $\text{TiO}_2$ , kā tas ir redzams 6.5. un 6.6. attēlā. Tika arī noskaidrots aizliegtās zonas platums (6.7 attēls), kas apstiprināja absorbcijas malas pārbīdi no 3.2 eV  $\text{TiO}_2$  paraugiem uz 2.7–2.8 eV kompozītam  $\text{TiO}_2/\text{WO}_3$ .

Savienojot  $\text{TiO}_2$  ar  $\text{WO}_3$ , iespējams pārbīdīt optiskās absorbcijas malas novietojumu redzamās gaismas diapazonā, tādējādi palielinot materiāla fotokatalītiskās īpašības. Savukārt, veidojot fotokatalizatoru, nepieciešams atrast un optimizēt abu oksīdu daudzumu attiecību augstākās aktivitātes iegūšanai.

## 7. Synthesis and research of nanosized materials for hydrogen storage applications

### Nanomateriālu sintēze un pētījumi ūdeņraža uzglabāšanas pielietojumiem

Pēteris Lesničenoks, Ingars Lukoševičs, Līga Grīnberga, Jānis Kleperis

Institute of Solid State Physics, University of Latvia  
Kengaraga iela 8, Rīga, LV-1063, Latvia  
E-mail: [peteris.lesnicenoks@cfi.lu.lv](mailto:peteris.lesnicenoks@cfi.lu.lv)

#### Contents

<i>7. Synthesis and research of nanosized materials for hydrogen storage applications</i>	
7.1. Review of nanosized materials for energy storage. . . . .	139
7.2. Methods to synthesize and research nanosized materials. . . . .	142
7.3. Results and discussion of hydrogen absorption peculiarities in nanosized materials . . . . .	144
7.4. Conclusions . . . . .	148
7.5. References . . . . .	149
7.6. Kopsavilkums . . . . .	150

#### 7.1. Review of nanosized materials for energy storage

On November 28, 2018, the European Commission published a strategic long-term vision for a prosperous, modern, competitive and climate neutral economy by 2050 – A Clean Planet for All [1]. The most efficient actions are presented that can lead to achieving net-zero greenhouse gas emissions by 2050 in a cost-efficient manner. The EU, responsible for 10% of global greenhouse gas emissions, is a global leader in the transition towards a net-zero-greenhouse gas emissions economy. The eight scenarios build upon no regret policies such as strong usage of renewable energy and energy efficiency. Most of them look at different technologies and actions, which foster the move towards a net-zero greenhouse gas economy. They vary the intensity of application of electrification, hydrogen and e-fuels (i. e. power-to-X), as well as the end user energy efficiency and the role of a circular economy as actions to reduce emissions. In all these pathways electricity consumption increases, but notable differences exist. The pathways that focus predominantly on electrification in end-use sectors see also the need for high deployment of energy storage (6 times today's levels) to deal with variability in the electricity system. To facilitate the transition from fossil fuels to technologies based on clean and renewable resources, problems concerning the energy storage must be solved. Wind and sun are the

most popular renewable energy sources, but they are available occasionally or periodically, that is, not at all times required by consumption [2]. Compared to electricity, hydrogen is an ideal energy carrier, because it can be stored almost without losses. In transport sector, hydrogen fuel cell technologies are currently being commercialized (Toyota, Hyundai from 2015), using hydrogen storage in the form of high pressure (700 bar) tanks [3]. The technology and economical means to make carbon composite high pressure tanks capable of providing travel distances up to 700 km – are well understood and the costs are reasonable. International Partnership of Hydrogen Energy (IPHE) [4] has gathered information about an impressive number (>4500) of already realized hydrogen demonstration projects in 9 countries: Australia, Canada, China, Germany, Japan, Korea, New Zealand, Norway, United States of America, and number of active on 2018 hydrogen filling stations (Table 7.1). In the near future, the demand for inexpensive and “green” hydrogen will increase, especially for transportation purposes [1].

*Table 7.1. Number of active hydrogen filling stations in 2018 worldwide*

Number of active hydrogen filling stations 2018			
State	Number	State	Number
Japan	93	Belgium	3
Germany	44	India	3
USA	39	Netherland	3
South Korea	12	Australia	2
England	11	Finland	2
Denmark	10	Brazil	1
Norway	9	Costa Rica	1
France	9	Czech Republic	1
China	8	Slovenia	1
Canada	6	Taiwan	1
Austria	5	Turkey	1
Italy	4	United Arab Emirates	1
Scotland	4	Wales	1
Spain	4		
Sweden	4		
Switzerland	4	<b>Total 2018:</b>	<b>287</b>

Source: The Hydrogen Tools Portal: <https://h2tools.org/>

High pressure composite vessels can be charged only using powerful multi-stage compressors, which is profitable at filling stations, but not in the private sector and small farms. Creating a capacious, not too heavy and large containers with porous, solid materials containing stored hydrogen could solve this problem, because these materials can be recharged at low pressures, for example, at which typical electrolyzers work (up to

30 bar). Regarding the application of this technology for vehicles, the materials with high volumetric and gravimetric densities of hydrogen storage are required [3–5].

Researchers from institutions worldwide are focusing on storage targets defined by DOE [5] of on-board vehicular hydrogen storage systems allowing millage greater than 500 km, while meeting packaging, cost, safety, and performance requirements to be competitive with current vehicles. The respective DOE target for the year 2020 is 4.5 wt% (kg H<sub>2</sub>/kg system) at 233–358 K and 3–100 bars, but ultimate target – 6.5 wt% [5]. Hydrogen safety aspects are important and as it is recognized for transport applications, safest storage method is solid state storage [5, 6]. Different traditional and innovative materials are researched for solid state hydrogen storage, including high surface area adsorbents, metal organic frameworks, and metal hydrides, as well as the approaches that are regenerable off-board such as chemical hydrides and liquid carrier [3, 7].

High surface adsorbents (zeolite and graphene) are the subject of this research. Zeolites as media for hydrogen storage are researched by different authors, and common recognition is that hydrogen adsorbs on zeolites mostly at cryogenic temperatures (below 100 K) [8]. Intercalation of metals in zeolites enhances the amount of adsorbed hydrogen, but no information is found about increase of adsorption temperatures. Different mechanisms are proposed to explain hydrogen binding with zeolites. Xiaoming Du [8] proposes that intercalated cations and oxygen atoms of the framework on pore surfaces are the main adsorption sites of hydrogen molecules at lower temperature, whereas the stable adsorption sites are only oxygen atoms of zeolites framework at higher temperature. Optimum thermodynamic and kinetic windows are needed for hydrogen absorption and desorption in solids at reasonable temperatures and pressures [9]. The pores in zeolites with dimensions of 4 Å – 7 Å are suitable to store hydrogen molecules with kinetic diameter of 2.89 Å up to 1.74% weight fraction, as it is shown, at low temperature (–196 °C) and H<sub>2</sub> pressure (15 bar) [10]. Recently, it was announced that at low temperatures (–196 °C) zeolite templated carbons show an exceptional gravimetric hydrogen uptake – weight fraction 7.3% at 20 bars [11], which is the highest recorded figure for carbon materials. Only some of the research is devoted to hydrogen storage capability in zeolite-type structures at higher temperatures. Weitkamp, et al. in 1993 [12] reported that the zeolites containing sodalite cages in their structure show hydrogen storage capacity 9.2 cm<sup>3</sup>/g, if loaded at 573 K and at 10.0 MPa.

Carbon nanostructured materials (nanotubes, nanoballs (fullerenes), nanosheets (graphene)) are novel nanoporous materials with ability to become most promising materials for future hydrogen storage [9]. The hydrogen storage in carbon nanomaterials is probably the most controversial topic as far as the solid state hydrogen storage is concerned – the reported gravimetric storage capacity between 10 and 20 wt% was not confirmed [3, 14]. Its storage capacity diminishes to less than 1.0 wt% at the room temperature. Re-adsorption data of Pd, and V-doped CNTs have indicated that more than 70% of hydrogen is spilled onto the low-energy binding sites, such as external wall or groove sites of nanotubes [15]. Transition metal doped CNTs increases the hydrogen adsorption at least by 30%, and it has indicated that more than 70% of hydrogen is spilled onto the low-energy binding sites such as the external wall or groove sites of nanotubes [13, 15]. Studies [16] demonstrate that one can achieve chemical storage of ~5 wt% of hydrogen in few-layer graphene. Using synchrotron spectroscopic techniques and density functional theory DFT calculations, it is shown [17] that only a sub-monolayer amount of hydrogen adsorption on the topmost

layer results in a transition of the entire few-layer graphene (FLG) film from a graphite-like to a diamond-like structure. It was found that the catalytic effect of few-layer, highly wrinkled graphene nanosheet (GNS) addition to  $\text{MgH}_2$  reflect on the dehydrogenation/rehydrogenation performance [18] – lower sorption temperature, faster sorption kinetics, and more stable cycling performance than that of pure-milled  $\text{MgH}_2$ .

Carbonaceous materials are attractive candidates for hydrogen storage because of a combination of adsorption ability, a high specific surface area, layered or pore microstructures, and a low mass density. In spite of extensive results available on hydrogen uptake by carbonaceous materials, the actual mechanism of storage still remains a mystery. Hydrogen molecule can interact with carbon surface through van der Waals attractive forces (physical sorption), or dissociate in atoms and are chemisorbed. The physical sorption of hydrogen limits the hydrogen-to-carbon ratio to less than one hydrogen atom per two carbon atoms (i. e., 4.2 wt.%), while in chemisorption, the ratio of two hydrogen atoms per one carbon atom (8.4 wt.%) is reported in the case of polyethylene [17–19]. Physisorbed hydrogen normally has a binding energy on the order of 0.1 eV, while chemisorbed hydrogen has C–H covalent bonding, with a binding energy of more than 2–3 eV [17]. The graphene has some advantages for hydrogen storage because the  $\text{sp}^2$  covalent-bonding arrangement of the carbon atoms in the honeycomb structure allows efficient binding to hydrogen atoms [19]. Graphene is stable, light, with high theoretical surface; it is mechanically flexible, and can be charged/discharged in room conditions through hydrogen-carbon binding on local curvatures [19].

As it can be concluded from the above review concerning experimental results only, reversible adsorption of hydrogen on graphene mostly studied at 77 K is not practically applicable and several challenges in practice still remain, such as control of the binding sites, porosities and functionalities. In our work, the natural and synthetic zeolites (clinoptilolite group) as nanoporous material and few-layer graphene layers as nanostructured material are subjects of research for reversible hydrogen adsorption/desorption. For enhancement of hydrogen storage, the chemical, electrochemical and extraction pyrolysis methods for intercalation of materials are performed with metal and non-metal species (Pd, Li, Mg).

In this chapter our research results have been summarized based on publications [20–22] about the role and properties of nanostructured carbon materials for hydrogen storage applications.

## 7.2. Methods to synthesize and research nanosized materials

Zeolite is a tetrahedral aluminosilicate structure stabilized by various cations. In the case of clinoptilolite, the ratio between Si/Al is  $> 4$ , and anionic lattice is supported by Ca, Mg, Na, K cations, which can be exchanged and in natural zeolites vary depending on the site of origin. Our samples of natural Clinoptilolite comes from Ukraine – Sokirnitza deposit (Ukraine, Transcarpathian region). Zeolite samples were prepared by ion exchange with  $\text{MgCl}_2$  (1 mol/l) and washing in deionized water solution. The 1 ml/l salt solutions were prepared to exchange cations in zeolite. For the magnesium, lithium and ammonia ion exchange the washed zeolite samples were placed in 1M salt solutions of  $\text{MgCl}_2$ ,  $\text{CH}_3\text{COOLi}$  and  $\text{ClH}_4\text{N}$ , respectively. The solutes were mixed by magnetic stirring in deionised water for 48 h at 40°C. After the ion exchange procedures, the samples were washed with deionised water at least 3 times and dried in air at 100 °C for 12 h. The zeolite

sample was characterized by XRD and EDS as natural clinoptilolite with some ferrite impurities (Table 7.2).

*Table 7.2. Natural Clinoptilolite with Si/Al Ratio 10.319 – EDS results*

Element	Series	Norm. at., %	Error, %
Aluminium	K – Series	2.619	0.219
Silicon	K – Series	28.808	1.889
Oxygen	K – Series	65.703	6.984
Potassium	K – Series	1.012	0.108
Sodium	K – Series	0.353	0.066
Iron	K – Series	0.538	0.106
Carbon	K – Series	0.314	0.391
Magnesium	K – Series	0.332	0.059
Calcium	K – Series	0.322	0.060

Doping of natural clinoptilolite with Pd has been done with extraction-pyrolysis method in 1 mol/l PdCl solution, stirring the zeolite sample at 60 °C for 24 h and then heating zeolite at 300 °C while vacuuming sample with fore-vacuum pump. Synthetic zeolite was obtained from precursors in hydro-thermal reactor. XRD and EDS analysis Table 7.3 showed that zeolite with clinoptilolite structure is obtained.

*Table 7.3. Synthesized clinoptilolite sample with Si/Al ratio 8.372 – EDS results*

Element	Series	Norm. at., %	Error, %
Oxygen	K – Series	62.038	5.859
Silicon	K – Series	29.635	1.883
Aluminium	K – Series	3.542	0.265
Potassium	K – Series	2.728	0.203
Sodium	K – Series	0.372	0.057
Magnesium	K – Series	0.088	0.033
Carbon	K – Series	1.597	0.345

To obtain few-layer graphene (FLG) sheet stacks, the electrochemical exfoliation was used [19], taking graphite industrial waste rod as working electrode. Electrochemical exfoliation of graphene is an alternative to the mechanical or oxidation-driven options for bulk production of graphene from parent graphite [20]. An applied voltage drives the ionic species in an electrolyte to intercalate into the graphite electrode and increase the inter-layer distance. For example, in ammonium sulphate, the sulphate ions and water molecules migrate into the interstitial regions of the graphite and locally form gas bubbles (such as SO<sub>2</sub>, O<sub>2</sub>), which forces adjacent sheets apart. We used pulse power supply, pulse sequence 3s : 5s on the working electrode -10 V/+10 V for the synthesis. Piece of graphite

crucible used from bronze metallurgy for recycling it to more useful material. Acidic electrolyte is used to find optimal parameters of exfoliation process (3s : 5s, 1 mol/l  $\text{H}_2\text{SO}_4$ ) during which sulphate ions migrate into graphite, and upon the reversal of current graphene sheets are separated from bulk material and reduced during the longer sequence of negatively charged platinum support electrode. Another important step is sample submerging in an ultrasound bath (24 kHz) for 3–24 h. Purification – thinnest sheet material is lightest and can be easily separated with centrifuge or sedimentation. To be sure that the resulting material is graphene, not graphene oxide, the FLG samples were annealed in  $\text{Ar}/\text{H}_2$  (95 : 5) gas flow 15 ml/min at 600 °C for 4 hours – providing higher degree of reduction. Intercalation with cations was done during exfoliation process, by adding 0.01 mol/l  $\text{MgCl}_2$ ,  $\text{Li}_2\text{SO}_4$  solution to 1 mol/l  $\text{H}_2\text{SO}_4$  solution.

### Analysis of material composition, structure and morphology

The initial samples were characterized by X-ray diffraction, SEM (Hitachi S-400N; Bruker D8), elemental composition of samples was determined by EDS analysis. FTIR spectra were obtained with Hyperion 80 experimental device. FTIR spectra were obtained in transmittance mode using chamber consisting of stainless steel and KBr and KSR-5 (Thallium Bromide-Iodide) glasses. Suspended material flakes in ethanol or acetone were evaporated on KSR-5 glass at RT and then vacuumed and heated up to 120–140 degrees using resistance heating near outer glass surface. Then samples were exposed to hydrogen atmosphere at 0.2 bar and allowed to cool down to RT.

### Gas sorption measurements

Hydrogen sorption experiments were done by volumetric – Sievert's type method. In sample holder (100 to 475K, 2 bar) attached to RGA-100 Mass spectrometer, to determine exhaust gases of sample and cleanliness of experiment (high vacuum in system and hermetic seal at all times). Registered data have been recalculated to desorption graphs, to show consistency and desorbed hydrogen values. Heating is realized at about 10 deg/min. and only the maximum sorption value is analysed. Our powder samples were tested in non-commercial system which allows to determine process endpoints more precisely than the values during sorption – desorption cycle. Recalculation of pressure difference against mass of sample and weight percent (wt%) of stored hydrogen in solid state are achieved. The second method to calculate amount of hydrogen absorbed in sample was gas analysis using HORIBA EMGA – 830 AC Hydrogen Oxygen Nitrogen gas analyser (experiment limited till 100 s due to sensor saturation). Using this method, the loaded sample was burned in He plasma and compared to hydrogen free samples, which had been degassed. The percentage of gas content was recalculated from the mass of sample.

## 7.3. Results and discussion of hydrogen absorption peculiarities in nanosized materials

Spectroscopic Raman method is applied to examine synthesized FLG material. Raman Spectroscopy shows, that obtained material, contains various signals at defect ranges, but the number of layers can't be precisely determined if there is not a single layer reference material (Fig. 7.1). In literature, similar Raman spectra [20] suggests that it is few-layered, based on the relationships between 2D and G peaks.

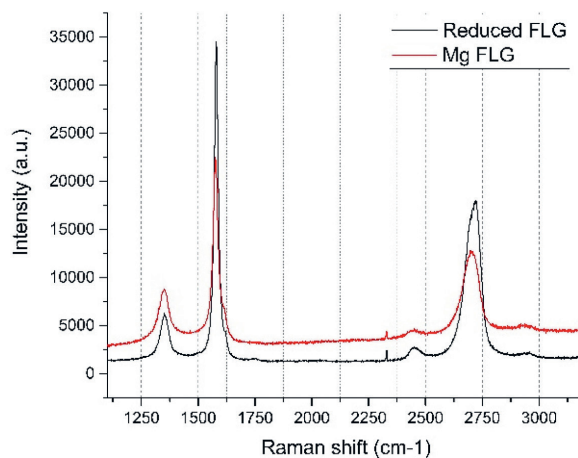
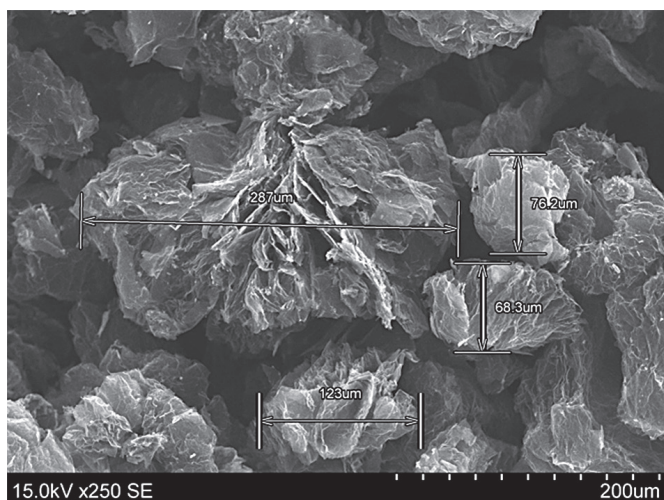


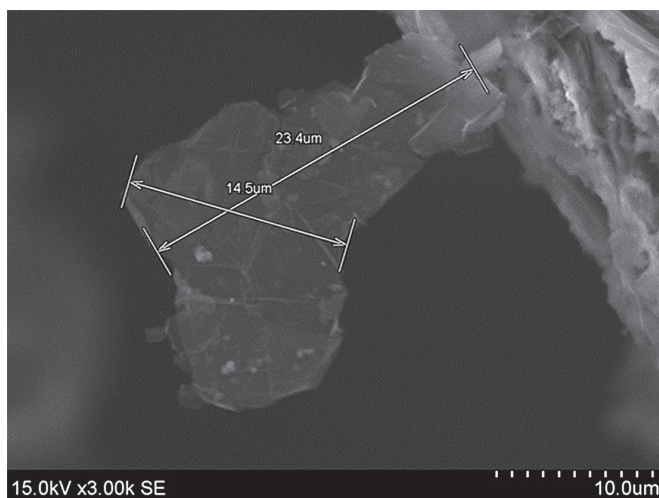
Figure 7.1. Raman spectra– red RLG un MG-FLG samples

SEM images allow to determine layered structure of FLG and result of reduction, layered structures, although present, have decreased in number and more defective surface is visible (Fig. 7.2 (a), (b)). Agglomeration occurs both in reduced and non-reduced samples. In case of graphene multi-layer stacks the reduction is important to increase surface area available for hydrogen adsorption. As it was measured with BET, the non-reduced Mg FLG sample showed significantly smaller surface area. Also, significant trend is clinoptilolite, most likely, it has nanopores, which allow for hydrogen sorption but almost does not show up at nitrogen porosimetry, but for FLG samples, most likely, there are open structures and plate surfaces are the sorption sites. Sievert type volumetric method in temperature region 100–400 K is applied to study an amount of adsorbed/desorbed hydrogen.

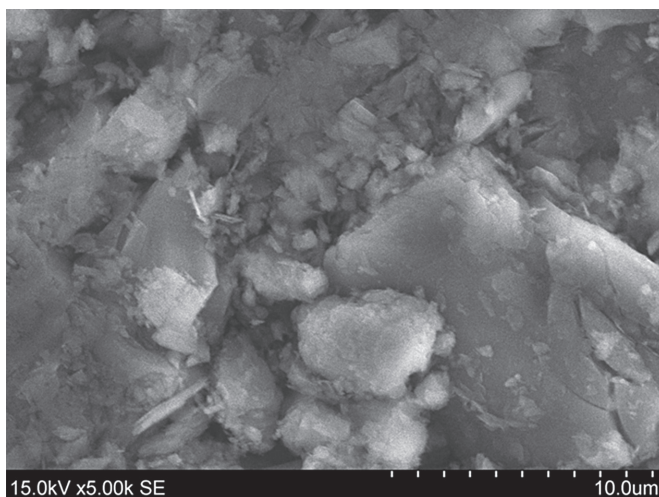
For zeolite, SEM images allow to visually interpret the size of particles and pores, although, samples easily polarize – being dielectric, and start moving at high energies of electron beam (Fig. 7.2 (c)).



(a)



(b)



(c)

Figure 7.2. FLG agglomerate (a), FLG sheet (b) and zeolite (c) after sonification and reduction

### Zeolite for hydrogen storage

The partial sorption level of clinoptilolite determined from volumetric measurements was ~1.1–0.6 wt%, also – after hydrogenation, natural clinoptilolite sample had changed color to greayer tone both in Sievert type device and in external hydrogenation apparatus for gas analysis measurements. XRD studies show that zeolite has indeed the heulandite type structure determined by XRF as Clinoptilolite. Gas analyser data showed hydrogen content for natural zeolite from 0.36–0.20 wt% (Table 7.4) [20] depending on the loading method (PCT apparatus or the external hydrogenation) for gas analysis measurements.

Table 7.4. Hydrogen desorption characteristics of measured samples [20]

Sample	Amount of desorbed Hydrogen, wt%	Temperature of desorption maximum, K	BET surface area m <sup>2</sup> /g	Pore volume mm <sup>3</sup> /g
Pd Clin	0.32	100	22.65	24.93
Mg FLG reduced	0.36	139	16.90	28.49
Li FLG reduced	0.30	143	16.90	28.49
Pd Clin FLG reduced 2.5%	0.20	100	–	–
Mg FLG	0.05	103	6.91	8.69
FLG reduced	0.04	100	16.25	18.17

### Few-layer graphene for hydrogen storage

For FLG samples, SEM pictures (Figures 7.2 (a) and (b)) show opened few-layer graphite/graphene structures with a higher surface area than if they were stacked together – determined by BET method – Mg FLG 0.43 m<sup>2</sup>/g and Reduced FLG – 12.4 m<sup>2</sup>/g. Calculated thickness from SEM pictures are around 37–54 nm as multilayer material up to 200 nm thickness, containing voids between graphene sheets of couple nm up to several μm. From the SEM pictures, the structures of graphene/graphite type. It was determined that chemical exfoliation produces open FLG structures. Reducing process breaks up the stacks of material, leaving open structures deep in the particles, but also exposing single sheets of FLG.

Results from hydrogen sorption experiments (Table 7.4) determined that reduced FLG samples do not show capabilities of high hydrogen storage, but cation exchanged graphene shows hydrogen storage capabilities at higher temperatures – this points to necessity to find even more useful intercalation atoms than Li or Mg to make material commercially and practically useful for hydrogen storage.

### Active carbon for hydrogen storage

Comparing the hydrogen adsorption performance of activated carbon (AC) from Latvian alder wood with few-layer graphene stacks FLGS intercalated with Li (Fig. 7.3) it can be seen that activated carbon (brown line) starts to adsorb hydrogen at temperature of approx. 230 K.

Calculated value of absorbed hydrogen mass in AC sample approaches 1.3 wt% and is promising value for further research and potential applications. Detailed analysis of the pressure and temperature output data for this sample (Fig. 7.4) shows pronounced hydrogen absorption region (coloured circle) with temperature and pressure oscillations, which indicate an exothermic reaction (heat is released).

If we consider mechanisms such as metal hydride formation, Li should not be favourable as low temperature hydride, but in our system – intercalated graphene surfaces, we are more concerned with stabilisation of defects in FLGS plates, thus Li FLGS is still considered because preliminary results (Fig. 7.4) show small but positive value – 0.1 wt% of adsorbed hydrogen starting from 170 K.

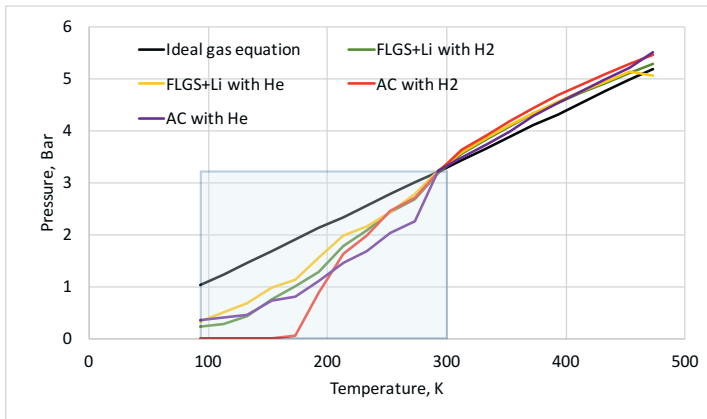


Figure 7.3. Pressure – temperature characteristics of two samples (AC and FLGS+Li) in two different atmospheres – helium and hydrogen. Only cooling curves are shown

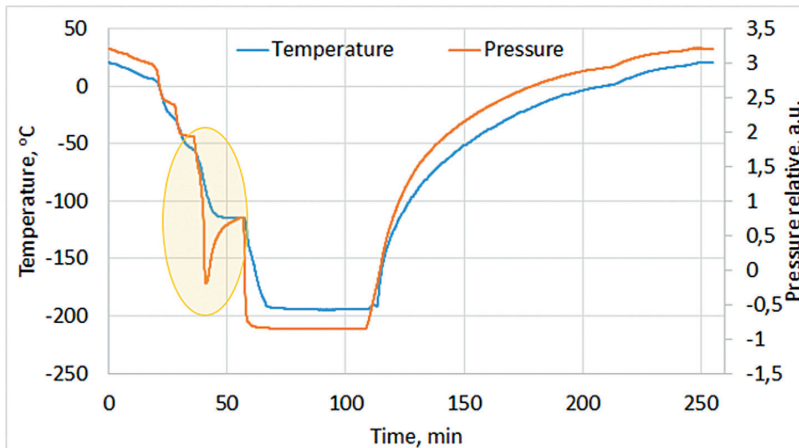


Figure 7.4. Pressure and temperature as function of time during cooling and heating sample AC in hydrogen atmosphere

## 7.4. Conclusions

XRD measurements show that analysed sample of natural zeolite is clinoptilolite with crystalline ferrierite and quartz impurities, but synthesized zeolite is clinoptilolite without impurities. Raman spectra approves the existence of graphene sheets in exfoliated few-layer graphite although wider spectra should be expected for FLG samples.

From volumetric measurements it is determined that the hydrogen uptake in natural zeolite at room temperature is around 0.6–1.1 wt%.

The pyrolytic gas analyser was applied to measure hydrogen amount in exfoliated few-layer graphite and the values – 0.39–0.46 wt% are obtained. Further studies are needed to intercalate graphene sheets – in few-layer graphite – with metal (Mg, Li, Pd) ions or larger anions to raise the amount of bounded hydrogen at a room temperature.

Modified FLG and clinoptilolite show higher desorption values for hydrogen, reaching up to 0.36 wt% at cryogenic temperatures. Non-reduced and non-modified FLG suggests that it is able to realize sorption on defects only at cryogenic temperatures, and this is also true for non-intercalated graphene at low hydrogen pressures. Mg and Li intercalation allows to reach higher temperature and wt% for hydrogen storage in FLG samples. As it is concluded from the results, intercalation of nanoporous zeolite materials is increasing the amount of bounded hydrogen.

Two type mechanisms to bind hydrogen with nanostructured material are proposed – strongly and weakly bonded to material, accordingly next mechanisms: (a) splitting of molecular hydrogen onto catalytic centres (introduced metals) into atomic hydrogen, spillover to specific surface states on substrate material (side defects, dopants); and (b) physical adsorption of molecular hydrogen. Desorption energy is higher for (a) type. Synergy between both adsorption mechanisms could increase amount of adsorbed hydrogen.

## 7.5. References

1. A Clean Planet for All. EC strategic long-term vision for a prosperous, modern, competitive and climate neutral economy by 2050. (2018) EC strategic long-term vision. Available at [https://ec.europa.eu/clima/sites/clima/files/docs/pages/com\\_2018\\_733\\_en.pdf](https://ec.europa.eu/clima/sites/clima/files/docs/pages/com_2018_733_en.pdf) (accessed November 30, 2018).
2. Bavykin, D. V., Zuttel, A., Borgschulte, A., Schlapbach, L. (eds.). (2008) Hydrogen as a Future Energy Carrier. *J. Appl. Electrochem.*, 38(10), 1483–1483.
3. Yoo, H, D; Markevich, E; Salitra, G; Sharon, D; Aurbach, D. (2014) On the challenge of developing advanced technologies for electrochemical energy storage and conversion. *Materials Today*, 17(3), 110–121.
4. International Partnership of Hydrogen Energy. Internet source <https://www.iphe.net/> (accessed November 30, 2018).
5. DOE-USA. DOE Hydrogen and Fuel Cells Program: Hydrogen Storage 2018: Available at <https://www.energy.gov/eere/fuelcells/doe-technical-targets-onboard-hydrogen-storage-light-duty-vehicles> (accessed November 11, 2018).
6. International Association for Hydrogen Safety. Internet source <https://www.hysafe.info/> (accessed November 28, 2018).
7. DOE-USA. Hydrogen Storage Materials Database – Search Page 2015. Available at <http://hydrogenmaterialssearch.govtools.us/> (accessed November 20, 2018).
8. Du, X. (2014) Molecular Simulation of Hydrogen Storage in Ion-Exchanged X Zeolites. *Adv. Mater. Sci. Eng.*, 1–10.
9. Klebanoff, L. (2012) Hydrogen Storage Technology: Materials and Applications – CRC Press Book.
10. Dong, J., Wang, X., Xu, H., Zhao, Q. and Li, J. (2007) Hydrogen storage in several microporous zeolites. *Int. J. Hydrogen Energy*, 32(18), 4998–5004.
11. Masika, E. and Mokaya, R. (2014) Exceptional gravimetric and volumetric hydrogen storage for densified zeolite templated carbons with high mechanical stability. *Energy Environ. Sci.*, 7(1), 427.
12. Weitkamp, J. (1995) Zeolites as media for hydrogen storage\*1, *Int. J. Hydrogen Energy*, 20(12), 967–970, Dec. 1995.
13. Sdanghi, Maranzana, G., Celzard, A., Fierro, V. (2018) Chapter 9, Hydrogen Adsorption on Nanotextured Carbon Materials. In: *Hydrogen Storage Technologies*, Sankir, M., Demirci Sankir, N. (eds.). Scrivener Publishing LLC, Wiley Online Library.
14. Broom, D. (2007) The accuracy of hydrogen sorption measurements on potential storage materials. *Int. J. Hydrogen Energy*, 32, 4871–88.

15. Zacharia, R., Rather, S., Hwang, S.W., Nahm, K.S. (2007) Spillover of physisorbed hydrogen from sputter deposited arrays of platinum nanoparticles to multi-walled carbon nanotubes. *Chem. Phys. Lett.* 434, 286–91.
16. Subrahmanyam, K. S., Kumar, P., Maitra, U., Govindaraj, A., Hembram, K.P.S.S., Waghmare, U. V., et al. (2011) Chemical storage of hydrogen in few-layer graphene. *Proc. Natl. Acad. Sci. U S A*, 108:2674–7.
17. Rajasekaran, S., Abild-Pedersen, F., Ogasawara, H., Nilsson, A., Kaya, S. (2013) Interlayer carbon bond formation induced by hydrogen adsorption in few-layer supported graphene. *Phys. Rev. Lett.* 111, 085503.
18. Liu, G., Wang, Y., Jiao, L., Yuan, H. (2014) Understanding the role of few-layer graphene nanosheets in enhancing the hydrogen sorption kinetics of magnesium hydride. *ACS Appl. Mater. Interfaces*, 6, 11038–46.
19. Tozzini, V. and Pellegrini, V. (2013) Prospects for hydrogen storage in graphene. *Phys. Chem. Chem. Phys.*, 15, 80–89.
20. Lesničenoks, P., Zemītis, J., Kleperis, J., Čikvaidze, G., Ignatāns, I. (2015) Studies of Reversible Hydrogen Binding in Nano-Sized Materials. Riga Technical University: Material Science and Applied Chemistry, 2015/31. doi: 10.7250/msac.2015.004.
21. Lesnicenoks, P., Zvine, M., Januskevica, A., Muzikants, V. L., Jurjans, M. K., Kaprans, K., Volperts, A., Kucinskis, G., Bajars, G., Dobeles, G., Kleperis, J. (2016) Nanostructured Carbon Materials as Promoters of Energy Storage. *Bulgarian Chemical Communications*, 48, Special Issue E2, 365–372.
22. Lesnicenoks, P., Grinberga, L., Jekabsons, L., Antuzevičs, A., Berzina, A., Knite, M., Taurins, G., Varnagiris, S., Kleperis, J. (2017) Nanostructured carbon materials for hydrogen energetics. *Journal of VBRI Press – Advanced Materials Letters*, 8(4), 518–523.
23. Prashant Tripathi, Ch., Ravi Prakash Patel, M. A. Shaz, O. N. Srivastava Synthesis of High-Quality Graphene through Electrochemical Exfoliation of Graphite in Alkaline Electrolyte 2012. Available at <http://arxiv.org/ftp/arxiv/papers/1310/1310.7371.pdf> (accessed November 20, 2018).
24. Achee, T. C., Sun, W., Hope, J. T., et al. (2018) High-yield scalable graphene nanosheet production from compressed graphite using electrochemical exfoliation. *Nature Scientific Reports*, 8, Article number: 14525.

## 7.6. Kopsavilkums

Rentgendifrakcijas mērījumi rāda, ka darbā analizētie dabiskā ceolīta paraugi ir klinoptilolīts ar kristāliska ferierīta un kvarca piejaukumiem, bet sintezētais ceolīts ir tīrs klinoptilolīts bez piejaukumiem.

Savukārt Ramana spektri pierāda, ka no grafitā eksfoliācijas procesā atdalītās plāksnes ir grafēns, lai gan spektrā būtu sagaidāmas platākas joslas tieši vairāku slāņu grafēnam.

Tilpuma metodē noteikts, ka ūdeņraža daudzums, ko spēj uzņemt dabiskais ceolīts istabas temperatūrā, ir 0,6–1,1 svara % (wt%).

Pirolītiskais gāzu analizators izmantots, lai izmērītu ūdeņradi gāzu sastāvā, kas rodas, hēlija plazmā sadedzinot paraugu. Atrasts, ka ūdeņradis paraugos ir 0.39–0.46 wt% apjomā. Jāturpina pētījumi, modificējot vairākslāņu grafēnu ar metāla (Mg, Li, Pd) joniem vai lielākiem anjoniem, lai palielinātu materiālā saistītā ūdeņraža daudzumu.

Modificētie vairākslāņu grafēna un klinoptilolīta paraugi zemās temperatūrās kā augstāko vērtību uzrāda 0,36 wt% ūdeņraža desorbcijas procesā. Izskatās, ka nereducēts un nemodificēts vairākslāņu grafēns spēj adsorbēt ūdeņradi uz defektainajām vietām tikai kriogēnās temperatūrās, kā arī pie paaugstinātiem spiedieniem. Mg un Li interkalācija vairākslāņu grafēnā ļauj sasniegt lielāku daudzumu adsorbētā ūdeņraža augstākās

temperatūrās. Kā var secināt no iegūtajiem rezultātiem, arī ceolītam jonu interkalācija palielina saistītā ūdeņraža daudzumu.

Divi mehānismi tiek piedāvāti, skaidrojot stipri saistīto un vāji saistīto ūdeņradi nanostrukturētā materiālā – (a) ūdeņraža molekulas sašķelšanās un atomāra ūdeņraža pārtecēšana (*spillover*) uz materiāla defektu vietām (slāņu malas, piemaisījumi) un (b) molekulāra ūdeņraža fizikāla adsorbēcija materiāla porās, starpplakņu spraugās. Lielāka desorbēcijas enerģija nepieciešama, lai atbrīvotu (a) tipa mehānismā saistīto ūdeņradi. Sinerģija starp abiem adsorbēcijas mehānismiem var palielināt adsorbētā ūdeņraža daudzumu.

## About authors



**Gunārs Bajārs, Dr. chem.,** e-mail: [gunars.bajars@cf.lu.lv](mailto:gunars.bajars@cf.lu.lv)

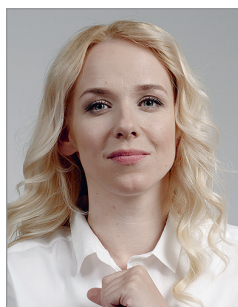
Senior researcher at *the Laboratory of Materials for Energy Harvesting and Storage*, Institute of Solid State Physics, University of Latvia (ISSP UL), is part of scientific staff of ISSP since 1979. His main research areas are materials and technologies for renewable energy sources, lithium ion batteries, photocatalysis, solar hydrogen technologies and sustainable development. Gunārs Bajārs is an author of 72 research papers, 4 books, 3 patents and 190 conference abstracts. He has participated in local and international projects on material science, ecodesign, energy and environment. Gunārs Bajārs is the member of International Societies of Electrochemistry and Solid State Ionics. Fields of specialization are material science, electrochemistry, solid state ionics, electrical and optical properties of materials, electrochromic phenomena, electrochemical storage devices, chemical gas sensors, electrolysis and photocatalysis.



**Sindija Briča-Zeltkalne, MSc. chem.,**

e-mail: [sindija.zeltkalne@lu.lv](mailto:sindija.zeltkalne@lu.lv)

Graduated chemistry programme in 2016, receiving master's degree at the University of Latvia, Riga. Research interests include synthesis and characterization of new surfactants.



**Ilze Dimanta, Dr. biol.,** e-mail: [ilze.dimanta@gmail.com](mailto:ilze.dimanta@gmail.com)

Researcher at the Faculty of Biology, University of Latvia, and scientific assistant at the Institute of Solid State Physics, University of Latvia. Her research is focused on biohydrogen production and storage possibilities in metal alloys, various waste substrate usage for hydrogen production and methane production. PhD studies completed in 2016 at the University of Latvia with internships in Austria, the University of Vienna Faculty of Physics and Lithuanian Energy Institute in Kaunas. An author/co-author of 12 research papers.



**Antonija Dindune, Dr. chem.,** e-mail: [Antonija.Dindune@rtu.lv](mailto:Antonija.Dindune@rtu.lv)

Leading researcher, Head of Laboratory of High Temperature Synthesis, Institute of Inorganic Chemistry, Riga Technical University, Faculty of Material Science and Applied Chemistry. Antonija Dindune has participated in various local and international projects related to the synthesis of inorganic phosphate and oxide compounds, glasses, crystal compounds and new condensed phosphates, and development of new materials, such as the solid electrolytes, ceramic and composite materials for bioceramic needs. She is an author of more than 220 scientific publications and one monograph. Member of the Latvian Council of Science Expert Commission for Chemistry, Expert of Promotion Council (Inorganic Chemistry) at the University of Latvia.



**Gaļina Dobele, Dr. habil. chem.,** e-mail: [gdobele@edi.lv](mailto:gdobele@edi.lv)

Gaļina Dobele acquired the title of engineer at Latvian Technical University in 1968, specialising in biologically active substances and the title of Dr. chem. at the Latvian State Institute of Wood Chemistry in 1984, awarded for her work in the field of thermocatalytical conversion of wood and wood components. Her Dr. habil. chem. title was received from the Latvian State Institute of Wood Chemistry for the research of levoglucosenone formation in the process of thermocatalytical pyrolysis in 1998. She held the position of a researcher in 1971–1989 at the Latvian State Institute of Wood Chemistry, and since 1990 she has held the position of head researcher. The main activities and scientific interests: fast and slow pyrolysis, carbon materials sorption theoretical and practical aspects and porous structure, liquid and solid products of lignocellulosics thermal degradation process and their chemical composition and properties. Her 256 publications include 1 monograph. H-index – 12. Co-author of 8 patents issued in Latvia and one international patent. Participated in different local and international projects related to plant biomass investigation.



**Līga Grinberga, Dr. phys.,** e-mail: [Liga.Grinberga@cfi.lu.lv](mailto:Liga.Grinberga@cfi.lu.lv)

Research scientist in Laboratory of Materials for Energy Harvesting and Storage at the ISSP UL. The main research areas are composites for hydrogen storage, material synthesis and characterisation for renewable energy applications. She has participated in and headed a number of local and international research projects and sub-projects, and currently involved in the H2020 teaming project. Specialization fields include material science, material synthesis and characterisation. Published more than 20 research papers and authored a chapter in a book.



**Artūrs Gruduls, MSc. biol.,** email: [arturs.gruduls@gmail.com](mailto:arturs.gruduls@gmail.com)

MSc. biol. degree received at the University of Latvia Faculty of Biology. The range of his scientific interests includes hydrogen technologies, biohydrogen, biogas technologies, microbial fuel cells. He has developed a number of prototypes for experiments and demonstration on international art exhibitions together with professional artists Rasa Šmite and Raitis Šmits. A couple of examples: simple bioreactor designed for hydrogen and methane gas producing microorganisms; “Pond Battery” installation in the Botanical Garden of the University of Latvia in 2014/15, and similar MBFC for demonstration abroad (Sweden, Denmark, Netherlands). An author of 5 publications.



**Liliya Jašina, MSc.,** e-mail: [liliya\\_jasina@inbox.lv](mailto:liliya_jasina@inbox.lv)

Her MSc degree was acquired at the Latvian State University, Faculty of Chemistry in 1983. Since 2004, she has held the position of engineer, and since 2006 works as a research assistant at the Latvian State Institute of Wood Chemistry. The main activities and scientific interests: characterization of a biomass and the components received on their basis (lignin, extractives substances) using UV (liquid and solid state), FTIR and Atomic Adsorption spectroscopy, characterization of sorption properties and porous structure of solid substances. The total number of publications – 7, H-index – 2. Participated in different local and international projects related to plant biomass investigation.



**Kaspars Kaprāns, MSc. ing.,** e-mail: [kaspars.kaprans@cfi.lu.lv](mailto:kaspars.kaprans@cfi.lu.lv)

Research assistant in the Laboratory of Materials for Energy Harvesting and Storage, the Institute of Solid State Physics, University of Latvia (ISSP UL), and has been a part of the scientific staff of ISSP since 2014. The main research areas are thin film electrodes for lithium ion batteries and synthesis of new composite materials for renewable energy sources. He has participated in various local projects related to material science; and is an author of 4 scientific publications. The fields of specialization include nanomaterials physics, material science, solid state ionics, methods for electrochemical investigation, materials for energy storage.



**Jānis Kleperis, Dr. phys.,** e-mail: [janis.kleperis@cfi.lu.lv](mailto:janis.kleperis@cfi.lu.lv)

Senior researcher and Head of the Laboratory of Materials for Energy Harvesting and Storage, the Institute of Solid State Physics, University of Latvia (ISSP UL), has been a part of scientific staff of ISSP since 1975. The main research areas are materials and technologies for renewable energy sources. He has participated in various local and international projects related to material science, energy and environment; and is an author of more than 200 scientific publications. The fields of specialization include semiconductor physics, material science, optical and electrical properties of materials, solid state ionics, electrochromic phenomena, chemical gas sensors, instruments with artificial intellect (electronic nose), hydrogen gas sensors, materials for hydrogen storage, hydrogen alloys for metal hydride batteries; electrolysis, membranes and MEA for fuel cells; DOAS for air pollution monitoring; air pollution measurement, emission calculations, forecasts.



**Ainārs Knoks, MSc. phys.,** e-mail: [ainars.knoks@cfi.lu.lv](mailto:ainars.knoks@cfi.lu.lv)

PhD student and researcher at the Laboratory of Materials for Energy Harvesting and Storage, the Institute of Solid State Physics, University of Latvia (ISSP UL). The main research areas include materials and technologies for renewable energy sources with focus on photocatalysis and synthesis of nanostructured TiO<sub>2</sub>. Ainārs Knoks has participated in various local and international projects related to material science and energy, specialization fields are semiconductor

physics, material science, optical and electrical properties of materials, electrochemical synthesis and investigation.



**Gints Kučinskis, Dr. phys.,** e-mail: [gints.kucinskis@cfi.lu.lv](mailto:gints.kucinskis@cfi.lu.lv)

Senior researcher at the Laboratory of Materials for Energy Harvesting and Storage at Institute of Solid State Physics, University of Latvia (ISSP UL), he is a part of scientific staff of ISSP since 2010, studied physics at University of Latvia. The main research areas include materials and technologies for lithium ion batteries. Gints Kučinskis is specialized in research of solid state mixed ionic and electronic conductors, material development for lithium ion batteries, deposition of thin films of lithium ion battery materials and elaborating fundamental working principles of materials for lithium ion batteries. He has worked with various lithium ion battery materials, including  $\text{LiFePO}_4$ ,  $\text{Li}_2\text{FeSiO}_4$ , graphene oxide,  $\text{LiNi}_{1/3}\text{Co}_{1/3}\text{Mn}_{1/3}\text{O}_2$ , LiPON,  $\text{Li}_2\text{SiO}_3$  and  $\text{Li}_4\text{Ti}_5\text{O}_{12}$ . Gints Kučinskis is an author of 8 research papers.



**Pēteris Lesničenoks, MSc.,** e-mail: [Peteris.Lesnichenoks@cfi.lu.lv](mailto:Peteris.Lesnichenoks@cfi.lu.lv)

PhD student of materials science at Riga Technical University, acquired his master's degree in materials science in 2015. His field of studies encompasses materials for hydrogen energetics, energy storage and gas sensors. Pēteris Lesničenoks is a researcher at the Laboratory of Energy Harvesting and Storage Materials, the Institute of Solid State Physics, University of Latvia, Kengragu iela 8, Riga, Latvia, and an author of more than 15 publications.



**Ingars Lukoševičs, BSc. phys., MSc.,**

e-mail: [ingars.lukosevics@cfi.lu.lv](mailto:ingars.lukosevics@cfi.lu.lv)

Graduated the bachelor's programme in physics at the University of Latvia, Riga in 2018. His research interests include nanosize carbon materials, such as exfoliated graphene, their structuring and physical methods of material characterization (morphology, structure, composition, electrical conductivity), formation of thin films for nitrogen oxide gas sensors, formation and structuring of catalysts on electrodes for electrochemical purposes.



**Vizma Nikolajeva, Dr. biol.,** e-mail: [vizma.nikolajeva@lu.lv](mailto:vizma.nikolajeva@lu.lv)

Leading researcher and associate professor at the University of Latvia Faculty of Biology. The Head of the Microbial Strain Collection University of Latvia, has participated in various local and international projects related to the development of antimicrobial and wound healing products and plant growth-promoting microorganisms, and to the research of biohydrogen production by anaerobic bacterial fermentation. She is an author of more than 100 scientific publications. Expert of the Latvian Council of Science in microbiology and biotechnology.



**Matiss Paiders**, BSc. biol., email: [mp14028@lu.lv](mailto:mp14028@lu.lv)

BSc. biol., engineer at the Institute of Solid State Physics, University of Latvia. Currently studying for a master's degree in biology at the University of Latvia. His research focuses on microbial hydrogen production from crude glycerol and microbial fuel cells.



**Juris Singatulovs**, MSc. chem.

Master's degree in chemistry received at the University of Latvia in 2017, research interests include ionic liquids and physical chemistry methods of material characterization.



**Einārs Sprūģis**, MSc. chem., e-mail: [einars8@gmail.com](mailto:einars8@gmail.com)

Master's degree in chemistry received at the University of Latvia in 2015, continuing with doctoral studies with specialisation in solid state polymer electrolytes for proton exchange membrane fuel cells. Research interests include polymer electrolytes and their composites with inorganic nanoparticles, and the methods for analysing these materials such as infrared spectroscopy, thermogravimetric analysis, electrochemical impedance spectroscopy.



**Guntars Vaivars**, Prof., Dr. chem., e-mail: [guntars.vaivars@cfi.lu.lv](mailto:guntars.vaivars@cfi.lu.lv)

Graduated the chemistry programme at the Latvian State University in Riga on 1983. On 1991 was awarded the degree of Dr. chem. by Latvian Academy of Science (thesis "Physical and Chemical Properties of Antimonic Acid Hydrates and Application in Electrochromic and Sensor Devices") with a specialization in electrochemistry and electrode process kinetics; 2001–2006 – postdoctoral studies at the University of Western Cape (Cape Town, RSA), South African Institute of Advanced Material Chemistry (SAIAMC, before 2004 –Porous Media Group). Since 2008 – lecturer and associate professor at the University of Latvia Faculty of Chemistry, and a senior researcher at the ISSP UL. The research activities since 1983 in numerous projects have been related to fuel cells and hydrogen economy. The research field encompasses electrochemistry, solid state chemistry and materials science of ion conducting materials, composites and energy producing devices. The research outputs are summarized in project reports and about 130 original papers and proceedings of international conferences (published in English, German, Russian, Latvian), including 8 patents.



**Aleksandrs Volperts, Dr. sc. ing.,** e-mail: [volperts@edi.lv](mailto:volperts@edi.lv)

Aleksandrs Volperts acquired his MSc degree at Riga Technical University in 1997 in the field of chemical processes and devices. He acquired a master of science degree at the Helsinki University of Technology in 1997 in the field of paper production. Dr. eng. chem. degree received at Riga Technical University in 2018 in the field of activated carbons and supercapacitors. Since 1998 he has held the position of research assistant at Latvian State Institute of Wood Chemistry, and since 2015 – researcher position. The main activities and scientific interests: synthesis of lignocellulosics based activated carbons with desired porous structure and characterization of their sorption properties. Total number of publications – 21, H-index – 7. Co-author of 1 patent issued by Latvian State and 1 international patent. Participated in different local and international projects related to plant biomass investigation.



**Andris Zicmanis, Prof., Dr. habil. chem.,** e-mail: [zicmanis@latnet.lv](mailto:zicmanis@latnet.lv)

He graduated chemistry engineering programme at Riga Polytechnic Institute, Riga in 1964, acquired his Dr. chem. degree in 1969 at Riga Polytechnic Institute (thesis “Unsaturated Cyclic Aminodiketones”), in 1992 was awarded the degree of Dr. habil. chem. (thesis “Polymer Supported Reagents and Catalysts in Organic Synthesis”) with specialization in fine organic synthesis. 1969–1990 – the Head of Laboratory and later a Deputy Director for research at the company “Biolar”, Olaine, Latvia. Since 1990 – Professor at the University of Latvia Faculty of Chemistry. The research activities since 1969 in numerous projects have been related to the elaboration of new methods in fine organic synthesis, including synthesis and applications of ionic liquids (during last 10 years). The research topics – organic synthesis, catalysis. The research outputs are summarized in more than 150 original research papers in English and Russian, over 120 presentations in international scientific conferences, as well as more than 50 patents acquired at the period of the Soviet Union.



**Aivars Žūriņš, Dr. sc. ing.,** e-mail: [aivarsz@edi.lv](mailto:aivarsz@edi.lv)

The engineer degree awarded for his work “Principal processes of the chemical industry and chemical cybernetics” at Riga Polytechnical Institute in 1979. Dr. sc. ing. degree received for his doctoral thesis “Ecological acceptable technology of the charcoal production and its realisation in practice” at Riga Polytechnical Institute in 1998. In 1998, he started his work in capacity of research assistant at the Latvian State Institute of Wood Chemistry, and since 2015 he is a researcher. Since 2012, he works as a leading researcher at the Latvian State Institute of Wood Chemistry, held the position of Institute director from 2010 to 2012. The main research activities and scientific interests include biomass thermochemical conversion, wood thermochemical processing, charcoal and activated carbon study and production. The total number of publications – 65, H-index – 7. Co-author of 9 patents issued by the state of Latvia. He has participated in various local and international projects related to plant biomass investigation, as well as lectured at Riga Technical University.





Nanostructured Composite Materials for Energy Storage and Conversion  
Nanostrukturēti kompozītmateriāli enerģijas uzkrāšanai un pārveidošanai

2019

---

Latvijas Universitātes Akadēmiskais apgāds  
Aspazijas 5, Rīga, LV-1050  
apgads@lu.lv